Measuring and modelling estuarine macroalgae blooms and water column nutrients

A thesis submitted in fulfilment
of the requirements for the degree of
Doctor of Philosophy in Earth Sciences
at
The University of Waikato
by
Marvin Alexander (Alex) Port

THE UNIVERSITY OF
WAIKATO
Te Whare Wānanga o Waikato

2016

Abstract

This thesis examines the dynamics of estuarine macroalgae blooms of the genus *Ulva* and the environmental factors controlling them, using process-based mathematical models as well as observation data from Tauranga Harbour (North Island, New Zealand).

Based on long-term monitoring datasets of water column nutrients, temperature and irradiance, the *Ulva* tissue nitrogen concentration is modelled using an algebraic short-term equilibrium solution to a classic set of ordinary differential equations describing tissue nutrient dynamics. A detailed sensitivity analysis of this equilibrium solution shows that although the variability in ambient concentration of inorganic nitrogen explains 60% of model output variance, the uncertainty in two of the most influential physiological parameters has a similar magnitude of influence (32% of variance). Repeated calibrations using an algorithm with random starting points and evolutionary adaptions lead to broad and in some cases multimodal distributions of physiological parameters. Although the model performs well in reproducing observations, calibrated parameter values from individual calibrations should therefore not be interpreted as reliable estimates of physiological properties.

Using a zero-dimensional simulation model of *Ulva* tissue nitrogen and phosphorus concentrations and biomass, seasonal and long-term population dynamics of *Ulva* are examined. Calibrating against a combination of all three state variables, long-term tissue nitrogen and biomass dynamics are reproduced well, while the seasonal amplitude of tissue phosphorus variability is underestimated. From the long-term observation datasets, seasonal scenarios are derived based on annual cosine fits to monthly percentiles of the observed forcing data. These scenarios represent above and below average seasons in the environmental conditions of ammonia, nitrate and phosphate concentrations in the water as well as temperature and irradiance. Comparison of the different scenarios points to the inorganic nitrogen concentrations (both ammonia and nitrate) as most influential in determining *Ulva* seasonal peak biomass and timing.

To improve upon the existing long-term observations of water column nutrients available for Tauranga Harbour, a sampling programme was designed taking into account the challenges of accurately measuring nutrients in a tidally dominated estuary with complex geometry. Samples were taken at consecutive ebb and flood tides at the same local tidal phase at sites representing distinct subregions within the estuary. Bimonthly samples at eight sites and fortnightly samples at two sites over one year show that the statistical distributions of nutrient fractions vary be-

tween sites and between tides. At the estuary mouth, phosphate is exported, while at site further upstream, ammonia and nitrate are exported. Modelling the passive transport of nutrients using a numerical hydrodynamical model shows differences in the connectivity between subregions, and in some cases mid-term upstream transport. The contribution of upstream subregions to individual sites changes rapidly during the tidal cycle, emphasising the importance of the local tidal phase. The data collected may help to improve the sampling design of the long-term monitoring programmes in Tauranga Harbour and provide a more accurate basis for future modelling studies of *Ulva* population dynamics.

Acknowledgements

First and foremost I would like to thank my supervisors for their guidance and diverse input over the last years: Karin Bryan, Conrad Pilditch, David Hamilton and Kai Bischof.

I would also like to thank all the other academic, technical and administrative staff members at the University of Waikato who have somehow been involved with this project. They are too many to count easily, and since I'm afraid if I start listing them individually I'll still forget one or two... I hope you'll still accept my heartfelt thanks if I say you know who you are :)

One extra mention that I would like to make is to the quite diverse group of people who have helped me in the field, including fellow students, technical staff, friends and volunteers (some of whom I'd never met before) willing to work at odd hours and under sometimes quite challenging conditions.

Thanks to all the friends and family near and far who have supported me in the years leading up and during my time as a PhD student.

The Bay of Plenty Regional Council provided the funding for my scholarship, living stipend and research expenses, as well historical data from environmental monitoring programmes in Tauranga Harbour.

The INTERCOAST programme, a joint graduate school between the University of Bremen and the University of Waikato, exposed me to a multitude of coastal research projects across disciplines, and facilitated my research stay with Kai Bischof's group at the University of Bremen, for which the New Zealand Ministry of Research, Science and Technology (MoRST) provided travel funding.

Previous publication and co-authorship statement

Chapter 2 was published in 2015 as "Algebraic equilibrium solution of tissue nitrogen quota in algae and the discrepancy between calibrated parameters and physiological properties", Ecological Modelling 312, pp. 281–291 (`http://dx.doi.org/10.1016/j.ecolmodel.2015.05.034`). The first author was (M.) A. Port and the co-authors were K. R. Bryan, C. A. Pilditch, D. P. Hamilton and K. Bischof. All the work presented was carried out by (M.) A. Port, and the co-authors contributed with discussions and revisions to the manuscript prior to submission.

Table of Contents

List of Figures

List of Tables

Chapter 1

General introduction

1.1 Background and relevance

The presence of unusually large amounts of benthic macroalgae in coastal and estuarine habitats, usually occurring seasonally, is often referred to as a "green tide" (Fletcher, 1996). Such events are drawing increasing attention both from the scientific community as well as the general public. Especially the accumulation and subsequent decomposition of macroalgae on the shoreline is a particularly conspicuous symptom. Green tides are now widespread, occurring regularly in several dozen countries around the world (Schramm and Nienhuis, 1996), and in extreme cases can lead to densities of accumulated biomass of up to 400 kg (wet weight) m^{-2} (Morand and Briand, 1996). This is not only a recent phenomenon. In 1911, Cotton reported "On the growth of *Ulva latissima* in excessive quantity with special reference to the *Ulva* nuisance in Belfast Lough" (Cotton, 1911) to the United Kingdom's "Royal Commission on Sewage disposal". While ecological consequences where apparently not of much interest at this time, concerns had been raised both about the "health of the population" and that "property in the vicinity is depreciated" (Cotton, 1910). This shows that already more than a century ago, excessive growth of benthic macroalgae such as *Ulva* spp. (sea lettuce) was an issue of public concern. Local residents as well as other recreational and commercial users of the affected areas often perceive green tides as a "nuisance" (Cousins, 2007, 2009, 2010; SunLive, 2010). The reasons for this are numerous and include macroalgae clogging boat motors, becoming entangled in fishing lines and nets, accumulating and decomposing on the shoreline (leading to unpleasant or even harmful concentrations of hydrogen sulphide in the air) or suppressing the desired growth of edible benthic fauna.

The different macroalgae species that contribute to nuisance blooms are not nec-

essarily closely-related. For example, both the phylum Chlorophyta (green algae) as well as Rhodophyta (red algae) include species involved in such blooms (Fletcher, 1996; Raven and Taylor, 2003). Nonetheless, most do share common characteristics, including a high ratio of surface area to volume and high growth rate (Raven and Taylor, 2003) as well as broad physiological tolerance (Fletcher, 1996). These are characteristics often co-occurring with "ephemeral" population dynamics, in other words blooms that usually include both an initial fast increase in population biomass as well as a similar magnitude of decrease at the end of the season, year or event (Raven and Taylor, 2003). In a list of world-wide reports of green tides compiled by Fletcher (1996), the majority of cases involve species of the genera *Ulva* or *Enteromorpha* (both Chlorophyta), the latter of which has since been reduced to synonymy with *Ulva* (Hayden et al., 2003).

Ephemeral species of *Ulva* and other genera of the family *Ulvaceae* have been introduced to a number of non-native habitats by human activities. Due to undesired ecological or economical impacts of their presence, they are then often referred to as "invasive" (in contrast to the less judgemental "introduced") species (Williams and Smith, 2007). In a global review of introduced seaweeds, Molnar et al. (2008) found the number of invasive species from the family *Ulvaceae* to be significantly higher than expected by chance. In contrast to species which grow excessively only in their role as an introduced species (usually due to the absence of predators or competitors in the new habitat), many *Ulvaceae* show this behaviour in their native habitat and are therefore sometimes also referred to as "proliferating" algae (Morand and Briand, 1996). In New Zealand, at least 19 distinct taxa of *Ulva* have been identified, including both native and introduced taxa (Heesch et al., 2007).

The research presented in this thesis is motivated by the documented but unexplained high interannual variability of *Ulva* abundance in Tauranga Harbour, an estuary on the east coast of the North Island of New Zealand. It seems unclear exactly which species of *Ulva* are involved in these blooms. Park (1996) found and identified *U. laetevirens*, *U. lactuca* and *U. rigida* based on morphological features, while Heesch et al. (2007) found and identified only *U. pertusa* and the unnamed "*U.* species 1" based on molecular sequencing data. Anecdotal reports of *Ulva* blooms in Tauranga Harbour can be traced back to around 1950, with first newspaper reports in 1988 (Park, 1996, p. 32). During seasons of particularly strong blooms (for example 1992), accumulations of up to 20 kg (wet weight) m^{-2} have been documented at individual sites (Park, 1996, p. 18). In response to public concerns, especially "about accumulations of algae on beaches" (Bioresearches, 1989), both the communal (Tauranga City Council, TCC) as well as regional administration (Bay

of Plenty Regional Council, BOPRC) have undertaken or commissioned a number of studies in this context (including: Bioresearches, 1989, 1991; de Winton et al., 1996; de Winton et al., 1998; Park, 2007, 2011). The factors that predominantly control or trigger blooms of *Ulva* in Tauranga Harbour are still unknown. Past and current hypotheses include the sporadic input of nutrients from coastal upwelling events (Park, 2007) as well as terrestrial, catchment-derived inputs (Bay of Plenty Polytechnic, 2010).

The aim of the research presented in this thesis is to help identify the role and relative importance of factors contributing to *Ulva* abundance in Tauranga Harbour, and more specifically further our understanding of why *Ulva* blooms have developed irregularly in only some years but not others since the early 1990s. The analysis is based on both empirical observations (pre-existing and collected within the scope of this thesis) as well as output from mathematical models. To complement previous work carried out using statistical analyses (Park, 1996, 2007, 2011), mechanistic / process-based mathematical models are now implemented and used both to recreate time series of biomass and tissue nutrients from the pre-existing data as well as to examine idealised scenarios derived from these data.

1.2 Thesis outline

In addition to this general introduction (Chapter 1), this thesis contains three main research chapters (Chapters 2, 3 and 4) as well as a general discussion (Chapter 5). Each of the three main research chapters is written to be as self-contained as possible within the thesis, to facilitate their separate publication as articles in peer-reviewed journals.

Based on a submodel of a classic, dynamic simulation model of *Ulva* growth and nutrient dynamics, Chapter 2 explores the influence of environmental conditions (nutrients, temperature and light) as well as uncertainty in physiological model parameters on the tissue nitrogen quota, a crucial component in biomass development. To this end, a unique algebraic solution of the short-term equilibrium of the tissue nitrogen quota is derived from the classic ordinary differential equation description using a computer algebra system.

The model for which the algebraic equilibrium solution was derived in Chapter 2 was also re-implemented as a zero-dimensional simulation model including *Ulva* biomass as a state variable. Forced with data from Tauranga Harbour, it was not able to reproduce the locally observed dynamics. It is possible that this is due to the strong coupling between dissolved oxygen concentrations and mortality in this

model, which in Tauranga Harbour may be less relevant due to relatively strong tidal mixing. Since historic data on dissolved oxygen are not available for Tauranga Harbour, this discrepancy was not explored further here. In the following chapter, a different model was therefore used, in which the description of *Ulva* mortality does not rely on dissolved oxygen concentrations.

In Chapter 3, a zero-dimensional simulation model which in addition to tissue nitrogen also includes tissue phosphorus and absolute biomass of *Ulva* as state variables is used to recreate time series of pre-existing observation data of these variables and examine different calibration strategies. Realistic annual scenarios representing years of unusually high and low values in the environmental forcing variables are derived from the pre-existing observation data and compared to determine which of these environmental factors are likely to have caused the difference in *Ulva* biomass dynamics between bloom and non-bloom years.

Both Chapter 2 and 3 highlight the importance of accurate observation data of water column nutrient concentrations for any *Ulva* modelling effort. Fieldwork was carried out over one year to address several shortcomings in the pre-existing nutrient data available for Tauranga Harbour, and these new nutrient data are presented and discussed in Chapter 4. A sampling programme was designed to assess both the short-term to seasonal as well as spatial variability of nutrient concentrations at different sites and in different subregions within the harbour. Physical transport processes influencing the nutrient dynamics are further explored with passive tracer modelling using a numerical hydrodynamical model. The data presented in this chapter are expected to be used in future work to improve the sensitivity analyses carried out in Chapter 2, the scenarios currently derived from only the pre-existing data in Chapter 3, and potentially also facilitate the calibration of a spatially explicit biogeochemical model of Tauranga Harbour.

Alongside the nutrient sampling programme described in Chapter 4, further fieldwork was carried out to collect data to support the future development of more detailed *Ulva* simulation models. Macroscopic characteristics of drifting *Ulva* populations were examined in samples captured in nets mounted in a rigid cage in a tidal channel (Appendix A), and the inter- and subtidal abundance of *Ulva* was recorded along cross-channel transects using a submersible video camera (Appendix B).

Chapter 2

Algebraic equilibrium solution of tissue nitrogen quota in algae and the discrepancy between calibrated parameters and physiological properties

Abstract

Tissue nutrient concentrations are a key factor in determining primary production in a variety of algae, for example the marine macroalga *Ulva*. We present a novel algebraic solution to calculate the equilibrium tissue nitrogen concentration or "quota" Q. The solution is derived from a classical mechanistic description of "luxury uptake" in marine macroalgae using a computer algebra system. Forced by ammonium (NH_4^+) and nitrate plus nitrite (NO_x^-) concentrations, water temperature and irradiance, equilibrium Q can be calculated directly without the need for numerical integration, and the model performs well in reproducing observations of Q in frondose *Ulva* spp. A Sobol' global sensitivity analysis reveals that the degree of uncertainty in physiological parameters has a similar magnitude of influence on model output as the typical environmental range of nutrient forcing data. The environmental forcing variables NH_4^+ and NO_x^- together account for 60% of variance in model output, while the two most influential physiological parameters together account for another 32% of variance. Repeated parameter calibrations with random first guesses and evolutionary adaptations lead to broad and even multimodal distributions for some parameters, as well as values at the extremes of their literature

ranges. This shows that although model performance as quantified by statistical measures is high, individual calibrations are not sufficient to give reliable parameter estimates that can be interpreted as physiological system properties.

Keywords: Ulva; tissue nitrogen; sensitivity analysis; calibration uncertainty

2.1 Introduction

Nuisance blooms of benthic marine macroalgae in coastal and estuarine environments have long been a cause for concern (Cotton, 1911) and lead to ecological, economic and societal problems, such as noxious odours, replacement of seagrass meadows or loss of benthic fauna due to anoxia (Valiela et al., 1997; Teichberg et al., 2010). In many cases, these blooms are dominated by species of the genus *Ulva*, including species previously classified as *Enteromorpha* (Hayden et al., 2003). For management and mitigation that goes beyond symptomatic treatment (e.g., bulk removal of macroalgae accumulations from the shoreline Liu et al., 2013), it is necessary to understand the diverse environmental factors leading to the high standing stocks observed. More recently, commercial harvest of *Ulva* spp. is also being explored as the basis for bioenergy production (Bruhn et al., 2011), where the chemical composition of the tissue (e.g., the ratio of carbohydrate to protein) determines yield and efficiency of the conversion.

For these and related questions, a number of process-based (or "mechanistic") mathematical models of *Ulva* spp. growth dynamics have been developed and applied for general scenarios (e.g., primary production regime shifts, Zaldívar et al., 2009) as well as specific case studies (e.g., Bendoricchio et al., 1994; Salomonsen et al., 1999; Brush and Nixon, 2010; Ren et al., 2014). For most applications, the model output of primary interest is either net primary production (growth) or absolute biomass (standing stocks). In both temperate and tropical waters ambient nutrient concentrations are often the limiting factor on these variables (Teichberg et al., 2010).

Ulva spp. is capable of "luxury uptake", (Fujita, 1985; Viaroli et al., 2005), an ability frequently found in ephemeral macroalgae (Campbell, 2001) that offers a competitive advantage in habitats with highly variable water column nutrient concentrations (Pedersen and Borum, 1997). For any dynamic model of such macroalgae, it is therefore crucial to describe this two-step process which potentially decouples nutrient uptake and growth in time. Droop (1968) first described this process for vitamin kinetics in microphytoplankton, where growth is based on the tissue or cell-internal concentration of a substance ("quota"), which in turn is based on the

external concentration in the medium. This concept was further developed first for phytoplankton (Nyholm, 1978) and later for macroalgae, leading to formulations such as the model developed by Solidoro et al. (1997) for *Ulva rigida*. Formulations equivalent or similar to the latter are now commonly implemented in marine macroalgae growth models (e.g., Coffaro and Bocci, 1997; Martins and Marques, 2002; Aldridge and Trimmer, 2009).

The submodel concerned with tissue nutrient concentrations is often parameterized based on controlled experiments in the laboratory. Solidoro et al. (1997) compared their submodel to laboratory data of nutrient concentrations in macroalgae tissue and the surrounding medium, on time scales of hours to days. Brush and Nixon (2010) compared simulation output from a similar submodel to field data with sampling intervals of weeks to months or two consecutive years. Comparisons with field data spanning the wide range of environmental conditions experienced on seasonal to interdecadal timescales, however, is rare, due to the labour- and cost-intensive requirement of collection and analysis of tissue nutrient samples. In addition, model studies on the time scale of years to decades usually explicitly simulate nutrient cycling and are analysed with regard to aggregate output variables such as standing stock biomass rather than tissue nutrient concentrations. Detailed analysis of individual submodels such as that describing tissue nutrient dynamics with long-term field data is therefore less likely to be carried out. Furthermore, the high computational cost of numerical integration schemes of mechanistic simulation models often prohibits extensive sensitivity analysis or repeated calibration procedures. Although individual calibrations may lead to high numerical model performance, the optimised set of parameters may not be sufficiently constrained, leading to "non-unique" calibrations (Janssen and Heuberger, 1995) and unrealistic values for some or all parameters, potentially determined by biases in the input data or deficiencies in model structure (Clark and Vrugt, 2006). Such "sloppy parameter sensitivities" have been found to be almost universal in systems biology models (Gutenkunst et al., 2007) and have recently also been identified in marine biogeochemical models (Ward et al., 2010). To date, they have not been examined in the context of macroalgae growth models, where individual calibrations prevail (e.g., Solidoro et al., 1997; Martins and Marques, 2002; Ren et al., 2014). A better understanding of how these issues influence macroalgae growth and especially tissue nutrient models will benefit both more complex coastal ecosystem models as well as potential stand-alone applications, e.g., examining macroalgae as suitable indicator organisms for environmental nutrient conditions (e.g., Ho, 1975; Barr, 2007) or computational metabolic modelling in the context of biofuel production

from macroalgae (Golberg et al., 2014).

The objective of this study is to assess whether the ranges of relevant physiological parameters for *Ulva* spp. models are known well enough to allow model applications without site-specific measurements of these parameters, and whether site-specific calibrations will in turn lead to well-constrained estimates of these parameters which can be interpreted as biological or ecological system properties, e.g., physiological adaption. To this end, we examine the tissue nitrogen quota submodel used in the *Ulva* spp. growth model of Solidoro et al. (1997). First we present a novel algebraic equilibrium solution obtained using a computer algebra system, which is valid for short-term (days to weeks) equilibrium conditions under the assumption of constant (laboratory) or averaged (field) water column dissolved inorganic nitrogen concentrations. We then analyse the sensitivity of this algebraic equilibrium solution to the range of uncertainty in physiological parameters as well as the range of variability in environmental conditions. Finally, we examine the uncertainty in site-specific parameter calibrations caused by underdetermined model behaviour.

2.2 Methods

2.2.1 Model description

Biomass of *Ulva* populations is difficult to estimate due to the advective transport of free-floating thalli and their frequent layered or clumped occurrence, leading to high-frequency variability in both space and time. Especially estimates of intertidal abundance should be interpreted as qualitative or relative rather than absolute values (e.g., as a "biomass index"; Ren et al., 2014). In contrast, the tissue nitrogen quota Q responds more slowly (averaging conditions over space and time), and is easily measured as an absolute concentration. We therefore focus on Q, which is better suited to the long-term but zero-dimensional (box-model) approach taken in this study, and do not explicitly model biomass. Changes in ambient concentrations of ammonium (NH_4^+) and nitrate plus nitrite (NO_x^-) caused by changes in biomass (uptake and decay/remineralisation) are consequently not represented in the model, and NH_4^+ and NO_x^- are considered only as environmental forcing (rather than state) variables. Figure 2.1 shows a conceptual diagram of the main model elements used in the present study, and a full list of variables and parameters is given in Table 2.1.

Solidoro et al. (1997) developed one of the first growth models for species of the genus *Ulva*, and similar or equivalent formulations are commonly used in macroal-

Table 2.1: Model parameter/variable symbols, descriptions, default values and units, adopting the notation of Solidoro et al. (1997) where possible. Symbols in italic script (NH_4^+, NO_x^-, Q, $Temp$ and Irr) denote environmental forcing data, variables which in a simulation model would be continuously variable in time, and in the short-term equilibrium model presented here are variable between independent evaluations for each date of a time series. Symbols in non-italic (roman) script denote parameters which are assumed to be constant over the time span of a simulation or evaluation period.

symbol	description	default value	unit
μ_{max}	maximum growth rate	0.016	h^{-1}
NH_4^+	external ammonium concentration	0.025	$mg\,l^{-1}$
$V_{mNH_4^+}$	maximum uptake rate for NH_4^+	5.2	$mg\,N\,(g\,dw)^{-1}\,h^{-1}$
$k_{NH_4^+}$	half saturation constant for NH_4^+	0.7	$mg\,N\,l^{-1}$
NO_x^-	external nitrate + nitrite concentration	0.05	$mg\,l^{-1}$
$V_{mNO_x^-}$	maximum uptake rate for NO_x^-	0.9	$mg\,N\,(g\,dw)^{-1}\,h^{-1}$
$k_{NO_x^-}$	half saturation constant for NO_x^-	0.07	$mg\,N\,l^{-1}$
Q	tissue nitrogen quota	–	$mg\,N\,(g\,dw)^{-1}$
Q_{min}	minimum Q	10	$mg\,N\,(g\,dw)^{-1}$
Q_{max}	maximum Q	45	$mg\,N\,(g\,dw)^{-1}$
k_c	Q growth limitation factor	8	$mg\,N\,(g\,dw)^{-1}$
$Temp$	temperature	16.7	°C
ζ_P	temperature factor	0.3	$°C^{-1}$
ϑ_P	reference temperature	10	°C
Irr	irradiance	60000	lux
I_0	irradiance factor	5800	lux

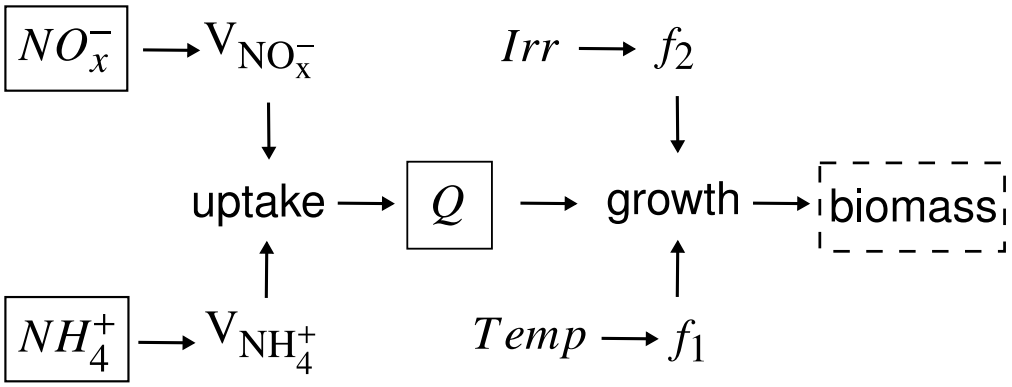

Figure 2.1: Conceptual diagram of the model structure, with elements defining the uptake and growth processes as used in the ordinary differential equations taken from Solidoro et al. (1997). Boxes indicate elements which in a dynamic implementation would be considered (nitrogen) mass balance compartments. Under the equilibrium assumption that uptake is equal to growth (Q has reached a steady state), we can derive an algebraic equilibrium solution for Q, termed Q^*. The dashed box around "biomass" indicates that in the formulation used in this study, biomass is not explicitly considered. For symbol definitions see Table 2.1.

gae growth models. Following this structure, the evolution over time of Q is determined by the rate of external nutrient uptake for tissue nitrogen quota and incorporation of nitrogen into new tissue biomass. For the simplest case of just one external nutrient, namely NH_4^+, the flux of external nutrients to tissue nutrient quota may then be defined as

$$V_{NH_4^+} = V_{mNH_4^+} \cdot \frac{NH_4^+}{k_{NH_4^+} + NH_4^+} \cdot \frac{Q_{max} - Q}{Q_{max} - Q_{min}} \tag{2.1}$$

where $V_{mNH_4^+}$ is the maximum uptake rate for NH_4^+, $k_{NH_4^+}$ the half-saturation constant for NH_4^+ uptake, and Q_{min} and Q_{max} the tissue nitrogen quota minimum and maximum concentrations, respectively. $V_{NH_4^+}$ is thus dependent on NH_4^+ via a rectangular hyperbolic (Monod / Michaelis-Menten / Holling type II) function, and on Q by a linear decrease from 1 to zero over the interval Q_{min} to Q_{max}. Ignoring any other potentially limiting factors for now, the flux of nitrogen from tissue quota to new tissue biomass depends on Q through

$$g_1(Q) = \frac{Q - Q_{min}}{Q - k_c} \tag{2.2}$$

where k_c is the growth limitation factor for Q. The relative growth rate μ when limited only by Q may thus be defined as

$$\mu = \mu_{max} \cdot g_1(Q) \tag{2.3}$$

where μ_{max} is the maximum growth rate. The evolution over time of Q is determined by the difference between uptake and growth:

$$\frac{dQ}{dt} = V_{NH_4^+} - \mu \cdot Q \tag{2.4}$$

$$\frac{dQ}{dt} = V_{mNH_4^+} \cdot \frac{NH_4^+}{k_{NH_4^+} + NH_4^+} \cdot \frac{Q_{max} - Q}{Q_{max} - Q_{min}} - \mu_{max} \cdot \frac{Q - Q_{min}}{Q - k_c} \cdot Q. \tag{2.5}$$

We now consider the equilibrium state in which the increase in Q due to the uptake of external nutrients is balanced by the decrease due to the incorporation into new tissue material:

$$\frac{dQ}{dt} = V_{NH_4^+} - \mu \cdot Q = 0 \tag{2.6}$$

$$V_{NH_4^+} = \mu \cdot Q \tag{2.7}$$

$$V_{mNH_4^+} \cdot \frac{NH_4^+}{k_{NH_4^+} + NH_4^+} \cdot \frac{Q_{max} - Q}{Q_{max} - Q_{min}} = \mu_{max} \cdot \frac{Q - Q_{min}}{Q - k_c} \cdot Q. \tag{2.8}$$

Additional terms influencing the flux of external (ambient) nutrients to Q may now be added on the left side of Eq. (2.8), and further terms influencing the flux of Q to new biomass to the right side of Eq. (2.8). We add terms for uptake of NO_x^- on the left and for the effect of temperature and irradiance on growth on the right. The second nutrient uptake term for NO_x^- is

$$V_{NO_x^-} = V_{mNO_x^-} \cdot \frac{NO_x^-}{k_{NO_x^-} + NO_x^-} \cdot \frac{Q_{max} - Q}{Q_{max} - Q_{min}} \tag{2.9}$$

where $V_{mNO_x^-}$ is the maximum uptake rate and $k_{NO_x^-}$ the half-saturation constant for NO_x^-. Growth limitation by the (water) temperature $Temp$ is described by

$$f_1(Temp) = \left[\left(1 + e^{-\zeta_P \cdot (Temp - \vartheta_P)}\right)\right]^{-1} \tag{2.10}$$

where ζ_P is the temperature coefficient and ϑ_P the reference temperature. Growth limitation by irradiance Irr is described by

$$f_2(Irr) = 1 - e^{-\frac{I_0}{Irr}} \tag{2.11}$$

The final description of the evolution over time of Q is thus

$$\frac{dQ}{dt} = (V_{NH_4^+} + V_{NO_x^-}) - \mu \cdot Q \cdot f_1(Temp) \cdot f_2(Irr) \tag{2.12}$$

and in equilibrium

$$V_{NH_4^+} + V_{NO_x^-} = \mu \cdot Q \cdot f_1(Temp) \cdot f_2(Irr). \tag{2.13}$$

Solving for Q using a computer algebra system ("Sage"; Stein et al., 2013), we obtain the algebraic equilibrium solution Q^* (available in the online supplementary material). Preliminary simulations with the ODE model showed that equilibrium concentrations of Q were reached after a maximum of approximately 10 days simulation time. We therefore consider Q^* to represent a "short-term" equilibrium, under the assumption of constant or rather averaged environmental conditions of NH_4^+, NO_x^-, $Temp$ and Irr over a time scale of days to weeks. Although it is rather unwieldy, it is a unique solution and may easily be evaluated directly for any given values of environmental conditions and parameters.

2.2.2 Case study location, organism and data sources

Our case study is based on an approximately bimonthly dataset documenting the high seasonal and interannual variability of *Ulva* spp. tissue nitrogen quotas over 20 years in Tauranga Harbour, a mesotidal estuarine lagoon on the east coast of the North Island of New Zealand. It is unclear which species of *Ulva* are involved in the blooms occurring here, with Park (1996) reporting *U. laetevirens*, *U. lactuca* and *U. rigida* based on morphological features, while Heesch et al. (2007) found and identified only *U. pertusa* and the unnamed "*U.* species 1" based on molecular sequencing data. We will therefore consider frondose *Ulva* spp. in general, hereafter referred to simply as *Ulva*.

Observation data of *Ulva* tissue nitrogen quota and water column dissolved inorganic nitrogen (DIN, comprising NH_4^+ and NO_x^-) concentrations were provided by the Bay of Plenty Regional Council. For the water column DIN concentrations, the observation period spans 18 years from 1991 to 2009, while the *Ulva* tissue nitrogen quota data extend from 1991 to early 2012. For details of the relevant sampling and analysis methodology see Park (1996).

Tissue nitrogen quota data were from site 1a in the northern basin of Tauranga Harbour and sites 2 and 3 in the southern basins, as shown in Figure 2.2. Water column DIN data were from the same sites except for the case of site 1a, where water column DIN data were not available, and data from the separate site 1b were used instead. This site was chosen since among those available, it is expected to be most similar in environmental conditions to site 1a. Water column DIN data from three additional monitoring sites in Tauranga Harbour were added to the dataset

only to obtain a more reliable estimate of the 95th percentile upper bounds for the sensitivity analysis described below.

Water column DIN and *Ulva* tissue nitrogen samples were not always available from the same date. In such cases, the *Ulva* tissue nitrogen data were linearly interpolated in time if samples from dates within 90 days of the missing date were available. If no such samples were available, this date was not considered for the analysis. Water column DIN data were not interpolated, and only dates when both NH_4^+ and NO_x^- data were available were considered.

Solar irradiance was measured by an automated weather station at Tauranga airport (see Figure 2.2) and was freely available via New Zealand's National Climate Database ("CliFlo", http://cliflo.niwa.co.nz, station agent number 1615 / "Tauranga Aero AWS"). Irradiance is reported for the 400 to 700 nm photosynthetically active radiation (PAR) band in units of MJ m^{-2} day^{-1}. Data were converted to lux assuming a photoperiod of 12 hours and the equivalences of 1 MJ = 4.6 mol as well as 1 µmol m^{-2} s^{-1} = 56 lux. To account for vertical attenuation of irradiance in the water column to derive approximate in situ values from these surface measurements, we assumed an attenuation coefficient of 0.4 m^{-1} and a water depth of 0.9 m, corresponding to the approximate depth at which the *Ulva* tissue samples were collected. Water temperature data were provided by the Port of Tauranga and were based on measurements from a sensor at "Salisbury Wharf" (see Figure 2.2). The same solar irradiance and water temperature data were used to "force" the algebraic equilibrium solution at all three sites examined.

The time series of environmental forcing variables solar irradiance, water temperature and water column DIN concentrations are shown together in Figure 2.3.

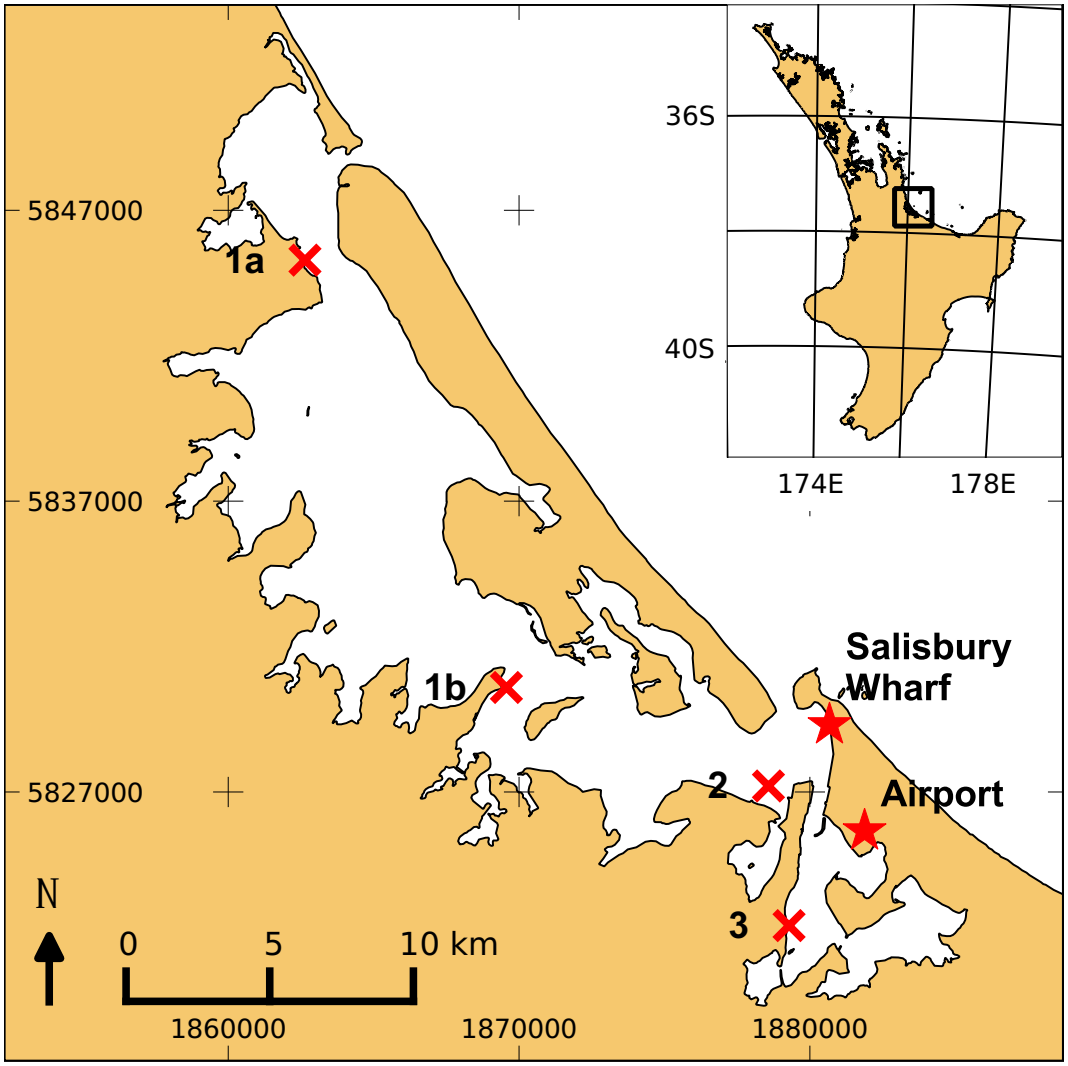

Figure 2.2: Map of the southern basin of Tauranga Harbour (inset: location of Tauranga Harbour on the North Island of New Zealand) and location of sites for water column DIN, *Ulva* abundance and *Ulva* tissue nitrogen data. From north to south, the sites are: 1a ("Ongare"), 1b ("Omokoroa"), 2 ("Otumoetai") and 3 ("Town Reach" or "Grace Street"). Water temperature was measured at "Salisbury Wharf" and irradiance at the (Tauranga) "Airport". Map projections are NZTM2000, main map with coordinates in metres, inset map with coordinates in degrees.

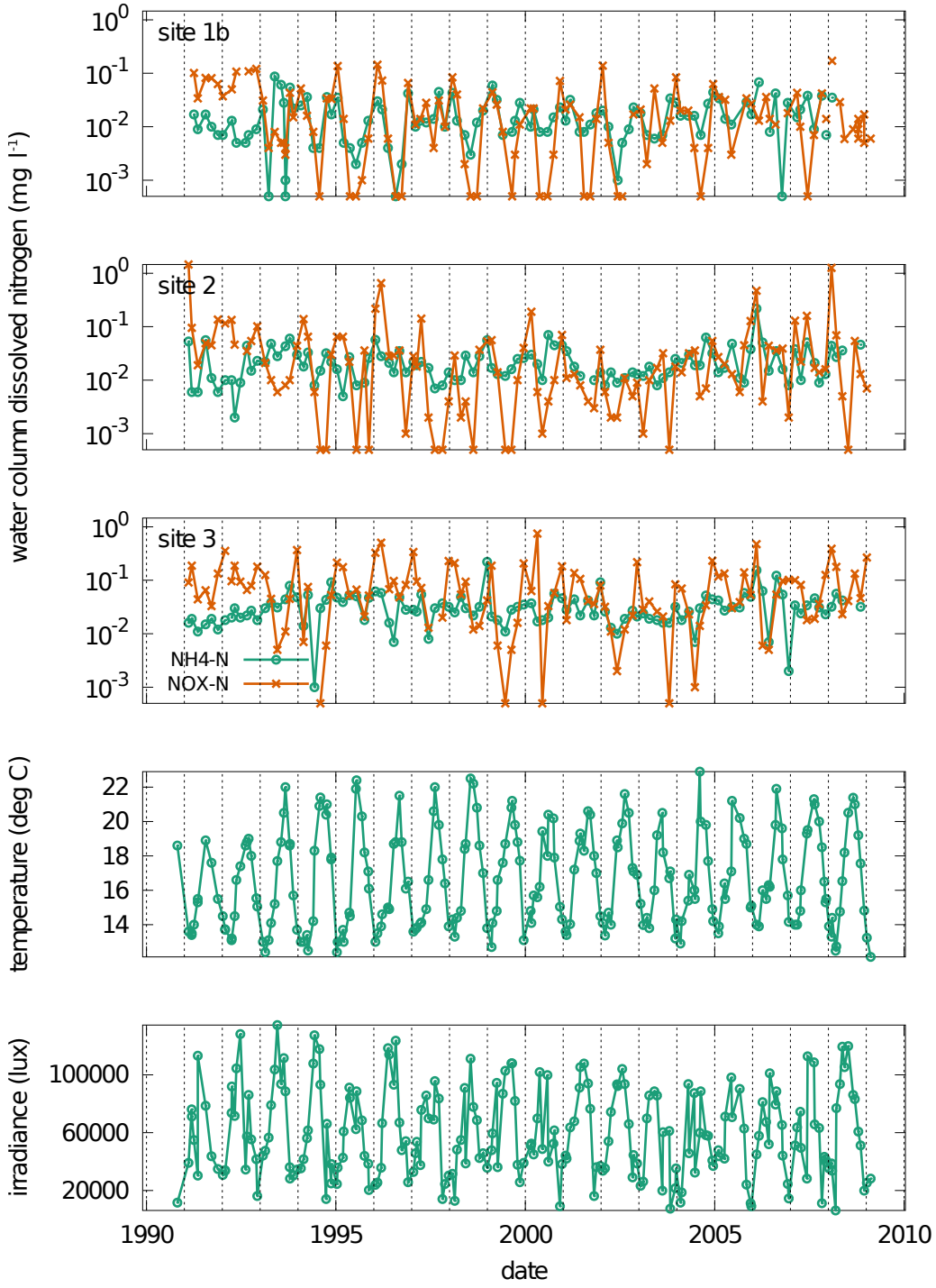

Figure 2.3: Time series of the environmental forcing variables, from top to bottom: water column dissolved inorganic nitrogen species NH_4^+ and NO_x^- for each of the three Tauranga Harbour sites, as well as water temperature and irradiance from Salisbury Wharf and the airport, respectively, and assumed to be representative for all three sites. Dashed vertical lines show the 1st of July of each calendar year to indicate average winter minima timing of temperature and irradiance.

2.2.3 Calibration and sensitivity analysis

The model was calibrated using the "controlled random search with local mutation" (CRS2-LM) global optimisation algorithm (Kaelo and Ali, 2006; Johnson, 2013). CRS2-LM is randomly initialised and introduces random "mutations" in further iterations, so that repeated calibrations may lead to different local optima. The parameters' distributions from repeated calibrations can be examined to give insight into the reliability of any individual calibration. Since this algorithm does not allow for the consideration of "inequality constraints" (e.g., the constraint of $Q_{min} < Q_{max}$, or $k_c < Q_{min}$), care must be taken when choosing lower and upper bounds for the parameter ranges, so that meaningless combinations of parameter values are excluded.

The years 1991 to 1999 were used as the calibration period, and the years 2000 to 2009 as the validation period. The objective function was defined to be the mean absolute deviation between modelled and observed values, which here is deemed the preferred measure of model performance, compared to, for example, the root mean square deviation (Willmott, 1982; Willmott and Matsuura, 2005). The algorithm was terminated when the relative change in the cost function, one or more of the parameters, or both, was less than 0.1%, or when the number of model evaluations was $\geq 20 \cdot k$.

The tissue nitrogen quota equilibrium solution Q^* was evaluated independently for each point of the timeseries of NH_4^+, NO_x^-, $Temp$ and Irr data for the sensitivity analysis and calibration as well as the final model evaluations. Absolute values of model Q^* are shown as time series, however, to ease interpretation and comparison with the observation data time series.

Model parameter ranges (Table 2.2) and default values (Table 2.1) were surveyed in the literature, from published models utilising the same mathematical description of tissue nitrogen quota dynamics as described here. Ranges for the environmental forcing nutrient concentrations (NH_4^+ and NO_x^-) were based on the local observation data from Tauranga Harbour. The lower bounds were set to zero, and the upper bounds to the maximum of the 95th percentiles calculated separately for six different sites around the harbour, from nutrient monitoring data based on samples taken in the period from April 1991 until August 2009. Arithmetic mean values for for Tauranga Harbour were used as defaults for other forcing variables ($NH_4^+ = 0.025\,\mathrm{mg\,l^{-1}}$, $NO_x^- = 0.05\,\mathrm{mg\,l^{-1}}$, $Temp = 16.7\,°\mathrm{C}$ and $Irr = 60000\,\mathrm{lux}$).

To assess the relative importance of uncertainty in physiological parameters of the model, as well as uncertainty and natural variability in the environmental forcing data (NH_4^+, NO_x^-, $Temp$ and Irr), a sensitivity analysis (SA) was carried out (Saltelli et al., 2000; Loucks et al., 2005). Due to the relatively low number of parameters

Table 2.2: Model parameter ranges derived from the literature. Rates per day were converted to rates per hour for calculations. In cases where only a single value was found, the range was set to that value ±10%.

symbol	value	unit	reference
$V_{mNH_4^+}$	2	mg N (g dw)$^{-1}$ h^{-1}	Coffaro and Bocci (1997), Bendoricchio et al. (1994), Guimaraens et al. (2005)
	5.2	mg N (g dw)$^{-1}$ h^{-1}	Solidoro et al. (1997)
	8.5	mg N (g dw)$^{-1}$ h^{-1}	Solidoro et al. (1995)
$k_{NH_4^+}$	0.1	mg N l^{-1}	Solidoro et al. (1995)
	0.5	mg N l^{-1}	Coffaro and Bocci (1997), Bendoricchio et al. (1994), Guimaraens et al. (2005)
	0.7	mg N l^{-1}	Solidoro et al. (1997)
$V_{mNO_x^-}$	0.45	mg N (g dw)$^{-1}$ h^{-1}	Solidoro et al. (1995)
	0.7	mg N (g dw)$^{-1}$ h^{-1}	Coffaro and Bocci (1997), Guimaraens et al. (2005)
	0.9	mg N (g dw)$^{-1}$ h^{-1}	Solidoro et al. (1997)
$k_{NO_x^-}$	0.05	mg N l^{-1}	Solidoro et al. (1995)
	0.07	mg N l^{-1}	Solidoro et al. (1997)
	0.25	mg N l^{-1}	Coffaro and Bocci (1997),Guimaraens et al. (2005)
Q_{max}	42	mg N (g dw)$^{-1}$	Solidoro et al. (1995)
	45	mg N (g dw)$^{-1}$	Solidoro et al. (1997)
	40	mg N (g dw)$^{-1}$	Coffaro and Bocci (1997), Bendoricchio et al. (1994)
Q_{min}	10	mg N (g dw)$^{-1}$	Solidoro et al. (1995), Solidoro et al. (1997), Coffaro and Bocci (1997), Bendoricchio et al. (1994)
μ_{max}	0.3	day^{-1}	Öberg (2005)
	0.36	day^{-1}	Lapointe and Tenore (1981), Guimaraens et al. (2005)
	0.4	day^{-1}	Coffaro and Bocci (1997)
	0.45	day^{-1}	Solidoro et al. (1995), Solidoro et al. (1997), Bendoricchio et al. (1994)
	0.5	day^{-1}	Henley and Ramus (1989)
k_c	8	mg N (g dw)$^{-1}$	Solidoro et al. (1997)

in the model, an initial screening to reduce the number of parameters considered in further analyses was not necessary. Following Wainwright et al. (2013), we carry out a local, one-(factor-)at-a-time (OAT) SA as a first step, followed by the global, variance-based method of Sobol' (1990, 1993). This method has been successfully applied to similar models examining *Ulva* in coastal lagoon systems, for example by Pastres et al. (1999) to a dynamic simulation model with higher complexity (15 state variables) on a shorter time scale (one year). Although computationally more efficient algorithms are available, for example the Fourier amplitude sensitivity test (FAST, Cukier et al., 1973), since evaluating the algebraic steady-state solution in this study requires very little computation time, preference was given to the straightforward sampling and analysis procedure of Sobol'.

Sobol' first-order sensitivity indices S_i for each of the k model parameters may be interpreted as quantifying the fraction of total model output variance which would disappear if that parameter were fixed. In this method, all S_i values are normalised by the total variance of model output, so that their sum is equal to one. "Total-order" or "total-effect" sensitivity indices S_{Ti} indicate the total contribution of a parameter to model output variance including all interaction effects with other parameters. A sample size of $N = 10000$ was deemed adequate after examining both the convergence of the sensitivity indices for increasing N (in intervals up to $N = 20000$) as well as the absolute values of the indices' bootstrapped (1000 resamples) 95% confidence intervals. Using the modified quasi-Monte Carlo sampling method of Saltelli (2002), estimates for first-order as well as total sensitivity indices were calculated for the $k = 10$ model parameters using $N \cdot (2 \cdot k + 2) = 220000$ model evaluations.

The Sobol' SA was performed for four different scenarios. In scenario 1, the physiological parameters were varied by ±10% around their default values, while the DIN concentrations were held fixed at default values for Tauranga Harbour. In scenario 2, both the physiological parameters as well as the DIN concentrations were varied by ±10% around their default values. In scenario 3, the physiological model parameters were varied over their literature range, while the DIN concentrations were again fixed at default values as in scenario 1. In scenario 4, the physiological parameters were varied over their literature range as in scenario 3, and the DIN concentrations were varied over the range for Tauranga Harbour. Scenario 4 thus represents most accurately the degree of uncertainty in our present knowledge of the physiological model parameters as well the range of variability in environmental conditions at the study sites.

To examine the uncertainty in the calibration results, the calibration procedure

with the initial setup was repeated 100 times with random initialisation and local mutation. Additionally, 100 calibrations were run with "scaling factors" $s_{NH_4^+}$ for NH_4^+ and $s_{NH_4^+}$ for NO_x^- added to the set of existing parameters. The NH_4^+ and NO_x^- values were multiplied by the corresponding scaling factor. The calibration range for both scaling factors was set to the interval between 0 and 2.

2.3 Results

Ulva tissue nitrogen quota observations are shown in Figure 2.4, together with calibrated model results. In the observation data, most seasons show a winter maximum, followed by a sharp decrease to lower levels within two to four months. Some individual seasons deviate from this general pattern, for example in 1997/1998, when site 2 shows a decrease relatively late in summer. In the same season, site 1a shows no clear summer minimum, with values instead fluctuating just below 20 mg N (g dw)$^{-1}$ over almost the entire season. Seasonal minima show much lower variability between years than seasonal maxima. Summer minima at site 1a are often lower than at the other two sites, and repeatedly fall below 10 mg N (g dw)$^{-1}$. Average values and winter maxima are highest at site 3, at up to 40 mg N (g dw)$^{-1}$.

2.3.1 Individual calibrations and model performance

Optimised values of the model parameters after separate calibration for each site against data from the calibration period are shown in Table 2.3. For all three sites, $V_{mNH_4^+}$ is at the minimum and $k_{NH_4^+}$ at the maximum of the prescribed range. $V_{mNO_x^-}$ for sites 2 and 3 is at the maximum, and at an intermediate value for site 1a/b, while $k_{NO_x^-}$ for site 1a/b and 2 is at the minimum and for site 3 at the maximum. A large proportion of calibrated values is at or near the limit of the assigned range, with only a few intermediate values. The latter occur also for several parameters for which the model shows a very low sensitivity, e.g., ζ_P and I_0.

After calibration for each site separately, the model was evaluated again for all dates with the parameter values optimised for the respective site. The results are shown together with the observation data and model validation performance statistics in Figure 2.4. Until 1994 the vast majority of observations were below 15 mg N (g dw)$^{-1}$ at site 1a/b, with short periods of rapid increase in summer, while during this period the model predicts values approximately 10 mg N (g dw)$^{-1}$ higher, with very little seasonal variation. From 1994 until the end of the calibration period in 1999, the observed seasonal variation is higher, and is closely matched by the model. During the validation period, the model follows most seasonal variations well, but keeps summer minima at a similar level as during the calibration period, while multiple observations of summer minima are now below 10 mg N (g dw)$^{-1}$). At the same time, winter maxima are also overestimated, leading to a Pearson correlation coefficient of 0.48 ($p<0.01$) or r^2 of 0.23, mean relative error (MeanRE) of 29% and positive bias of 2.4 mg N (g dw)$^{-1}$. At site 2, with the exception of several individual winter maxima, the model again generally overestimates in the first half

Table 2.3: Results of individual model calibrations for each of the three Tauranga Harbour sites separately, using the CRS2-LM algorithm and calibration period 1991-1999.

symbol	unit	default value	site 1a/b	site 2	site 3
$V_{mNH_4^+}$	mg N (g dw)$^{-1}$ h^{-1}	5.2	2.000	2.000	2.000
$k_{NH_4^+}$	mg N l^{-1}	0.7	0.700	0.700	0.700
$V_{mNO_x^-}$	mg N (g dw)$^{-1}$ h^{-1}	0.9	0.656	0.900	0.900
$k_{NO_x^-}$	mg N l^{-1}	0.07	0.050	0.050	0.250
Q_{min}	mg N (g dw)$^{-1}$	10	11.000	11.000	11.000
Q_{max}	mg N (g dw)$^{-1}$	45	40.000	40.000	45.000
k_c	mg N (g dw)$^{-1}$	8	7.200	7.200	7.200
μ_{max}	h^{-1}	0.016	0.017	0.017	0.011
ζ_P	°C^{-1}	0.3	0.270	0.330	0.275
ϑ_P	°C	10	11.000	9.000	11.000
I_0	lux	5800	5220.000	5220.000	5658.269

of the calibration period. During the validation period, the majority of summer minima are still slightly overestimated, while some winter maxima are underestimated, resulting in the model's seasonal range in most cases being smaller than that of the observations. At site 2, the Pearson correlation coefficient is 0.43 ($p<0.01$) and r^2 is 0.18, the MeanRE 23% and there is a small positive bias of 0.2 mg N (g dw)$^{-1}$. Site 3 also shows relatively high observation values in the first years of the observation period, which at this site are well reproduced by the model, while the second half of the calibration period has very few observation data points compared to the other sites. In the validation period, observation values are generally higher than at the other sites, with several summers staying above 15 mg N (g dw)$^{-1}$, but also the highest number of missing values of all three sites. Although the model underestimates a number of observation dates, the Pearson correlation coefficient of 0.66 ($p<0.001$) or r^2 of 0.44 is still the highest of the three sites together with the lowest MeanRE of 19% and a negative bias of -1.9 mg N (g dw)$^{-1}$.

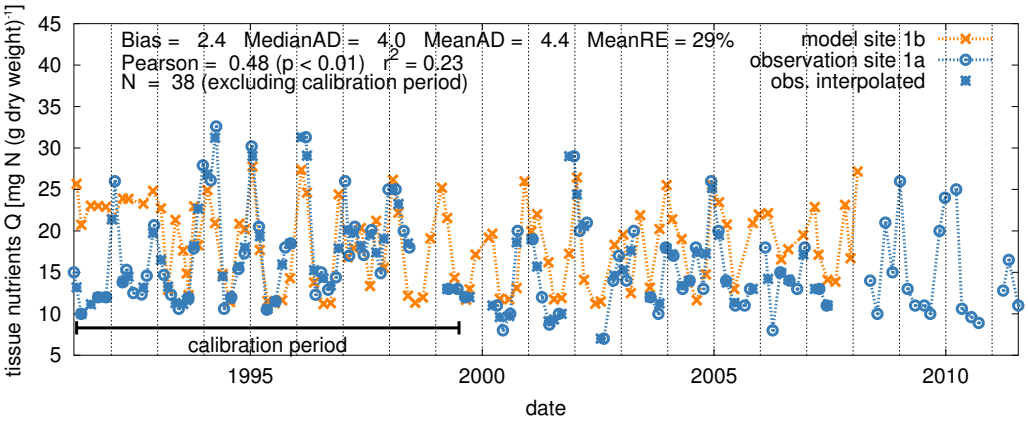

(a) tissue nitrogen model Q* (based on site 1b NH_4^+ and NO_x^- data) vs. observations site 1a

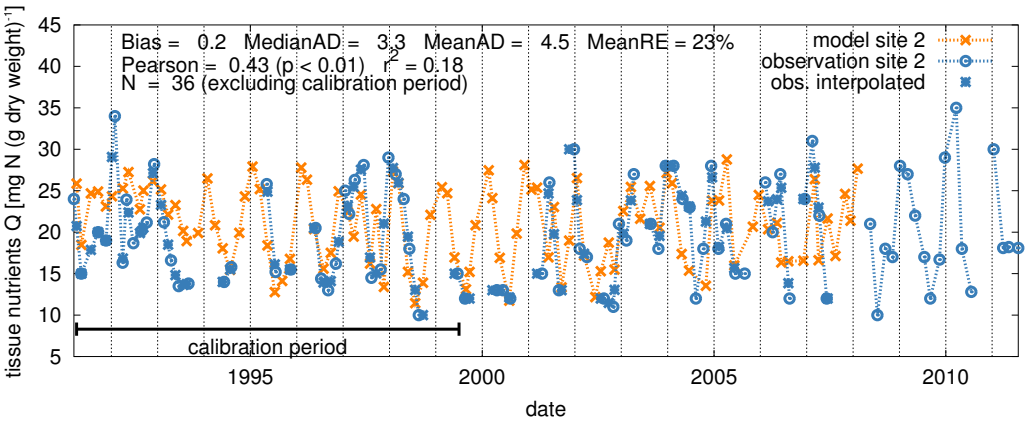

(b) tissue nitrogen model Q* (based on site 2 NH_4^+ and NO_x^- data) vs. observations site 2

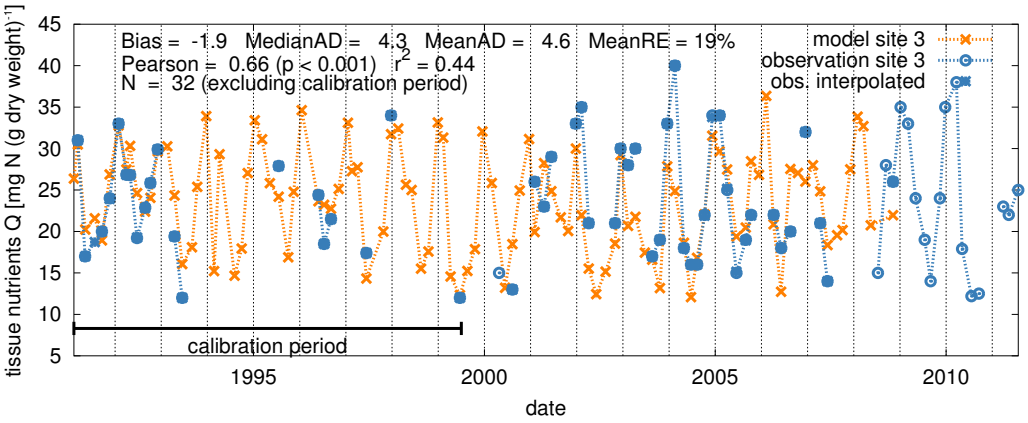

(c) tissue nitrogen model Q* (based on site 3 NH_4^+ and NO_x^- data) vs. observations site 3

Figure 2.4: Calibrated tissue nitrogen model Q* compared with tissue nitrogen observations at 3 sites. The same *Temp* and *Irr* data were used for all three sites. The calibration period (1991 to 1999) is indicated by a black horizontal bar. Corresponding calibrated parameter values are given in Table 2.3. Summary statistics for the validation period (2000 to 2009) are given for each site: bias, median absolute deviation (MedianAD), mean absolute deviation (MeanAD), mean relative error (MeanRE), Pearson's correlation coefficient (Pearson, with p-value), r^2 and number of samples (N).

2.3.2 Sensitivity analysis

Results of the OAT SA are shown in Table 2.4 in the form of parameter sensitivity "ranks" and corresponding absolute as well as relative change in the model output of tissue nitrogen concentration. Ranks were assigned according to decreasing values of relative change in model output. For the parameter default values ±10%, the top ranks are occupied by Q_{max}, μ_{max} and Q_{min}, and the environmental forcing variables all occupy lower ranks (*Temp* at rank 5, NO_x^- at rank 7, NH_4^+ at rank 12 and *Irr* at rank 14). For the calculations at the minimum and maximum of the range reported in the literature (for physiological parameters) or based on the 18 years of observations in Tauranga Harbour (for the environmental forcing variables), NO_x^- and NH_4^+ occupy ranks 1 and 2, followed by $k_{NH_4^+}$ and $k_{NO_x^-}$ at ranks 3 and 4. *Temp* occupies rank 8 and *Irr* rank 12. Increasing the width of the OAT SA interval stepwise from 10% to 80% leads to a monotonic increase in relative change in model output for all parameters, but in a clearly nonlinear fashion for several parameters, leading to changes in rank (Figure available in the online supplementary material).

The convergence of first-order (S_i) and total (S_{Ti}) sensitivity indices based on the Sobol' SA was initially analysed for a range of different sample sizes. Changes in the ranks of indices were observed only for relatively small sample sizes of up to 600 model evaluations, and S_i and S_{Ti} values converged quickly for sample sizes greater than about 800. A sample size of 10000 was therefore deemed adequate and used in all subsequent analyses. The results of the Sobol' SA are shown in Table 2.5. Confidence intervals (data omitted in table for sake of brevity) were ≤ 10% of the mean in all cases. In scenario 1, values of S_i and S_{Ti} for each model parameter are nearly identical. The model showed highest sensitivity to Q_{max}, μ_{max} and Q_{min}, which together accounted for 71% of model output variance, and lowest sensitivity to $k_{NH_4^+}$, ζ_P and I_0, which together account for only 3% of model output variance. In scenario 2, values of S_i and S_{Ti} for each model parameter are again nearly identical. The ranking of parameter sensitivity is identical to that obtained in scenario 1 for those parameters present in both scenarios, and still dominated by Q_{max}, μ_{max} and Q_{min}. The environmental forcing variables are spread out, with *Temp* contributing 8%, NO_x^- 3%, NH_4^+ 2% and Irr < 1%. The differences between S_i and S_{Ti} values increase slightly in scenario 3 compared to scenario 1, but S_i values still account for 87% or more of S_{Ti} for the leading four ranks. The highest ranks are given to $k_{NH_4^+}$ and $V_{mNH_4^+}$, together accounting for 80% of model output variance, followed by μ_{max} and $k_{NO_x^-}$ with 8% each, and the remaining parameters contributing ≤ 3% each. In scenario 4, the differences between S_i and S_{Ti} values again increase compared to the previous scenarios. The four most sensitive parameters and variables together

Table 2.4: Results of the one-factor-at-a-time (OAT) sensitivity analysis. The absolute change in the model's output value is given by OAT_{abs}, the relative change by OAT and ranks were assigned by decreasing value of OAT. All calculations were carried out once at the parameters' default values ±10%, and a second time at the minimum and maximum of the range reported in the literature (for physiological parameters) or based on Tauranga Harbour data (for the environmental forcing variables NH_4^+, NO_x^-, $Temp$ and Irr). Parameters are listed in the order of rank as determined in the analysis of default values ±10%.

	default value ±10%			min./max. of range		
symbol	OAT_{abs}	OAT	rank	OAT_{abs}	OAT	rank
	mg N (g dw)$^{-1}$			mg N (g dw)$^{-1}$		
Q_{max}	2.08	0.08	1	1.23	0.05	10
μ_{max}	2.05	0.08	2	4.43	0.17	5
Q_{min}	1.91	0.08	3	1.91	0.08	9
$V_{mNO_x^-}$	1.38	0.05	4	4.16	0.16	6
$Temp$	1.24	0.05	5	3.15	0.12	8
k_c	0.94	0.04	6	0.94	0.04	11
NO_x^-	0.81	0.03	7	15.33	0.60	1
$k_{NO_x^-}$	0.81	0.03	8	6.49	0.26	4
ϑ_P	0.73	0.03	9	0.73	0.03	13
$V_{mNH_4^+}$	0.66	0.03	10	4.16	0.16	7
$k_{NH_4^+}$	0.64	0.03	11	8.80	0.35	3
NH_4^+	0.64	0.03	12	8.86	0.35	2
ζ_P	0.49	0.02	13	0.49	0.02	14
Irr	0.00	0.00	14	0.80	0.03	12
I_0	0.00	0.00	15	0.00	0.00	15

account for 92% of model output variance, with NH_4^+ at rank 1 and NO_x^- at rank 3 together contributing 60%. $k_{NH_4^+}$ and $V_{mNH_4^+}$ are at ranks 2 and 4, respectively, and together contribute 32%. All other parameters and variables contribute $\leq 4\%$.

Table 2.5: Estimates of Sobol' first order (S_i) and total (S_{Ti}) sensitivity indices for four different scenarios of parameter/variable ranges, sorted in order of decreasing values of S_{Ti} for scenario 4. In scenarios 1 and 2, parameters were varied over the range of their default values ±10%, while in scenarios 3 and 4 they were varied over the full range of literature values. In scenarios 1 and 3, environmental forcing variables were fixed at local empirical mean values (based on Tauranga Harbour data; $NH_4^+ = 0.025\,\mathrm{mg\,N\,l^{-1}}$, $NO_x^- = 0.05\,\mathrm{mg\,N\,l^{-1}}$, $Temp = 16.7\,°\mathrm{C}$, $Irr = 60000\,\mathrm{lux}$), while in scenario 2 they were varied over the range of their local empirical mean values ±10%, and in scenario 4 over the local empirical ranges (based on Tauranga Harbour data). Values ≥ 100 are rounded to zero, others to two decimal places.

				scenario 1		scenario 2				scenario 3		scenario 4	
symbol	unit	min	max	S_i	S_{Ti}	S_i	S_{Ti}	min	max	S_i	S_{Ti}	S_i	S_{Ti}
NH_4^+	$\mathrm{mg\,N\,l^{-1}}$	0.02	0.03			0.02	0.02	0.00	0.08			0.39	0.44
$k_{NH_4^+}$	$\mathrm{mg\,N\,l^{-1}}$	0.63	0.77	0.02	0.02	0.02	0.02	0.10	0.70	0.48	0.49	0.16	0.18
NO_x^-	$\mathrm{mg\,N\,l^{-1}}$	0.04	0.06			0.03	0.03	0.00	0.36			0.13	0.16
$V_{mNH_4^+}$	$\mathrm{mg\,N\,(g\,dw)^{-1}\,h^{-1}}$	4.68	5.72	0.03	0.03	0.02	0.02	2.00	8.50	0.29	0.31	0.12	0.14
μ_{max}	$\mathrm{h^{-1}}$	0.01	0.02	0.24	0.24	0.21	0.21	0.01	0.02	0.08	0.08	0.04	0.04
$V_{mNO_x^-}$	$\mathrm{mg\,N\,(g\,dw)^{-1}\,h^{-1}}$	0.81	0.99	0.11	0.11	0.09	0.10	0.45	0.90	0.03	0.03	0.02	0.03
$k_{NO_x^-}$	$\mathrm{mg\,N\,l^{-1}}$	0.06	0.08	0.04	0.04	0.03	0.03	0.05	0.25	0.07	0.08	0.02	0.03
$Temp$	°C	15.03	18.37			0.08	0.08	13.00	21.50			0.02	0.02
Q_{max}	$\mathrm{mg\,N\,(g\,dw)^{-1}}$	40.50	49.50	0.25	0.26	0.22	0.22	40.00	45.00	0.01	0.01	0.01	0.02
Q_{min}	$\mathrm{mg\,N\,(g\,dw)^{-1}}$	9.00	11.00	0.21	0.21	0.18	0.18	9.00	11.00	0.02	0.02	0.01	0.01
k_c	$\mathrm{mg\,N\,(g\,dw)^{-1}}$	7.20	8.80	0.05	0.05	0.04	0.04	7.20	8.80	0.00	0.00	0.00	0.00
ϑ_P	°C	9.00	11.00	0.03	0.03	0.03	0.03	9.00	11.00	0.00	0.00	0.00	0.00
Irr	lux	54000	66000			0.00	0.00	15000	120000			0.00	0.00
ζ_P	$°\mathrm{C^{-1}}$	0.27	0.33	0.01	0.01	0.01	0.01	0.27	0.33	0.00	0.00	0.00	0.00
I_0	lux	5220	6380	0.00	0.00	0.00	0.00	5220	6380	0.00	0.00	0.00	0.00

2.3.3 Calibration uncertainty

Examples of results from the two calibration (uncertainty) analyses are shown in Figure 2.5 for the NH_4^+ and NO_x^- uptake parameters $k_{NH_4^+}$, $V_{mNH_4^+}$, $k_{NO_x^-}$ and $V_{mNO_x^-}$. In the initial setup without scaling factors, the optimal $k_{NH_4^+}$ and $V_{mNH_4^+}$ values are entirely concentrated at the upper and lower end of their range, respectively. $k_{NO_x^-}$ is concentrated at the lower end of its range, with slightly higher spread then $k_{NH_4^+}$, and $V_{mNO_x^-}$ shows a multimodal distribution, with the highest frequencies occurring at the upper end, second-highest at the lower end and a third peak at intermediate values. The scaling factors show very strong concentration at the lower end of the range when applied to NH_4^+ ($s_{NH_4^+}$) and strong concentration with slightly more spread at the upper end of the range when applied to NO_x^- ($s_{NO_x^-}$). Both $k_{NH_4^+}$ and $V_{mNH_4^+}$ show bimodal distributions in the presence of scaling factors, with slightly higher frequencies at the respective higher and lower end of their range. $k_{NO_x^-}$ shows frequencies decreasing away from the lower end of the range, similar to the results without scaling factors but with slightly higher spread over the entire range. $V_{mNO_x^-}$ shows the least amount of change from the results without scaling factors, but with almost equal frequencies at the lower and upper end of the range.

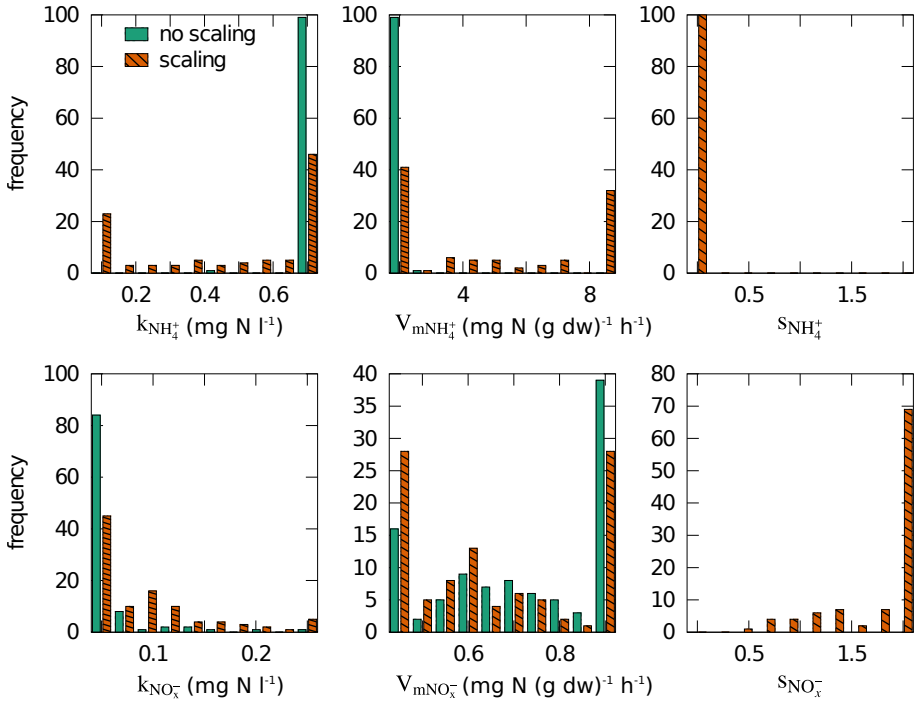

Figure 2.5: Histograms showing results from 100 independent calibrations with no scaling factors (solid green bars) compared to those with added scaling factors $s_{NH_4^+}$ for NH_4^+ and $s_{NH_4^+}$ for NO_x^- (hatched orange bars). Frequency refers to the number of calibrations that led to the respective value of the physiological model parameter or scaling factor. Shown here are only the half-saturation constants and maximum uptake rates for NH_4^+ ($k_{NH_4^+}$ and $V_{mNH_4^+}$) and NO_x^- ($k_{NO_x^-}$ and $V_{mNO_x^-}$) for both cases, as well as the scaling factors themselves for the latter case.

2.4 Discussion

2.4.1 Equilibrium solution and individual calibration performance

An algebraic solution Q^* to the equilibrium state of the tissue nitrogen quota model was easily obtained using a computer algebra system. The computational cost of evaluating Q^* is much lower than numerical integration, which in this study allowed a comprehensive application of sensitivity analysis and calibration algorithms than would otherwise have been possible. For the case of an equilibrium solution, numerical integration would additionally require checking when the equilibrium has been approximated. Furthermore, the algebraic solution requires only basic mathematical functions and could thus easily be implemented in spreadsheet software, facilitating its application by a wider group of users. We therefore believe that it would be beneficial to routinely consider the use of computer algebra systems as an alternative or complementary approach to numerical simulations and manual algebraic analysis.

After calibration for each site, median absolute deviation was ≤ 4.3 mg N (g dw)$^{-1}$, MeanRE between 19% and 29% and r^2 between 0.18 and 0.44 for all three sites. Since it is an intermediate variable in most model setups, output statistics for Q are usually not reported, making a direct comparison with the performance of similar models difficult. Compared to the performance statistics for mechanistic aquatic (planktonic) biogeochemical models compiled by Arhonditsis and Brett (2004), the performance for Q found in this study lies in a similar range as that commonly found for state variables of ammonia or phytoplankton biomass (much higher than for bacteria, much lower than for physical variables such as dissolved oxygen or water temperature). Given the low density of data available (20-40 points of data for each calibration period) and the fact that these were spread over a wide range environmental conditions (seasonal to interdecadal), this is a satisfactory result. The novel algebraic equilibrium solution derived from the classic model formulation is accurate and flexible enough to be applied to interannual and interdecadal datasets.

Regarding the individual, site-specific calibrations, the most prominent feature is shown by the uptake parameters $V_{mNH_4^+}$ and $k_{NH_4^+}$ which are calibrated at the lower (maximum uptake rate) and upper (half-saturation constant) bound, respectively, for all three sites. Since the literature ranges considered here are already relatively wide, and we have no reason to believe that the nutrient uptake kinetics of *Ulva* found in Tauranga Harbour are fundamentally different from *Ulva* elsewhere, it seems unlikely that these calibrated parameters are realistic estimates of the physiological properties of *Ulva* specific to the sites. Likewise, for all three sites, k_c is

calibrated at the lower end of the considered range, and the growth "affinity" for Q is reduced. This results in higher equilibrium values of Q, but with the largest differences compared to a higher value of k_c occurring at low values of Q close to Q_{min}, as usually occurs in summer. In contrast to, for example, Q_{min} or $V_{mNH_4^+}$, k_c cannot be measured directly. Instead, it can only be derived from related empirical data under the assumption of a specific functional relationship as given in eq. 2.2. Further research is necessary to determine whether alternative formulations of this relationship could provide a more structurally realistic model.

The model's performance might be improved further if a better approximation of the average conditions in the period preceding each individual evaluation date were used instead of instantaneous measurements. This would require forcing data at higher frequencies, which for NH_4^+ and NO_x^- are not available during the period examined here. Output from a spatially explicit biogeochemical model should therefore be considered as an alternative data source.

2.4.2 Sensitivity analysis

The results of the OAT SA to a certain degree match those of the Sobol' SA scenario 2 in terms of the ranks of the influential parameters. This indicates that for the relatively small interval of ± 10% around the default values used in scenario 2, the response in model output is close to linear, and the local OAT SA not misleading. For the Sobol' SA scenario 4, varying over the entire parameter ranges considered, there is little agreement in ranks (e.g., NO_x^- ranks above NH_4^+ in the OAT SA, while NH_4^+ accounts for almost three times the variance of NO_x^- in the corresponding Sobol' SA scenario 4). This emphasises again that care must be taken when interpreting results of OAT SA, and, whenever possible, preference should be given to global, for example variance-based, SA methods.

The marked differences between the Sobol' SA scenarios 1 and 3 show the importance of obtaining reliable ranges for physiological parameters. "Global" SA for process-based, applied ecological models is rarely performed for the full range of mathematically valid parameter values, which in many cases would be unbounded and therefore difficult to analyse with numerical methods. Instead, it is often based upon and must be considered in the context of the limited empirical data available to constrain parameter ranges. For the case of frondose *Ulva*, this is especially difficult due to taxonomic revisions and difficulties in species identification (Hayden et al., 2003). Together with the fact that closely related and in many cases morphologically similar species of *Ulva* exhibit marked differences in physiology (e.g., Han et al., 2008; Rautenberger and Bischof, 2006), this makes it especially challenging

to extract accurate physiological parameter ranges from empirical studies.

Results from the Sobol' SA scenario 4, which most accurately represents the degree of uncertainty in our present knowledge of the physiological model parameters as well the range of variability in environmental conditions at the study sites, show the strong influence of uncertainty in physiological parameters. Although the dominant environmental forcing variables NH_4^+ and NO_x^- together account for 60% in model output variance, the two highest-ranking physiological parameters, $k_{NH_4^+}$ and $V_{mNH_4^+}$, together still contribute 32%. This finding again emphasises the need for more autecological research to constrain the physiological parameters used in modelling *Ulva* spp. (Brush and Nixon, 2010), in the present case especially on a lower taxonomic level, site-specific or if possible both.

We assumed uniform distributions in the SA not only for the physiological parameters, but also for the environmental forcing variables NH_4^+, NO_x^-, temperature and irradiance. If sufficient data are available, non-uniform distributions derived from observations should be used instead. The distributions of water temperature and surface irradiance are relatively well known, as they can be routinely sampled at high frequency compared to the expected frequency of variability, and they are measured well within the limit of the sensors' ranges. Estuarine water column NO_x^- and NH_4^+ concentrations, in contrast, are often measured near the lower limits of analytical detection and at relatively low frequency. Among other uncertainties, it is unclear what distribution properties to assume when approaching a concentration of zero. Based solely on the long-term, bimonthly dataset of NH_4^+ and NO_x^- used here, these issues seem unlikely to be resolved. Additional short-term studies using alternative sampling and analysis methods would be necessary to obtain reliable distribution estimates for NH_4^+ and NO_x^-.

2.4.3 Calibration uncertainty

The repeated, randomly initialised calibrations of the base model (without the addition of DIN scaling factors) show that some of the most influential DIN uptake parameters are well-determined ($k_{NH_4^+}$, $V_{mNH_4^+}$), while other, less influential parameters exhibit broader ($k_{NO_x^-}$) or even multimodal distributions (NO_x^-). Model performance may be quite satisfactory as indicated by quantitative measures of agreement between model output and observations, but even the relatively intensive individual calibration procedure applied here cannot be relied upon to provide unique optimised parameter values. This issue has also been referred to as "underdetermination" (Ward et al., 2010) or the problem of "practical identifiability" (e.g., Raue et al., 2009), and has been found to occur in chemical (Brodersen et al., 1987), systems

biology (Gutenkunst et al., 2007) and marine biogeochemical models (Ward et al., 2010), and is especially likely in models with closely correlated parameters such as maximum uptake rate and half-saturation constants (Li and Vu, 2013). At present, this effect is not routinely quantified nor checked in ecological models. This study shows that if differences in calibration results between datasets (sites, time periods, species, etc.) are to be interpreted as system properties, further research is needed to alleviate this "sloppy" calibration behaviour (Gutenkunst et al., 2007) and ensure that the model is not just "getting the right answers for the wrong reasons" (Ward et al., 2010).

After the addition of scaling factors for NH_4^+ and NO_x^-, the calibration almost entirely dampens the influence of NH_4^+, and correspondingly the NH_4^+ uptake parameters show broader distributions as they now have very little, if any, influence on the model output. NO_x^-, on the other hand, is amplified to the maximum of the permitted range (factor 2), with little change in the quality of the distribution of $k_{NO_x^-}$ and $V_{mNO_x^-}$, but rather only a slightly more even distribution being visible for both uptake parameters. Further research is necessary to determine whether this effect is due to a more noisy character of the NH_4^+ forcing (higher spatial and temporal variability, higher relative measurement error due to low absolute values near the chemical analytical detection limits), or possibly an inadequate description of NH_4^+ uptake in the model.

2.5 Conclusion

Using a computer algebra system, we derived a novel algebraic solution to calculate equilibrium tissue nitrogen quotas in frondose *Ulva* spp. from a classic description formulated as ODEs. The algebraic solution performed well in predicting quotas based on measured NH_4^+, NO_x^-, temperature and irradiance from an 18 year dataset of approximately bimonthly estuarine tissue samples, confirming the capacity of both the algebraic solution as well as the classic ODE formulation to predict equilibrium tissue nitrogen quotas. A global sensitivity analysis revealed that although NH_4^+ and NO_x^- forcing explained 60% of model output variance, the uncertainty in key physiological parameters also had a high contribution of over 30%, showing that literature ranges for the parameters controlling tissue nitrogen dynamics in *Ulva* spp. are not well-constrained. These findings emphasise the need for further autecological studies to constrain the physiological parameters used in growth models of *Ulva* spp. Repeated, randomly initialised calibrations lead to broad and even multimodal distributions for some parameters, showing that calibration uncertainty

analysis should be a routine procedure since individual calibrations do not necessarily lead to reliable estimates of the considered biological or ecological system properties.

Acknowledgements

We thank the Bay of Plenty Regional Council for providing *Ulva* tissue nutrient data, water column DIN data as well as funding for the INTERCOAST PhD scholarship (a joint graduate school between the University of Bremen and the University of Waikato) for AP, and the New Zealand Ministry of Research, Science and Technology (MoRST) for travel funding for AP. We thank two anonymous reviewers and the corresponding editor for their thoughtful and constructive comments on a previous version of this manuscript.

2.A Supplementary material: Algebraic solution for equilibrium Q^*

The algebraic solution for equilibrium Q^* obtained via Sage is reproduced below, together with the steps needed to obtain it (tested in Sage version 5.11). Variable and parameter names contain only upper- and lowercase letters of the Roman/Latin alphabet, numerals as well as underscores, and are defined in Table 2.6. The following operators and special characters are used: `+-*/^` for addition, subtraction, multiplication, division, and exponentiation, as well as `()` for grouping and function arguments. The square root function is denoted by `sqrt()`. The backslash is used as the line continuation character. This format should be easy to transfer to most programming languages, the most common adaptation necessary being replacement of `e^` by `exp` for languages that do not recognise `e` as Euler's number in this context. Two solutions exist, only the first of which lies in the relevant interval between Q_{min} and Q_{max}.

Table 2.6: Algebraic solution variable names, description, default values and units.

variable name	description	default value	unit
`mumax`	maximum growth rate	0.016	h^{-1}
`nh`	external ammonium concentration	0.025	$mg\,l^{-1}$
`vmnh`	maximum uptake rate for NH_4^+	5.2	$mg\,N\,(g\,dw)^{-1}\,h^{-1}$
`knh`	half saturation constant for NH_4^+	0.7	$mg\,N\,l^{-1}$
`no`	external nitrate + nitrite concentration	0.05	$mg\,l^{-1}$
`vmno`	maximum uptake rate for NO_x^-	0.9	$mg\,N\,(g\,dw)^{-1}\,h^{-1}$
`kno`	half saturation constant for NO_x^-	0.07	$mg\,N\,l^{-1}$
`qmin`	minimum Q	10	$mg\,N\,(g\,dw)^{-1}$
`qmax`	maximum Q	45	$mg\,N\,(g\,dw)^{-1}$
`kc`	Q growth limitation factor	8	$mg\,N\,(g\,dw)^{-1}$
`T`	temperature	16.7	°C
`zeta_P`	temperature factor	0.3	$°C^{-1}$
`theta_P`	reference temperature	10	°C
`I`	irradiance	60000	lux
`I_0`	irradiance factor	5800	lux

```
# define variables
```

```
vmnh,nh,knh,vmno,no,kno,qmax,q,qmin,mumax,kc,T,zeta_P, \
    theta_P,I,I_0 = var('vmnh','nh','knh','vmno','no','kno \
    ','qmax','q','qmin','mumax','kc','T','zeta_P','theta_P \
    ','I','I_0')
# define equation
eq = ( vmnh*nh/(knh+nh)*(qmax-q)/(qmax-qmin) + vmno*no/(kno \
    +no)*(qmax-q)/(qmax-qmin) == mumax*((q-qmin)/(q-kc)*q) * \
     ((1+exp(-zeta_P*(T-theta_P)))^(-1)) * (1-exp(-I/I_0)) )
# solve equation
solve(eq, q)
```

```
# first solution as returned by Sage
q_solution_1 = 1/2*(((knh*kno*mumax + kno*mumax*nh + (knh* \
    mumax + mumax*nh)*no)*qmax*qmin - (knh*kno*mumax + kno* \
    mumax*nh + (knh*mumax + mumax*nh)*no)*qmin^2 - ((knh*kno \
    *mumax + kno*mumax*nh + (knh*mumax + mumax*nh)*no)*qmax* \
    qmin - (knh*kno*mumax + kno*mumax*nh + (knh*mumax +  \
    mumax*nh)*no)*qmin^2 + (kc*kno*nh + kc*nh*no + (kno*nh + \
     nh*no)*qmax)*vmnh + ((knh + nh)*no*qmax + (kc*knh + kc* \
    nh)*no)*vmno)*e^(I/I_0))*e^(T*zeta_P - theta_P*zeta_P) - \
     ((kc*kno*nh + kc*nh*no + (kno*nh + nh*no)*qmax)*vmnh +  \
    ((knh + nh)*no*qmax + (kc*knh + kc*nh)*no)*vmno)*e^(I/ \
    I_0) + sqrt(((knh^2*kno^2*mumax^2 + 2*knh*kno^2*mumax^2* \
    nh + kno^2*mumax^2*nh^2 + (knh^2*mumax^2 + 2*knh*mumax \
    ^2*nh + mumax^2*nh^2)*no^2 + 2*(knh^2*kno*mumax^2 + 2* \
    knh*kno*mumax^2*nh + kno*mumax^2*nh^2)*no)*qmax^2*qmin^2 \
     - 2*(knh^2*kno^2*mumax^2 + 2*knh*kno^2*mumax^2*nh + kno \
    ^2*mumax^2*nh^2 + (knh^2*mumax^2 + 2*knh*mumax^2*nh +  \
    mumax^2*nh^2)*no^2 + 2*(knh^2*kno*mumax^2 + 2*knh*kno* \
    mumax^2*nh + kno*mumax^2*nh^2)*no)*qmax*qmin^3 + (knh^2* \
    kno^2*mumax^2 + 2*knh*kno^2*mumax^2*nh + kno^2*mumax^2* \
    nh^2 + (knh^2*mumax^2 + 2*knh*mumax^2*nh + mumax^2*nh^2) \
    *no^2 + 2*(knh^2*kno*mumax^2 + 2*knh*kno*mumax^2*nh +  \
    kno*mumax^2*nh^2)*no)*qmin^4)*e^(2*T*zeta_P - 2*theta_P* \
    zeta_P + 2*I/I_0) - 2*((knh^2*kno^2*mumax^2 + 2*knh*kno \
    ^2*mumax^2*nh + kno^2*mumax^2*nh^2 + (knh^2*mumax^2 + 2* \
    knh*mumax^2*nh + mumax^2*nh^2)*no^2 + 2*(knh^2*kno*mumax \
    ^2 + 2*knh*kno*mumax^2*nh + kno*mumax^2*nh^2)*no)*qmax \
```

```
^2*qmin^2 - 2*(knh^2*kno^2*mumax^2 + 2*knh*kno^2*mumax \
^2*nh + kno^2*mumax^2*nh^2 + (knh^2*mumax^2 + 2*knh* \
mumax^2*nh + mumax^2*nh^2)*no^2 + 2*(knh^2*kno*mumax^2 + \
 2*knh*kno*mumax^2*nh + kno*mumax^2*nh^2)*no)*qmax*qmin \
^3 + (knh^2*kno^2*mumax^2 + 2*knh*kno^2*mumax^2*nh + kno \
^2*mumax^2*nh^2 + (knh^2*mumax^2 + 2*knh*mumax^2*nh +  \
mumax^2*nh^2)*no^2 + 2*(knh^2*kno*mumax^2 + 2*knh*kno* \
mumax^2*nh + kno*mumax^2*nh^2)*no)*qmin^4)*e^(2*T*zeta_P \
 - 2*theta_P*zeta_P + I/I_0) + ((knh^2*kno^2*mumax^2 +  \
2*knh*kno^2*mumax^2*nh + kno^2*mumax^2*nh^2 + (knh^2* \
mumax^2 + 2*knh*mumax^2*nh + mumax^2*nh^2)*no^2 + 2*(knh \
^2*kno*mumax^2 + 2*knh*kno*mumax^2*nh + kno*mumax^2*nh \
^2)*no)*qmax^2*qmin^2 - 2*(knh^2*kno^2*mumax^2 + 2*knh* \
kno^2*mumax^2*nh + kno^2*mumax^2*nh^2 + (knh^2*mumax^2 + \
 2*knh*mumax^2*nh + mumax^2*nh^2)*no^2 + 2*(knh^2*kno* \
mumax^2 + 2*knh*kno*mumax^2*nh + kno*mumax^2*nh^2)*no)* \
qmax*qmin^3 + (knh^2*kno^2*mumax^2 + 2*knh*kno^2*mumax \
^2*nh + kno^2*mumax^2*nh^2 + (knh^2*mumax^2 + 2*knh* \
mumax^2*nh + mumax^2*nh^2)*no^2 + 2*(knh^2*kno*mumax^2 + \
 2*knh*kno*mumax^2*nh + kno*mumax^2*nh^2)*no)*qmin^4 +  \
((kc^2*kno^2*nh^2 + 2*kc^2*kno*nh^2*no + kc^2*nh^2*no^2  \
+ (kno^2*nh^2 + 2*kno*nh^2*no + nh^2*no^2)*qmax^2 - 2*( \
kc*kno^2*nh^2 + 2*kc*kno*nh^2*no + kc*nh^2*no^2)*qmax)* \
vmnh^2 + ((knh^2 + 2*knh*nh + nh^2)*no^2*qmax^2 - 2*(kc* \
knh^2 + 2*kc*knh*nh + kc*nh^2)*no^2*qmax + (kc^2*knh^2 + \
 2*kc^2*knh*nh + kc^2*nh^2)*no^2)*vmno^2 - 2*(2*(kc*knh* \
kno^2*mumax*nh + kc*kno^2*mumax*nh^2 + (kc*knh*mumax*nh  \
+ kc*mumax*nh^2)*no^2 + 2*(kc*knh*kno*mumax*nh + kc*kno* \
mumax*nh^2)*no)*qmax^2 + (kc*knh*kno^2*mumax*nh + kc*kno \
^2*mumax*nh^2 + (kc*knh*mumax*nh + kc*mumax*nh^2)*no^2 + \
 2*(kc*knh*kno*mumax*nh + kc*kno*mumax*nh^2)*no + (knh* \
kno^2*mumax*nh + kno^2*mumax*nh^2 + (knh*mumax*nh +  \
mumax*nh^2)*no^2 + 2*(knh*kno*mumax*nh + kno*mumax*nh^2) \
*no)*qmax)*qmin^2 - ((knh*kno^2*mumax*nh + kno^2*mumax* \
nh^2 + (knh*mumax*nh + mumax*nh^2)*no^2 + 2*(knh*kno* \
mumax*nh + kno*mumax*nh^2)*no)*qmax^2 + 3*(kc*knh*kno^2* \
mumax*nh + kc*kno^2*mumax*nh^2 + (kc*knh*mumax*nh + kc* \
```

```
mumax*nh^2)*no^2 + 2*(kc*knh*kno*mumax*nh + kc*kno*mumax \
*nh^2)*no)*qmax)*qmin)*vmnh - 2*(2*((kc*knh^2*mumax + 2* \
kc*knh*mumax*nh + kc*mumax*nh^2)*no^2 + (kc*knh^2*kno* \
mumax + 2*kc*knh*kno*mumax*nh + kc*kno*mumax*nh^2)*no)* \
qmax^2 + ((kc*knh^2*mumax + 2*kc*knh*mumax*nh + kc*mumax \
*nh^2)*no^2 + (kc*knh^2*kno*mumax + 2*kc*knh*kno*mumax* \
nh + kc*kno*mumax*nh^2)*no + ((knh^2*mumax + 2*knh*mumax \
*nh + mumax*nh^2)*no^2 + (knh^2*kno*mumax + 2*knh*kno* \
mumax*nh + kno*mumax*nh^2)*no)*qmax)*qmin^2 - (((knh^2* \
mumax + 2*knh*mumax*nh + mumax*nh^2)*no^2 + (knh^2*kno* \
mumax + 2*knh*kno*mumax*nh + kno*mumax*nh^2)*no)*qmax^2  \
+ 3*((kc*knh^2*mumax + 2*kc*knh*mumax*nh + kc*mumax*nh \
^2)*no^2 + (kc*knh^2*kno*mumax + 2*kc*knh*kno*mumax*nh + \
 kc*kno*mumax*nh^2)*no)*qmax)*qmin - ((kc^2*knh*nh + kc \
^2*nh^2)*no^2 + ((knh*nh + nh^2)*no^2 + (knh*kno*nh +  \
kno*nh^2)*no)*qmax^2 + (kc^2*knh*kno*nh + kc^2*kno*nh^2) \
*no - 2*((kc*knh*nh + kc*nh^2)*no^2 + (kc*knh*kno*nh +  \
kc*kno*nh^2)*no)*qmax)*vmnh)*vmno)*e^(2*I/I_0) + 2*((2*( \
kc*knh*kno^2*mumax*nh + kc*kno^2*mumax*nh^2 + (kc*knh* \
mumax*nh + kc*mumax*nh^2)*no^2 + 2*(kc*knh*kno*mumax*nh  \
+ kc*kno*mumax*nh^2)*no)*qmax^2 + (kc*knh*kno^2*mumax*nh \
 + kc*kno^2*mumax*nh^2 + (kc*knh*mumax*nh + kc*mumax*nh \
^2)*no^2 + 2*(kc*knh*kno*mumax*nh + kc*kno*mumax*nh^2)* \
no + (knh*kno^2*mumax*nh + kno^2*mumax*nh^2 + (knh*mumax \
*nh + mumax*nh^2)*no^2 + 2*(knh*kno*mumax*nh + kno*mumax \
*nh^2)*no)*qmax)*qmin^2 - ((knh*kno^2*mumax*nh + kno^2* \
mumax*nh^2 + (knh*mumax*nh + mumax*nh^2)*no^2 + 2*(knh* \
kno*mumax*nh + kno*mumax*nh^2)*no)*qmax^2 + 3*(kc*knh* \
kno^2*mumax*nh + kc*kno^2*mumax*nh^2 + (kc*knh*mumax*nh  \
+ kc*mumax*nh^2)*no^2 + 2*(kc*knh*kno*mumax*nh + kc*kno* \
mumax*nh^2)*no)*qmax)*qmin)*vmnh + (2*((kc*knh^2*mumax + \
 2*kc*knh*mumax*nh + kc*mumax*nh^2)*no^2 + (kc*knh^2*kno \
*mumax + 2*kc*knh*kno*mumax*nh + kc*kno*mumax*nh^2)*no)* \
qmax^2 + ((kc*knh^2*mumax + 2*kc*knh*mumax*nh + kc*mumax \
*nh^2)*no^2 + (kc*knh^2*kno*mumax + 2*kc*knh*kno*mumax* \
nh + kc*kno*mumax*nh^2)*no + ((knh^2*mumax + 2*knh*mumax \
*nh + mumax*nh^2)*no^2 + (knh^2*kno*mumax + 2*knh*kno* \
```

```
mumax*nh + kno*mumax*nh^2)*no)*qmax)*qmin^2 - (((knh^2* \
mumax + 2*knh*mumax*nh + mumax*nh^2)*no^2 + (knh^2*kno* \
mumax + 2*knh*kno*mumax*nh + kno*mumax*nh^2)*no)*qmax^2  \
+ 3*((kc*knh^2*mumax + 2*kc*knh*mumax*nh + kc*mumax*nh \
^2)*no^2 + (kc*knh^2*kno*mumax + 2*kc*knh*kno*mumax*nh + \
 kc*kno*mumax*nh^2)*no)*qmax)*qmin)*vmno)*e^(I/I_0))*e \
^(2*T*zeta_P - 2*theta_P*zeta_P) + 2*(((kc^2*kno^2*nh^2  \
+ 2*kc^2*kno*nh^2*no + kc^2*nh^2*no^2 + (kno^2*nh^2 + 2* \
kno*nh^2*no + nh^2*no^2)*qmax^2 - 2*(kc*kno^2*nh^2 + 2* \
kc*kno*nh^2*no + kc*nh^2*no^2)*qmax)*vmnh^2 + ((knh^2 +  \
2*knh*nh + nh^2)*no^2*qmax^2 - 2*(kc*knh^2 + 2*kc*knh*nh \
 + kc*nh^2)*no^2*qmax + (kc^2*knh^2 + 2*kc^2*knh*nh + kc \
^2*nh^2)*no^2)*vmno^2 - (2*(kc*knh*kno^2*mumax*nh + kc* \
kno^2*mumax*nh^2 + (kc*knh*mumax*nh + kc*mumax*nh^2)*no \
^2 + 2*(kc*knh*kno*mumax*nh + kc*kno*mumax*nh^2)*no)* \
qmax^2 + (kc*knh*kno^2*mumax*nh + kc*kno^2*mumax*nh^2 +  \
(kc*knh*mumax*nh + kc*mumax*nh^2)*no^2 + 2*(kc*knh*kno* \
mumax*nh + kc*kno*mumax*nh^2)*no + (knh*kno^2*mumax*nh + \
 kno^2*mumax*nh^2 + (knh*mumax*nh + mumax*nh^2)*no^2 +  \
2*(knh*kno*mumax*nh + kno*mumax*nh^2)*no)*qmax)*qmin^2 - \
 ((knh*kno^2*mumax*nh + kno^2*mumax*nh^2 + (knh*mumax*nh \
 + mumax*nh^2)*no^2 + 2*(knh*kno*mumax*nh + kno*mumax*nh \
^2)*no)*qmax^2 + 3*(kc*knh*kno^2*mumax*nh + kc*kno^2* \
mumax*nh^2 + (kc*knh*mumax*nh + kc*mumax*nh^2)*no^2 +  \
2*(kc*knh*kno*mumax*nh + kc*kno*mumax*nh^2)*no)*qmax)* \
qmin)*vmnh - (2*((kc*knh^2*mumax + 2*kc*knh*mumax*nh +  \
kc*mumax*nh^2)*no^2 + (kc*knh^2*kno*mumax + 2*kc*knh*kno \
*mumax*nh + kc*kno*mumax*nh^2)*no)*qmax^2 + ((kc*knh^2* \
mumax + 2*kc*knh*mumax*nh + kc*mumax*nh^2)*no^2 + (kc* \
knh^2*kno*mumax + 2*kc*knh*kno*mumax*nh + kc*kno*mumax* \
nh^2)*no + ((knh^2*mumax + 2*knh*mumax*nh + mumax*nh^2)* \
no^2 + (knh^2*kno*mumax + 2*knh*kno*mumax*nh + kno*mumax \
*nh^2)*no)*qmax)*qmin^2 - (((knh^2*mumax + 2*knh*mumax* \
nh + mumax*nh^2)*no^2 + (knh^2*kno*mumax + 2*knh*kno* \
mumax*nh + kno*mumax*nh^2)*no)*qmax^2 + 3*((kc*knh^2* \
mumax + 2*kc*knh*mumax*nh + kc*mumax*nh^2)*no^2 + (kc* \
knh^2*kno*mumax + 2*kc*knh*kno*mumax*nh + kc*kno*mumax* \
```

```
nh^2)*no)*qmax)*qmin - 2*((kc^2*knh*nh + kc^2*nh^2)*no^2 \
 + ((knh*nh + nh^2)*no^2 + (knh*kno*nh + kno*nh^2)*no)* \
qmax^2 + (kc^2*knh*kno*nh + kc^2*kno*nh^2)*no - 2*((kc* \
knh*nh + kc*nh^2)*no^2 + (kc*knh*kno*nh + kc*kno*nh^2)* \
no)*qmax)*vmnh)*vmno)*e^(2*I/I_0) + ((2*(kc*knh*kno^2* \
mumax*nh + kc*kno^2*mumax*nh^2 + (kc*knh*mumax*nh + kc* \
mumax*nh^2)*no^2 + 2*(kc*knh*kno*mumax*nh + kc*kno*mumax \
*nh^2)*no)*qmax^2 + (kc*knh*kno^2*mumax*nh + kc*kno^2* \
mumax*nh^2 + (kc*knh*mumax*nh + kc*mumax*nh^2)*no^2 +  \
2*(kc*knh*kno*mumax*nh + kc*kno*mumax*nh^2)*no + (knh* \
kno^2*mumax*nh + kno^2*mumax*nh^2 + (knh*mumax*nh +  \
mumax*nh^2)*no^2 + 2*(knh*kno*mumax*nh + kno*mumax*nh^2) \
*no)*qmax)*qmin^2 - ((knh*kno^2*mumax*nh + kno^2*mumax* \
nh^2 + (knh*mumax*nh + mumax*nh^2)*no^2 + 2*(knh*kno* \
mumax*nh + kno*mumax*nh^2)*no)*qmax^2 + 3*(kc*knh*kno^2* \
mumax*nh + kc*kno^2*mumax*nh^2 + (kc*knh*mumax*nh + kc* \
mumax*nh^2)*no^2 + 2*(kc*knh*kno*mumax*nh + kc*kno*mumax \
*nh^2)*no)*qmax)*qmin)*vmnh + (2*((kc*knh^2*mumax + 2*kc \
*knh*mumax*nh + kc*mumax*nh^2)*no^2 + (kc*knh^2*kno* \
mumax + 2*kc*knh*kno*mumax*nh + kc*kno*mumax*nh^2)*no)* \
qmax^2 + ((kc*knh^2*mumax + 2*kc*knh*mumax*nh + kc*mumax \
*nh^2)*no^2 + (kc*knh^2*kno*mumax + 2*kc*knh*kno*mumax* \
nh + kc*kno*mumax*nh^2)*no + ((knh^2*mumax + 2*knh*mumax \
*nh + mumax*nh^2)*no^2 + (knh^2*kno*mumax + 2*knh*kno* \
mumax*nh + kno*mumax*nh^2)*no)*qmax)*qmin^2 - (((knh^2* \
mumax + 2*knh*mumax*nh + mumax*nh^2)*no^2 + (knh^2*kno* \
mumax + 2*knh*kno*mumax*nh + kno*mumax*nh^2)*no)*qmax^2  \
+ 3*((kc*knh^2*mumax + 2*kc*knh*mumax*nh + kc*mumax*nh \
^2)*no^2 + (kc*knh^2*kno*mumax + 2*kc*knh*kno*mumax*nh + \
 kc*kno*mumax*nh^2)*no)*qmax)*qmin)*vmno)*e^(I/I_0))*e^( \
T*zeta_P - theta_P*zeta_P) + ((kc^2*kno^2*nh^2 + 2*kc^2* \
kno*nh^2*no + kc^2*nh^2*no^2 + (kno^2*nh^2 + 2*kno*nh^2* \
no + nh^2*no^2)*qmax^2 - 2*(kc*kno^2*nh^2 + 2*kc*kno*nh \
^2*no + kc*nh^2*no^2)*qmax)*vmnh^2 + 2*((kc^2*knh*nh +  \
kc^2*nh^2)*no^2 + ((knh*nh + nh^2)*no^2 + (knh*kno*nh +  \
kno*nh^2)*no)*qmax^2 + (kc^2*knh*kno*nh + kc^2*kno*nh^2) \
*no - 2*((kc*knh*nh + kc*nh^2)*no^2 + (kc*knh*kno*nh +  \
```

```
kc*kno*nh^2)*no)*qmax)*vmnh*vmno + ((knh^2 + 2*knh*nh +  \
nh^2)*no^2*qmax^2 - 2*(kc*knh^2 + 2*kc*knh*nh + kc*nh^2) \
*no^2*qmax + (kc^2*knh^2 + 2*kc^2*knh*nh + kc^2*nh^2)*no \
^2)*vmno^2)*e^(2*I/I_0)))/(((knh*kno*mumax + kno*mumax* \
nh + (knh*mumax + mumax*nh)*no)*qmax - (knh*kno*mumax +  \
kno*mumax*nh + (knh*mumax + mumax*nh)*no)*qmin - ((knh + \
 nh)*no*vmno + (knh*kno*mumax + kno*mumax*nh + (knh* \
mumax + mumax*nh)*no)*qmax - (knh*kno*mumax + kno*mumax* \
nh + (knh*mumax + mumax*nh)*no)*qmin + (kno*nh + nh*no)* \
vmnh)*e^(I/I_0))*e^(T*zeta_P - theta_P*zeta_P) - ((knh + \
 nh)*no*vmno + (kno*nh + nh*no)*vmnh)*e^(I/I_0));
```

2.B Supplementary material: OAT sensitivity analysis figure

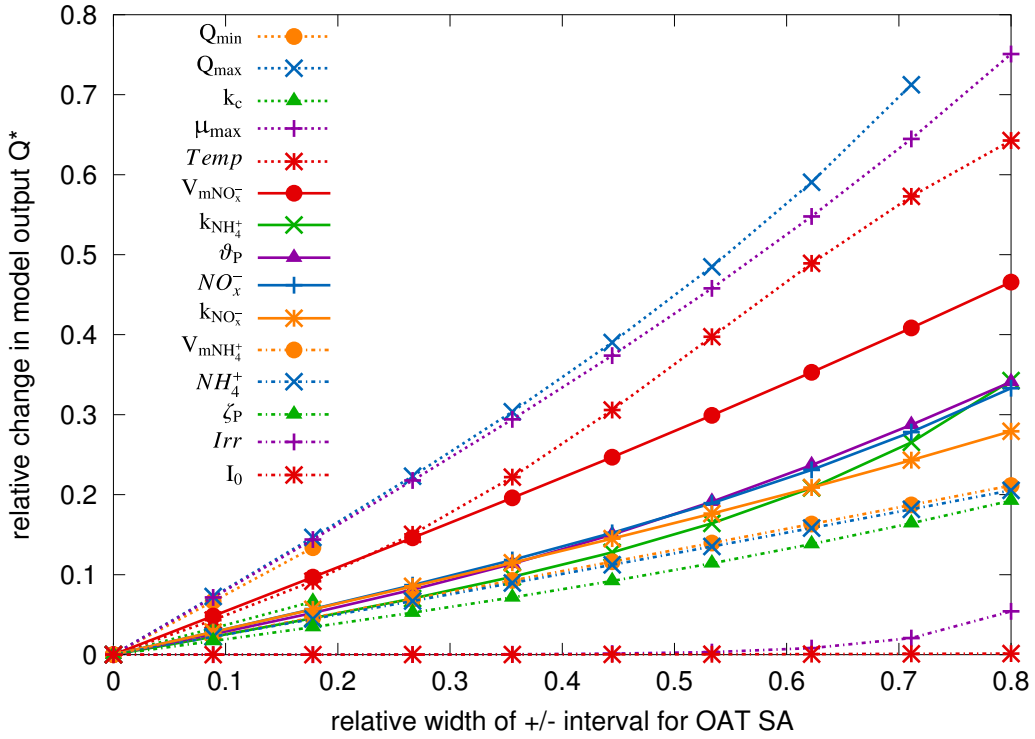

Figure 2.6: Results of the one-at-a-time (OAT) sensitivity analysis (SA) for increasing parameter variation intervals. A relative width of 0.5 for the OAT SA indicates that the model was evaluated at the parameter's default value ±50%. Lines not continued to the maximum relative interval width of 0.8 (Q_{min}, k_c, Q_{max}) are due to parameter combinations that lead to invalid solutions (e.g., $Q_{min} \leq k_c$). For parameter definitions see Table 2.1.

Chapter 3

Long-term and seasonal scenario simulations of *Ulva* spp. population dynamics

Abstract

We use a zero-dimensional, dynamic simulation model of *Ulva* biomass (B), tissue nitrogen quota (QN) and tissue phosphorus quota (QP) to examine the driving environmental factors leading to blooms observed in a temperate to subtropical estuarine lagoon. Both calibration uncertainty for parameters and model performance for individual state variables vary substantially when calibrating against observation data for individual state variables or a combination of all three. Long-term continuous simulations over more than a decade demonstrate the model's stability and reproduce biomass and tissue nitrogen well, while tissue phosphorus is simulated with realistic mean values but almost no seasonal variation, in contrast to the observation data. We derive seasonal scenarios based on annual cosine fits to monthly percentiles of the observed forcing data to represent above and below average conditions in the environmental forcing variables (NH_4^+, NO_3^-, PO_4^{3-}, temperature and irradiance). Comparison of scenario simulations point to dissolved inorganic nitrogen, both NH_4^+ and NO_3^-, in determining both peak *Ulva* biomass and timing.

3.1 Introduction

In the majority of marine ecosystems, photosynthetic algae as primary producers are an essential component of the food web; therefore algae growth processes form the basis of most ecosystem-scale mathematical modelling approaches in marine envi-

ronments (e.g., Moore et al., 2001; Baretta et al., 1995). While in the open ocean, these primary producers are almost exclusively microphytoplankton, in shallow coastal and especially estuarine systems, benthic as well as mixed benthic/planktonic macroalgae may also play an important role; in some cases they may even be the dominant group, especially if they outcompete rooted macrophytes such as eelgrass (Flindt et al., 1999; Zaldívar et al., 2009). Although usually not directly toxic to humans, these benthic/planktonic macroalgae can form blooms which are considered a nuisance to humans and may have a number of detrimental effects on the ecosystem (Valiela et al., 1997), and so it is becoming increasingly important to estuarine management to improve modelling of bloom-forming processes. In many locations around the world, these blooms are often formed by frondose species of the genus *Ulva*, which are therefore the focus of many applied studies (among others: Sfriso, 1995; Runca et al., 1996; Aveytua-Alcázar et al., 2008; Perrot et al., 2014). Estuaries in general, but especially those with considerable intertidal areas, show an extremely high range of variability of the environmental conditions that influence macroalgae growth processes, and are therefore particularly sensitive to how these processes are described, parameterised and calibrated in mathematical models (as shown in chapter 2).

Mechanistic (process-based) mathematical models are a valuable tool to increase our understanding of the dynamics of individual species, species assemblies and ultimately entire ecosystems (Cuddington et al., 2013). They are used in basic ecological research, e.g., to examine competition effects between species or genera (Aveytua-Alcázar et al., 2008), but also as applied management tools, e.g., to optimise harvest strategies for commercially relevant species (Duarte and Ferreira, 1997).

In contrast to equilibrium or "steady-state" models (such as the one used in chapter 2), simulation models explicitly take into account the relative timing of changes in all state and forcing variables, which is critical to understand the factors which force bloom conditions. Using simulation models is therefore justified in cases where the phenomenon of interest can by definition not be analysed averaged over time or only in equilibrium, and are often developed as extension of or alternative to simpler equilibrium models (e.g., Pauly et al., 2000). For example, for the development of seasonal and especially ephemeral macroalgae blooms such as those frequently encountered in the genus *Ulva*, considering only the temporal average of environmental conditions may lead to misleading results. For many applied studies, especially those concerning the occurrence of algal blooms at a specific site, a key question is the relative importance of the multitude of environmental

factors controlling growth and mortality (e.g., Runca et al., 1996; Martins et al., 2001; Öberg, 2005). Simulation models can be also used as "virtual laboratories" in which the population's response over time to controlled variations in individual environmental factors can be examined as separate "scenarios" (e.g., Salomonsen et al., 1999). Here we use a simulation model to understand the key drivers of *Ulva* blooms in a temperate to subtropical, shallow, tidally-dominated estuarine lagoon (Tauranga Harbour, North Island of New Zealand). We reimplement the *Ulva* population dynamics model of Guimaraens et al. (2005) (originally developed for a tropical coastal upwelling region), and apply the model to a long-term monitoring dataset of *Ulva* biomass (B, derived from intertidal coverage), tissue nitrogen quota (QN) and tissue phosphorus quota (QP).

One of the problems of simulation models is that they can become unstable if they are implemented over longer timescales. On a time scale of one or two years, and with strong enough seasonality in the physical environmental variables (especially inorganic nutrients, temperature and light, but in some cases also other factors such as wind and wave climate or herbivory), most macroalgae simulation models are adequately constrained to prevent unrealistically high growth rates and resulting unrealistic population densities (the model "exploding"). With weaker seasonal forcing, and particularly when calibration and validation datasets are short relative to the prediction time interval, this is not necessarily the case ("temporal divergence" Oreskes and Belitz, 2001). Since the phenomenon of interest, an individual "bloom event" occurs on a seasonal time scale, models are often developed, calibrated and validated with primarily this time scale in mind. Ideally, though, the model structure should be valid for a range of time scales, so that both short-term (e.g., laboratory experiments or idealised seasonal scenarios) and long-term (e.g., reproduction of monitoring time series) simulations can be successfully carried out with the same model. We therefore ask the research question 1: Can a typical mechanistic simulation model of macroalgae growth reproduce observed biomass and tissue nutrient data in a continuous simulation over more than a decade?

To ensure an adequate calibration and resulting model performance, and indirectly also to ascertain a certain degree of structural validity of the model, we should use observation data on as many state variables as possible. Additionally, the uncertainty in calibrated parameter values should also be quantified (chapter 2). This leads us to the research questions 2a: Do model calibrations against state variables other than biomass (individually or in combination) still lead to realistic output for all state variables? and 2b: Does the degree of uncertainty, and especially relative uncertainty, in calibrated parameter values depend on the choice of calibration vari-

able? For *Ulva*, the state variables describing the tissue nutrient concentrations are ideal candidates to consider in this context, since they are relatively easy and cheap to measure, and in many cases may even provide less noisy and more representative observation data than observations of coverage or biomass.

Scenario simulations contrast a system's behaviour under different conditions depicting either patterns recurring in past observations or predicted for the future. For time-invariant conditions (e.g., physiological parameters changing with species assemblage or long-term adaptation), the scenario factors may often simply be varied by a fixed percentage around a default or mean expected value, but there is no established procedure for factors which are not constant in time, but rather periodic (e.g., strongly seasonal environmental forcing). Considering that in temperate environments, the environmental forcing variables for *Ulva* growth models all show seasonal periodicity leads to our research question 3: How can we derive robust and realistic seasonal scenarios from historical data with intermittent strong seasonal signals but very high variability?

Finally, we use the model, calibration and scenario development procedure outlined above to address the question that originally motivated this study, research question 4: Which of the environmental factors are likely to have led to bloom and non-bloom years observed in Tauranga Harbour? We will therefore simulate a number of idealised seasonal scenarios that represent "extreme" high and low conditions for each of the environmental forcing variables and examine the resulting changes in the seasonal development (timing and magnitude of response) of biomass and tissue nutrients.

3.2 Methods

In chapter 2, we analysed QN observations from a monitoring dataset from Tauranga Harbour, New Zealand, using a subset of the model of Solidoro et al. (1997), in which we explicitly included only QN, and neither B nor QP in the model. The same dataset additionally contains observations of B and QP, which so far have not been analysed in conjunction with a process-based model. While the original model of Solidoro et al. (1997) does include B and QN as state variables, and adding QP would not be difficult, it additionally includes (and structurally relies upon) the dissolved oxygen concentration (DO) as well ammonium (NH), NO_x^- (NO) and phosphate (PO) as state variables. For the site and time period considered here, reliable estimates of DO are not available. Additionally, in contrast to the system examined by Solidoro et al. (1997), the estuary examined here is relatively well-mixed and

flushed, making it unlikely that the *Ulva* dynamics are controlled to a high degree by the occurrence of anoxic crises. Observation data of the water column concentrations of the nutrients NH, NO and PO are available at approximately the same frequency as those of B, QN, and QP, and few observation data are available to quantify the fluxes of nutrients at the landward and seaward boundaries of the system as well as to and from other biogeochemical components within the system. Therefore, we choose to use a model with reduced complexity by considering the water column nutrients as environmental forcing data in contrast to state variables (similar to the approach taken by Bendoricchio et al., 1994).

3.2.1 Model description

For this study, we reimplemented the *Ulva* spp. model first developed and described by Guimaraens et al. (2005), which considers the dynamics of *Ulva* spp. B, QN and QN. In overall structure, it is similar to the model of Solidoro et al. (1997), with the following differences: 1. dissolved inorganic N and P are considered as environmental forcing rather than state variables; 2. phosphorus dynamics are described by an internal (tissue) quota / luxury uptake process; 3. dissolved oxygen is not explicitly considered; 4. mortality is proportional to biomass and water temperature. The model is briefly summarised below, and further details may be found in Guimaraens et al. (2005). In the following, symbols in italic script denote state variables, functional terms or forcing variables which are continuously variable in time, while symbols in non-italic (roman) script denote constant parameters.

The model state variables are biomass B, tissue nitrogen quota QN and tissue phosphorus quota QP. The relative change in B (net relative growth rate) is determined by the difference between growth and mortality terms

$$\frac{\mathrm{d}B}{\mathrm{d}t} = (\mu - \Omega) \cdot B \tag{3.1}$$

where growth is defined in the multiplicative form of a maximum growth rate and limiting functions of temperature, irradiance, tissue nitrogen and tissue phosphorus

$$\mu = \mu_{\max} \cdot f_1(QN) \cdot f_2(QP) \cdot f_3(T) \cdot f_4(I). \tag{3.2}$$

For the mortality term, Guimaraens et al. (2005) use a less common formulation, where mortality is proportional to biomass and temperature, and additionally inversely proportional to the limiting functions

$$\Omega = \frac{\Omega_{\max} \cdot \Theta^{T-30} \cdot B}{B + \mathrm{K_d} \cdot f_1(QN) \cdot f_2(QP) \cdot f_3(T) \cdot f_4(I)}. \tag{3.3}$$

The limiting functions follow inverse hyperbolic relationships for tissue nitrogen

$$f_1(QN) = 1 - \frac{\mathrm{QN_{min}}}{N} \tag{3.4}$$

and tissue phosphorus

$$f_2(QP) = 1 - \frac{\mathrm{QP_{min}}}{P}, \tag{3.5}$$

a Gauss curve for temperature

$$f_3(T) = \mathrm{e}^{-\lambda(T-\mathrm{t_{opt}})^2}, \tag{3.6}$$

and a Monod curve for irradiance

$$f_4(I) = \frac{I}{I + \mathrm{K_i}}. \tag{3.7}$$

The change in QN is determined by the difference between uptake of N fractions NH and NO and use of QN for growth

$$\frac{\mathrm{d}QN}{\mathrm{d}t} = NH_{upt} + NO_{upt} - \mu \cdot QN, \tag{3.8}$$

and the change in QP is correspondingly determined by the difference between uptake of PO and use of QP for growth

$$\frac{\mathrm{d}QP}{\mathrm{d}t} = PO_{upt} - \mu \cdot QP. \tag{3.9}$$

Without a preferential uptake for either NO or NH, each respective uptake is proportional (NH_{pro}) or inversely proportional ($1 - NH_{pro}$) to their ratio

$$NH_{pro} = \frac{NH}{NO + NH}, \tag{3.10}$$

decreases linearly with increasing QN

$$N_{rep} = \frac{\mathrm{QN_{max}} - QN}{\mathrm{QN_{max}} - \mathrm{QN_{min}}}, \tag{3.11}$$

and follows a Monod relationship, resulting in

$$NH_{upt} = \mathrm{V_{mNH}} \cdot \frac{N_{rep} \cdot NH_{pro} \cdot NH}{NH + \mathrm{k_{NH}}} \tag{3.12}$$

and

$$NO_{upt} = \mathrm{V_{mNO}} \cdot \frac{N_{rep} \cdot (1 - NH_{pro}) \cdot NO}{NO + \mathrm{k_{NO}}}. \tag{3.13}$$

Uptake of PO is described in the same fashion, without the need for a ratio term between fractions since only a single fraction is considered, resulting in

$$P_{rep} = \frac{\mathrm{QP_{max}} - QP}{\mathrm{QP_{max}} - \mathrm{QP_{min}}} \tag{3.14}$$

and

$$PO_{upt} = \mathrm{V_{mPO}} \cdot \frac{P_{rep} \cdot PO}{PO + \mathrm{k_{PO}}}. \tag{3.15}$$

The model was implemented in GNU Octave (version 3.6.4, Eaton et al., 2014), and the ODE system integrated over time using the LSODE solver (Livermore Solver for Ordinary Differential Equations, Radhakrishnan and Hindmarsh, 1993).

Table 3.1: Symbols, units and minimum and maximum values of the simulation model's state variables and parameters. Unless otherwise noted in the comments, minimum and maximum parameter values were taken from Guimaraens et al. (2005).

symbol	units	min.	max.	comments
B	$(g\,dw)\,m^{-2}$			
QN	$mg\,N\,(g\,dw)^{-1}$			
QP	$mg\,P\,(g\,dw)^{-1}$			
μ_{max}	day^{-1}	0.36	0.50	
K_i	$W\,m^{-2}$	24.00	119.00	
t_{opt}	°C	20.00	30.00	
V_{mNH}	$mg\,N\,(g\,dw)^{-1}\,day^{-1}$	48.00	124.80	
V_{mNO}	$mg\,N\,(g\,dw)^{-1}\,day^{-1}$	16.80	19.70	
V_{mPO}	$mg\,P\,(g\,dw)^{-1}\,day^{-1}$	5.52	26.16	
k_{NH}	$mg\,N\,l^{-1}$	0.20	0.60	
k_{NO}	$mg\,N\,l^{-1}$	0.12	0.38	Guimaraens et al. (2005) default value ± 50%
k_{PO}	$mg\,P\,l^{-1}$	0.03	0.11	
QN_{max}	$mg\,N\,(g\,dw)^{-1}$	30.00	60.00	this study observation data
QN_{min}	$mg\,N\,(g\,dw)^{-1}$	1.00	15.00	this study observation data
QP_{max}	$mg\,P\,(g\,dw)^{-1}$	1.00	5.85	this study observation data
QP_{min}	$mg\,P\,(g\,dw)^{-1}$	0.01	1.65	this study observation data
λ	$°C^{-1}$	0.00	0.01	Guimaraens et al. (2005) default value ± 50%
Θ		0.56	1.70	Guimaraens et al. (2005) default value ± 50%
Ω_{max}	day^{-1}	0.01	0.49	this study observation data
K_d	$(g\,dw)\,m^{-2}$	1.00	1200.00	this study observation data

3.2.2 Biomass and tissue nutrient observation data

The most basic output used for calibration and verification of algae population dynamics models is spatially averaged biomass over time. Estimating the same quantity in the field is difficult, especially for macroalgae such as *Ulva*, due to the high spatiotemporal variability of biomass, including the difference between intertidal and subtidal fractions of the population, and the high cost of biomass sample collection and processing. Here we use visual estimates of abundance and convert these estimates to biomass using broad assumptions. Although not ideal, this shortcoming is counterbalanced by the long measurement timeframe (which is essential to our ability to understand the variation in blooms and calibration). Moreover, measurements are collected by the same individual reducing a potential source of variation.

The conversion factor from coverage to biomass is likely to depend both on the details of species assemblage and growth conditions. In addition to the conversion factor used by Guimaraens et al. (2005), from an upwelling region in southeastern Brazil, we also consider those used by Park (2007), from the same site as used in this study, and Alexander et al. (2008), from the Avon-Heathcote estuary on the South Island of New Zealand.

Assuming that the "0.25 m^2 quadrat" mentioned in Alexander et al. (2008) refers to a quadrat with 0.25 m side length and an area of 0.0625 m^2 (1/16 m^2, as seems likely given the conversions in Table 4.2 in their study), and that the linear regression shown in their study in Figure 4.20 is based on wet weight, their equation

$$B = -2.141\,(\text{g w.w.})\,\text{quadrat}^{-1} + 1.2883\,(\text{g w.w.})\,\text{quadrat}^{-1} \cdot C, \tag{3.16}$$

taking into account their dry weight to wet weight ratio of 0.26, is equivalent to

$$B = -8.9\,(\text{g d.w.})\,m^{-2} + 5.4\,(\text{g d.w.})\,m^{-2} \cdot C. \tag{3.17}$$

where C is cover in % and B is biomass in (g d.w.) m^{-2}, with a linear correlation coefficient of 0.84. Requiring an intercept of zero would in this case further decrease the slope to 5.24 (g d.w.) m^{-2}. Guimaraens et al. (2005) obtained a linear correlation coefficient of 0.83 when converting *Ulva* cover to biomass according to the equation

$$B = 4\,(\text{g d.w.})\,m^{-2} + 8.5\,(\text{g d.w.})\,m^{-2} \cdot C. \tag{3.18}$$

This agrees well with Park (2007), who found a relationship of

$$B = 8\,(\text{g d.w.})\,m^{-2} \cdot C \tag{3.19}$$

based on *Ulva* samples from our case study site in Tauranga Harbour, although noting that this relationship breaks down at or close to 100%. Since in our case, 100% coverage is rarely reached, especially when averaging observations from several sites, and since this conversion is based on data from the same site, we choose to use the conversion factor of Park (2007).

The Bay of Plenty Regional Council provided *Ulva* intertidal coverage and tissue N and P observation data from Tauranga Harbour from an ongoing monitoring programme (Park, 1996). Samples have been collected approximately bimonthly since 1991 at three sites (Ongare in the northern basin of Tauranga Harbour, and Otumoetai and Town Reach in the southern basins). The coverage and converted biomass as well as tissue N and P data are shown in Figure 3.1. For this study, we used only data averaged over all three available sites, shown as a solid black line in Figure 3.1.

3.2.3 Environmental forcing data

The environmental forcing data comprise the water column concentrations of the inorganic N and P fractions NH_4^+, NO_3^- and PO_4^{3-}, water temperature and solar irradiance. The data sources are mostly identical to those described in chapter 2, and we will here only briefly summarise them and describe differences (e.g., additional post-processing) where applicable.

Water column NH_4^+, NO_3^- and PO_4^{3-} concentration data were provided for several sites as part of an ongoing monitoring programme by the Bay of Plenty Regional Council (Park, 1996). Since we are here examining a single zero-dimensional ("box model") system, and the variability between sites is high so that averaging techniques would lead to discontinuities problematic for a simulation model, we use data from only a single site. The site "Kulim. Ave Otumoetai" was chosen since among those available, it is most likely to experience conditions representative of the southern basins of Tauranga Harbour. Solar irradiance data was acquired from New Zealand's National Climate Database ("CliFlo", http://cliflo.niwa.co.nz), based on measurements from an automated weather station at Tauranga airport, and approximate in situ values derived from these surface measurements as described in chapter 2. Water temperature data are based on measurements at "Salisbury Wharf", provided by the Port of Tauranga.

Before further post-processing, an annual cosine function was fitted to the raw observation data. Missing values were then replaced by values calculated by evaluating the fitted cosine function at the corresponding time, and the fitted cosine function was additionally used to provide forcing data for idealised scenarios (see

section 3.2.5). To avoid numerical issues when integrating the ODE system, the forcing data should be continuous and smooth in time, i.e., without discontinuities in the function itself or its first derivative. Piecewise cubic hermite interpolation was therefore used to interpolate in time between the individual observation data points for the simulations where realistic forcing data were used.

From 1991/08/10 until 1993/06/03, NO_3^- concentrations were measured using an ultraviolet (UV) sensor. From 1993/07/23 onward, the combined concentration of NO_2^- and NO_3^- (NO_x^-) was measured using wet chemical colorimetric analysis. Based on a related dataset of water column nutrients in Tauranga Harbour (data not shown) from which both NO_2^- and NO_3^- concentrations are available, we assume that NO_2^- concentrations are negligible for the purposes of this study, and therefore use the NO_x^- data in place of NO_3^- for the latter period. Based on a comparison of data from all individual sites before and after the change in methodology as well as two replicate data points analysed with both methods in 1995, we estimate that the UV NO_3^- data are overestimating concentrations by a factor of 2. UV NO_3^- data were therefore corrected by this factor before being merged with the wet chemical colorimetric data for statistical analysis and cosine fits, and the corresponding time period excluded from the simulations with realistic forcing.

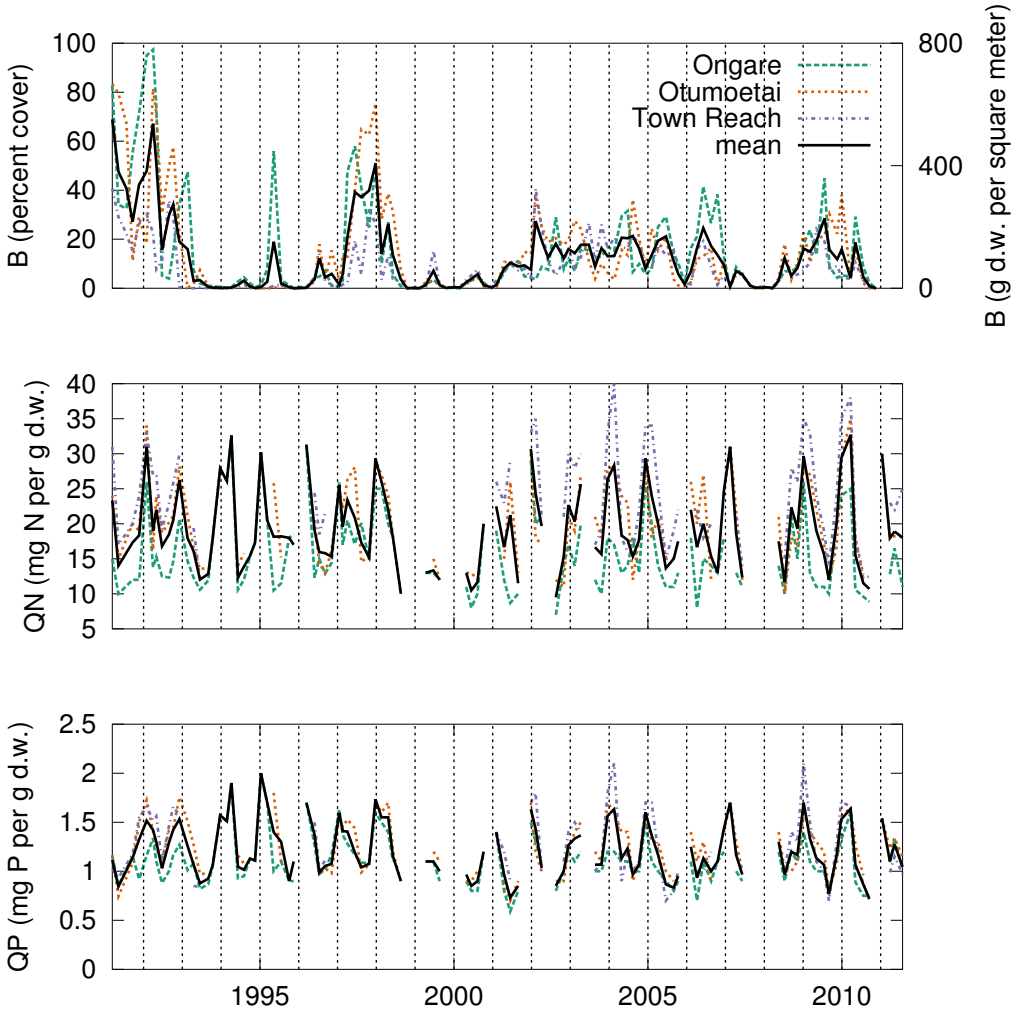

Figure 3.1: Observation data of the state variables B, QN and QP. B was measured in percent cover, see text for details of the approximate conversion to (g d.w.) m^{-2} as shown on the right-hand side axis of the top panel.

3.2.4 Calibration and calibration uncertainty

For calibration of both long-term and idealised seasonal scenario simulations, following the same approach as in chapter 2, we used the CRS2-LM global optimisation algorithm (Kaelo and Ali, 2006) in the implementation of Johnson (2013). All 17 parameters of the model were included in the calibration, with ranges as shown in Table 3.1.

The cost function F for calibrations is based on either an individual or a combination of all three of the state variables *B*, *QN* and *QP*. The mean absolute deviation

(MeanAD) was used as the cost function for an individual state variable

$$\mathrm{F}_1 = \mathrm{MeanAD} = \frac{1}{n} \cdot \sum_{i=1}^{n} |mod_i - obs_i| \,, \tag{3.20}$$

where mod_i are the modelled and obs_i the observed values for the i-th observation data point, and n is the total number of data points. Using the mean instead of just the sum in Eq. (3.20) has no influence on the calibration result, but may ease the interpretation of the progress and efficiency of the calibration algorithm. For the combined cost function based on all three state variables, we use normalised MeanAD values by dividing by the mean of the observations for each variable, the result of which may be considered a form of relative error (RE)

$$\mathrm{RE} = \frac{\frac{1}{n_j} \sum_{i=1}^{n_j} \left| mod_{ij} - obs_{ij} \right|}{\frac{1}{n_j} \sum_{i=1}^{n_j} obs_{ij}}, \tag{3.21}$$

where m is the number of state variables, n_j is the number of data points for the j-th state variable, mod_{ij} is the j-th data point of the i-th state variable of model output and obs_{ij} the corresponding observations data point. Dividing by n_j in both the numerator and the denominator of Eq. (3.21) is mathematically unnecessary, but has computational and code re-use advantages in the actual implementation. We then calculate the cost function as the sum of RE over all variables:

$$\mathrm{F}_2 = \sum_{j=1}^{m} \left(\frac{\frac{1}{n_j} \sum_{i=1}^{n_j} \left| mod_{ij} - obs_{ij} \right|}{\frac{1}{n_j} \sum_{i=1}^{n_j} obs_{ij}} \right). \tag{3.22}$$

Alternatively, more emphasis may be put on avoiding large RE for any individual state variable by defining the cost function to be the sum of the squares of the relative errors:

$$\mathrm{F}_3 = \frac{1}{m} \sum_{j=1}^{m} \left(\frac{\sum_{i=1}^{n_j} \left| mod_{ij} - obs_{ij} \right|}{\sum_{i=1}^{n_j} obs_{ij}} \right)^2 . \tag{3.23}$$

In contrast to using just the sum or mean of each individual variable's cost function, this formulation ensures that for example RE of 40%, 20% and 20% lead to a higher value of F than 30%, 25% and 25%.

If the calibration algorithm uses an ODE integration with unrealistic parameter combinations, the integration may be very slow or even fail due to numerical convergence issues. To prevent this, during all calibration procedures, sanity checks were performed on the parameter values, and the ODE integration only performed if all sanity checks passed. The checks were: $\mathrm{QN}_{\min} < \mathrm{QN}_{\max}$ and $\mathrm{QP}_{\min} < \mathrm{QP}_{\max}$.

For all long-term simulations, the spin-up period was from 1994/01/01 until 1995/06/30, the calibration period was from 1995/07/01 until 2002/06/30, and the validation period from 2002/07/01 until 2008/06/30.

To aid in the interpretation of the calibration uncertainty histograms, we define the discrepancy statistic w, loosely related to the Cramér-von Mises criterion. Let m be the sample size (number of independent calibration runs), n the number of histogram bins, and C_i the number of data points in bin i. If the calibrated parameter values followed a uniform distribution, we would expect all C_i to be equal to $E = \frac{m}{n}$. We can therefore calculate a measure of the discrepancy between this and the observed histogram as

$$w = \sqrt{\sum_{i=1}^{n} \left(\frac{C_i - E}{E} \right)^2}. \tag{3.24}$$

The discrepancy w can also be interpreted as the root mean square (RMS) of the relative deviation between observed sample frequencies and those expected under the assumption of a uniform distribution.

The total computational cost of the employed calibration methodology is high, due to the computational cost of each individual simulation, the large number of simulations required for a single calibration, and the need for multiple calibrations to analyse calibration uncertainty for each combination of either the long-term or idealised case with one of the cost functions. A single calibration required between approximately 200 and 4000 simulations, and each combination of the long-term or idealised case with a specific cost function between approximately 40000 and 90000 simulations, leading to a total on the order of 500000 simulations. The individual calibrations are independent of each other, and were therefore calculated in parallel on a computing cluster.

3.2.5 Idealised forcing simulations and seasonal scenarios

Idealised scenarios representing "high" and "low" value conditions for each of the five forcing variables NH_4^+, NO_3^-, PO_4^{3-}, temperature and irradiance were defined. For each variable, available observation data over all years were grouped by calendar month. For each variable and each month, the 5$^{\text{th}}$ (low) and 95$^{\text{th}}$ (high) percentile was calculated. An annual cosine function was then least-squares fitted to each variable's low and high monthly percentiles to derive continuous forcing functions for the corresponding low and high scenarios. For the nutrient forcing variables, the determination of phase was more difficult for the 5$^{\text{th}}$ percentile due to the high variability at low concentrations. The phase was therefore calculated first for the 95$^{\text{th}}$ percentile of all variables and then also applied to the corresponding lower percentile. The cosine fit for the 5$^{\text{th}}$ percentile is therefore no longer guaranteed to be optimal in the least-squares sense.

For the scenario simulations that were forced with and calibrated against annual cosine functions, the initial conditions of the state variables B, QN and QP were set to the mean value of the corresponding cosine function to decrease the time necessary for model spin-up. Preliminary investigation of individual scenario runs with >10 years simulation time showed that the spin-up time of 1.5 years chosen previously was again sufficient, after which a dynamic equilibrium with annual periodicity was reached. For further analysis and comparisons between scenarios, we therefore consider only the first year after spin-up.

3.3 Results

3.3.1 Long-term simulations

The results of a long-term simulation using the default parameter values of Guimaraens et al. (2005) are shown in Figure 3.2. While all three state variables are in the right order of magnitude, none are close to the observed mean values or annual range of variability. B shows a regular but weak annual signal, does not reproduce any of the observed bloom events and is overall grossly underestimated. QN shows a high positive bias, and is underestimating the amplitude of the annual signal. QP is overestimating by a factor of three or more, and shows a much smaller amplitude in the annual signal than the observations.

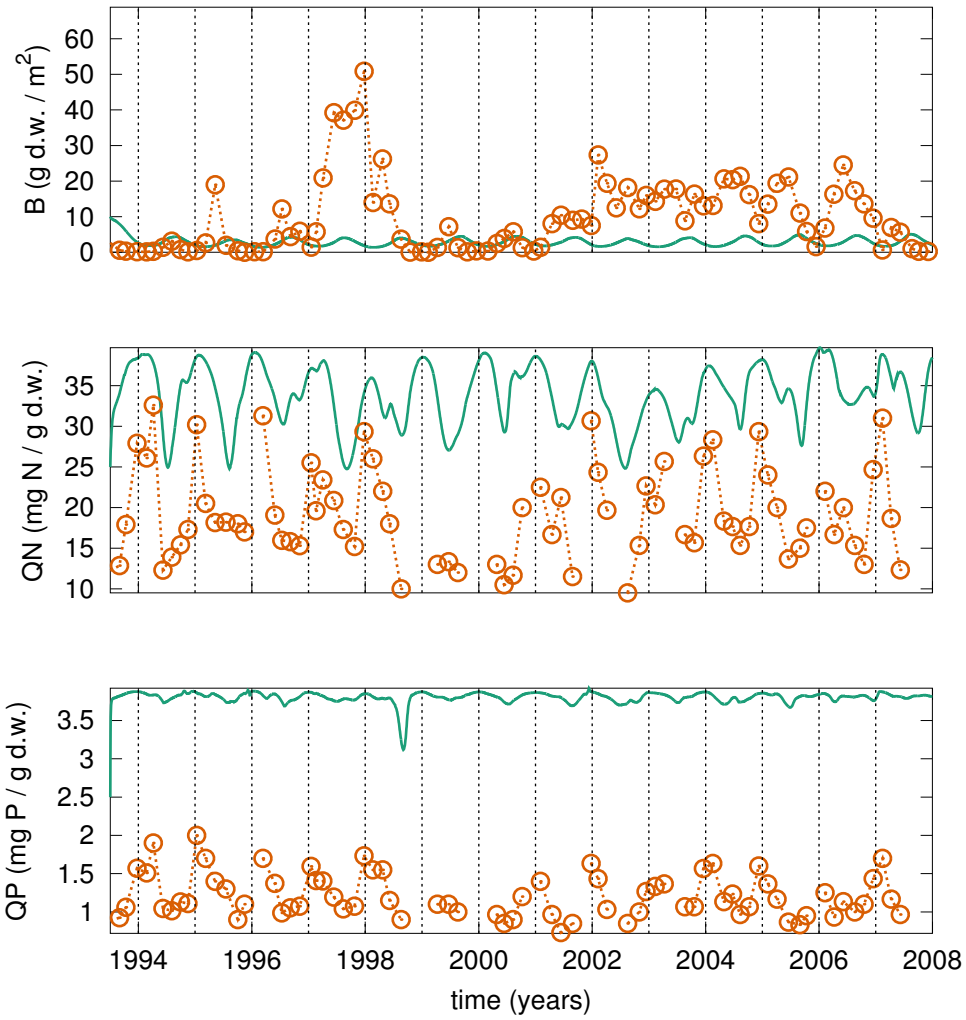

Figure 3.2: Comparison of the time series of observations with model results based on parameter values taken from Guimaraens et al. (2005).

Calibrations for the long-term simulations were carried out separately with cost functions for B, QN, QP and the normalised sum of all three. Figure 3.3 shows the results for the cost function for B. Peak values of B match the observations for several bloom events (e.g., 1997/1998 or 2006/2007), but still underestimate by a factor of two or more in others (e.g., 1998/1999 or 2002/2003). Overestimation occurs in only a single case (1995/1996). High B in winter which is seen repeatedly in the observations is not reproduced by the model, which decreases to almost zero in every winter.

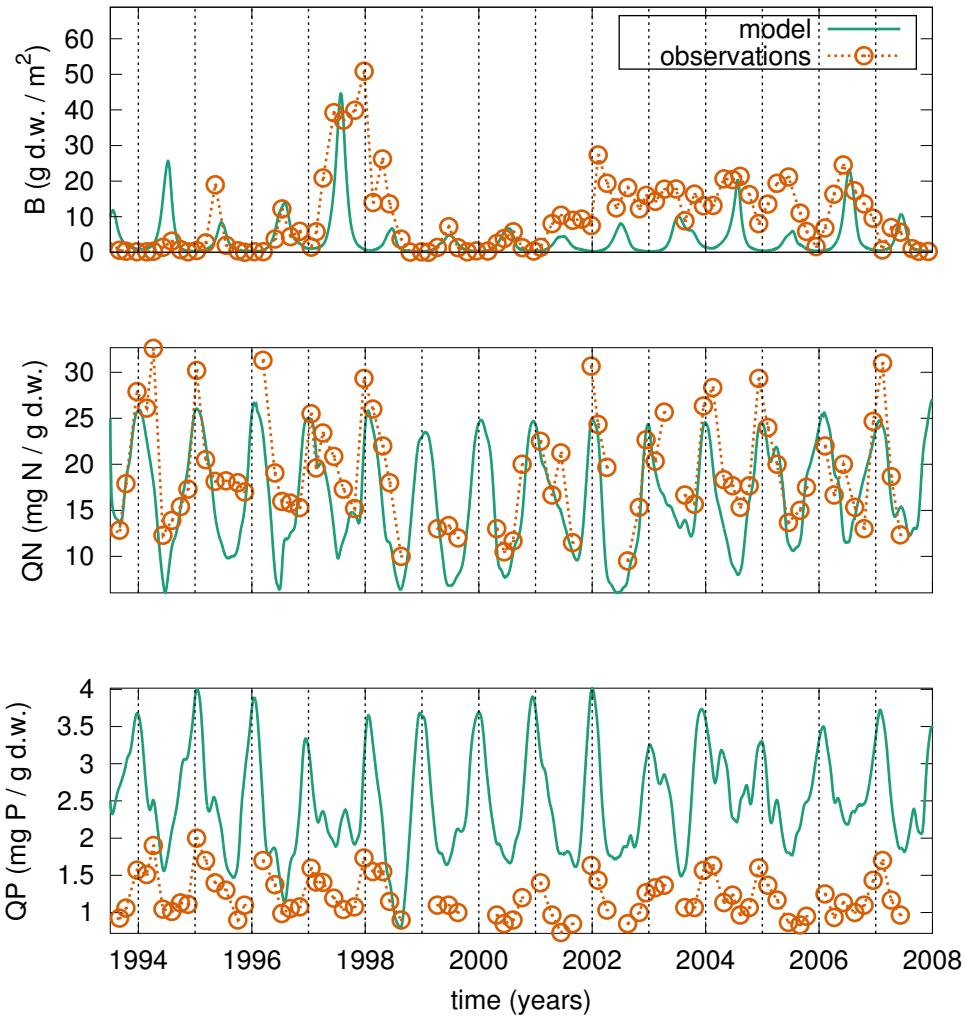

Figure 3.3: Comparison of the time series of observations with model results from a calibration aimed at minimising the cost function of B.

When calibrating with a cost function for QN, the model "explodes" as B reaches extremely high values which are biologically and even physically meaningless (Figure 3.4). QN is improved slightly compared to the previous calibration, with especially the summer minima matching the observations much better, while winter maxima are still underestimated. The positive bias for QP is increased again, while the amplitude of the annual signal is smaller and approaching that of the observations.

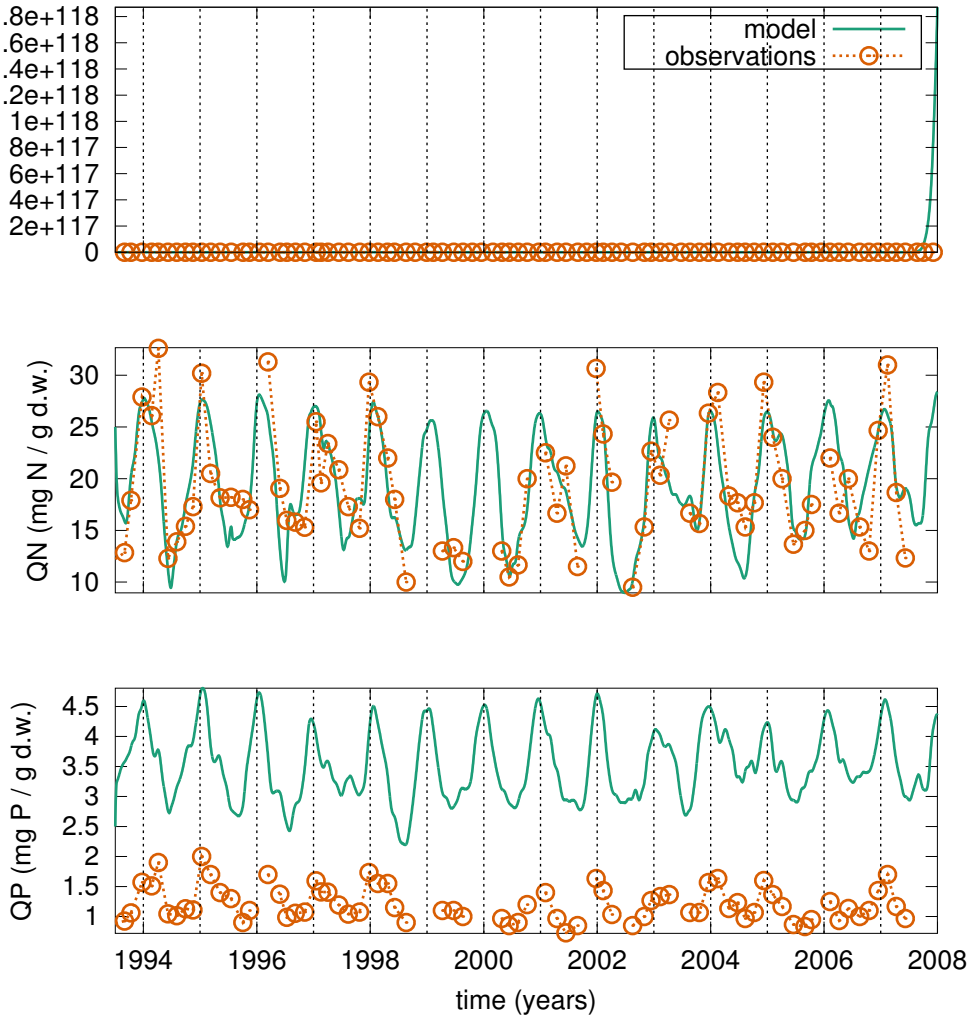

Figure 3.4: Comparison of the time series of observations with model results from a calibration aimed at minimising the cost function of QN.

When calibrating with a cost function for *QP* (Figure 3.5), *B* shows very narrow and high peaks in many summers (e.g., 1998/1999 or 2007/2008), in most cases overestimating, and not matching the observed relative height of summer maxima between seasons (i.e., bloom vs. non-bloom seasons), but does stay within the overall observed range. *QN* is greatly overestimated, both in terms of mean values as well as amplitude of the annual signal. Observations of *QP* are reproduced well, albeit with a conspicuous underestimation of the summer minimum in the 1998/1999 season.

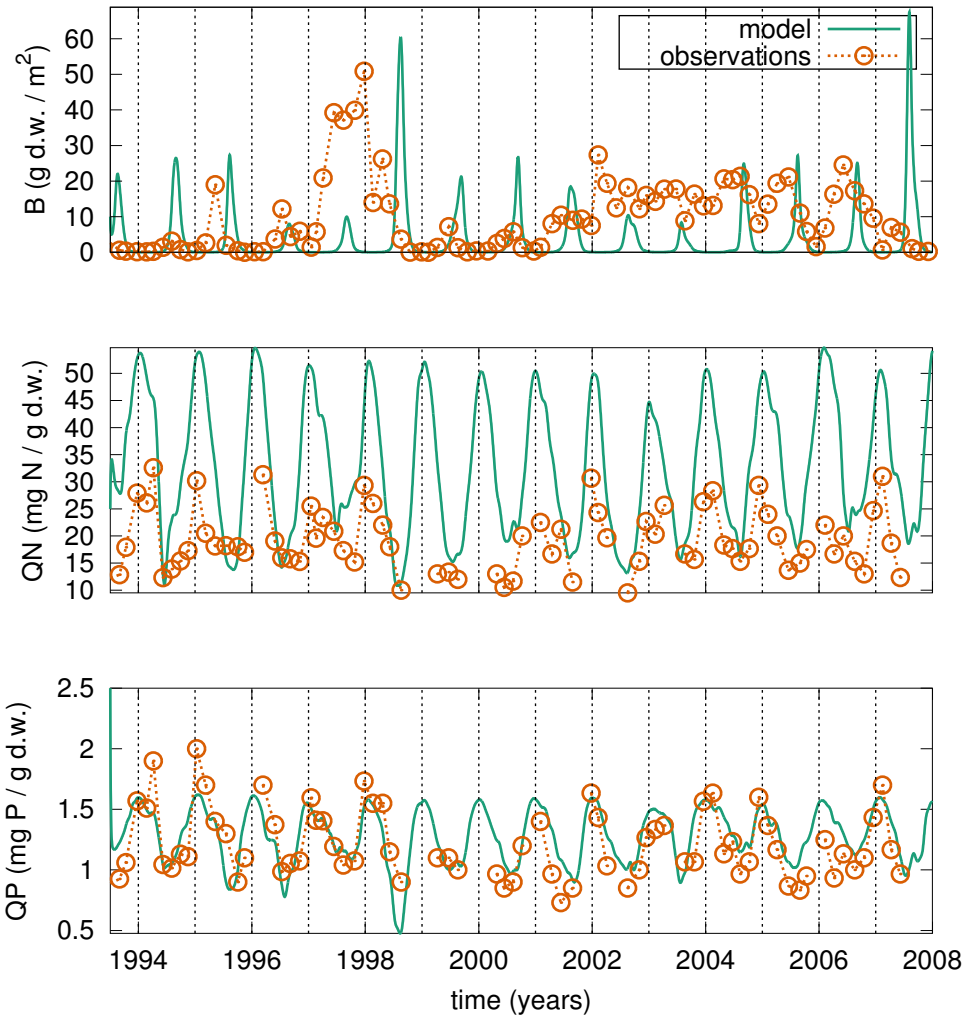

Figure 3.5: Comparison of the time series of observations with model results from a calibration aimed at minimising the cost function of QP.

Figure 3.6 shows the results of the calibration based on the normalised sum of the cost functions of all three state variables. Overall, *B* shows similar performance as in the calibration for *B* alone, with slightly higher variability between seasons and more cases of overestimated summer maxima (e.g., 2006/2007), but also improvements in phases which these were previously underestimated (e.g., 1998-2002). *QN* shows good agreement with the observations, especially in terms of the amplitude of the annual signal. *QN* now shows little bias but also extremely low variability, with only a few decreases in summer, which are very small compared to the annual range of the observations.

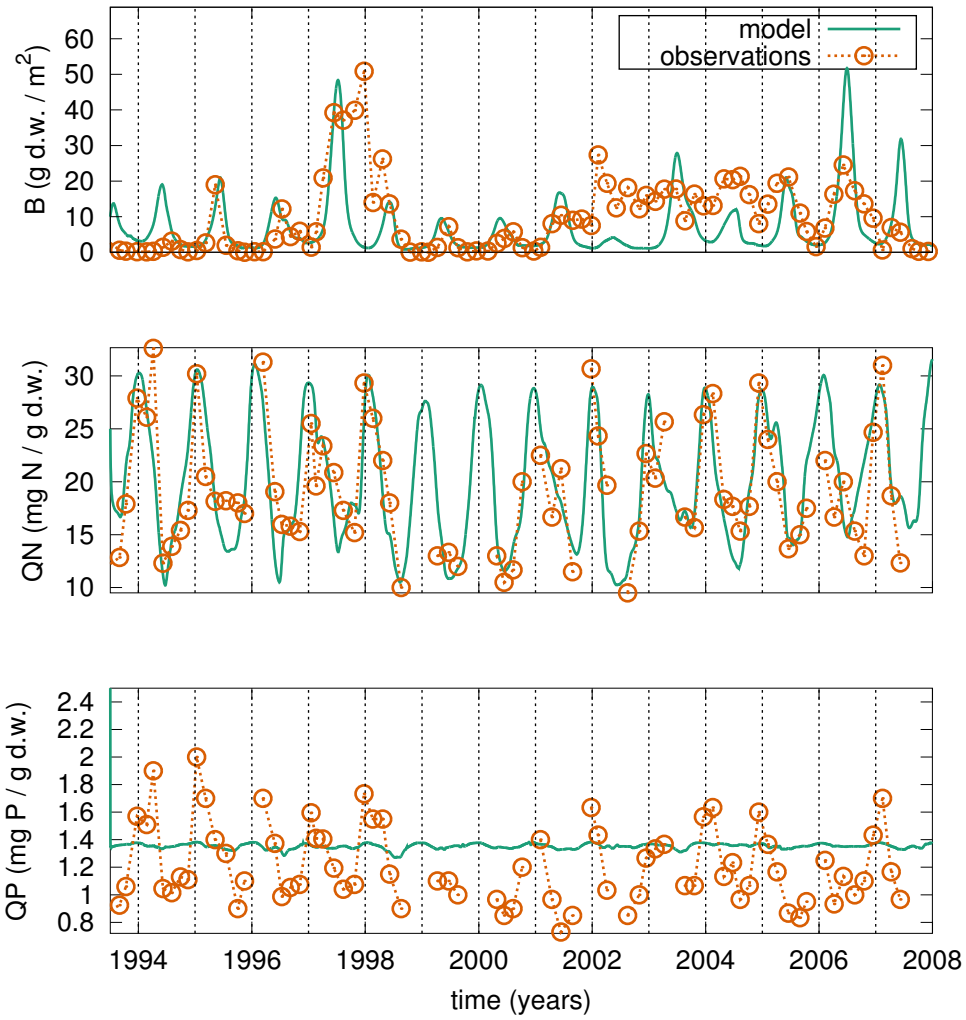

Figure 3.6: Comparison of the time series of observations with model results from a calibration aimed at minimising the normalised sum of the cost functions of B, QN and QP.

3.3.2 Calibration uncertainty

Calibration uncertainty histograms for four selected parameters from each of the four cost function cases from the long-term simulation calibration uncertainty analyses are shown in Figure 3.7. For each cost function case, the four parameters displaying the highest value for the discrepancy measure w were chosen. All but one (k_{NO} for the normalised sum cost function) show unimodal distributions.

For the B cost function, λ and t_{opt} have a clear maximum at the minimum of their range, but with a number of low frequencies spread across the entire range. Ω_{max} has a clear maximum at the maximum of its range and low frequencies spread down to approximately the middle of its range. Θ stands out as the only parameter which has a clear peak in frequency over several histogram bins, which appears almost symmetrical, and is located near the middle of its range. For the QN cost function, QN_{max}, K_i and V_{mNH} all have very clear maxima at the lower end of their range, and k_{NH} at the higher end of its range. QN_{max} is the only case overall where every single calibration determined a value in the same (lowest) bin of the parameter's range. For the QP cost function, the results are very similar to those for the QN cost function, but as expected with parameters related to QP (V_{mPO}, QP_{min} and k_{PO}) in place of those related to QN showing highest values of w, but again with K_i among the top four. For the normalised sum cost function, the four best constrained parameters are QN_{max}, QP_{max}, QP_{min} and k_{NO}, all of which are directly related to either QN or QP, and only indirectly to B. The distribution of QN_{max} is similar to the case of the QN cost function, although with a few values in the adjacent bins, but still near the lower end of the parameter's range.

For reference, Appendix 3.A contains calibration uncertainty histograms for all 17 model parameters for each of the four cost functions in Figures 3.15 to 3.18, and the corresponding parameter values from the individual calibrations that resulted in the minimum cost function value overall in Table 3.2.

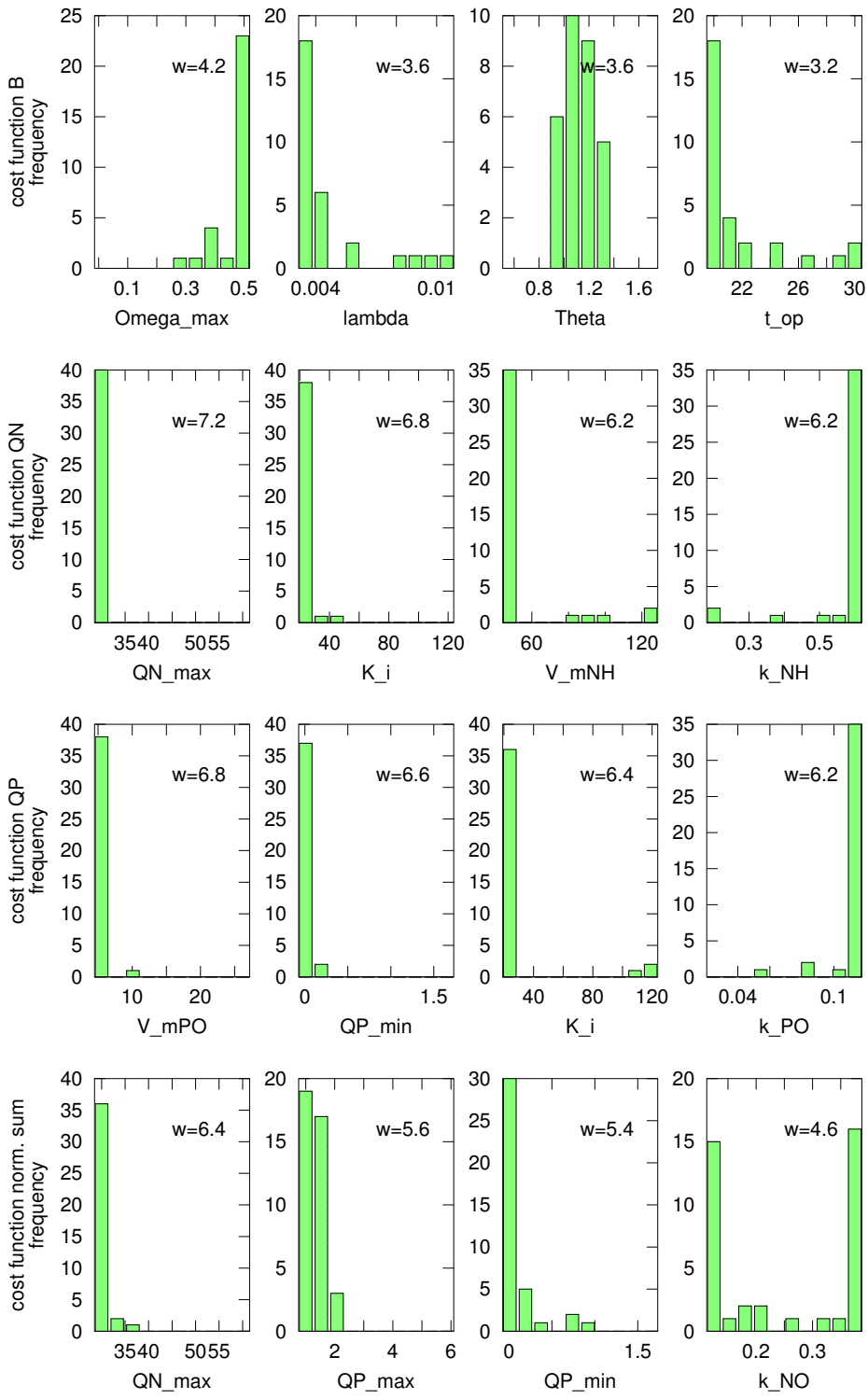

Figure 3.7: Calibration uncertainty histograms for four selected parameters from each of the four cost function cases (from top to bottom: cost function for B, QN, QP and the normalised sum of all three). Frequency refers to the number of calibrations that led to the respective value of the model parameter. Parameters selected based on decreasing value of discrepancy measure w (see section 3.2.4 for details).

3.3.3 Idealised forcing simulations and seasonal scenarios

The annual cosine fits to the forcing data required for the idealised simulations are shown in Figure 3.8. For *NH*, the amplitude is on the same order of magnitude in almost all seasons (except for a very high winter maximum in the observation data in 2006), but frequently underestimates the annual range of the observations by a factor of approximately two, and none of the individual seasons show very good agreement with the observations. *NO*, on the other hand, shows very good overall agreement in several seasons, also reproduces the summer minimal well in most seasons but also underestimates winter maxima in several seasons. The *PO* fit has a very small amplitude compared to the range of variability in the observation data, frequently underestimating this range by a factor of ten or more. The long-term bias is low, with no obvious pattern in the sequence of over- and underestimated periods. Temperature shows very good agreement overall, although some maxima are under- and some minima overestimated, the latter especially in the first years until 1997. Irradiance also shows very good agreement, with only a few summer maxima being slightly underestimated.

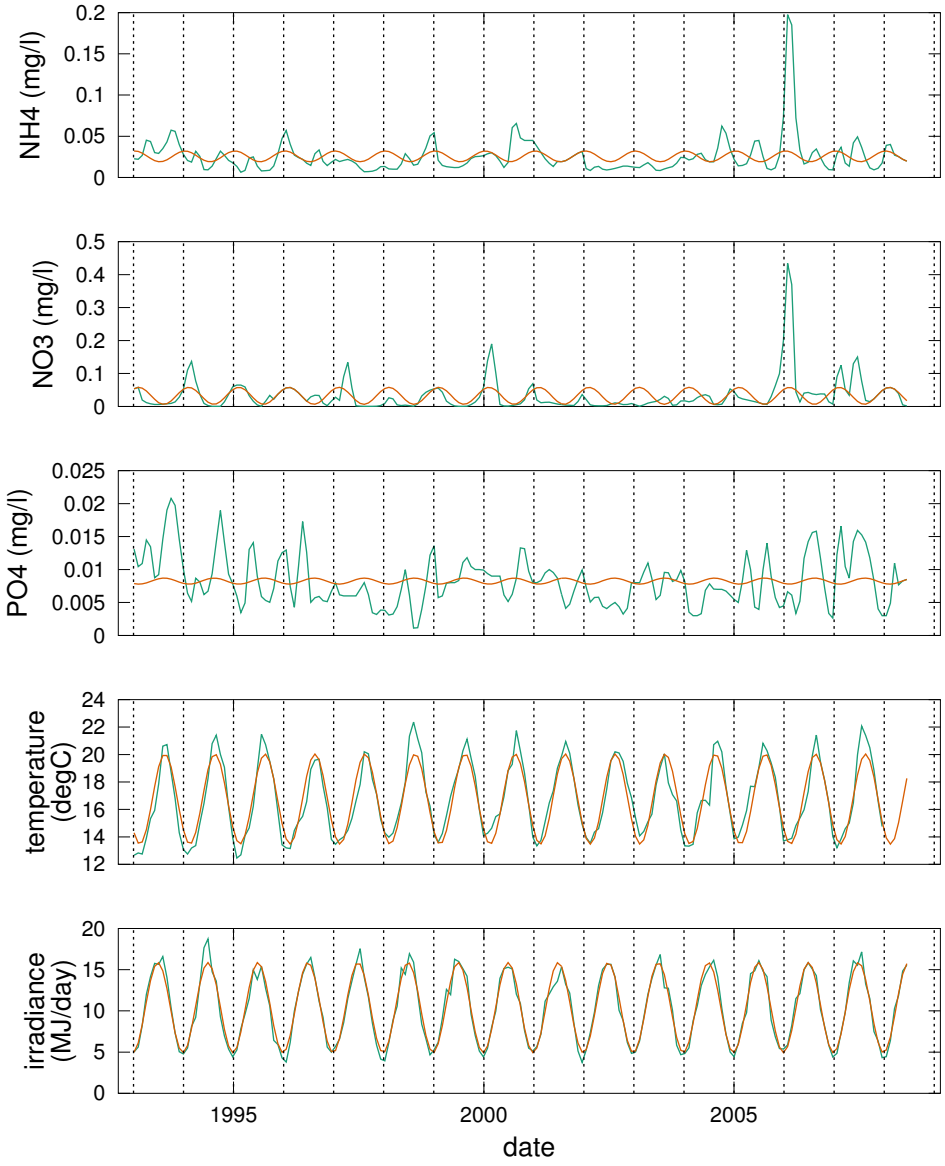

Figure 3.8: Annual cosine fits to the five environmental forcing variables (*NH*, *NO*, *PO*, temperature and irradiance) as required for the idealised simulations.

Results from the idealised simulation calibration for a cost function for B are shown in Figure 3.9. Amplitude and phase for *B* are matched well and with low bias, albeit with a small but clear positive trend, and the resulting time series shows broad and symmetrical summer peaks close to a cosine shape. *QN* is strongly overestimated by 10 to 15 mg N $(\mathrm{g\,dw})^{-1}$, and the annual range is underestimated by a factor of two or more.

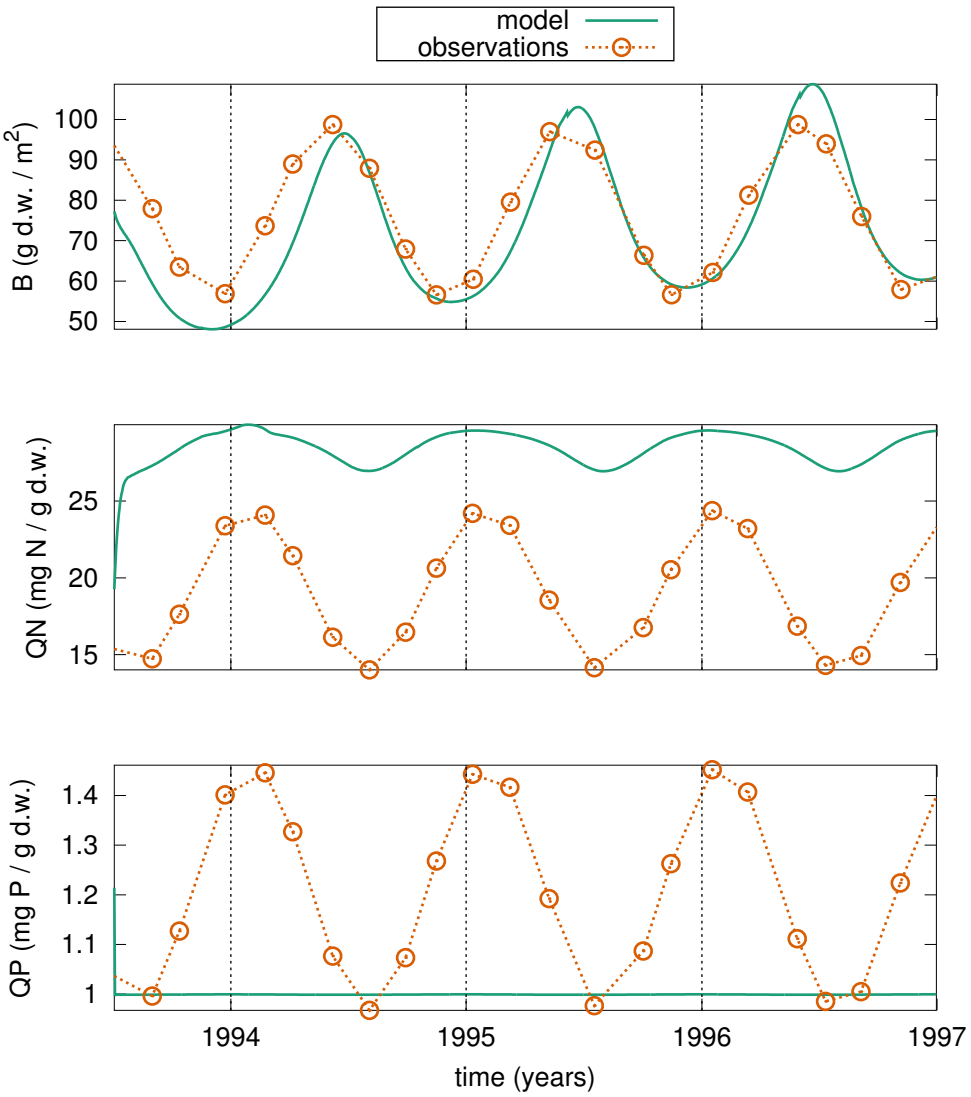

Figure 3.9: Comparison of the time series of idealised observations with model results from a calibration aimed at minimising the cost function of B.

When calibrating with a cost function for QN, B in the model explodes similar to the corresponding long-term calibration case, once again leading to biologically and physically meaningless values. QN itself, on the other hand, calibrates almost perfectly. QP is consistently overestimated, with positive bias of approximately $3\,\mathrm{mg\,P\,(g\,dw)^{-1}}$, but does show a clear annual cycle with amplitude slightly larger than in the idealised observation data.

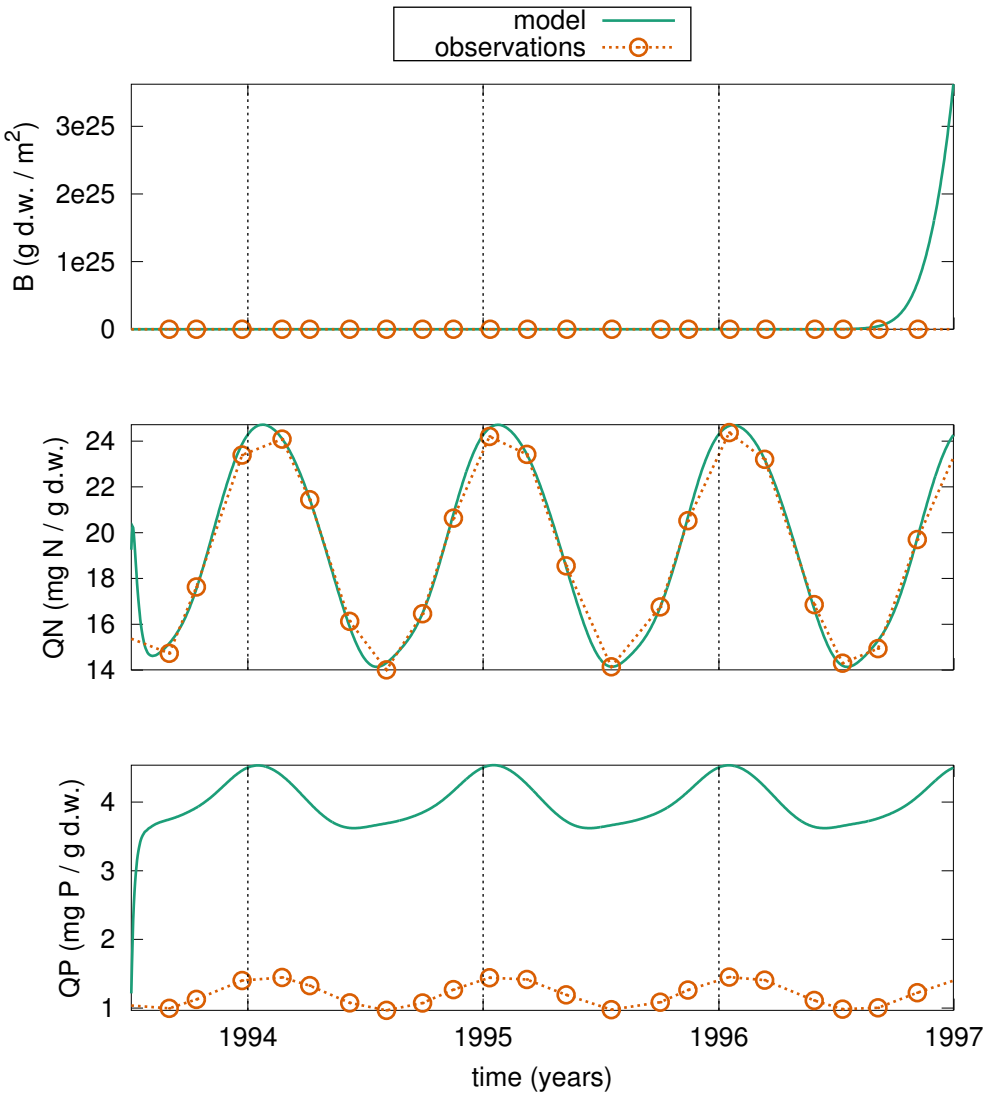

Figure 3.10: Comparison of the time series of idealised observations with model results from a calibration aimed at minimising the cost function of QN.

For the case of a *QP* cost function calibration, all three state variables stay within conceivable bounds (Figure 3.11). *B* does show annual cycles, but underestimates summer maxima by a factor of approximately 7, with an additional phase shift so that the peak values occur later in the season, and drops to almost zero each winter.

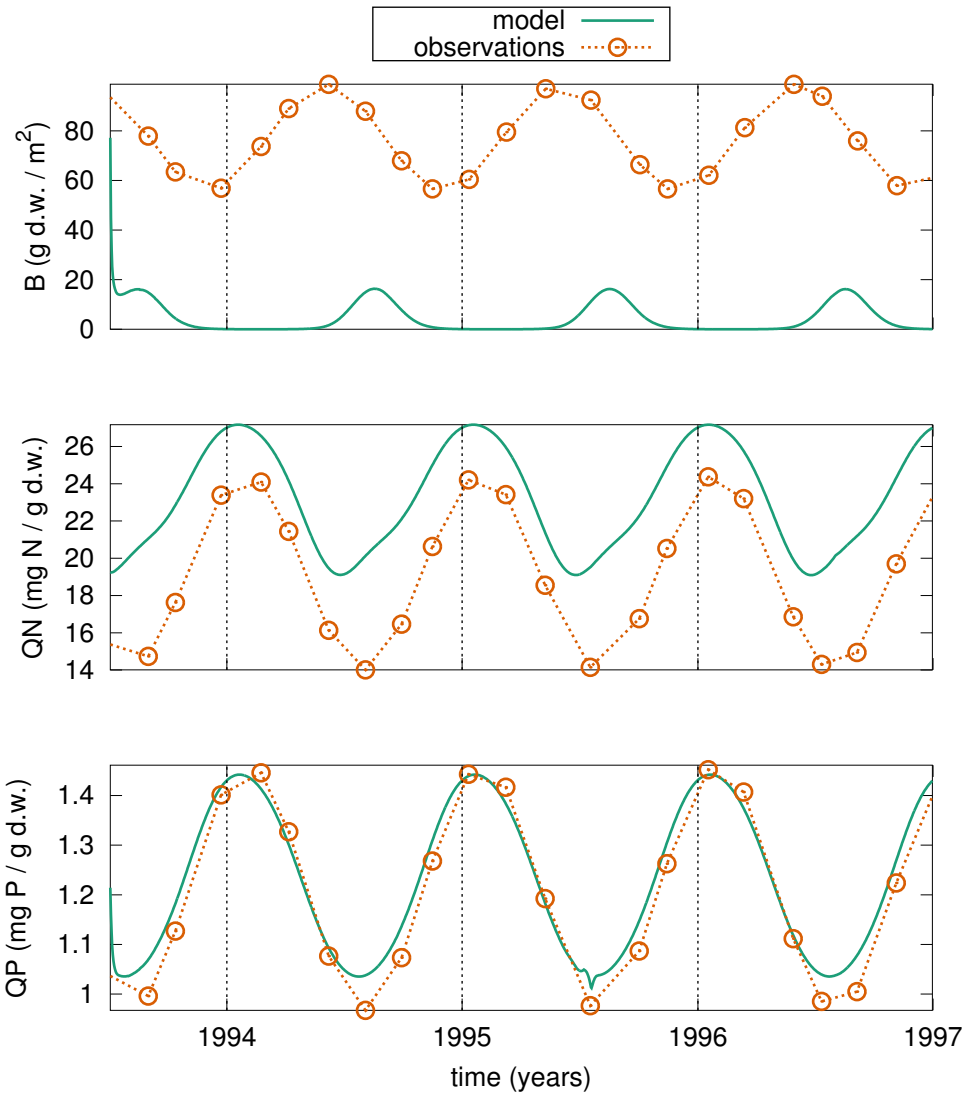

Figure 3.11: Comparison of the time series of idealised observations with model results from a calibration aimed at minimising the cost function of QP.

Using a combined cost function, aimed at minimising the normalised sum of the squared relative errors of B, QN and QP, leads to the results shown in Figure 3.12. B shows good agreement, but consistently overestimates maxima and underestimates minima. In contrast to the idealised observations, the seasonal peaks are also highly asymmetrical, and the minima occur slightly later in the season. QN data are very well reproduced, with only a slight underestimation of the summer minima by approximately $1\,\mathrm{mg\,N\,(g\,dw)^{-1}}$. QP, in contrast, vastly underestimates the amplitude of the seasonal signal, and while showing good agreement in the timing of the maxima, does not exhibit clear minima, with slow increases at a time of the season at which the idealised observation data are still decreasing.

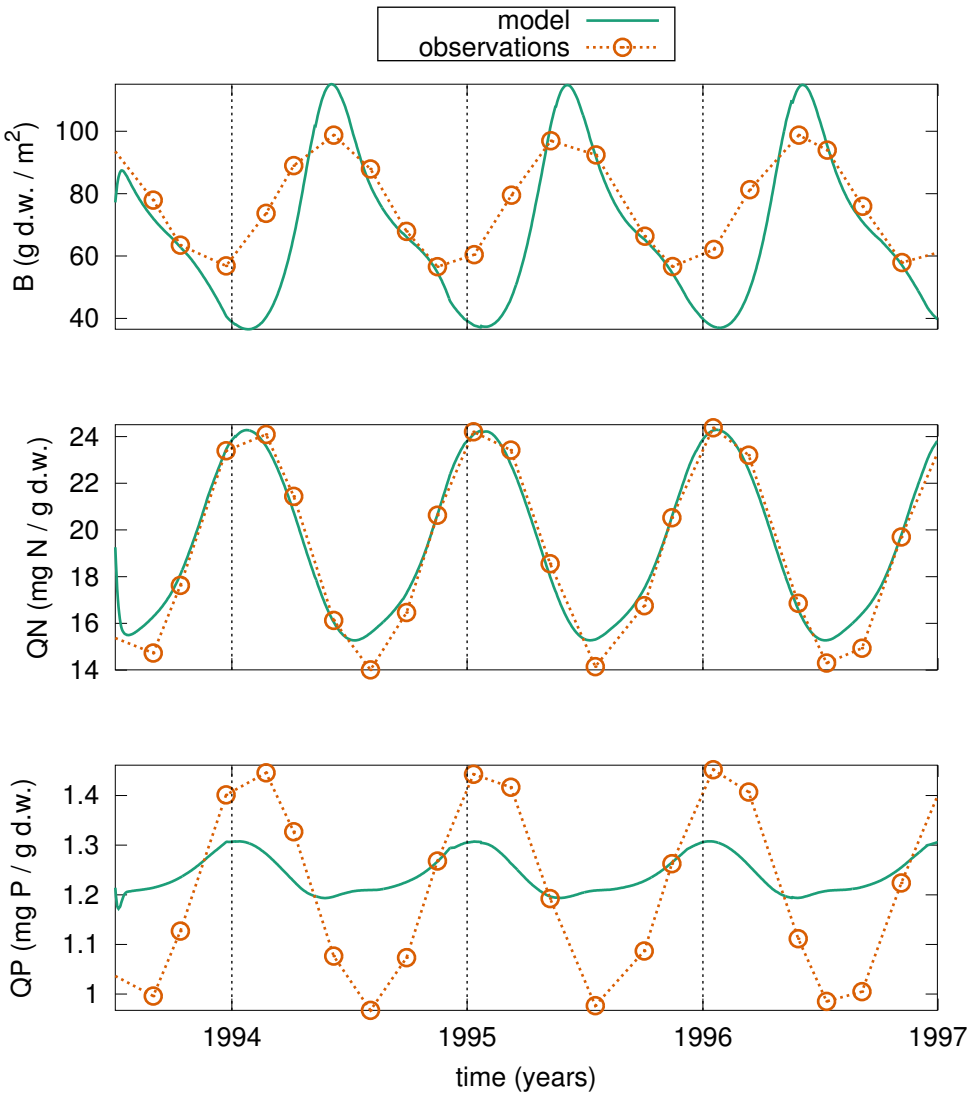

Figure 3.12: Comparison of the time series of idealised observations with model results from a calibration aimed at minimising the normalised sum of the squared relative errors of B, QN and QP.

Seasonal scenarios were implemented to examine the influence of seasons with high or low conditions of the five environmental forcing variables as well as turbidity (vertical attenuation coefficient Irr_k). Figure 3.13 shows the monthly percentiles and derived cosine fits for the low (5^{th} percentile) and high (95^{th} percentile) scenarios, as well for visual reference also the 50^{th} percentile, which was not used in the scenario runs presented here. For temperature and irradiance, both the high and low cosine fits follow the observed percentiles well, while for all three nutrient fractions, the relative deviations are much higher, especially for the high cosine fit.

Figure 3.14 shows the results from all 12 scenario simulations for all three state

variables, each together with results from the reference run (RR). The reference run is based on the calibration of idealised forcing simulations with a combined cost function. High NH more than doubles the highest values of B in summer, with a slightly later peak and slower decline but reaching a similar winter minimum as the RR, increases QN by between approximately 2 and 4 mg N (g dw)$^{-1}$ with very little change in the temporal evolution, and slightly decreases QP over summer. Low NH lead to an earlier and slightly lower spring/summer peak in B, which then decreases rapidly to very low values in late summer, slightly recovering to winter values still below those of the RR. Winter values of both QN and QP are similar to the RR, but QN is decreased in summer, while QP shows a late summer peak not observed in any of the other scenarios, at the same time of the B and QN minimum.

High NO increases the spring/summer peak in B to similar values as high NH, but with a more rapid decline and values similar to the RR in late summer. QN is approximately 4 mg N (g dw)$^{-1}$ higher in winter, but similar and for a short period even lower than in the RR in late summer, while QP shows identical values in winter but slightly lower values in early summer. Low NO leads to a very broad summer peak of B with a later but even slightly higher maximum than in the RR, similar values of QN except for an earlier and stronger increase in late summer, and also very similar values of QP except for a longer and slightly stronger decrease in late summer.

Both high and low PO lead to no noticeable change in B or QN. With low PO, QP is decreased slightly in winter and vastly in summer, while with high PO it is slightly increased over the entire season.

Temperature, irradiance and turbidity all show very similar results for QN and QP, with only very small changes overall, but generally slightly higher values for low temperature and irradiance and high turbidity, and vice versa. Irradiance and turbidity also show similar results for B, where the qualitative temporal evolution is not different from the RR, but constantly slightly increased or decreased, with the largest differences occurring in summer. While neither high nor low temperature increase maximum summer or minimum winter values of B, high temperature does lead to a slightly earlier peak and more rapid decline, while low temperature has the opposite effect, resulting in a more asymmetrical peak with higher values until early winter.

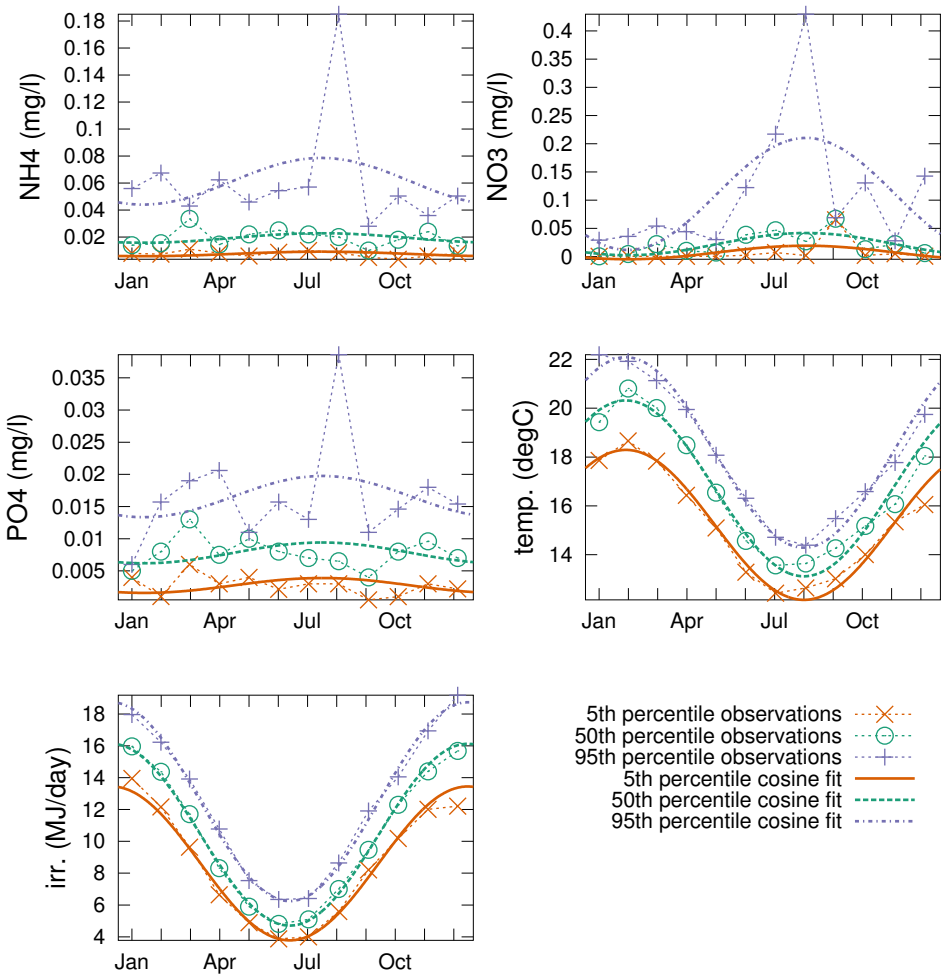

Figure 3.13: Monthly percentiles and derived scenario cosine fits for the forcing variables NH_4^+, NO_3^-, PO_4^{3-}, temperature and irradiance. The 5^{th}, 50^{th} and 95^{th} percentiles of the observation data for each calendar month are shown together with the corresponding annual cosine fits.

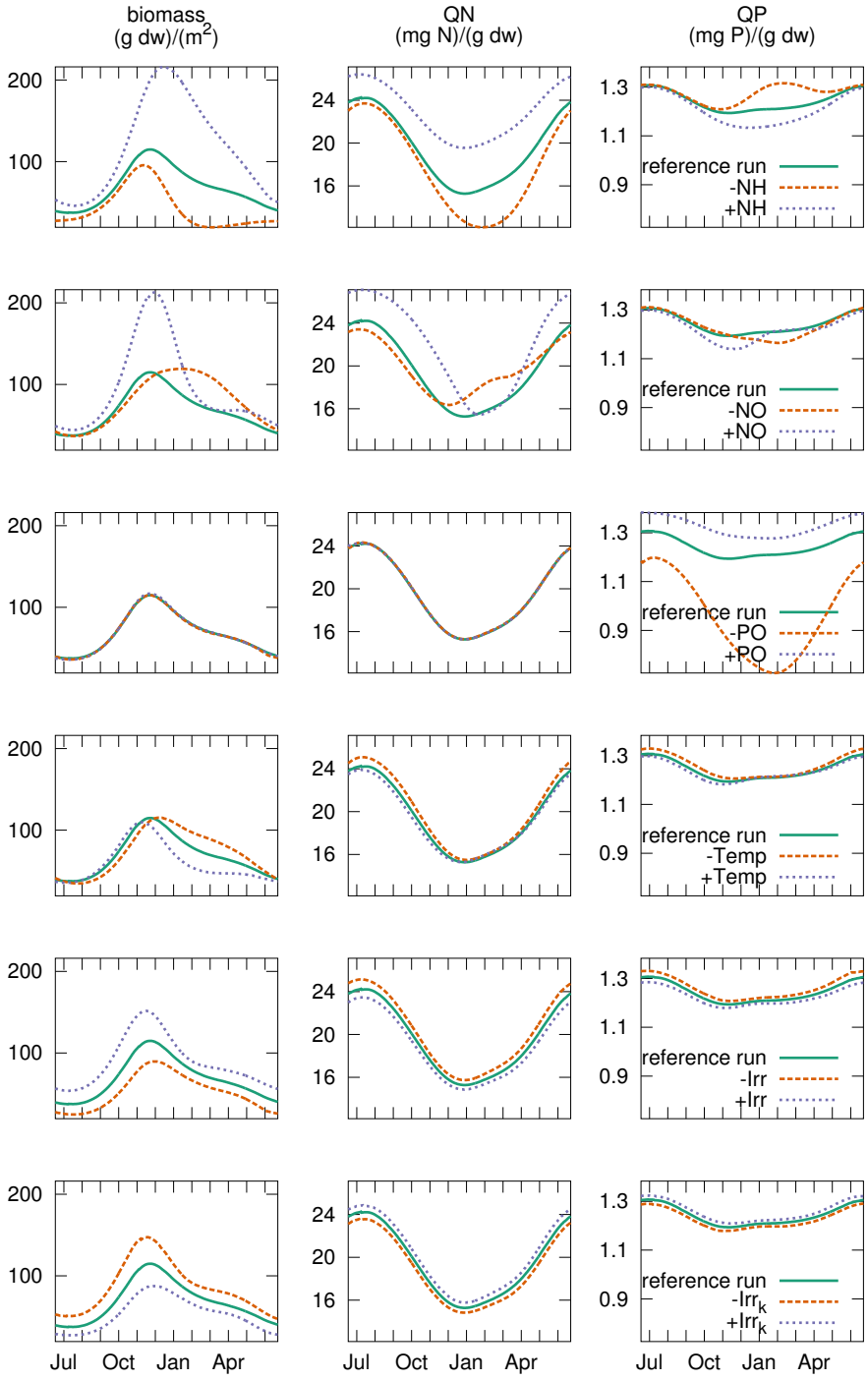

Figure 3.14: One-year timeseries of scenario simulation results from winter to winter, after 1.5 years spin-up. Each column of plots shows a state variable: biomass, QN and QP. Each row shows a set of low ("-", orange dashed line) and high ("+", purple dotted line) scenarios for one of the forcing variables or parameters: ammonia (NH), nitrate (NO), phosphate (PO), temperature (Temp), irradiance (Irr) or attenuation coefficient (Irr_k). Results from the reference run are shown alongside each scenario to aid visual comparison.

3.4 Discussion

We have demonstrated that a typical *Ulva* growth model even with only the three state variables B, QN and QP can reproduce observation data in continuous long-term simulations over more than a decade. Calibrating the model against observation data from all three state variables at once leads to good performance, but none of the examined calibrations could reproduce the magnitude of seasonal variability of both QN and QP at the same time. We also successfully calibrated the model with idealised annual cosine forcing, resulting in seasonal dynamics for all three state variables with timing and amplitude in realistic ranges, but again with a clear trade-off in performance between QN and QP. Using idealised high and low scenario forcing for all environmental forcing variables, we determined that the environmental factors deciding between observed bloom and non-bloom years are most likely the dissolved inorganic nitrogen fractions NH and NO.

3.4.1 Long-term simulations and calibration uncertainty

Based on the model structure developed by Guimaraens et al. (2005), we implemented a dynamic simulation model of *Ulva* growth with the three state variables B, QN and QP. After calibration against observation data of all three state variables, a continuous long-term simulation over a time period of 14 years produced good agreement for B and QN, but underestimated the seasonal variability of QP. Calibrating against individual state variables revealed that a consistent trade-off between performance for QN and QP, and the danger of an "explosion" of the model with physically meaningless values of B if calibrating only against QN.

Of the 17 model parameters, Guimaraens et al. (2005) determined 14 based on values from the literature and calibrated the three remaining parameters. Given that the literature ranges for most of these parameters are quite large, this may restrict the model more than necessary. Recent local measurements involving the same species as considered in the modelling study should always be given preference, but are rarely available. In lack of such empirical data, as many parameters should be included in the calibration as possible, which will usually be limited by the available computational resources. Although in principle all calibration algorithms are subject to the "curse of dimensionality", many can easily be adapted to use the parallel execution facilities of modern high performance computing (HPC) infrastructures, increasing the computational resources available in a given timeframe by several orders of magnitude.

Which parameters are best constrained by a calibration (in most cases indicated

by high values of w in the calibration uncertainty analysis) clearly depends on the cost function. As expected, for the three cost functions based on single state variables, parameters that have a direct influence on that state variable feature prominently (e.g., Ω_{max} and Θ for B, or V_{mPO}, QP_{min}, and k_{PO} for QP). For the normalised sum cost function, the four best constrained parameters are all directly related either to QN or QP. An ideal result of a calibration uncertainty analysis would show unimodal distributions with well-defined and narrow peaks for all parameters, located well within the range of values that is considered realistic for that parameter. In contrast, our study revealed this kind of result to be the exception rather than the rule. Although we were able to examine this only with respect to one specific model and dataset, the degree of complexity of the model as well as size and quality of the dataset are certainly not unusual for studies using process-based simulation models applied to ecological questions.

Calibrating with a cost function for B as expected greatly improves model performance for B, but also almost entirely removes the previously observed high positive bias in QN, which is now sometimes, but only slightly, underestimated. The overall bias in QP is also reduced, but the maximum values are still overestimated by a factor of two, and the amplitude of the annual signal is now greatly overestimated. This indicates that the coupling between B and QN is stronger than that between B and QP. In the absence of tissue nutrient observations, a calibration with a cost function for B might therefore still give a good estimate of QN, but should not be relied upon to estimate QP. Alternative formulations of the interactions between nitrogen and phosphorus uptake should be explored.

3.4.2 Idealised forcing simulations and seasonal scenarios

Applying average idealised (annual cosine) forcing derived from the historic observation data, the model performs well when calibrated against a combination of data from all three state variables. We observed periodic solutions for all three state variables when also calibrating against all three, while calibrating against individual state variables led to unrealistic outcomes for others, especially when calibrating against B or QN. Calibrating against individual state variables in all cases led to bias in at least one of the other state variables, and when calibrating against QN even to the "explosion" of the model, resulting in physically meaningless values of B. It should be noted that in the prevalent formulations of QN and QP dynamics, both a lower and upper bound is usually imposed, while an upper bound is often not explicitly given for B. Therefore, neither QN nor QP can ever obviously "explode" when calibrating against B, as is most common. Extra care should be taken to also

examine these "internal" state variables with regard to realistic simulation outcomes even if only B is of primary concern for the specific application.

For the scenario simulations, we used idealised forcing data easily derived from annual cosines fitted to monthly percentiles. They provide improved scenario conditions compared to varying around a mean expected value by a fixed percentage of the range, or by increasing mean values but retaining amplitude for periodic forcing variables (e.g., Zaldívar et al., 2009). This is especially important when developing scenarios for or comparing model sensitivity to both parameters and forcing variables (chapter 2; Aveytua-Alcázar et al., 2008). Since the methodology used in classic sensitivity analysis overlaps substantially with that used for scenario simulations, more specific terminology should be used whenever possible, for example "parameter sensitivity analysis" instead of "sensitivity analysis" (Swaney et al., 2008). For temperature and irradiance, the derived high and low cosine fits correspond well to the observed monthly percentiles, while for the nutrient fractions the relative deviations are much higher. Nevertheless, even for the case of PO_4^{3-} (weak annual periodicity), fitting to monthly percentiles results in high and low scenarios which are in line with visual estimates of high and low years based on the continuous time series of the observation data. Low nutrient scenarios based on different percentiles could also be used as "reduction scenarios" for policy development, providing realistic forcing conditions that are known to already occur in the system (albeit rarely) in contrast to fixed loading or concentrations values chosen manually (e.g., Perrot et al., 2014). Further research could examine the robustness of such idealised annual cosine forcing data, especially with respect to the derived amplitudes, which in some cases may be dominated by data from one or two months only.

The seasonal simulations with "high" and "low" forcing scenarios clearly show the dominance of the inorganic nitrogen fractions NH_4^+ and NO_x^- in controlling peak biomass in an idealised, seasonal *Ulva* bloom event resembling conditions in Tauranga Harbour. PO_4^{3-} has no visible effect on biomass, and the physical factors temperature, irradiance and turbidity at most have an effect at about half the magnitude of that of NH_4^+ or NO_x^-. This outcome contrasts with the findings of Ren et al. (2014), who developed an *Ulva* model for the Avon-Heathcote Estuary on the South Island of New Zealand, and found light and temperature to be more limiting for growth than nutrients. The Avon-Heathcote Estuary is located approximately 650 km further south than Tauranga Harbour, but whether the differences in system response are due to differences in the light and temperature climate, nutrient concentrations, or other factors is unknown. While our result is of course based on a

number of assumptions, including those determining the model structure, as well as the character of both the *B*, *QN* and *QP* data used for calibration and the environmental forcing data, it does give a good indication of which factors to examine further. In particular, reliable and representative measurements of the spatiotemporally highly variable inorganic nutrient fractions in the water column are crucial.

3.4.3 Coverage/biomass and wet/dry weight conversions

In many cases, long-term datasets of *Ulva* abundance are based on visual estimates of *Ulva* coverage of the sediment. The required conversion of observed *Ulva* coverage to absolute biomass is not necessarily straightforward, especially due to the highly variable thickness of mats encountered at high coverage (Alexander et al., 2008). While a lower bound for this conversion could easily be derived under the assumption that only a single layer of *Ulva* is present over the observed area, the variability caused by folding of individual tissue sheets and layering of multiple sheets is high. Additionally, this relationship is likely to be nonlinear due to the correlation between overall abundance and average tissue size, i.e., the fact that a large number of small tissue pieces are less likely to fold and layer over one another than a small number of large tissue pieces. Therefore, some authors even generally recommended against using this kind of data (Nezlin et al., 2007), but for the present study, no alternative data sources were available.

Having a non-zero intercept in the linear regression of biomass on sediment coverage, although possibly leading to a higher correlation coefficient for a specific dataset, has disadvantages for the special cases of zero percent cover (resulting in non-zero biomass) as well as zero biomass (resulting in non-zero percent cover). The fact that in some examples taken from the literature (e.g., Alexander et al., 2008), when not required to pass through the origin, the intercept term is negative is likely to be caused by the higher spread but fixed lower bound close to 100% cover. The relationship is therefore likely to have positive curvature and might be better approximated by requiring a zero intercept but introducing for example a positive second order polynomial term.

There is some uncertainty regarding the dry weight to wet weight ratio for *Ulva*. This uncertainty in many cases propagates to the coverage to biomass conversion, and also casts doubt on the comparability of absolute dry weight data between studies. For example, Park (1996) determined a conversion factor of 0.14 while Alexander et al. (2008) determined a conversion factor of almost twice that magnitude at 0.26. While some natural variability caused by phenotypical and physiological state factors is likely, additional variation is probably introduced by differences in

methodology. Sample preparation (e.g., standardisation of the size of tissue fragments) and exact drying temperatures and times vary. It would be highly desirable to examine the influence of these differences in methodology on the determination of the dry weight to wet weight ratio, and establish a standard methodology as well as if possible adjustment factors for data from previous studies with differing, but well-documented methodology. Ideally, population size should be quantified by carbon content, the absolute measurement of which is easily carried out with modern instruments and which is therefore a preferable measure to compare between studies.

3.4.4 Outlook

When fitting an annual cosine to the nutrient forcing data, a phase shift was observed between the 5^{th} and 95^{th} percentiles. For the present study, this was interpreted as an error introduced by the higher variability in the lower percentile. Although this higher variability is clearly present, it is also conceivable that this is only in addition to a real phase shift present in the data. The phase of seasonal minima and maxima might be correlated with the average concentrations on an annual time scale. The potential effect of the resulting differences in the relative phase between environmental forcing variables on *Ulva* population dynamics could be examined with the same model presented here. It would require a more extensive setup of scenarios, and most likely over a time span of several years for each individual simulation to account for carry-over effects between years.

For the multi-objective optimisation used for the calibration, using the squared formulation in F_3 (Eq. 3.23) gave good results, but is effectively a (somewhat arbitrary) choice of weighting between different magnitudes of deviations, but applied equally to all objectives (in this case calibration variables). However, we would generally expect even the relative uncertainty in the observation data for B to be higher than that for QN and QP. The cost function could be refined to utilise this information by assigning additional weights based on the expected uncertainty in the observation data for each calibration variable. For the case of B, where each observation is actually based on a number of replicate estimates of *Ulva* coverage of the intertidal sediment, a measure of spread within these replicates (and/or sites) could additionally be used as weights to differentiate between more or less uncertain data points within one calibration variable.

In this study, the most suitable cost function for calibration proved to be the one based on all state variables for which observation data are available. In most studies, the majority of parameters are fixed based on literature values, and only a

small number of parameters are included in the calibration. An alternative approach might be to calibrate all parameters, but not all at the same time. Groups of parameters which we expect to be constrained primarily by one state variable could be calibrated with a cost function based on that state variable alone. Which parameters are expected to be constrained by which state variables could be estimated by the mathematical structure of the model, a dedicated "screening" sensitivity analysis for each of the state variables as output or the somewhat analogous results from a calibration uncertainty analysis with different cost functions. The calibrated values of that group of parameters would then be fixed, and the procedure sequentially repeated for all of the other state variables. In our case, a preliminary examination of the full results from the calibration uncertainty analysis suggests several promising candidates. These include Θ, Ω_{max} and possibly also λ for the *B* cost function, QN_{min} and QP_{max} for the *QN* cost function and V_{mPO}, k_{PO}, QP_{max}, and QP_{min}, but interestingly possibly also t_{opt}, for the *QP* cost function.

3.A Appendix: calibration uncertainty histograms

Complete results from the long-term simulation calibration uncertainty analyses for all parameters are shown in Figures 3.15, 3.16, 3.17 and 3.18 for the cost functions of *B*, *QN*, *QP* and their normalised sum, respectively. The corresponding parameter values from the single calibration that resulted in the minimum cost function value overall are shown in Table 3.2.

Table 3.2: Results of individual model calibrations for each of the different cost functions. Default values refer to Guimaraens et al. (2005).

symbol	unit	default value	B	QN	QP	norm. sum
μ_{max}	day^{-1}	0.36	0.36	0.5	0.5	0.5
K_i	$W\,m^{-2}$	1e+02	24	24	24	24
t_{opt}	°C	23	20	20	25	20
V_{mNH}	$mg\,N\,(g\,dw)^{-1}\,day^{-1}$	48	48	48	1.2e+02	48
V_{mNO}	$mg\,N\,(g\,dw)^{-1}\,day^{-1}$	17	17	17	20	17
V_{mPO}	$mg\,P\,(g\,dw)^{-1}\,day^{-1}$	5.5	5.5	5.5	5.5	24
k_{NH}	$mg\,N\,l^{-1}$	0.5	0.6	0.6	0.6	0.6
k_{NO}	$mg\,N\,l^{-1}$	0.25	0.12	0.12	0.2	0.12
k_{PO}	$mg\,P\,l^{-1}$	0.025	0.11	0.11	0.11	0.049
QN_{max}	$mg\,N\,(g\,dw)^{-1}$	40	30	30	60	35
QN_{min}	$mg\,N\,(g\,dw)^{-1}$	10	1	1	1	6.3
QP_{max}	$mg\,P\,(g\,dw)^{-1}$	3.9	5.8	5.8	1.7	1.4
QP_{min}	$mg\,P\,(g\,dw)^{-1}$	1.1	0.01	1.6	0.01	0.034
λ	$°C^{-1}$	0.007	0.0035	0.01	0.011	0.0062
Θ		1.1	1.1	1.6	0.56	1.1
Ω_{max}	day^{-1}	0.33	0.49	0.021	0.01	0.47
K_d	$(g\,dw)\,m^{-2}$	6e+02	1	1	1.2e+03	8.1

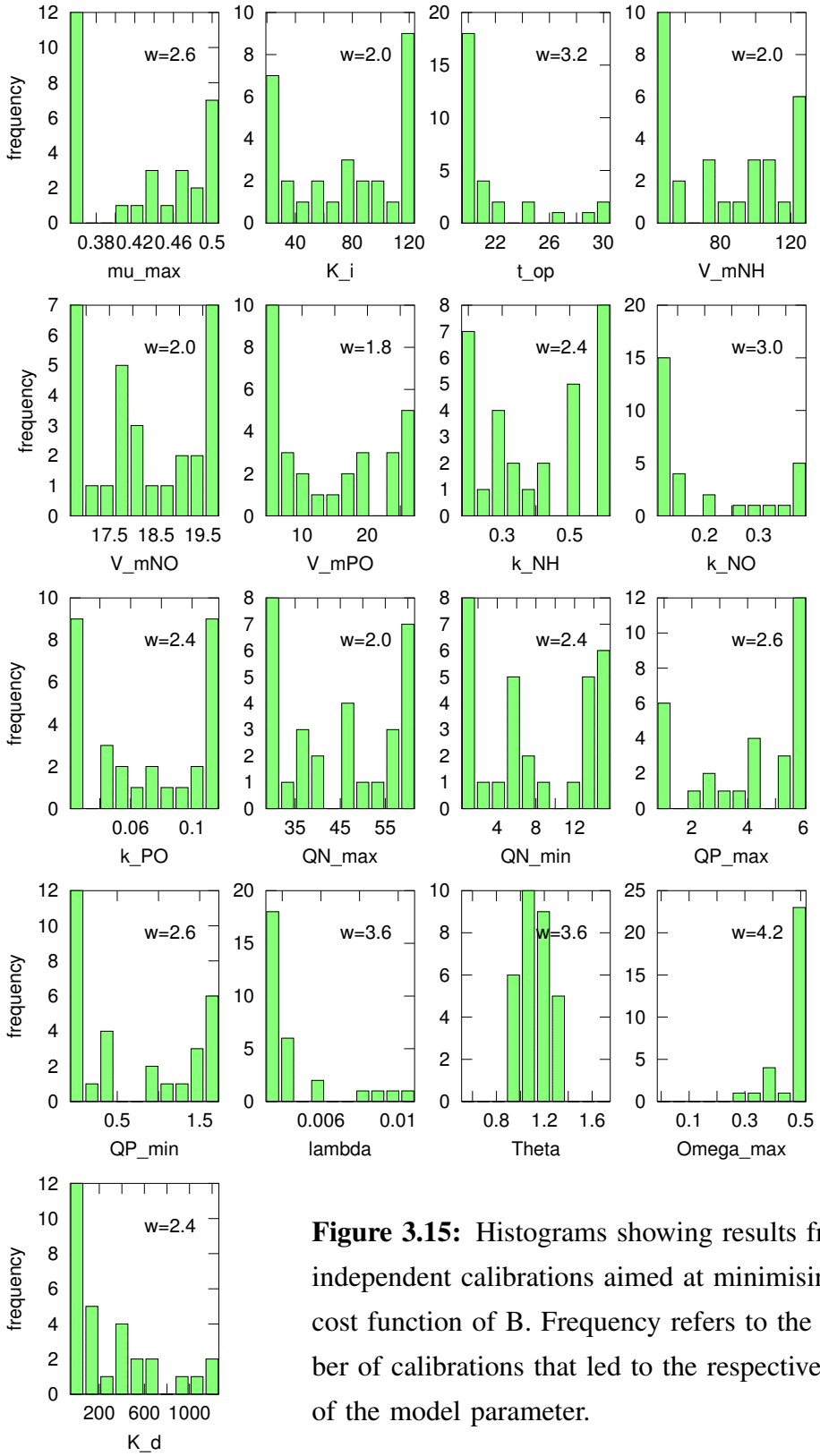

Figure 3.15: Histograms showing results from independent calibrations aimed at minimising the cost function of B. Frequency refers to the number of calibrations that led to the respective value of the model parameter.

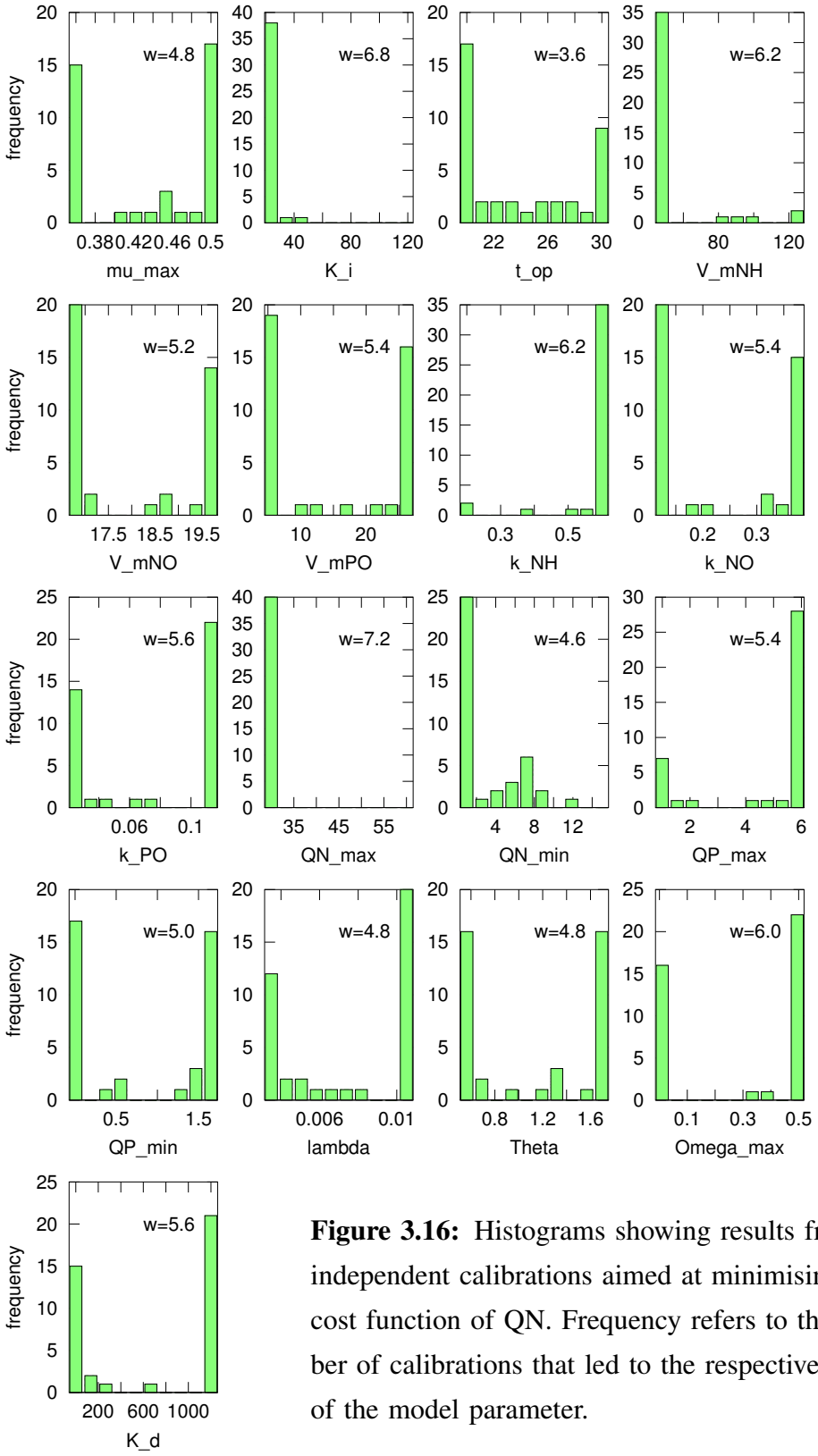

Figure 3.16: Histograms showing results from independent calibrations aimed at minimising the cost function of QN. Frequency refers to the number of calibrations that led to the respective value of the model parameter.

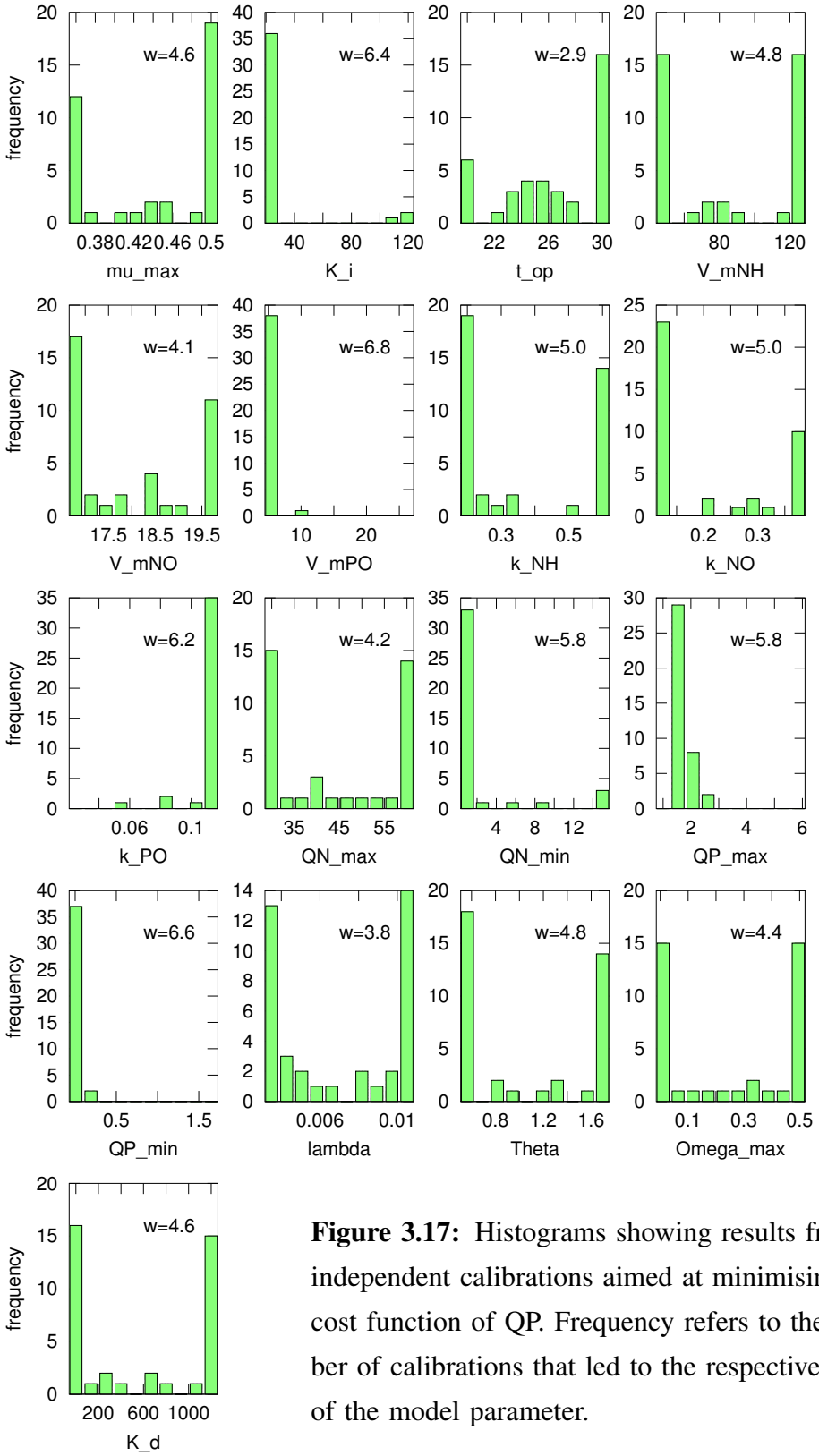

Figure 3.17: Histograms showing results from independent calibrations aimed at minimising the cost function of QP. Frequency refers to the number of calibrations that led to the respective value of the model parameter.

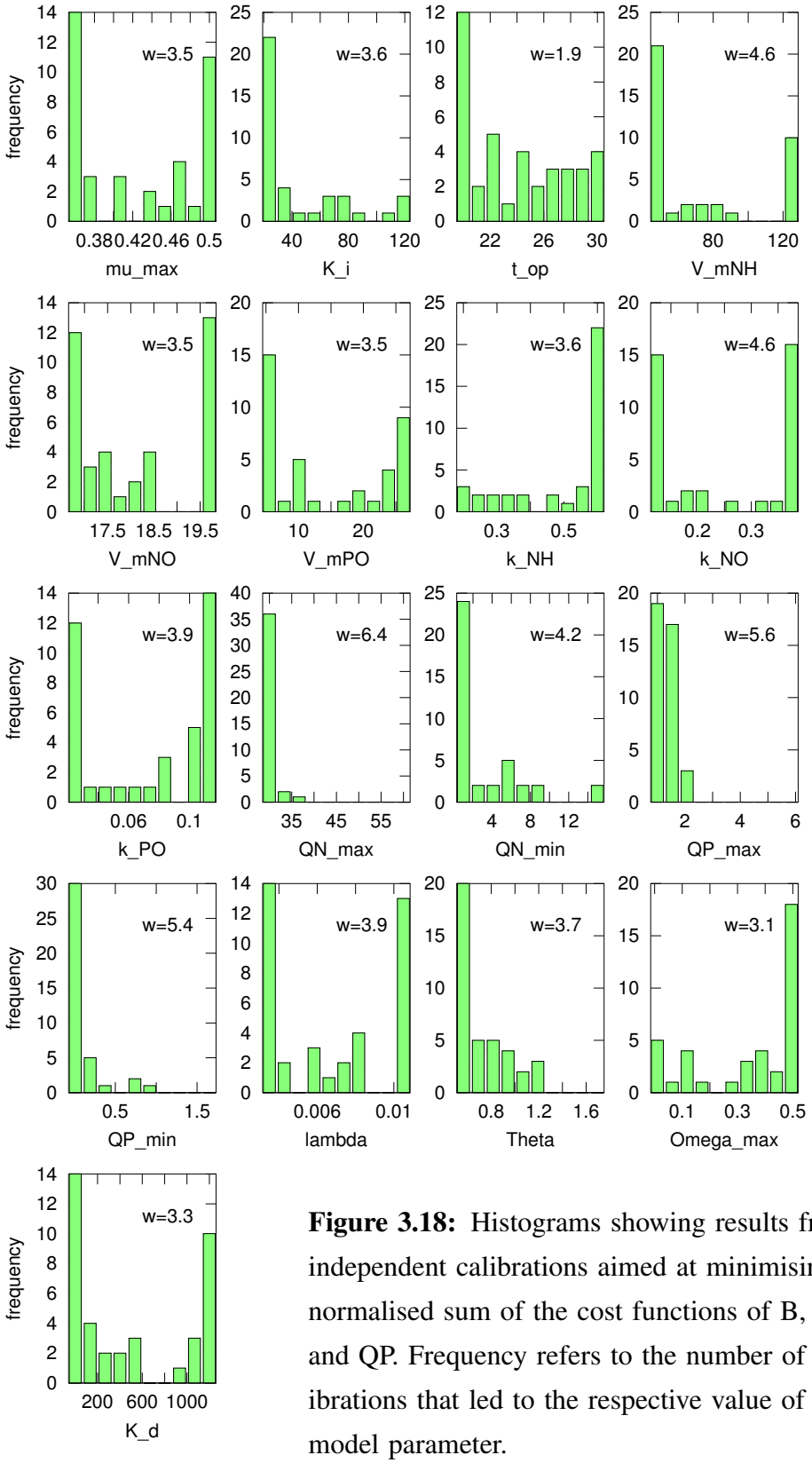

Figure 3.18: Histograms showing results from independent calibrations aimed at minimising the normalised sum of the cost functions of B, QN and QP. Frequency refers to the number of calibrations that led to the respective value of the model parameter.

Chapter 4

Spatiotemporal variation of water column nutrient concentrations and fluxes in Tauranga Harbour

Abstract

We examine the water column nutrient concentrations, mass fluxes and dominant transport processes for sites and subregions of a tidally dominated estuary with complex geometry. To analyse spatial variability within the harbour, we sampled eight sites from the harbour entrance to upstream sub-estuaries at approximately bimonthly intervals over one year, and two of these sites approximately fortnightly to examine the relative influence of seasonal patterns and episodic events. To minimise the influence of periodic changes within each tidal cycle, samples were taken at approximately the same local M2 tidal phase of two consecutive ebb and flood tides. Based on the fortnightly data, PO_4^{3-} showed statistically significantly higher concentrations on the ebb than on the flood tide at the harbour entrance, while for a site further upstream, this was the case for NH_4^+ and NO_3^-. Probability density estimates for the inorganic nutrient fractions vary between sites, and might best be described by gamma distribution functions. We used a numerical hydrodynamic model to simulate passive tracers, representing the short-term transport of nutrients due only to physical processes. Tracer simulations show that the connectivity between subregions varies substantially within the harbour. Tidal mixing leads to mid-term upstream transport of sizeable fractions of waterbodies entering the main harbour further downstream. The contribution of upstream subregions to the waterbody being sampled at a site changes rapidly during the tidal cycle, emphasising the need to account for the local tidal phase in sampling times.

4.1 Introduction

Elevated nutrient concentrations in coastal and especially estuarine ecosystems often lead to episodic adverse effects such as nuisance macroalgae blooms, toxic phytoplankton blooms, oxygen depletion, or a combination thereof (Smith, 2003), and in the long term potentially fundamental and sustained changes in ecosystem structure (Flindt et al., 1999). As an essential basis for primary production, knowledge of the spatial and temporal patterns of nutrient concentrations in estuaries is crucial for the application of process-based water quality, algal growth (e.g., chapter 2; chapter 3) or more general biogeochemical models (e.g., Sfriso, 1995; Alvera-Azcárate et al., 2003; Marinov et al., 2008). In addition, "state of the environment" monitoring of nutrient concentrations is a requirement in many jurisdictions (e.g., based on the "Clean Water Act" in the U.S.A., the "Water Framework Directive" in the E.U. or the "Resource Management Act" in New Zealand) and must be routinely carried out by local and regional environmental administrative bodies (e.g., Park, 2011; Gregory et al., 2013). Data required to fulfil these needs can include long-term, estuary-wide import-export balances as well as average differences and transport patterns between subregions within an estuary, statistical descriptions (e.g., probability density functions) of the range of conditions encountered by organisms living in the estuary, but also short-term changes in concentrations, for example due to meteorological events. Accurate and efficient sampling strategies are therefore needed to quantify the ambient concentrations as well as fluxes of water column nutrients in time and space. It is therefore crucial to take into account the influence of hydrodynamic transport and mixing processes both for the design of an estuarine water quality sampling programme and for the interpretation of the collected data (Imberger et al., 1983).

Since the vast majority of the world's coastlines are exposed to tidal forcing, many estuaries are partially or well-mixed, i.e., display little or no vertical structure in water column properties. Horizontal variations, on the other hand, are frequently encountered. Testing for causal links between changes in water column nutrient concentrations and related ecosystem processes (e.g., the occurrence of macroalgae blooms), can be extremely difficult because of the high horizontal spatial as well as temporal variability in concentrations resulting from both transport and transformation processes. The relative influence of nutrient fluxes between the estuary and the landward side on one hand, and the seaward side on the other hand can be particularly difficult to quantify, but at the same time a critical factor in the design of eutrophication management strategies and goals (Timmermann et al., 2010).

Estuaries may be classified based on different physical parameters such as tidal influence, salt and fresh water mixing, sedimentology or morphology, but also biological or socioeconomic factors (Dyer, 1973; Haslett, 2009). The morphology or shape is one of the determining factors for the development of spatial heterogeneity of water column properties such as nutrient concentrations. Some types or classes of estuaries have relatively simple shapes, for example tidal river mouths shaped as elongate basins steadily widening towards the ocean (Hume et al., 2007). Such simple estuaries, especially under the influence of constant freshwater input at the head of the estuary, will often show a relatively simple concentration gradient mainly determined by the distance from the head of the estuary. This gradient may be modulated in the short term by the presence of strong tidal forcing, but the long-term average concentrations will still follow a one-dimensional gradient from land to sea. In contrast to this, in the case of more complex morphology such as upstream branching, seaward barriers or constricted sub-estuaries, this is usually not the case. Estuaries with an especially wide variety of complex morphologies are encountered on barrier coasts (FitzGerald and Miner, 2013), which make up approximately 15% of the world's coastlines (Swart and Zimmerman, 2009). Hume and Herdendorf (1988) further classified barrier-enclosed estuaries depending on their enclosure type (single-spit, double-spit, tombolo) or for example occurrence together with a dominant river mouth type estuary (e.g., spit-lagoon). The most complex morphologies are found in estuaries which, often as the result of post-glacial flooding of terrestrial topographic structures, include several distinct sub-estuaries or subregions of different types and may thus be called "compound" estuaries (Hume and Herdendorf, 1988). The case study presented here (Tauranga Harbour, New Zealand) is an example of such a compound estuary with complex morphology in which the horizontal concentration and flux patterns of water column nutrients are particularly difficult to sample and quantify, let alone predict.

Dissolved inorganic nitrogen (DIN) and phosphorus (DIP) compounds are the water column nutrient fractions most likely to be relevant in the formation of macroalgae blooms (Valiela et al., 1997; Teichberg et al., 2010). DIN and DIP are therefore often of primary concern from an ecosystem management perspective, for example to identify sources (Ménesguen et al., 2006) or to aid in the formulation of restoration policies (Runca et al., 1996). In this study, we therefore examine the DIN fractions NH_4^+ and NO_3^-, and DIP as PO_4^{3-}, as well as the corresponding total nitrogen (TN) and total phosphorus (TP) fractions. In addition to time series and time-averaged values, we also aim to estimate probability density functions (PDFs) to support more realistic sensitivity analyses of mathematical models using

nutrients as environmental forcing variables (chapter 2). We focus on the estuarine waterbody itself, since data from the major landward surface freshwater inputs are available from an ongoing monitoring programme of the Bay of Plenty Regional Council (BOPRC, see for example Park, 2011). Based on a nutrient sampling design tailored to this environment as well as numerical modelling of the dominant hydrodynamic transport processes, we aim to answer the following questions:

- Can PDFs be derived for the inorganic N and P fractions, and to what extent do they differ between sites? What kind of statistical distribution best describes the observed PDFs?
- What are the dominant seasonal signals in the inorganic N and P fractions, the N/P ratios and ebb/flood ratios?
- Do subregions within the estuary or groups thereof show distinctive seasonal patterns in inorganic and total N and P fractions?
- What are the nutrient mass flux contributions of individual subregions to the entire estuary as well as between the harbour mouth and the coastal ocean?
- What is the magnitude of tidal transport and consequent connectivity between subregions and how does this influence the composition of spot samples taken at a specific time of the M2 tidal cycle?

Our research questions address estuarine nutrient dynamics in general, but are more specifically also motivated by the data demands of estuarine ecological models, and especially macroalgae growth models (chapter 3).

4.2 Methods

4.2.1 Study area

As stated in the previous chapters, Tauranga Harbour (Figure 4.1) is an estuary in the Bay of Plenty region on the east coast of the North Island of New Zealand, located at 37.6° S, 176.0° E. It is a micro- to mesotidal environment with dominant semi-diurnal tides. Current estimates of tidal ranges near the southern entrance (Land Information New Zealand, 2014) are 1.2 m for neap tides, 1.8 m for spring tides and 2.2 m for maximum astronomical tides, while past studies have estimated the average spring tidal range alone at 2.2 m (Davis and Healy, 1993). Following the definition of Kjerfve (1994), Tauranga Harbour is a restricted coastal lagoon, separated from the ocean by a sand barrier (Matakana island) and connected to the ocean

by two restricted inlets, the Bowentown / Katikati inlet to the north (not shown in Figure 4.1) and the Mount Maunganui / Tauranga inlet to the south of Matakana island. A very large intertidal area and change of the general direction of the ebbing tide (intertidal drainage divide) just south of Matahui Point and Tirohanga Point separates Tauranga Harbour into two basins, the Katikati basin in the northwest and the Tauranga basin in the southeast (de Lange and Healy, 1990). The two basins are considered separate waterbodies (Tay et al., 2013), and only the southern basin is considered in this study.

The areas and volumes of subregions within southern Tauranga Harbour were calculated based on the 75 m equidistant rectangular gridded bathymetry data of Tay et al. (2013). Mean high and low spring (MHWS, MLWS) and neap (MHWN, MLWN) tidal levels were taken from Land Information New Zealand (2013), and highest and lowest astronomical tidal levels (HAT, LAT) from Land Information New Zealand (2014). Mean high and low tides were calculated as the arithmetic mean of the respective spring and neap tides. All depths and tidal levels were converted from chart datum to mean sea level.

4.2.2 Sampling sites, timing and protocol

While long-term monitoring of water column nutrient concentrations fortunately has been carried out in Tauranga Harbour (Park, 1996, 2007, 2011), the available data have two major shortfalls. Firstly, samples were taken only from a number of easily accessible sites near the landward shores of the estuary, and not from within the water bodies of the estuary's different subregions. Secondly, samples were taken at varying times of the semi-diurnal M2 tidal cycle. Since strong tidal signals for water column nutrients during most of the year have been confirmed by Tay et al. (2011) at nearby sites, it is unclear how much of the variability in the long-term monitoring data is caused by this variation in sampling times relative to the M2 tidal cycle. The sampling programme carried out for this study was therefore designed to address these shortfalls.

Nutrient sampling site locations (Figure 4.1) were chosen to represent distinct upstream subregions or confluences within Tauranga Harbour such as freshwater dominated subestuaries, deep central channels or the main harbour entrance (Figure 4.2). Representative sampling sites for most of the subregions are not accessible from land, and so 6 of these 8 sites can only be sampled by boat. Subregion numbers are identical to the corresponding downstream sampling site, so that for example subregion 1 is the water body that was intended to be sampled at site 1 on an outgoing tide. Where possible, confined channels were sampled (sites 2, 4, 6 and 7)

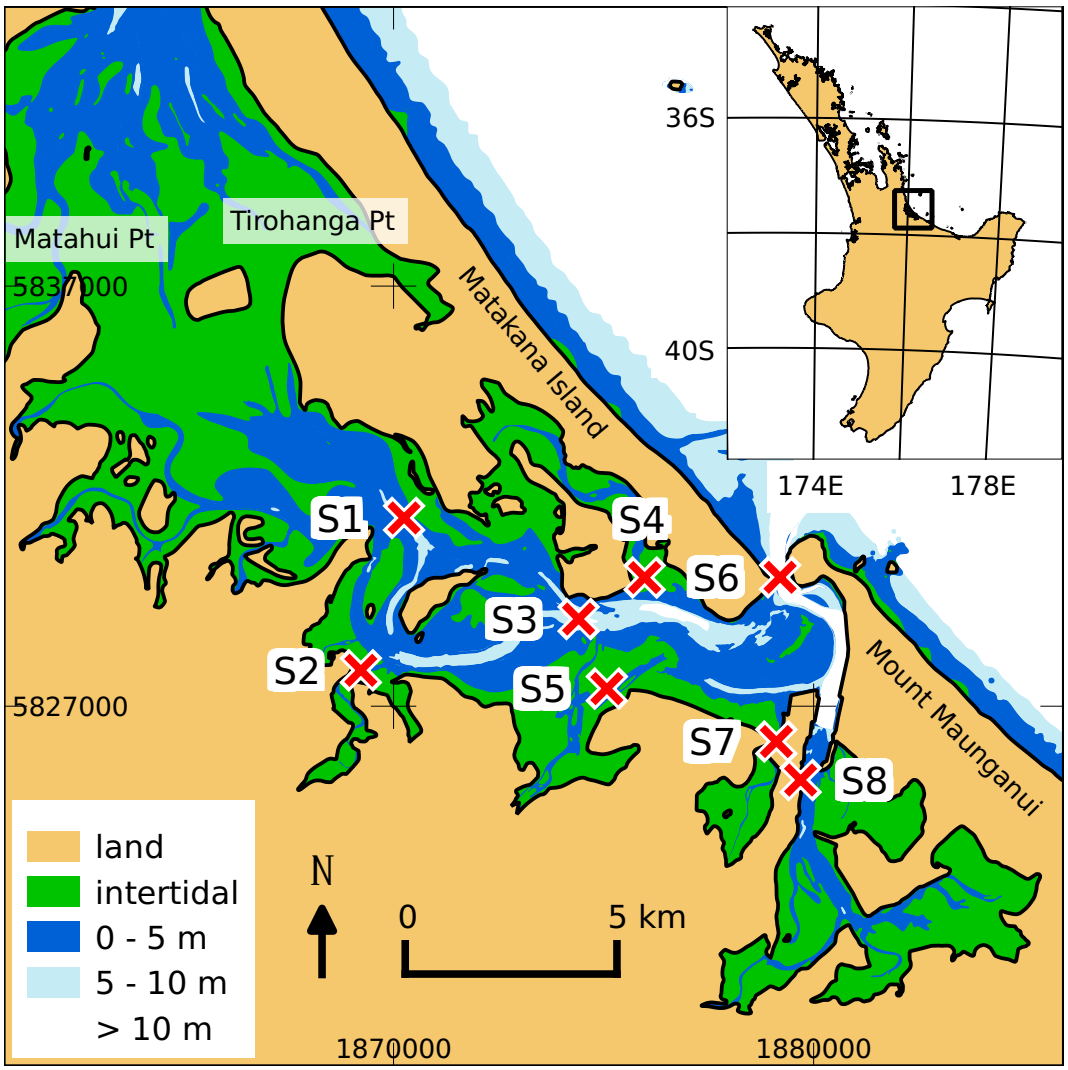

Figure 4.1: Map of the southern basin of Tauranga Harbour (inset: location of Tauranga Harbour on the North Island of New Zealand) and location of sampling sites for water column nutrients (S1-S8). Depth are colour-coded according to the legend. Map projections are NZTM2000, main map with coordinates in metres, inset map with coordinates in degrees.

to ensure clear attribution to a certain waterbody in both upstream and downstream directions. The constriction and on average higher velocities in such channels are expected to increase both horizontal and vertical mixing. Consequently, the influence of small-scale patchy distributions of nutrients especially in shallow areas is reduced and a more representative sample should be obtained. Sites 2, 5 and 7 each represent an upstream subregion with a single fluvial freshwater input on the mainland side (Te Puna stream, Wairoa river and Kopurererua stream), while site 4 represents the only sizeable subregion on the barrier island (Matakana island) side. Site 1 is located just downstream of a constriction separating the northernmost, extensive but shallow subregion from the rest of southern Tauranga Harbour. Site 3 is located just upstream of the entry point of the single largest fluvial freshwater input (Wairoa river) to the main body of the estuary. Site 8 represents several upstream subregions feeding into the deeper and dredged channel downstream of site 8 before reaching the main body of the estuary, and site 6 is the main harbour entrance and only connection between southern Tauranga Harbour and the coastal ocean. Sites 7 and 8 were chosen to be accessible from land, all other sites are only accessible by boat.

Bimonthly sampling dates were chosen to cover one full seasonal cycle from (southern hemisphere) winter over summer to the next winter. In addition to the bimonthly survey samples, the main harbour entrance (site 6) as well one of the upstream subestuaries with a large intertidal area as well as surface freshwater input (Waikareao, site 7) were sampled at approximately fortnightly intervals to provide larger sample sizes for probability density function estimates and well as flux and harbour-wide nutrient budget calculations, and to increase the chance of obtaining samples influenced by an episodic meteorological event. These two sites were chosen to represent “intermediate” and “seaward” conditions, since “landward” conditions (both in the tributaries upstream of any tidal influence as well as near their inflows to the main harbour) have already been sampled more frequently.

Since this study is focused on spatial and seasonal patterns in concentrations as well as net fluxes, sites were always sampled both on an outgoing (ebb) and the next incoming (flood) tide. In order to minimise variation due to diurnal cycles related to photosynthetic activity, dates were chosen so that the ebb tide was always sampled in the morning and the flood tide in the afternoon. In addition, the seasonal variation in the time between sunrise and the ebb samples was also minimised as far as possible, resulting in an average of 2.5 hours and a maximum range of between 1.5 and 4 hours. The phase lag of the M2 semi-diurnal tidal constituent between the furthest downstream site 6 and furthest upstream site 1 was estimated to be approximately

60 to 80 minutes (Tay et al., 2013, and personal observations). To ensure the highest possible similarity in local M2 phase between samples from different sites, all sites were sampled within 90 to 120 minutes, starting with the furthest downstream site 6 and progressing upstream together with the M2 phase. Following this protocol, we estimate the maximum difference in local M2 phase between sample sites to be 30 minutes.

Water samples for nutrient analysis were taken at a depth between 0 m and 1 m from the surface, depending on water depth and conditions at the site. In very shallow water with a depth of less than approximately 4 m, samples were taken halfway between the surface and the bottom. When deploying a Niskin bottle or Schindler trap was impractical due to high waves in shallow water, a plastic measuring jug on a rope was used instead. In this case, care was taken to fully submerge the sampling container in order to avoid oversampling the neuston. The sample was then transferred to a measuring jug for subsampling, and homogenised by gentle stirring before each subsample was taken. Subsamples were stored in either new (sterile) or acid-washed 50 ml polypropylene screw-top tubes. An acid-washed plastic syringe was rinsed at least twice with sample, then approximately 60 ml were drawn into the syringe and the 50 ml polypropylene tube rinsed twice with approximately 7.5 ml of sample. The final sample volume was approximately 45 ml. For the determination of dissolved nutrient fractions, samples were filtered with in-line syringe filters while subsampling on site, using either reusable filters (grade "GF/C", binder free, glass microfibre filters; Whatman, Maidstone, UK) or disposable filters (0.45 µm pore size, 28 mm diameter, surfactant-free cellulose acetate; Minisart® NML Syringe Filters 16555-K, Sartorius, Göttingen, Germany) filters. Samples were immediately stored on ice in the dark, then frozen within 12 hours until analysis. All equipment in contact with the final volume of nutrient samples was either new and sterile or acid-washed and triple-rinsed with deionized water prior to use.

4.2.3 Chemical analysis

Water column nutrient samples were analysed by the University of Washington's Marine Chemistry Laboratory (Seattle, Washington, USA) using a Technicon AAII gas segmented / continuous flow system (SFA). Filtered samples were analysed for NH_4^+ (EPA method 349; MDL 0.12 µM), NO_3^- (EPA method 353.4, 2.0, 1997; MDL 0.15 µM), NO_2^- (EPA method 353.4, 2.0, 1997; MDL 0.02 µM), PO_4^{3-} (EPA method 365.5, 1.4, 1997; MDL 0.03 µM), TDN (SM 4500-P J; MDL 0.44 µM) and TDP (SM 4500-P J; MDL 0.04 µM). Unfiltered samples were analysed for TN and TP after digestion with the same methods and MDL as in the filtered case.

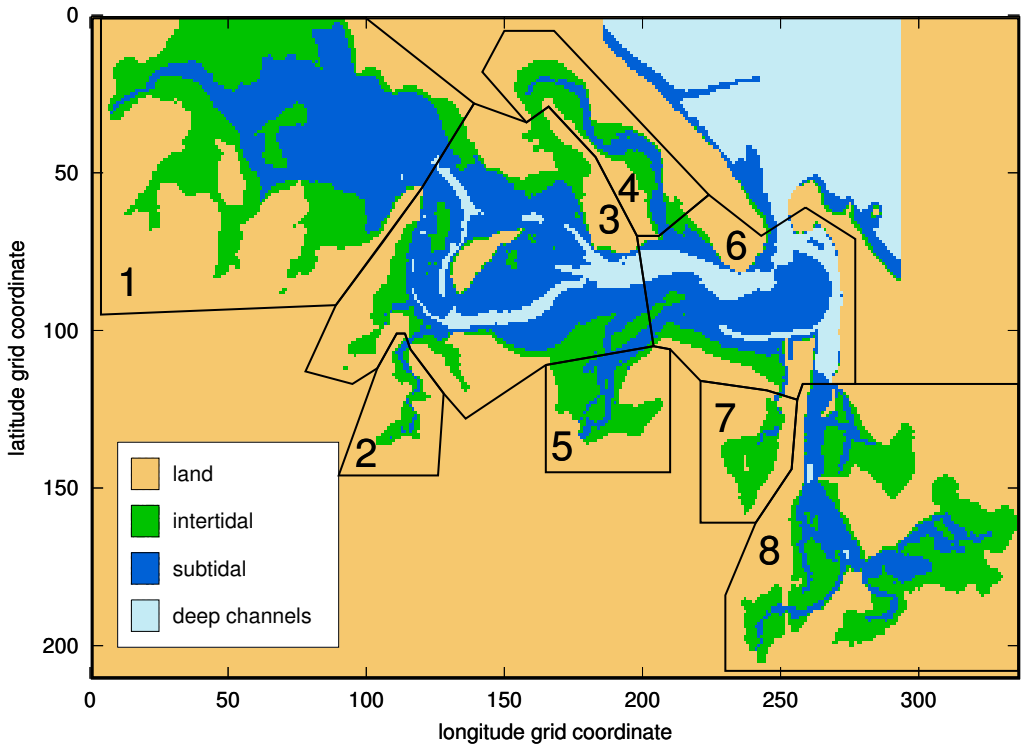

Figure 4.2: Southern Tauranga Harbour subregions (polygons outlined in black) shown on the 75 m equidistant rectangular grid used for area and volume calculations (table 4.2). The bathymetry is simplified to clearly show the intertidal and subtidal areas used in the calculations, with the intertidal defined as between mean high and low water. Deep channels defined as deeper than 5 m below mean sea level are additionally shown for illustrative purposes only. For all calculations, the non-simplified bathymetry was used.

4.2.4 Data post-processing & statistical analysis

Three values of nutrient concentrations were reported at a concentration of exactly zero (2012/09/27, site 7, flood tide, NO2; 2013/02/08, site 1, flood tide, NO3; 2012/12/24, site 7, ebb tide, NO2), and three values were reported at a concentration of less than zero (2012/09/27, site 3, ebb tide, PO4 and NO2; 2012/09/27, site 6, flood tide, NO3) and set to zero. Some nutrient concentrations were reported below the respective MDL (7 values for NH4, 29 values for NO3, 19 values for NO2 and 6 values for PO4). Although these values may still provide useful information, they are usually not deemed fit for quantitative analysis, and were therefore replaced with the respective MDL value. Visual comparison of histograms of all affected nutrients before and after this replacement showed no qualitative change in distributions.

Based on ADCP flow and water level measurements, Tay et al. (2011) found

peak flows at the mouth of Te Puna estuary to be symmetric and to occur at mid-tide, and therefore calculated net fluxes as the difference between ebb and flood nutrient samples taken three hours around mid-tide. Following the same reasoning, we calculate net fluxes for all sites as the difference between ebb and flood samples taken at mid-tide.

Sensitivity analyses of algae growth models rely on assumptions about the statistical distributions underlying each parameter or environmental forcing variable examined. As discussed in chapter 2, due to the absence of suitable empirical data for the inorganic nutrient fractions, uniform distributions were used. Estimating PDFs from the more suitable data presented here addresses this shortcoming by making these data available in the form necessary to facilitate further growth model sensitivity analyses. Additionally, PDFs are used in this study to aid in the interpretation of differences between sites that do not change over time. PDFs were estimated using non-parametric kernel density estimation (KDE) with a Gaussian kernel and Silverman's "rule of thumb" bandwidths, and only over the interval between zero and the maximum observed value. It should be noted that PDF estimation in this manner is inherently "smooth", and the degree of smoothness dependent on the choice of kernel and bandwidth. Therefore, comparisons within a study using identical methodology are helpful, but care must be taken when comparing PDF estimates between studies.

4.2.5 Hydrodynamic model setup and data analysis

To examine typical nutrient transport patterns within the estuary, the 3-D hydrodynamic "Estuary, Lake and Coastal Ocean Model" (ELCOM, version 2.2; Hodges and Dallimore, 2006) was used to simulate the transport of passive tracers representing dissolved nutrients. Tay et al. (2013) prepared, calibrated and validated an ELCOM model setup for the southern basins of Tauranga Harbour with a horizontal grid resolution of 75 by 75 m and 12 vertical layers. The same setup was used in this study with only minor modifications to the bathymetry to further improve the tidal draining and flooding in shallow regions near freshwater inflows.

To allow passive tracers to be "injected" at any given time and with constant concentration across relatively large areas of the model domain requires the definition of "update sets" containing several thousand grid cells. The ELCOM executable initially available did not provide this functionality, so the ELCOM source code was modified accordingly and recompiled. The model build process as well as tracer simulations were carried out on the University of Waikato's high-performance computing cluster "Symphony". Additionally, since the manual creation of the up-

date set definition and data files necessary for subregion-wide tracer injections is not feasible for such a large number of cells, a number of scripts were created to automate this process based on subregions defined as polygons within the model domain (Figure 4.2).

Tracer transport was simulated for both high and low tidal range conditions chosen from tidal records of the year 2006. For each date, the model was run once for tracer initialisation ("injection") at high tide to examine the downstream transport during an outgoing ebb tide, and once at low tide to examine the upstream transport during an incoming flood tide. For each of these four scenarios, the model was first run for 3 days of "spin-up" time before tracer injection, and subsequently another 3 days for tracer transport. Freshwater inflows are not marked with tracer, so that freshwater inflow in a specific subregion leads to dilution rather than addition of tracer over time. Tracer crossing the seaward open boundaries of the model domain (approximately 5 km seaward of the harbour entrance) was lost.

The main harbour entrance site 6 is of particular interest for all questions related to a harbour-wide import/export balance of nutrients. To examine the time-varying contribution of water masses originating in the 8 upstream subregions, time series of tracer concentrations at this site were extracted from model output after a high tide tracer injection in each of the subregions.

To illustrate the varying degree of hydrodynamic "connectivity" between subregions, the mass of tracer originally injected in each "origin" subregion was spatially integrated over each of the subregions ("targets", including the origin itself) at each time step. Normalised by the mass of tracer present in the origin subregion at the time of injection, these values show the exchange of water between all subregions over time. For specific points in time, these ratios are here displayed as percentages in a "connectivity matrix" of origin versus target subregions. Tracer transported outside the harbour by outgoing tides is first still present in the model in the adjacent coastal ocean region, and subsequently partly returned to subregions inside the harbour by incoming tides and partly lost at the seaward open boundaries of the model domain.

4.3 Results

4.3.1 Probability density function estimates

At sites 6 and 7, the number of samples analysed for inorganic N and P fractions was deemed high enough to warrant PDF estimation. For NH_4^+ (Figure 4.3, top panel), both sites show mainly unimodal density with a shoulder towards higher concentrations. At site 6, the peak is around 0.5 μM with positive skewness and a sharp drop-off towards zero. At site 7, the peak is around 2 μM, and except for the mentioned shoulder fairly symmetrical. For NO_3^- (Figure 4.3, middle panel), site 6 shows a highly positively skewed density peaking close to zero, while site 7 has lower but still positive skewness with a peak around 3 μM. Maximum values are below 5 μM for site 6, but up to approximately 15 μM for site 7. PO4 (Figure 4.3, bottom panel) is the only nutrient fraction examined here that shows fairly symmetrical density for both sites, and with peaks at high enough concentrations to give a gradual drop-off towards zero at zero concentration, although the latter is less pronounced at site 7. Site 6 shows a broad peak centred around approximately 0.2 μM with slightly positive skewness, while site 7 shows a maximum density at almost 0.3 μM, but with a slight shoulder just below 0.2 μM.

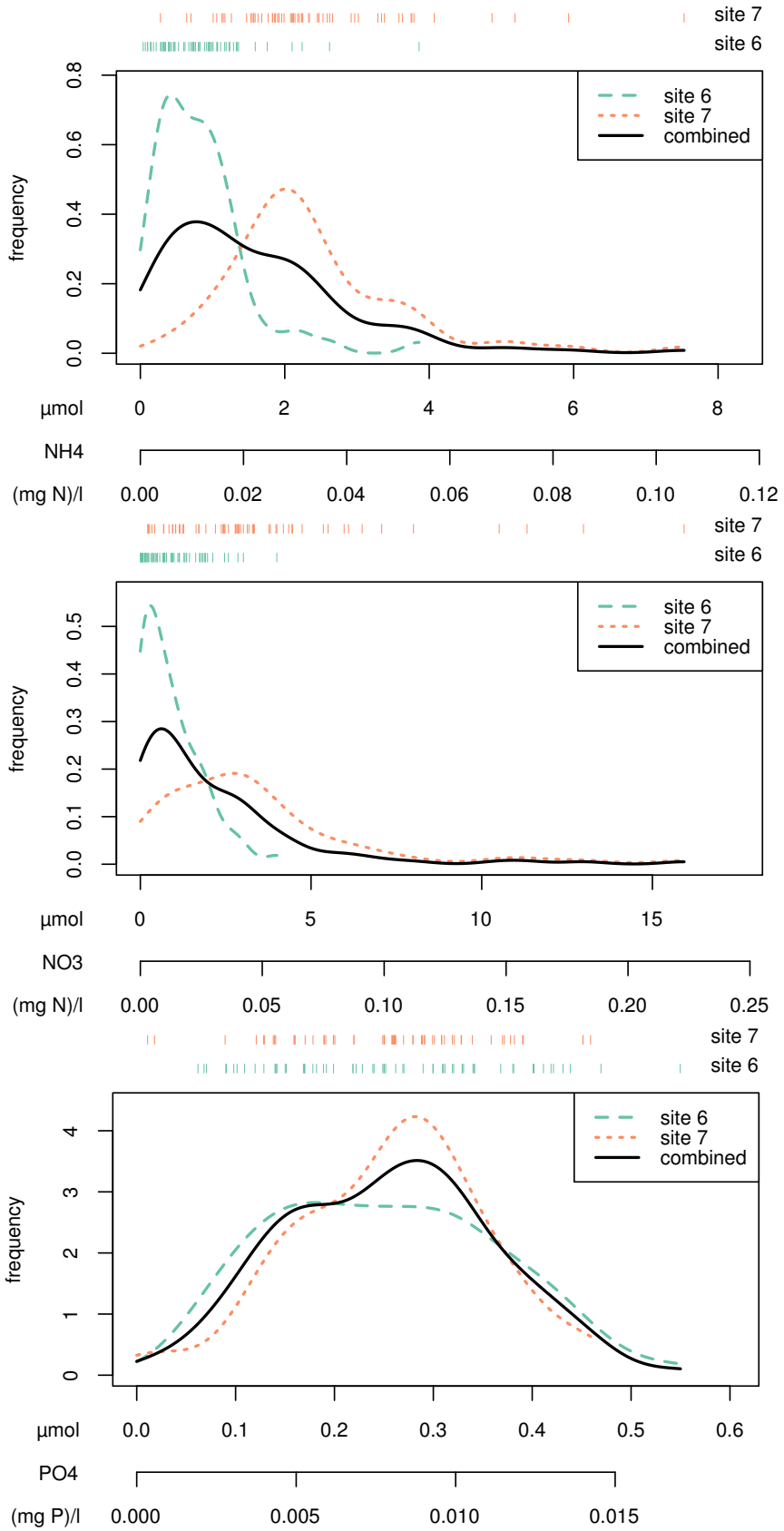

Figure 4.3: Probability density function (PDF) estimates for NH_4^+, NO_3^- and PO_4^{3-} based on fortnightly samples from sites 6 and 7. PDFs were estimated using non-parametric kernel density estimation (KDE) with a Gaussian kernel and Silverman's "rule of thumb" bandwidths, and calculated only over the interval between zero and the maximum observed value.

4.3.2 Time series inorganic fractions and ratios

The fortnightly time series of ebb and flood concentrations of the inorganic N and P fractions at sites 6 and 7 are shown in Figures 4.4 to 4.6, from southern hemisphere winter 2012 over summer to winter 2013. Rainfall data is shown alongside these nutrient time series as one of the typical physical seasonal drivers.

NH_4^+ concentrations are in most cases lower at site 6 than at site 7, although site 6 shows several high ebb values in summer coinciding with no or low rainfall. Both sites show an increase over winter, and site 7 a gradual decrease until late spring / early summer. Overall, both sites appear to have both a broad peak in late winter, early spring or both, and a second peak in the middle of summer. For NO_3^-, site 7 shows a clear and relatively smooth seasonal signal with a maximum in late winter and minimum, especially for flood values, in summer. Site 6 shows a similar summer to early autumn phase of very low values with little change between dates, but a less clear maximum in the period between late winter and early summer. PO_4^{3-} shows an increasing trend at both sites during the first winter, but otherwise no clear seasonal signal, with fluctuations in both ebb and flood values at both sites. In contrast to both NH_4^+ and NO_3^-, values are often similar between both sites, and in quite a few cases even higher at site 6 than at site 7.

The seasonal and semi-diurnal tidal changes in the inorganic N:P ratio (DIN/PO4) are shown for sites 6 and 7 in figure 4.7. At site 6, all values are below 30 and all but two values in late winter are below 16. Ebb tide values are consistently higher only in summer, while the two highest values in late winter are on flood tides. At site 7, over 50% of the values are above 16, and over 25% above 30. The highest values occur in winter and early spring, with the winter of 2012 having distinctly more high values than the winter of 2013.

The ebb/flood ratios of NH_4^+, NO_3^- and PO_4^{3-} at sites 6 and 7 are shown in Figure 4.8. NH_4^+ shows the strongest seasonal signal, with both sites showing high export in the summer months and frequent import in the winter months. There is no clear overall distinction between sites, but in summer, site 6 does show higher export than site 7 on all dates except one. A visual estimate of a high (summer) export is on the order of a ratio of 5 to 1. The seasonal signal is much less clear for NO_3^-, but both sites still show overall lower ratios in the winter months compared to the other seasons. Site 7 is exporting on almost all dates, while site 6 fluctuates between import and low export values for most of the year, with a few higher export values during the warmer months. The by far highest value was found at site 7 in spring, with a NO_3^- ebb/flood ratio of over 30 to 1. A visual estimate of a high (summer) export is on the order of an ebb/flood ratio of 10 to 1. PO_4^{3-} shows the

weakest seasonal signal of the three inorganic nutrient fractions described here, but the overall lowest values still occur in winter. A visual estimate of a high (summer) export is on the order of a ratio of 4 to 1.

A paired difference (Wilcoxon signed-rank) test was applied to the ebb and flood data of each nutrient fraction at each site (table 4.1) to judge the significance of calculated net downstream export or upstream import. For bimonthly samples collected at sites 1-5 and 8, a p value < 0.05 was obtained only for NH_4^+ at site 1. For the fortnightly samples, p values < 0.05 were obtained for NH_4^+ and NO_3^- at site 7, and PO_4^{3-} at site 6. For the inorganic fractions from fortnightly samples at sites 6 and 7, these results agree with visual comparison of PDFs estimated separately for the ebb and flood tides (Appendix 4.A; e.g., site 7 shows a pronounced shift in peaks between ebb and flood samples for NO_3^-).

Table 4.1: Results (p values) of the paired difference (Wilcoxon signed-rank) test between ebb and flood tides for different nutrient fractions at all 8 sites. Values of $p < 0.05$ are shown in bold.

	S1	S2	S3	S4	S5	S6	S7	S8
NH4	**0.031**	0.438	0.844	0.688	0.844	0.400	**0.003**	0.625
NO3	0.787	0.059	0.156	0.207	0.094	0.290	**6e-09**	0.062
PO4	0.588	0.141	0.248	0.134	1.000	**0.002**	0.532	0.188
TN	0.812	0.063	0.438	0.438	0.563	0.219	0.062	0.812
TP	0.812	0.418	0.410	0.141	0.438	0.104	0.062	0.058

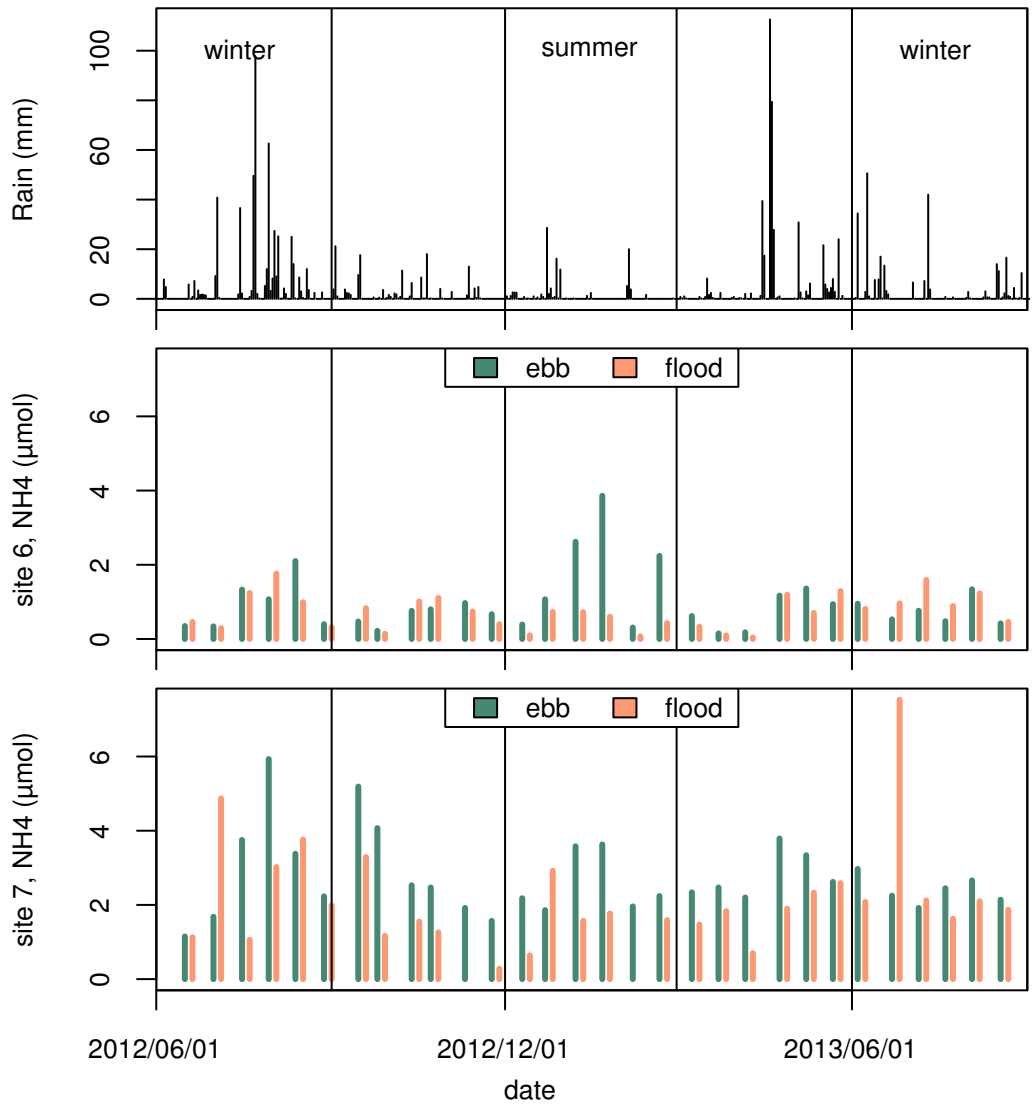

Figure 4.4: Ebb and flood concentrations of NH_4^+ at sites 6 and 7, at approximately fortnightly sampling intervals from southern hemisphere winter 2012 over summer to winter 2013. Top panel shows daily rainfall in mm.

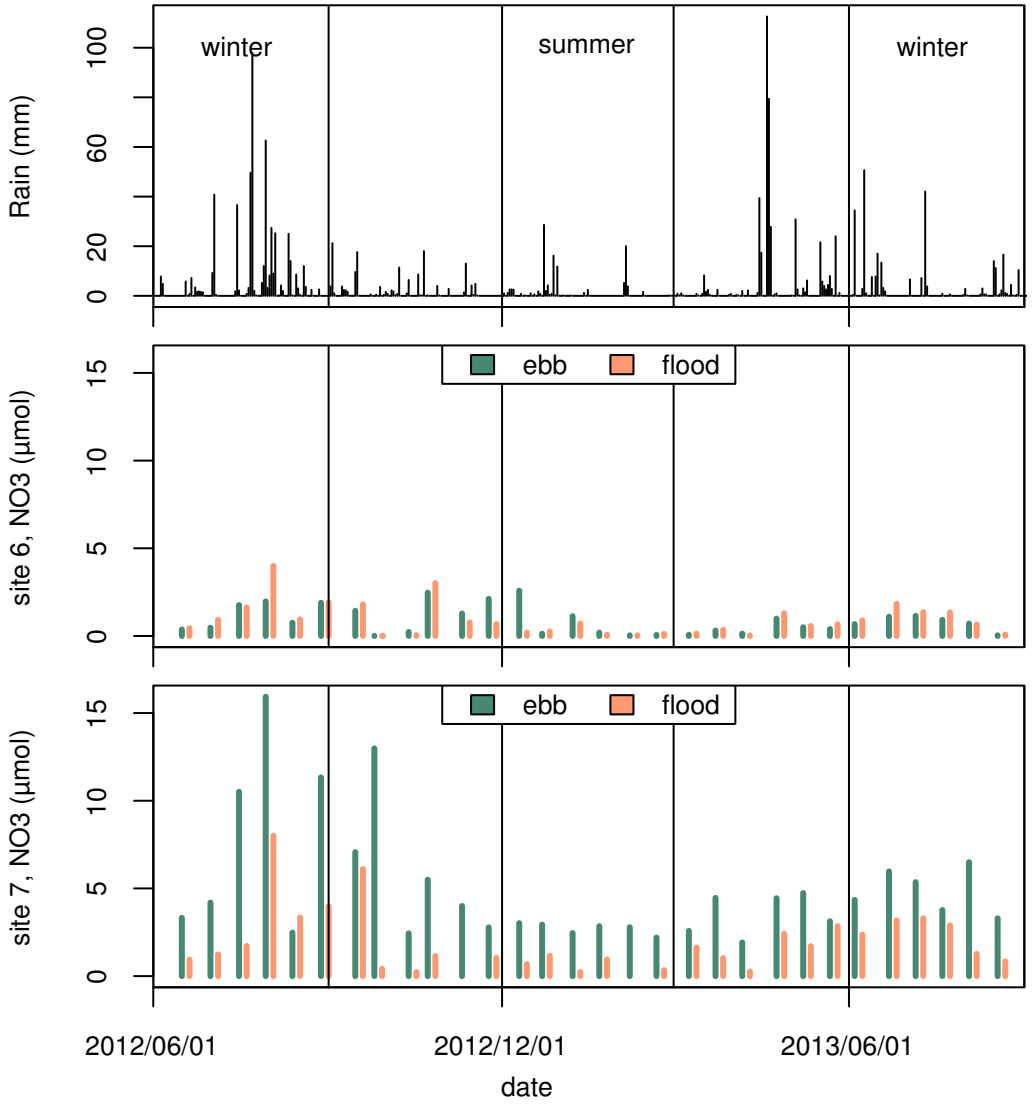

Figure 4.5: Ebb and flood concentrations of NO_3^- sites 6 and 7, at approximately fortnightly sampling intervals from southern hemisphere winter 2012 over summer to winter 2013. Top panel shows daily rainfall in mm.

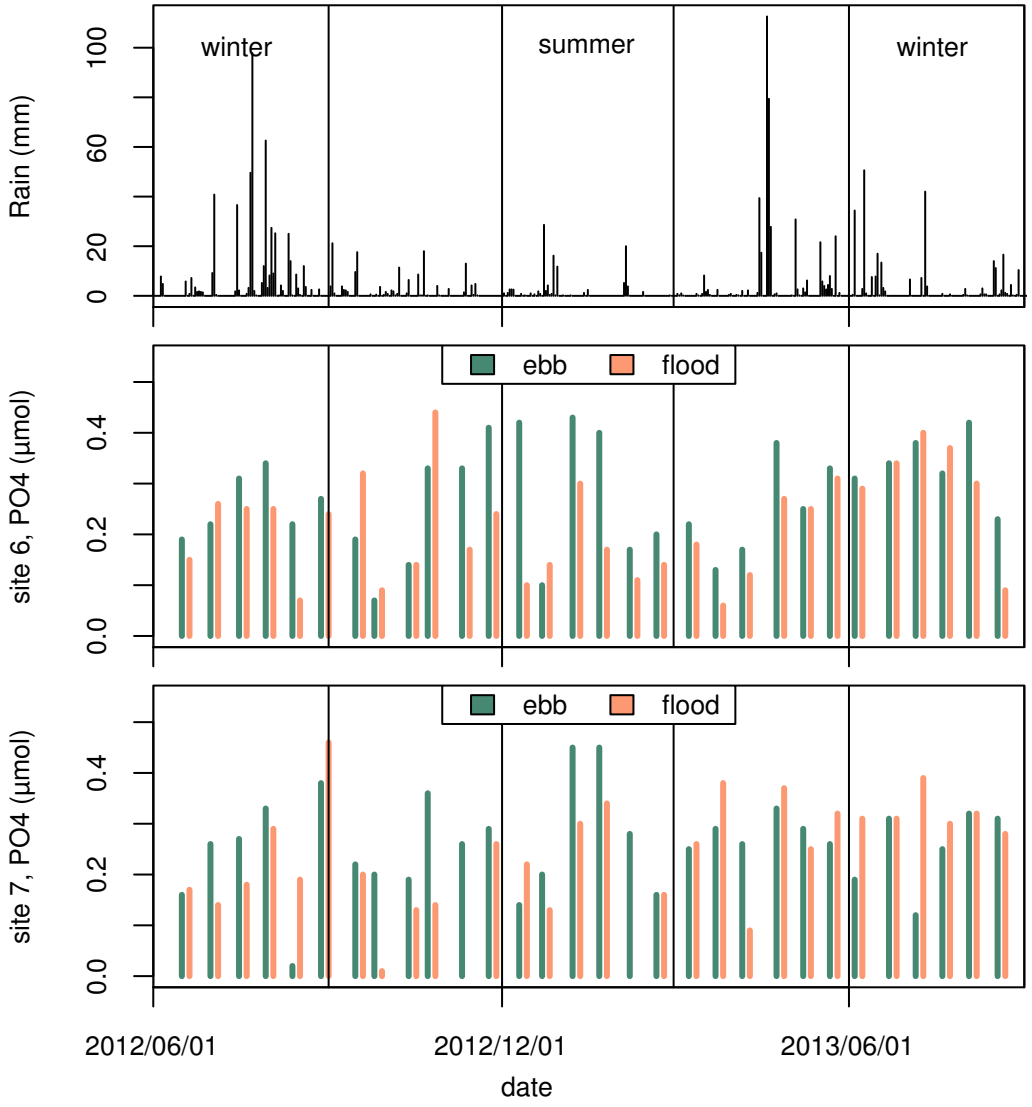

Figure 4.6: Ebb and flood concentrations of PO_4^{3-} at sites 6 and 7, at approximately fortnightly sampling intervals from southern hemisphere winter 2012 over summer to winter 2013. Top panel shows daily rainfall in mm.

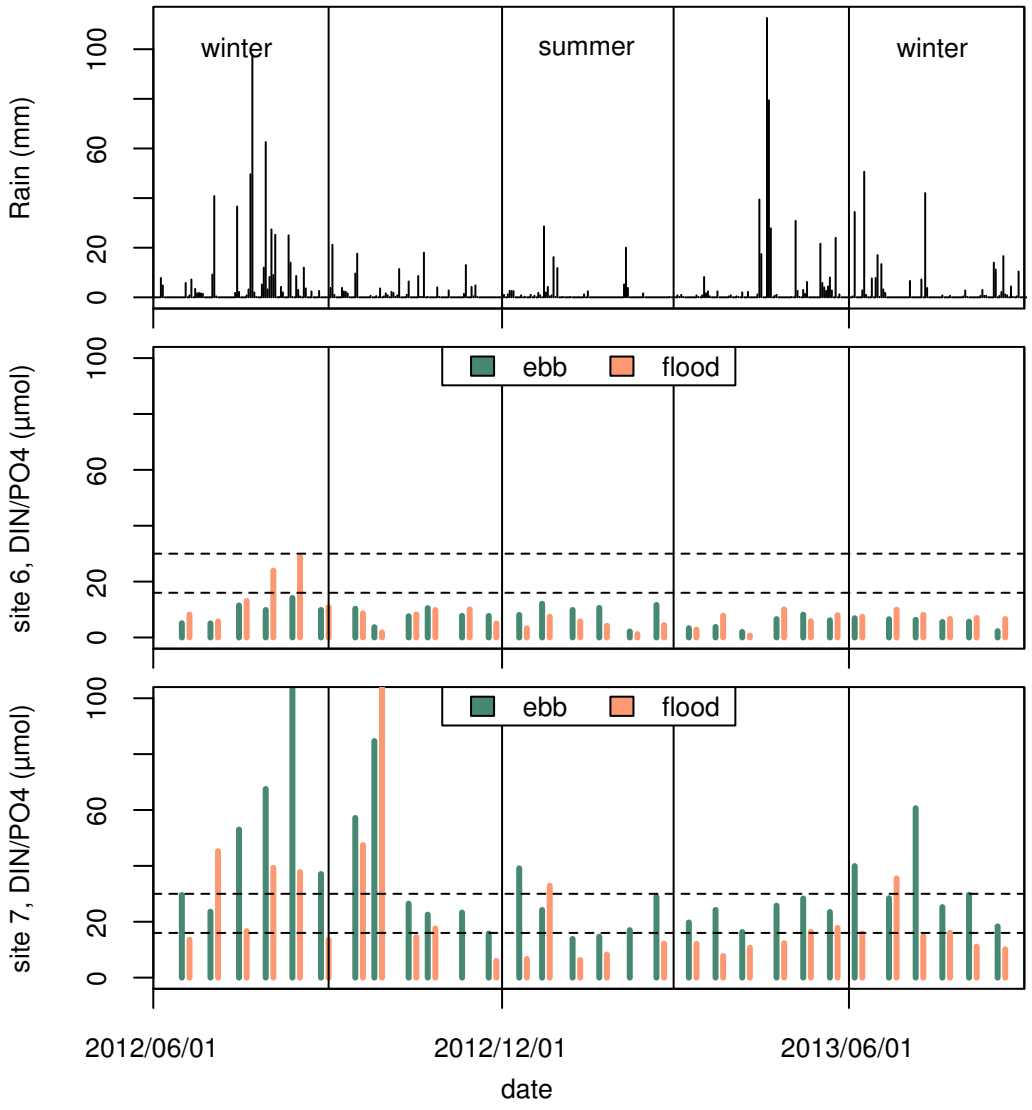

Figure 4.7: Nutrient time series, sites 6 and 7, DIN/PO4. Dashed horizontal lines indicate ratios of 16 and 30 for comparison. At site 7, the following values above 100 were truncated: 174 on flood tide 2012/09/27 and 292 on ebb tide 2012/08/15. Top panel shows daily rainfall in mm.

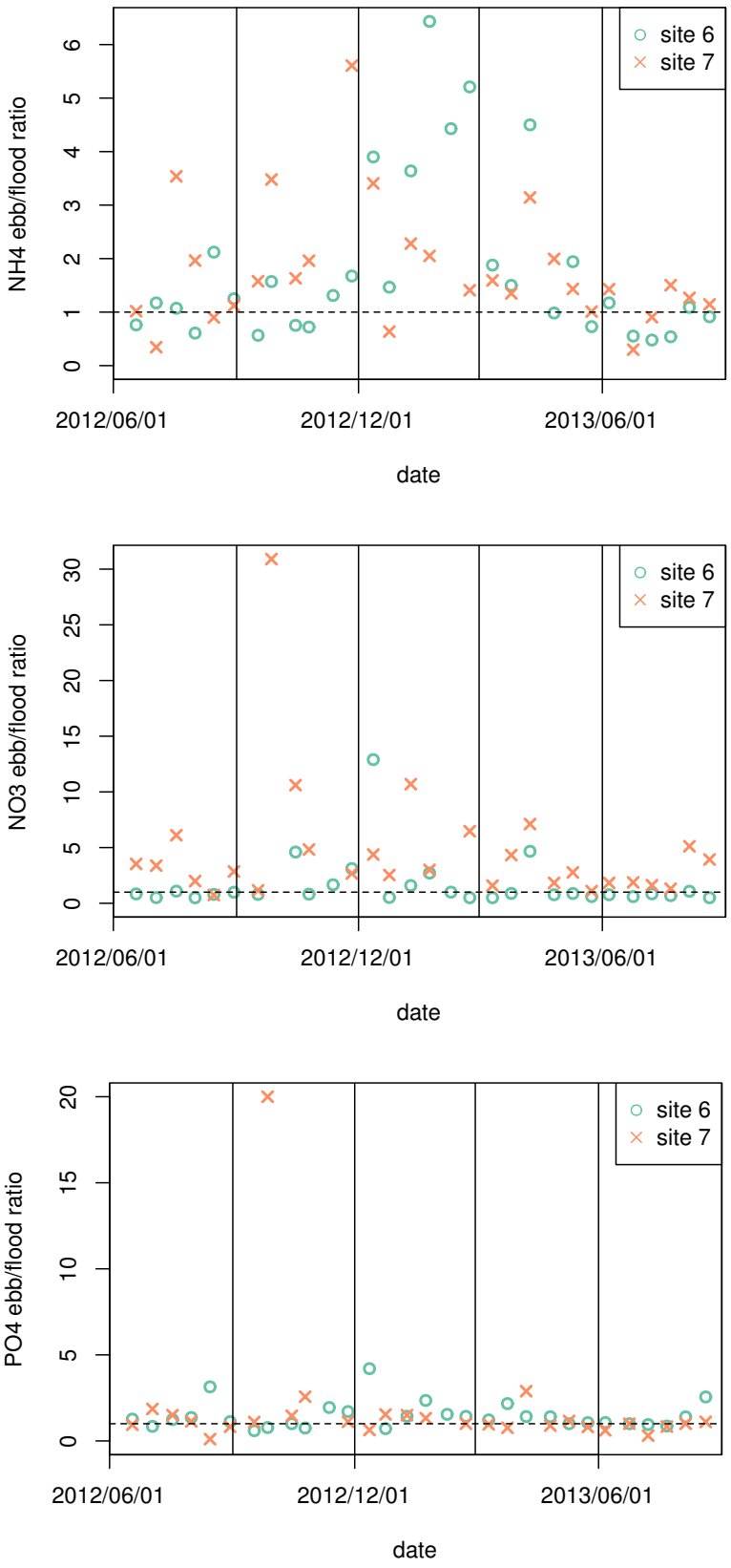

Figure 4.8: Fortnightly ebb/flood ratios of NH_4^+, NO_3^- and PO_4^{3-} at sites 6 and 7. The dashed horizontal line indicates a ratio of one for comparison.

4.3.3 Seasonal spatial concentration and flux patterns

The bimonthly seasonal nutrient survey results separated into 4 groups of sites are shown in Figure 4.9 for the ebb tides. For group 1 close to surface freshwater inputs, a clear seasonality with summer minima is observed for NH_4^+, NO_3^- and TN, although especially for NO_3^- the values are much higher in the first compared to the second winter, consistent with the fortnightly observations at site 7. PO_4^{3-} and TP have no clear seasonal signal, with TP showing even less variation over the year, but with slightly higher values in summer. Group 2 with lower freshwater inputs shows a strong seasonal signal for NH_4^+ but with generally lower values than group 1, with larger differences in summer, and with the exception of the second date where a single very high value at one site leads to the second highest average value for all groups and dates. With the exception of the third date, NO_3^- again shows a similar but weaker seasonality, and generally lower values than group 1. PO_4^{3-}, TN and TP show no clear seasonality, but both TN and TP show increasing average values for dates 1 to 4. Group 3 shows a strong seasonality for NH_4^+ at overall lower values than groups 1 and 2, again with the larger relative differences in summer. NO_3^- shows a slightly weaker seasonality since date 3 has higher values than dates 2 and 4. PO_4^{3-} is on average lower than for groups 1 and 2, but of similar magnitude, has the lowest values over all groups and dates on date 2, and overall no strong seasonality. TN and TP show no seasonality and similar average values as group 2, but lower than group 1. Group 4, containing only S6, is the only group in which NH_4^+ values in summer (dates 3 and 4) are higher than at dates 2 and 5, although still lower than at dates 1 and 6. Dates 3 and 4 are higher than in group 3 but lower than groups 1 and 2, while all other dates are lower than in all other groups. For all other nutrient fractions, no strong seasonality is visible, partly due to the fact that date 3 has higher values than both dates 1 and 2. Across all groups, date 2 had the lowest PO_4^{3-} values of the year. The corresponding flood tide grouped survey results are shown in Figure 4.10. Differences between groups are in most cases smaller than for the ebb tides, and in several cases, group 2 has higher values for one of the inorganic fractions than group 1.

Corresponding plots for both ebb and flood tides for all 8 individual sites are shown in Appendix 4.B.

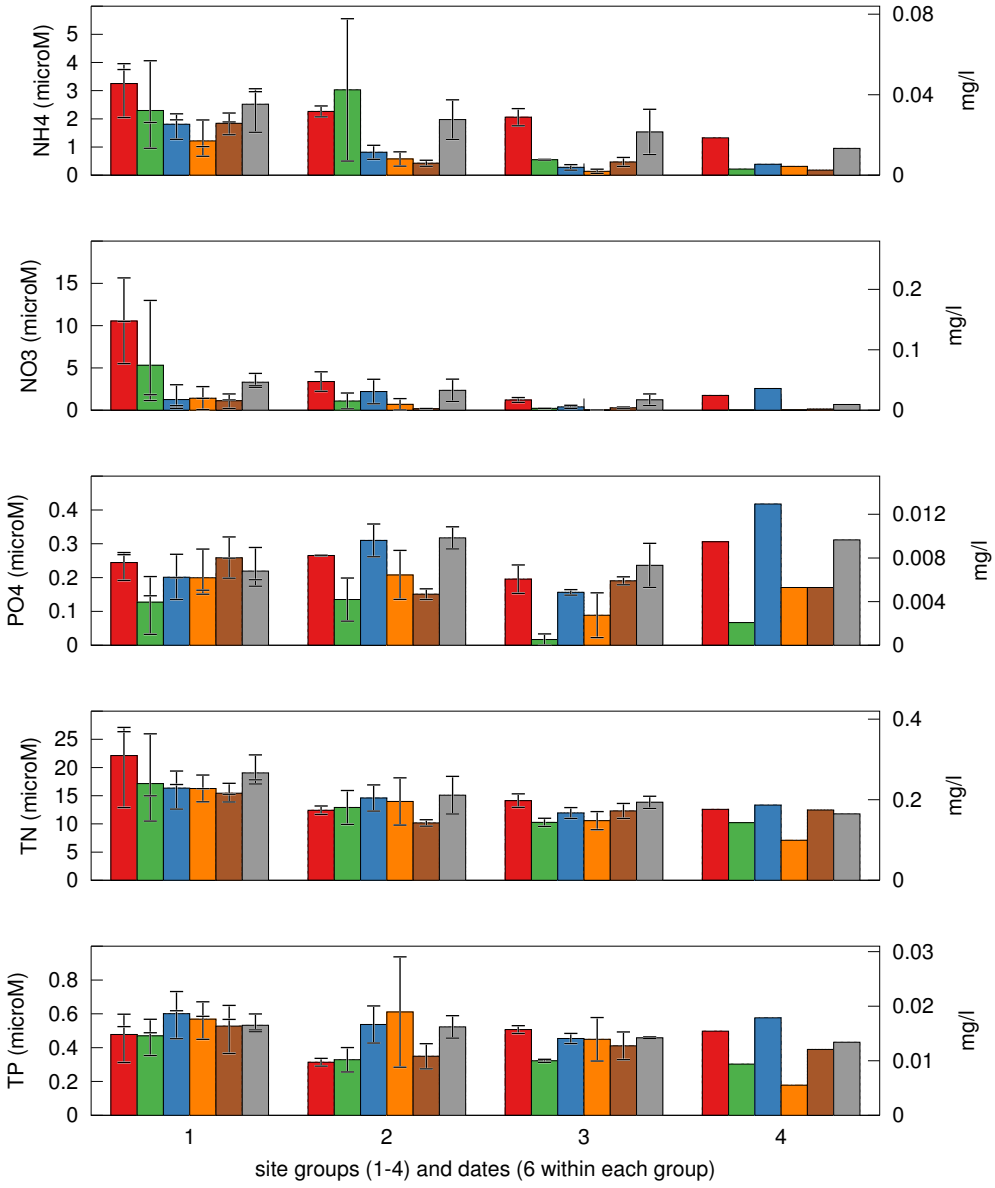

Figure 4.9: Outgoing / ebb tide water column nutrient concentrations at 4 groups of sites. Each bar within a group shows data from a single date (southern hemisphere winter to winter, from left to right: 2012/07/18, 2012/09/27, 2012/12/12, 2013/02/08, 2013/04/08, 2013/06/06). Group 1 has high surface freshwater inputs (sites 2, 5 and 7), group 2 lower freshwater inputs (sites 4 and 8), group 3 covers deep channels within the harbour (sites 1 and 3) and "group" 4 includes only site 6, the main harbour entrance. Except for group 4 / site 6, the height of the solid bars indicates mean values, and short horizontal lines indicate individual values (not to be confused with "error bars").

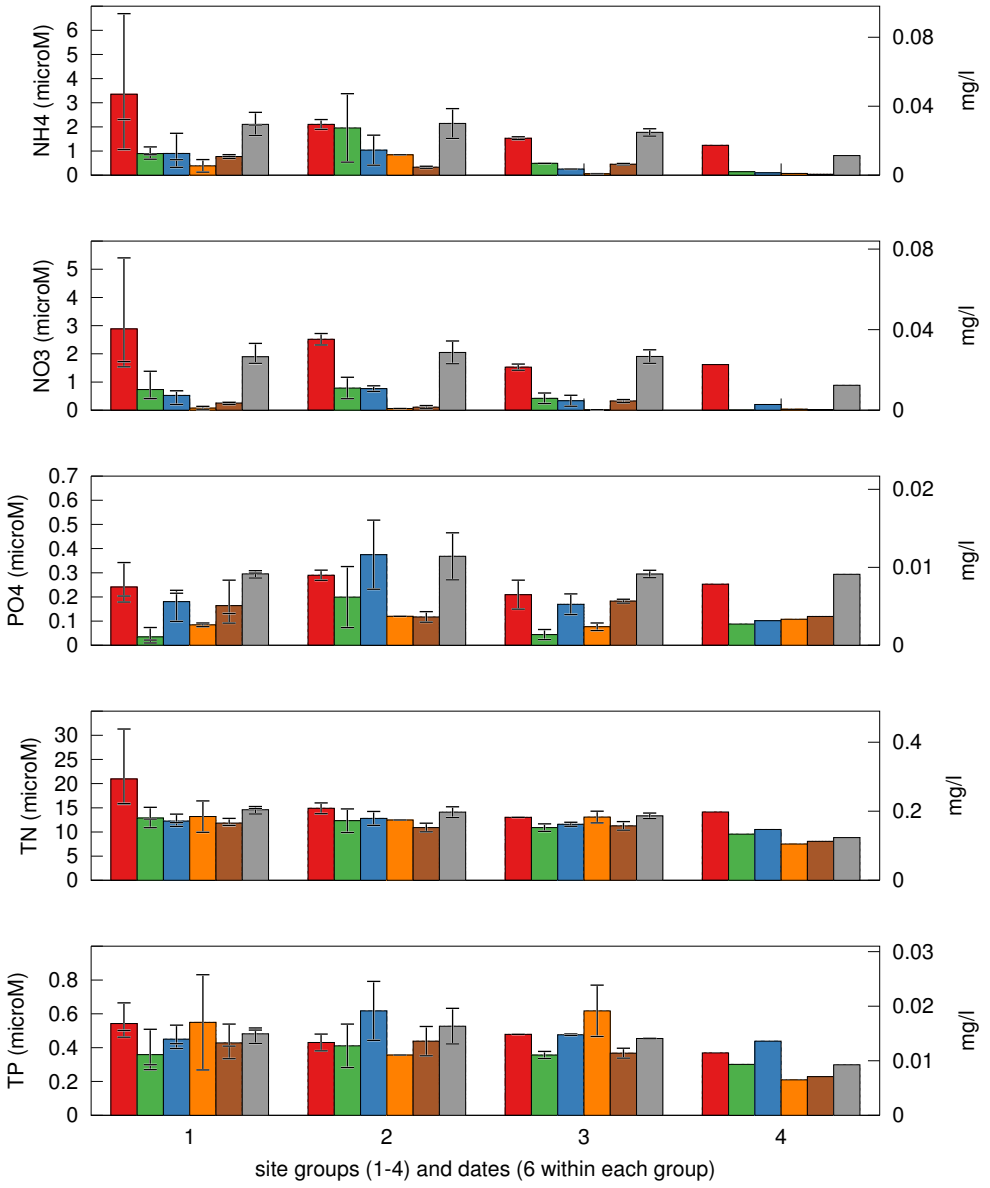

Figure 4.10: Incoming / flood tide water column nutrient concentrations at 4 groups of sites. Each bar within a group shows data from a single date (southern hemisphere winter to winter, from left to right: 2012/07/18, 2012/09/27, 2012/12/12, 2013/02/08, 2013/04/08, 2013/06/06). Group 1 has high surface freshwater inputs (sites 2, 5 and 7), group 2 lower freshwater inputs (sites 4 and 8), group 3 covers deep channels within the harbour (sites 1 and 3) and "group" 4 includes only site 6, the main harbour entrance. Except for group 4 / site 6, the height of the solid bars indicates mean values, and short horizontal lines indicate individual values (not to be confused with "error bars").

To facilitate the interpretation of connections between sites and corresponding subregions, the average ebb and flood concentrations as well as mass fluxes of each nutrient fraction at all sites are shown as directional bar plots superimposed on the hydrodynamic model's bathymetry grid in Figures 4.11 to 4.15. Downstream exports or upstream imports with p-values less than 0.05 according to Table 4.1 are mentioned explicitly as statistically significant in the following.

For NH_4^+ (Figure 4.11), the south-western, landward sites 7, 8, 2 and 5 feature prominently in terms of concentrations, and especially sites 7 and 2 also in terms of difference in concentration between ebb and flood tides. Although an export is visible at sites 1 and 2, this is not apparent at the downstream site 3, but is again present at the main harbour entrance site 6. Site 5 which is located downstream of the largest river tributary also does not show a clear export, and site 4 bordering on the seaward barrier island shows a small import. Downstream export is statistically significant at sites 1 and 7. In terms of mass flux, of the aforementioned south-western, landward sites only site 8 shows ebb and flood fluxes similar in magnitude to those seen at the central deep channels of site 3, both somewhat larger than at site 1. Sites 2, 5, 7 and 4 show very small fluxes relative to the other sites, and no obvious net import or export. Net export is clearly visible only at site 1 as well as the at the main harbour entrance site 6.

For the second DIN fraction, NO_3^- (Figure 4.12), concentrations on the ebb tide are higher than on the flood tide for all four landward sites (2, 5, 7 and 8, with statistically significant downstream export at site 7), and also higher than at all four remaining sites. In terms of mass flux, of the landward sites only site 8 remains with a sizeable downstream export. Site 3 shows an upstream import while the remaining sites including the harbour entrance at site 6 show no clear import or export.

PO_4^{3-} concentrations (Figure 4.13) vary less between sites than either of the DIN fractions. Site 6 at the harbour entrance shows a statistically significant downstream export that also remains clearly visible in terms of mass flux. The mass flux at the landward sites 2, 5 and 7 as well as site 4 on the Matakana Island side seem negligible compared to the other sites.

TN and TP (Figures 4.14 and 4.15) show overall similar behaviour, with higher concentrations on the ebb tide especially apparent at site 7, and downstream export in terms of mass flux at site 6.

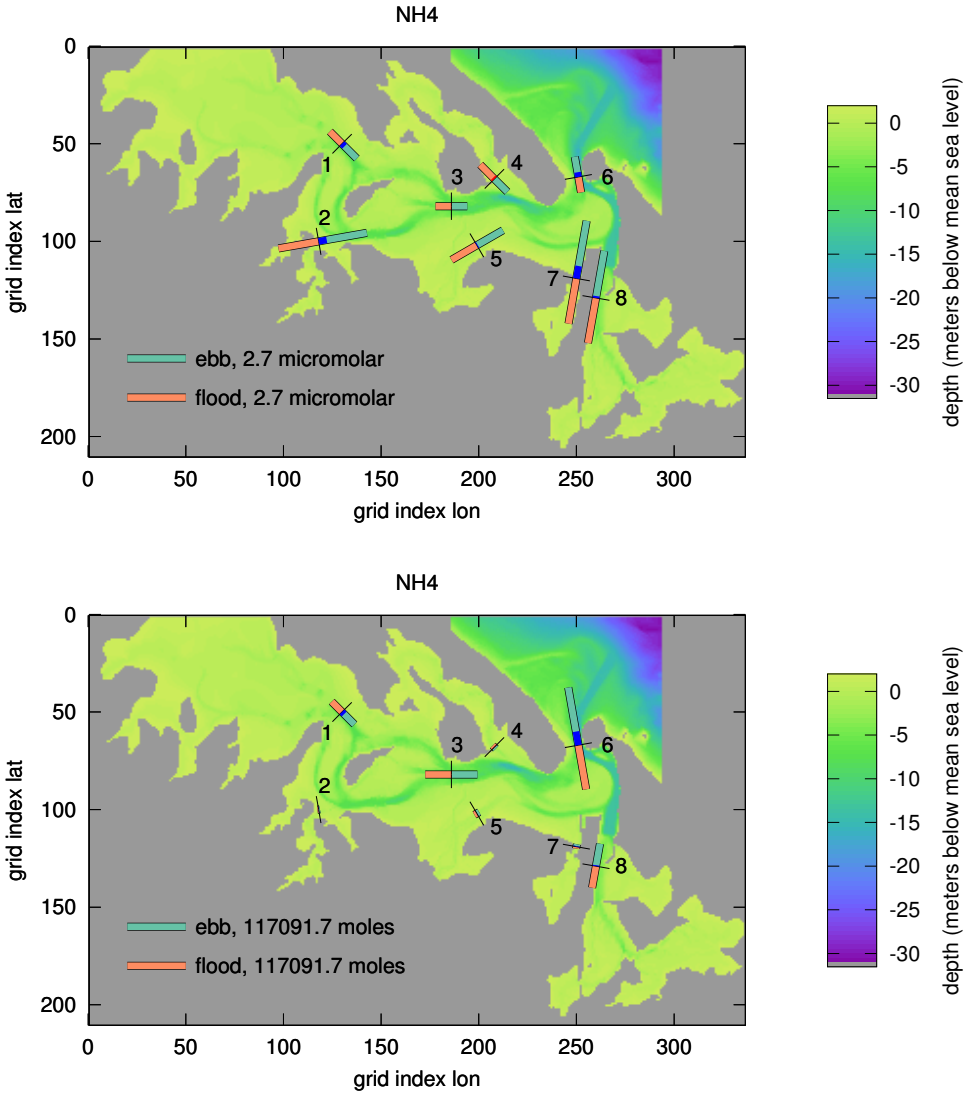

Figure 4.11: Average concentrations (top panel) and mass fluxes (bottom panel) of NH_4^+ for the ebb (green bars in downstream direction) and flood (orange bars in upstream direction) tides as well as the difference between ebb and flood or "net" values (darker shaded bars in direction and colour of the tide with the higher value) at 8 sites, based on one year of sampling (from winter to winter) at approximately bimonthly (sites 1-5 and 8) or fortnightly (sites 6 and 7) intervals.

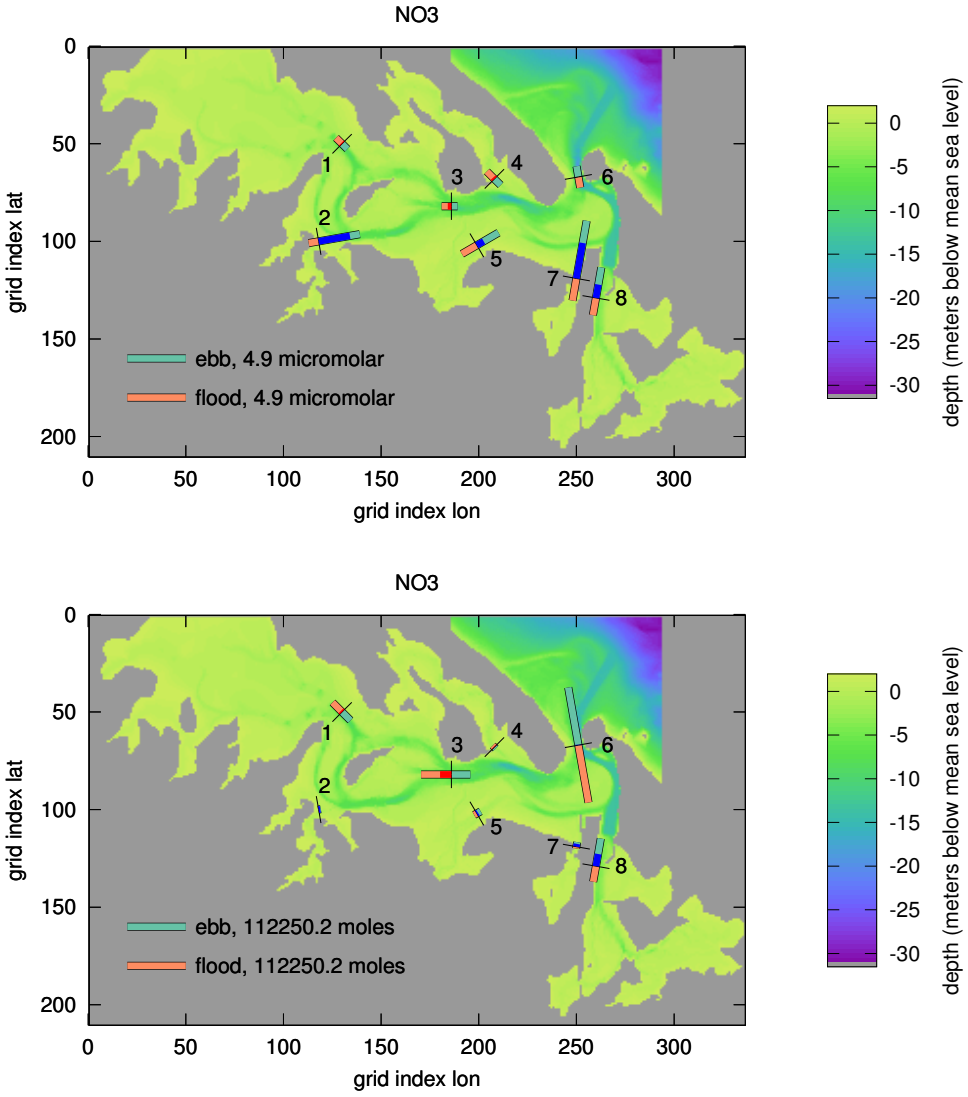

Figure 4.12: Average concentrations (top panel) and mass fluxes (bottom panel) of NO_3^- for the ebb (green bars in downstream direction) and flood (orange bars in upstream direction) tides as well as the difference between ebb and flood or "net" values (darker shaded bars in direction and colour of the tide with the higher value) at 8 sites, based on one year of sampling (from winter to winter) at approximately bimonthly (sites 1-5 and 8) or fortnightly (sites 6 and 7) intervals.

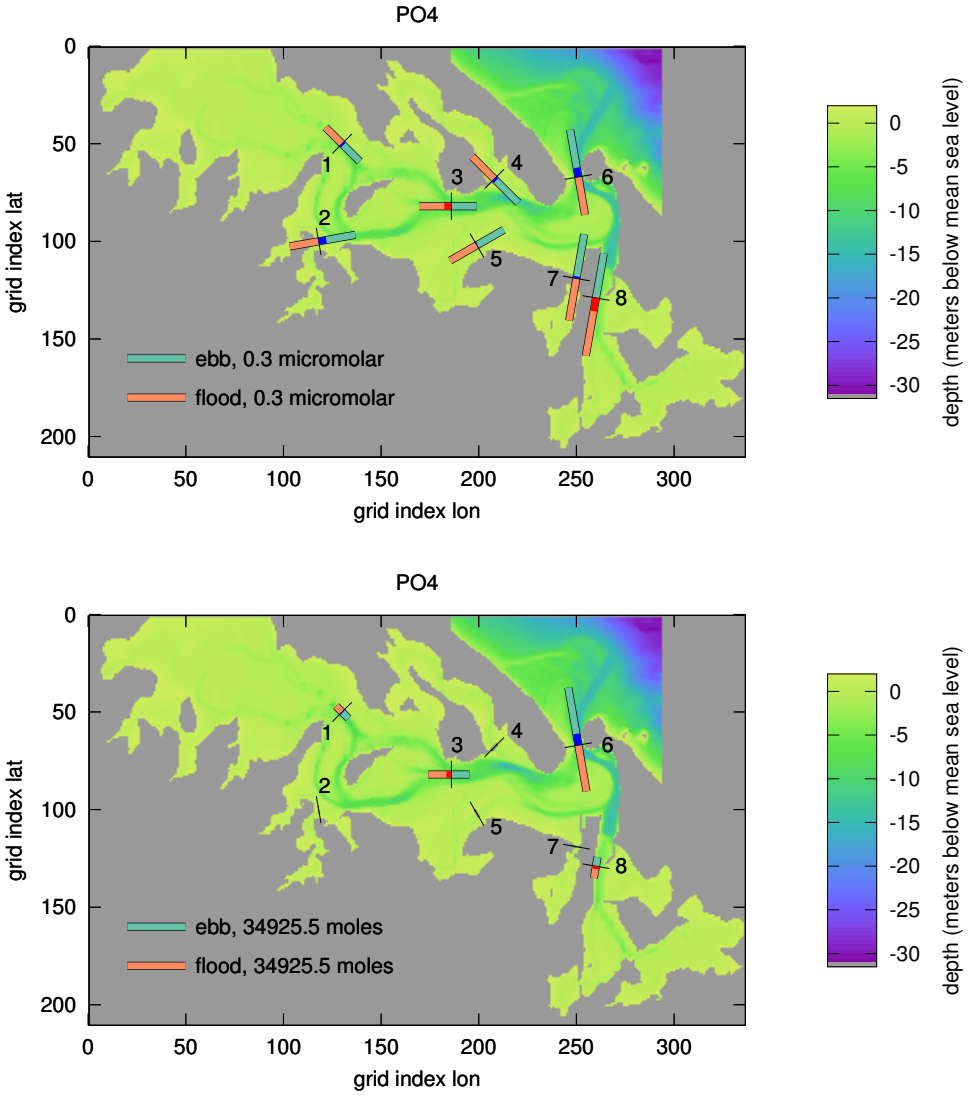

Figure 4.13: Average concentrations (top panel) and mass fluxes (bottom panel) of PO_4^{3-} for the ebb (green bars in downstream direction) and flood (orange bars in upstream direction) tides as well as the difference between ebb and flood or "net" values (darker shaded bars in direction and colour of the tide with the higher value) at 8 sites, based on one year of sampling (from winter to winter) at approximately bimonthly (sites 1-5 and 8) or fortnightly (sites 6 and 7) intervals.

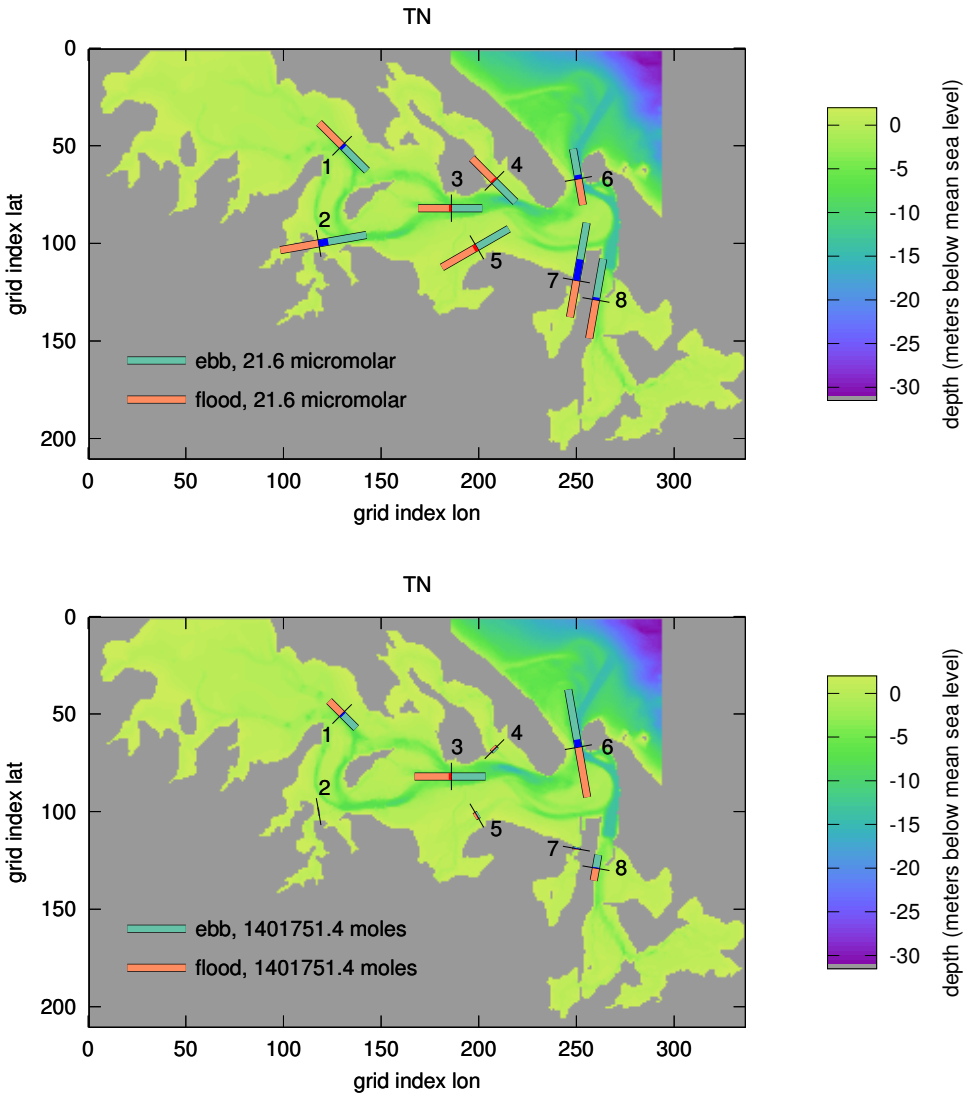

Figure 4.14: Average concentrations (top panel) and mass fluxes (bottom panel) of TN for the ebb (green bars in downstream direction) and flood (orange bars in upstream direction) tides as well as the difference between ebb and flood or "net" values (darker shaded bars in direction and colour of the tide with the higher value) at 8 sites, based on one year of sampling (from winter to winter) at approximately bimonthly (sites 1-5 and 8) or fortnightly (sites 6 and 7) intervals.

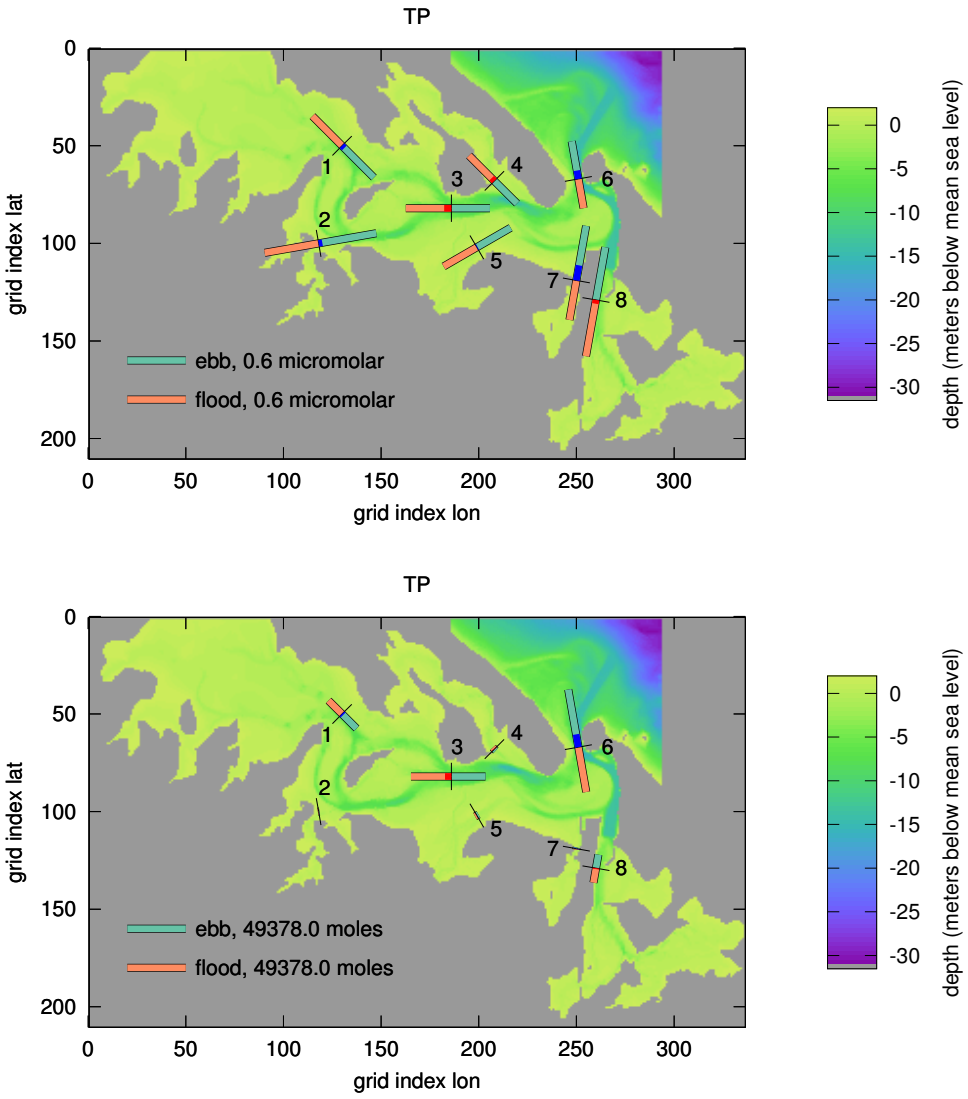

Figure 4.15: Average concentrations (top panel) and mass fluxes (bottom panel) of TP for the ebb (green bars in downstream direction) and flood (orange bars in upstream direction) tides as well as the difference between ebb and flood or "net" values (darker shaded bars in direction and colour of the tide with the higher value) at 8 sites, based on one year of sampling (from winter to winter) at approximately bimonthly (sites 1-5 and 8) or fortnightly (sites 6 and 7) intervals.

Table 4.2: Southern Tauranga Harbour subregions' (SR) area, volume at mean high and low water and volume of the tidal prism.

SR	name	area (10^6 m^2)	volume high (10^3 m^3)	volume low (10^3 m^3)	tidal prism (10^3 m^3)
1	Omokoroa	34.69	47714	10928	36786
2	Te Puna	1.76	1293	101	1192
3	Western Channel	28.37	80798	46857	33940
4	Hunter's Creek	5.70	6017	1092	4925
5	Wairoa	4.01	4441	473	3967
6	Harbour entrance	15.46	82921	61827	21094
7	Waikareao	2.33	1858	56	1802
8	Town Reach	20.04	29200	8301	20898
9	total	112.36	254246	129638	124608

4.3.4 Passive tracer transport modelling

The loss over time of tracer injected in the six subregions at high tide is shown in Figure 4.16. The minima of tracer mass remaining after an outgoing tide occur at different times for each subregion, with subregion 6 being the first and subregion 7 being the last. At consecutive high tides (integer multiples of the M2 period after injection), relatively low dilutions are observed for subregions 1, 7, 8 and 4, with between approximately 85 and 50% of initial tracer mass returning or remaining after one M2 tidal cycle. The rank of these four subregions with respect to dilution also does not change over the simulation period of six M2 tidal cycles. Higher dilution is observed for subregions 4, 2, 5 and 6, with between approximately 40 and 15% of initial tracer mass returning or remaining after one M2 tidal cycle. Subregion 5 shows a further small but marked increase in dilution compared to the other subregions over time. When ranked by increasing dilution, subregion 5 advances from rank 4 after one M2 tidal cycle to rank 1 after six M2 tidal cycles. Subregion 3 shows an early peak in tracer mass just before each high tide, followed by a second, smaller peak just after high tide before dropping off towards low tide. A similar pattern, although less pronounced, is also apparent for subregion 4.

The concentration of tracer originating in each of the eight upstream subregions to the water mass at the harbour entrance is shown over six M2 tidal cycles in Figure 4.17. From tracer injection until the first low tide, losses at the coastal ocean open boundary have no upstream influence, and dilution by landward freshwater

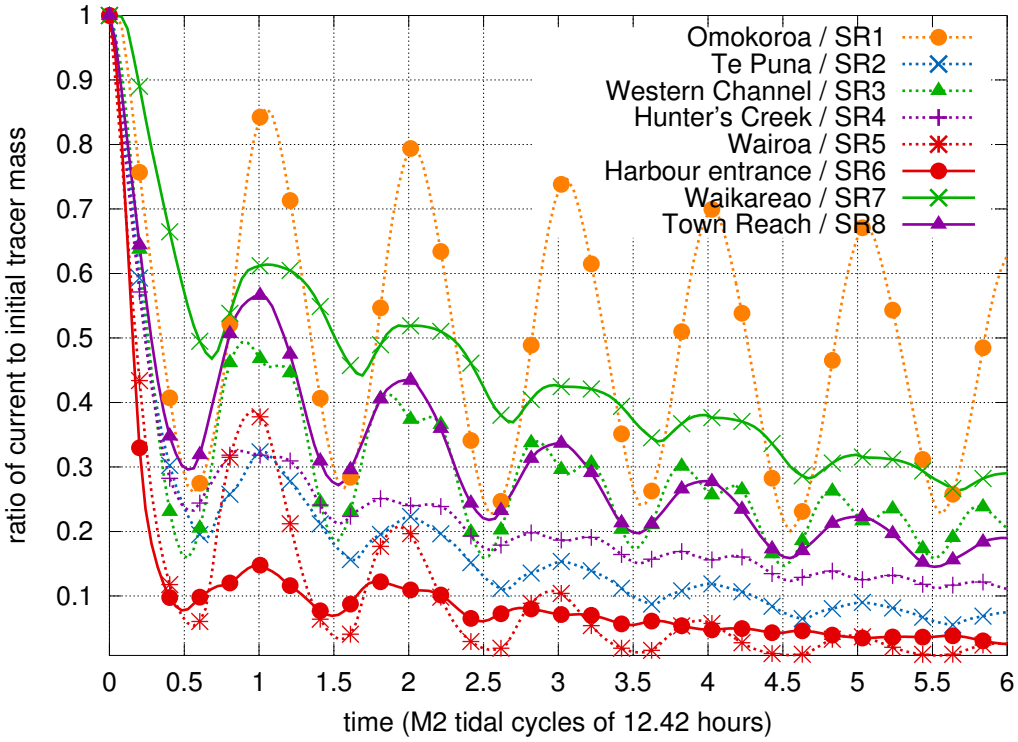

Figure 4.16: Modelled passive tracer dilution over time for Tauranga Harbour subregions for high tidal range conditions and tracer injection at high tide. The initial concentration was constant over each entire subregion, resulting in different total masses in each subregion. Shown is the ratio of each subsequent mass divided by the corresponding initial mass.

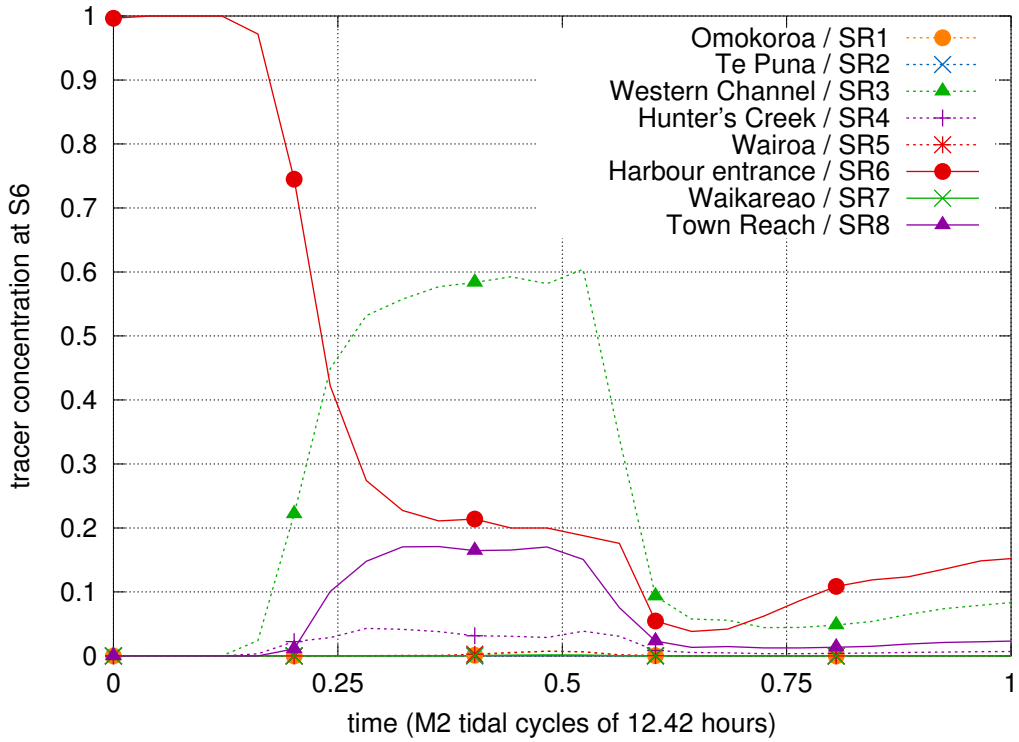

Figure 4.17: Modelled passive tracer concentrations at the main harbour entrance for high tidal range conditions and tracer injection at high tide. The initial concentration was constant for each subregion.

inflows is negligible. Until this time, the sum of all tracer concentrations at the harbour entrance is consequently close to or equal to one (data not shown), and the tracer concentrations can therefore be interpreted as percent of the water mass originating in the corresponding upstream subregion. For the first part of the outgoing tide after injection, only tracer originating from the adjacent subregion 6 is present. After a little less than half of the outgoing tide (0.25 M2 cycles), tracer from subregions 3, 8 and 4 start to contribute, with subregion 3 quickly replacing subregion 6 as the highest contributor. After exactly half of the outgoing tide, subregion 3 dominates slightly with 47% contribution, followed by subregion 6 with 43% and subregions 8 and 4 with approximately 5% each. At the first low tide after injection, subregion 3 clearly dominates with 65%, followed by subregion 6 with 16%, subregion 8 with 9% and subregion 4 with 5%, while at this time all other subregions contribute less than 1%. Examination of the time series of the vertically integrated 2D fields of tracer concentrations (data now shown) shows that a large part of tracer originating in subregion 6 is lost to the northern coastal ocean open boundary towards the end of the first outgoing tide.

To emphasise the importance of keeping sampling times constant relative to local M2 phase, the contribution of upstream subregions to the water mass at the harbour entrance (site 6, directly downstream of SR6) was interpolated from the data shown in Figure 4.17 at ±0.25 and ±0.5 hours around the target sample time at mid-tide, and the results are shown in Table 4.3. The initially highest contributor, SR6, decreases from 68% to 26% within 1 hour, while the initially second highest contributor, SR3, increases from 27% to 54% in the same time, and during the central 0.5 hours within this period, SR6 decreases 20% from 52% to 32%. SR8 increases from 3% to 15% within 1 hour.

Table 4.3: Contributions (in %) of upstream subregions to the water mass at the harbour entrance (site 6, directly downstream of SR6) at ±0.25 and ±0.5 hours around the target sample time at mid-tide (t0).

	contribution of upstream subregions (%)							
time	SR1	SR2	SR3	SR4	SR5	SR6	SR7	SR8
t0-0.50h	0	0	27	2	0	68	0	3
t0-0.25h	0	0	38	3	0	52	0	7
t0+0.00h	0	0	47	3	0	39	0	11
t0+0.25h	0	0	51	4	0	32	0	13
t0+0.50h	0	0	54	4	0	26	0	15

The connectivity matrices for exchange of water between all subregions are shown over five M2 tidal cycles for high and low tidal range conditions in figures 4.18 and 4.19, respectively. Data shown in the diagonal elements of the matrices (excluding the additional rightmost column '9') are identical to those shown in figure 4.16. Subregion 1 shows the highest retention, with only 25% in subregion 3 after 5 M2 tidal cycles, and only 1% in subregion 6 as well as lost to outside the harbour after 3 M2 tidal cycles. Subregion 2 shows low retention, with 20%, 37% and 10% in subregions 1, 3 and lost to outside the harbour after just 1 M2 tidal cycle. Only the loss to outside the harbour increases clearly to 28% after 5 M2 tidal cycles. After 1 M2 tidal cycle, subregion 3 loses 6% upstream to subregion 1, twice that amount downstream to subregion 6 and already 26% to outside the harbour. After 2 and more M2 tidal cycles, the losses to subregions 1 and 6 become more similar, reaching 7% and 6% after 5 M2 tidal cycles, with losses to outside the harbour of 58% at that time. Subregion 4 after 1 M2 tidal cycle looses 25% indirectly upstream to subregion 2, only 12% downstream to subregion 6, and already 28% to outside the harbour. Subregion 5 after just one M2 tidal cycle already looses 43% to subregion 3, followed by 8% to subregion 8, 6% to subregion 6 and just 2% lost to outside the harbour. The loss to subregion 3 stays at least a factor of 3 higher than that to subregion 6 during the entire 5 M2 tidal cycles examined, although between 1 and 3 M2 tidal cycles, the loss to subregion 6 still slightly increases, while that to subregion 3 already decreases. The loss to subregion 8 increases slightly to 10% after 3 M2 tidal cycles before starting to decrease. Losses to outside the harbour increase steadily, leading to 48% after 5 M2 tidal cycles. Subregion 6 looses 73% to outside the harbour after 1 M2 tidal cycle, with only further 7% and 5% to subregions 3 and 8 and no noticeable losses to any other subregions. Up to 5 M2 tidal cycles, only the loss to outside the harbour increases, mirrored by decreases in subregions 3, 8 and the origin subregion 6 itself, while no other subregions receive noticeable input.

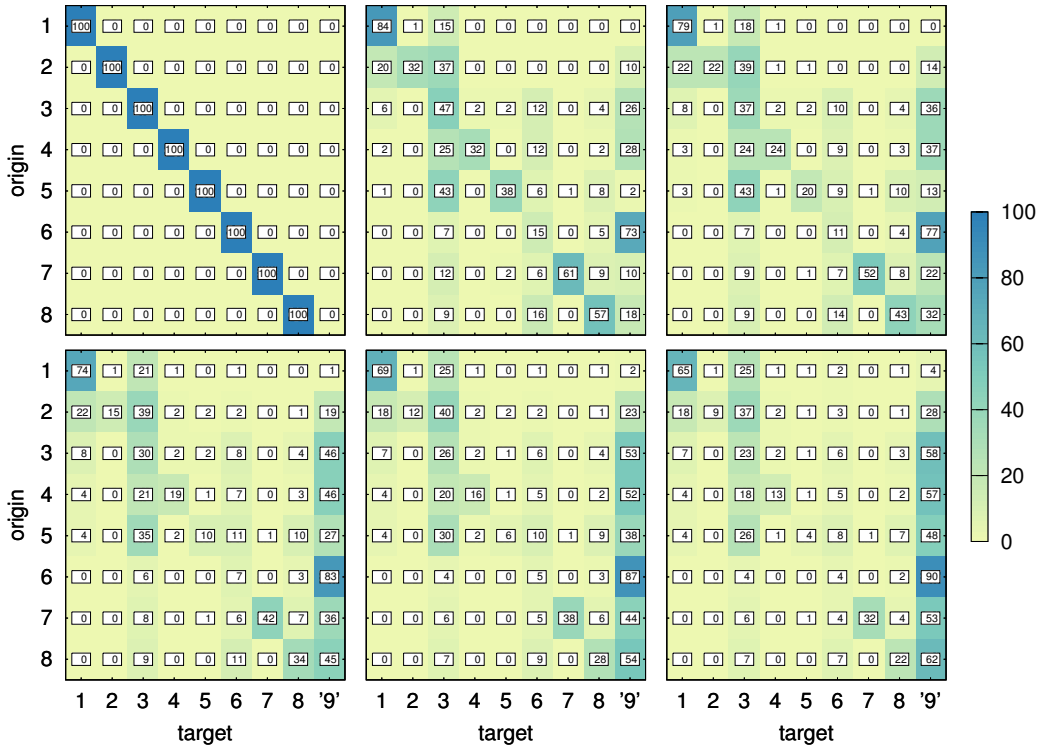

Figure 4.18: High tidal range, high tide tracer injection "connectivity" matrix: in each matrix, tracer originating in subregion i ("origin") and currently present in subregion j ("target") is shown in the i-th row, j-th column. Values are given in percent of mass originally present in the origin subregion, additionally colour-coded according to the colourbar. Target subregion '9' shows the percentage of tracer unaccounted for within the 8 subregions. From left to right, the matrices in the top row show values after 0 (shown only to ease visual interpretation), 1 and 2 M2 tidal cycles, in the bottom row after 3, 4 and 5 M2 tidal cycles.

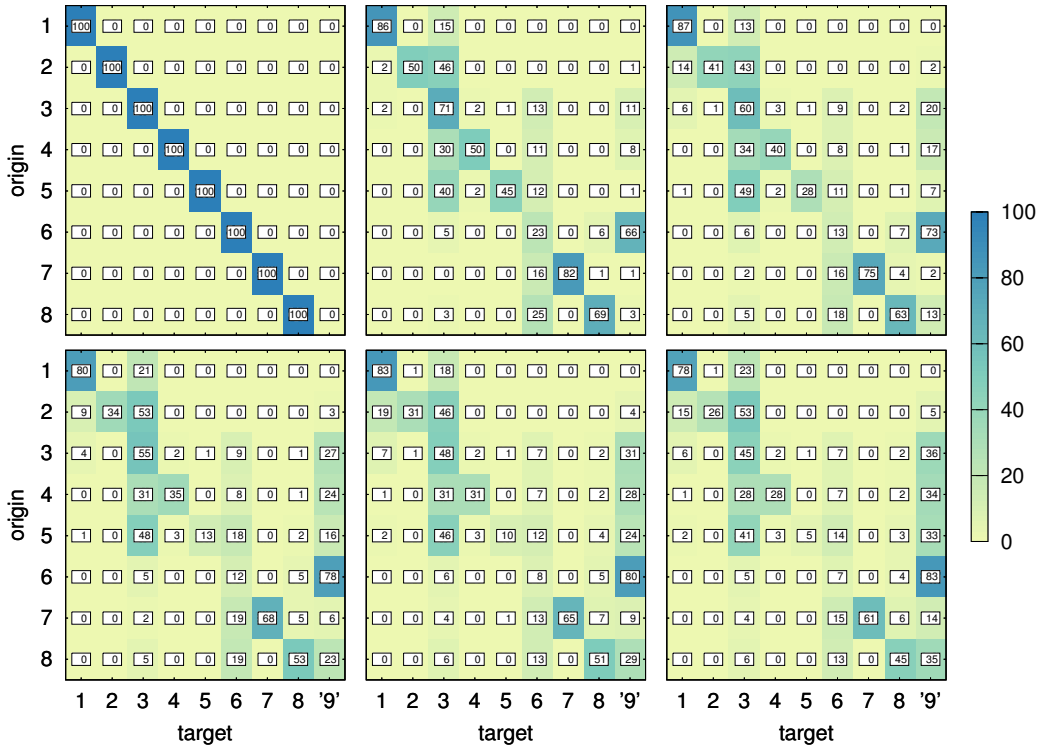

Figure 4.19: Low tidal range, high tide tracer injection "connectivity" matrix: in each matrix, tracer originating in subregion i ("origin") and currently present in subregion j ("target") is shown in the i-th row, j-th column. Values are given in percent of mass originally present in the origin subregion, additionally colour-coded according to the colourbar. Target subregion '9' shows the percentage of tracer unaccounted for within the 8 subregions. From left to right, the matrices in the top row show values after 0 (shown only to ease visual interpretation), 1 and 2 M2 tidal cycles, in the bottom row after 3, 4 and 5 M2 tidal cycles.

4.4 Discussion & conclusion

4.4.1 Probability density function estimates

An accurate description of nutrient concentration PDFs is valuable for both modelling as well as observation-based studies, and our findings show that these are highly variable both between nutrient fractions and between sites. Although some of the PDF estimates for NH_4^+, NO_3^- and PO_4^{3-} do show shoulders that potentially indicate mixture distributions (especially when combining data from several sites), a unimodal family of distributions could still be assumed as a first approximation. Due to the high differences in skewness from almost symmetrical for PO4 to highly positive at site 6 for both NH_4^+ and NO3, the two-parameter family of gamma distributions seems the best choice to approximate these empirically observed distributions. Site- and nutrient-specific gamma distribution fits could be calculated based on these data to improve sensitivity analysis of models with nutrient forcing, which are often based on uniform, triangular or other distributions not directly related to observed data (Li et al., 2015; McCallum, 2000). This is of particular interest in cases where the model's sensitivity with regard to both model parameters and model forcing variables is examined (chapter 2; Aveytua-Alcázar et al., 2008). Using distribution fits from a single family would facilitate the comparison between nutrient fractions, sites or studies, as well as their application to mechanistic model sensitivity analyses.

For some cases where high probability densities are observed close to concentrations of zero (e.g., NO3 at site 6), the PDF estimate approaches that of an exponential distribution. Further investigations are necessary to unravel the combined influence of potentially high uncertainty of individual measurements near the method detection limit together with potential "boundary bias" (Jones, 1993; Zhang et al., 1999) in the kernel density estimation in these cases.

4.4.2 Tidally-dominated nutrient transport

In tidally-dominated estuaries with complex geometry, such as Tauranga Harbour, hydrodynamic advection due to tidal currents and freshwater inputs alone already leads to complex horizontal transport patterns (Tay et al., 2013). Often, these patterns are counter-intuitive and can not be explained by or reduced to the relatively simple upstream/downstream effects more prevalent in for example fjord-like or river delta estuaries. Especially the constrictions between the main harbour water body (subregions 3 and 6) and well-defined upstream sub-estuaries (subregions 1,

2, 4, 7 and 8), as well as sandbanks and islands diverting the flow (especially within subregions 3 and 6) greatly influence the transport and mixing processes.

Tauranga Harbour experiences partly mixed semi-diurnal tides, with the tidal range of two consecutive M2 tides regularly differing by up to 0.3 m, and the high tide water level by up to 0.2 m. Especially in subregions with extensive shallow intertidal areas, such differences may influence the transport patterns observed for two or more consecutive tides. Further study is needed to examine whether this effect is substantial with respect to the behaviour under high, low and "average" tidal range conditions, which are usually interpreted to correspond to high, low and "average" tidal mixing conditions.

Analysis of the fortnightly data of ebb/flood ratios of the inorganic nutrient fractions NH_4^+, NO_3^- and PO_4^{3-} at sites 6 and 7 revealed that although the annual average indicates downstream export, all three fractions frequently fluctuate between import and export. NH_4^+ showed the strongest seasonal signal with almost only export at both sites in summer. This may be related to the temperature dependence of autochthonous production, especially benthic remineralisation (Herbert, 1999), or other ecosystem processes (MacKenzie, 2004; Zeldis, 2004). Sharp changes between dates with less of a seasonal dependence in NO_3^- ebb/flood ratios could be caused by allochthonous sources, especially rapid changes in river and stream input due to rainfall events (Arhonditsis et al., 2002). Both mechanisms could be further explored by statistical analysis of the corresponding physical environmental conditions, e.g., air temperature (or if possible water temperature), solar irradiance (especially in connection with subregions with a large proportion of intertidal areas) and precipitation over the watersheds.

The variety of pathways taken by the waterbodies in a tidally-dominated estuary with complex geometry make it difficult to trace sources. The average downstream mass flux (export) of NH_4^+ at the main harbour entrance site 6 can not easily be explained by contributions from the upstream sites surveyed in this study. Site 7 shows high concentrations and also net export, but at very small volumes of water, and while site 8 shows high concentrations at a much larger volume of water, no net export is apparent. Several mechanisms to explain this difference are conceivable. Although site 5 is downstream of the largest freshwater input, the shallow and forked bathymetry in this area may lead to the larger volume of riverine water sometimes or always flowing into the deeper channel just downstream of site 3, but passing west of site 5. In this way, large fluxes into subregion 6 could go undetected by the current survey sites. At both sites 5 and 8, which were only sampled in the bimonthly surveys, the small number of samples over a single year may have led to

misleading results. In the exploratory (in contrast to confirmatory) study carried out here, only very few combinations of sites and nutrient fractions showed statistically significant differences between ebb and flood concentrations. Lastly, the subregion 6 itself, although having only a relatively low proportion of intertidal areas compared to all other subregions except subregion 3, may itself be contributing a sizeable mass flux of autochthonous NH_4^+.

In shallow estuaries, both circulation and resuspension is strongly influenced by local wind effects, and this effect has also been demonstrated for Tauranga Harbour (Tay et al., 2013). Weather station data shows that daily precipitation is positively correlated with daily wind run in Tauranga Harbour (data not shown), as is frequently the case in temperate coastal environments. Since the catchments are relatively short, events of high input of nutrients from increased river, stream and surface runoff are therefore likely to coincide with both increased mixing and direct sediment resuspension caused by wind generated waves (Corbett, 2010). A more detailed passive tracer hydrodynamic modelling study analysing typical precipitation and wind events could show to what extent this leads to increased horizontal transport and subsequently flushing of nutrients from the harbour. Ideally, a coupled hydrodynamic-biogeochemical model should be used to include benthic-pelagic fluxes of nutrients in addition to watershed-estuary fluxes and examine their respective contributions (Arhonditsis et al., 2002). Beyond that, event-driven sampling of water column nutrients during and after high-rainfall events from rivers entering the estuary out to the tidal mixing plume outside of the harbour entrance would help to quantify the influence of changes in the properties of short-term extreme events compared to potential trends in the more frequently encountered moderate conditions (Verity, 2002).

4.4.3 Passive tracer transport modelling

Shallow, tidally-dominated estuaries are frequently characterised by networks of meandering channels (van Maanen et al., 2013), which pose unique challenges to the application of numerical hydrodynamic models. In the hydrodynamic model setup used for this study, the shallow regions are generally more problematic due to the fact that the calibration and validation of Tay et al. (2013) was focused on deeper areas. In some areas, for example the narrow meandering channel in Hunter's Creek / subregion 4, the horizontal and vertical discretisation leads to overly sharp drop-offs and "holes". For example, depth may increase from +0.5 m to -1.2 m from one grid cell to the next and subsequently decrease again a few grid cells further along the axis of tidal flows. Whether based on natural features or artefacts of the bathy-

metric data processing (McGrath et al., 2007), the corresponding flow behaviour in the discretised model seems unrealistic. Examination of time series of the 2D fields of vertically integrated tracer mass (data not shown) suggests that water bodies may become "trapped" in these features. Although the influence on larger-scale velocities and water levels is negligible, this trapping of tracer is likely to markedly increase retention of tracers where such bathymetry features are common. The straightforward solution to this problem is an increase in spatial resolution either for the entire uniform grid or the use of a non-uniform grid. Alternatively, a detailed examination and possibly improvement of how such high gradients in the bathymetry are handled in the hydrodynamic model could be considered.

Defining high or low tide injection times that will lead to comparable results for all subregions is difficult due to the large tidal phase shift within the harbour. For example, examination of the time series of 2D fields of vertically integrated tracer mass (data now shown) reveals that at the chosen high tide injection time, the tide is already going out at the border between subregion 3 and the downstream subregion 6, while it is still coming in at the border between subregion 3 and the upstream subregion 1.

The two consecutive peaks observed for subregion 3 are most likely due to tracer advected further upstream into subregion 1, which then re-enters subregion 3 early on the outgoing tide. There is no obvious explanation for the similar pattern appearing for subregion 4, since there should be no further upstream subregion, but a similar mechanism may be in action here due to the unclear delineation of the watershed in the very shallow area between subregions 4 and 3, which in fact connects only during above average high tide water levels. Uncertain watershed boundaries ("topographic flow divides") are common in intertidal areas, where water is often exchanged between watersheds at high tide levels (Novakowski et al., 2004). A similar problem arises around the branched and meandering outflow of the Wairoa River in subregion 5 towards subregions 3 and 6, which makes it difficult to exactly delineate the most sensible boundaries between these subregions for the desired analysis.

In the current implementation, freshwater inputs do not carry any tracer. When analysing contributions of tracer from different upstream subregions, for example at the harbour entrance, such inputs will consequently appear simply as dilutions. Since the average total volume of freshwater inputs to Tauranga Harbour is relatively small, this is unlikely to have a large effect, especially not for the first tidal cycle after a high tide tracer injection. Nevertheless, differences in tracer contribution especially for the smaller subregions with similar volume but large differences

in freshwater inputs (especially subregions 2, 5 and 7) cannot be ruled out. To analyse this difference, an improved implementation could assign an additional tracer to each subregion's surface freshwater inputs, distinct from that injected once into the subregion volume.

A somewhat similar issue arises at the open boundary towards the coastal ocean, where tracers may leave the model domain, but the incoming water volume has no tracers assigned. The total mass of tracers could be balanced by keeping track of all tracers lost at the open boundary, and assigning corresponding concentrations to the water volume entering the domain again at the same boundary. This would imply that no mixing is taking place outside the model domain, i.e., the ebb tidal plume re-enters the model domain without having been diluted by the coastal ocean water body. This assumption could at least be relaxed by assuming a fixed mixing ratio, so that concentrations of tracer re-entering the domain are diluted by coastal ocean water at a fixed ratio. Alternatively, the model domain could be extended seaward up to a point where the influence of the tidal plume is negligible, but due to the high horizontal velocities of the ebb tidal plume, this would require a much larger domain than in the current implementation. In this case, an unstructured grid would be especially well suited since the velocities in this outer part of the model domain would be much lower than in the estuary itself, so that high accuracy could be achieved even with much lower local grid resolution than in the current implementation.

Tay et al. (2011) observed marked differences between sites in the change of nutrient concentrations over a tidal cycle. For example, nitrate concentrations at a winter sampling date showed an increase before, plateau at and decrease after low tide with a smooth change in slope resembling a sinusoid at a site near S2, but in contrast an almost exponential increase until low tide, lack of plateau and discontinuity in slope at a site near S7. This kind of difference in behaviour between sites could be examined with a refined implementation of the hydrodynamic model, requiring higher horizontal resolution to resolve the flooding and draining through the constricted channels at these sites, which in the current implementation introduce flow restriction artefacts due to low grid resolution and orientation in these channels.

4.4.4 Nutrient sampling strategy

Our results highlight the critical importance of timing when collecting nutrient samples in tidally-dominated estuaries. Apart from site locations, another major difference between the previously available, historical as well as ongoing monitoring

samples on one hand and the survey and fortnightly samples collected in this study on the other hand is exactly this timing. For the first, there is a high variation in local M2 phase at the time of sampling, while for the latter this was minimised. The passive tracer transport modelling confirmed that even small changes in local M2 phase can have a large influence on the composition of the water body and consequently the nutrient spot sample.

The decision to take samples at mid-tide was based on the assumption that due to the high horizontal velocities at this point in the tidal cycle, the confounding influence of horizontal heterogeneity (especially patchy distribution) in nutrient concentrations could be minimised. Although this influence could not be quantified due to the lack of simultaneous sampling, visual observations of the surface currents during the sampling process do indicate high rates of horizontal mixing at most sites at this time in the tidal cycle. Exceptions do exist, such as sporadically occurring fronts on the outgoing tide at S3 (convergence of two upstream channels), and on the incoming tide at S7 (changing contributions of the downstream channel in comparison to the adjacent shallow tidal flats to the northwest). Such fronts were indicated by foam and scum lines on the water surface, and are most likely caused by a combination of temperature and salinity differences between several upstream waterbodies. Overall, given the constraint of having only a single boat available and aiming to sample at similar local tidal phase at all sites, the current timing and extent (six to eight sites) is an efficient strategy to examine both net fluxes as well as differences in average concentrations between subregions from the same set of samples. A mix of sites accessible by boat and from land seems optimal, so that those sites accessible from land may either be sampled more frequently or simply aid in keeping sampling times within the desired short time windows of local M2 tidal phase by being sampled concurrently by a second team.

Analysis of modelled mid-tide tracer concentrations at the nutrient sampling sites indicate that the relative contributions of different upstream subregions vary quickly at this time of the tidal cycle. Decreasing the influence of spatial variability by sampling at mid-tide, when both vertical and horizontal mixing is intense, may thus increase the influence of small changes in sampling time which are often unavoidable. This trade-off could maybe be examined further using a refined implementation of the hydrodynamic model, but requiring higher spatial resolution to resolve the horizontal heterogeneity in nutrient concentrations, especially where sampling sites are located in narrow tidal channels in close vicinity to intertidal flats. The results also show that even within a relatively small time window such as 30 minutes around a “target” or optimal sampling time at mid-tide, large changes

in the relative contribution of different upstream subregions may occur that ideally should be taken into account when comparing samples from different dates. This is especially relevant when, as in the present study, a number of sites are sampled in sequence from a single vessel, so that possible delays will add up and make a sample from a later local M2 phase more likely to occur at the last sites.

The number of potential upstream contributions to a site naturally increases in the downstream direction until reaching the harbour mouth. For the case of sites with several upstream subregions, in this study sites 6 (harbour entrance) and 3 (central deep channel approximately 5km upstream), the model results also clearly show that due to the high tidal currents, a single downstream sample taken at mid-tide will in most cases give a mixed signal from several upstream water bodies instead of just one. Care must be taken when interpreting these data, but results from passive tracer modelling could help in determining upstream concentrations based on the relative contribution of each water body at the time of sampling.

For the calculation of net fluxes, a critical assumption is that both the ebb and flood samples are equally representative for the corresponding entire outgoing or incoming tide when taken at mid-tide. Tay et al. (2011) examined hourly samples over two tidal cycles at two sites in Tauranga Harbour close to S2 and S7. Although their results do not indicate a systematic asymmetry in the temporal change in nutrient concentrations between the ebb and flood tide, they do show the most rapid changes in concentrations around mid-tide, similar to the modelled changes in tracer contributions in this study. This emphasises the need for consistent timing based on the tidal phase both between consecutive ebb and flood samples as well as between sampling dates. It is crucial that the local tidal phase at each sampling site is determined to avoid spurious differences in net fluxes between sites. Furthermore, small but possibly systematic asymmetries between the evolution of nutrient concentrations for ebb and flood tides still cannot be ruled out. This issue could be examined further with tracer modelling, in which case especially the constricted channel geometries between sub-estuaries and the main harbour would probably require higher horizontal resolution, possibly indicating the use of an irregular horizontal grid.

4.4.5 Conclusion

Based on one year of approximately fortnightly samples at two sites, we have estimated probability density functions (PDFs) for inorganic N and P nutrient fractions. PDFs are highly variable in shape both between fractions and between sites, but might best be approximated and parameterised by gamma distribution functions. Average annual ebb/flood ratios show downstream export at both sites on an

annual time scale, but frequent fluctuations between import and export on shorter time scales, indicating the possible relevance of sporadic events. A seasonal shift towards export in summer is most pronounced for NH_4^+, less for NO_3^- and not apparent for PO_4^{3-}. The inorganic N/P ratio shows a seasonal signal for an upstream subregion, with winter values regularly exceeding 16:1 and in many cases also 30:1, while at the harbour entrance, a clear seasonality is not apparent, and the N/P ratio only rarely exceeds 16:1. Approximately bimonthly samples taken at eight sites indicate high variability between subregions within the harbour, both in terms of nutrient concentrations and resulting mass fluxes, but the small sample size does not allow for a clear comparison between all subregions. Passive tracer transport modelling shows that the contribution of distinct upstream waterbodies to a nutrient sample taken at mid-tide varies quickly, emphasising that to obtain nutrient samples that are comparable between sites and dates, the local dominant tidal phase must be taken into account.

4.A Appendix: sites 6 and 7 PDF plots ebb vs. flood

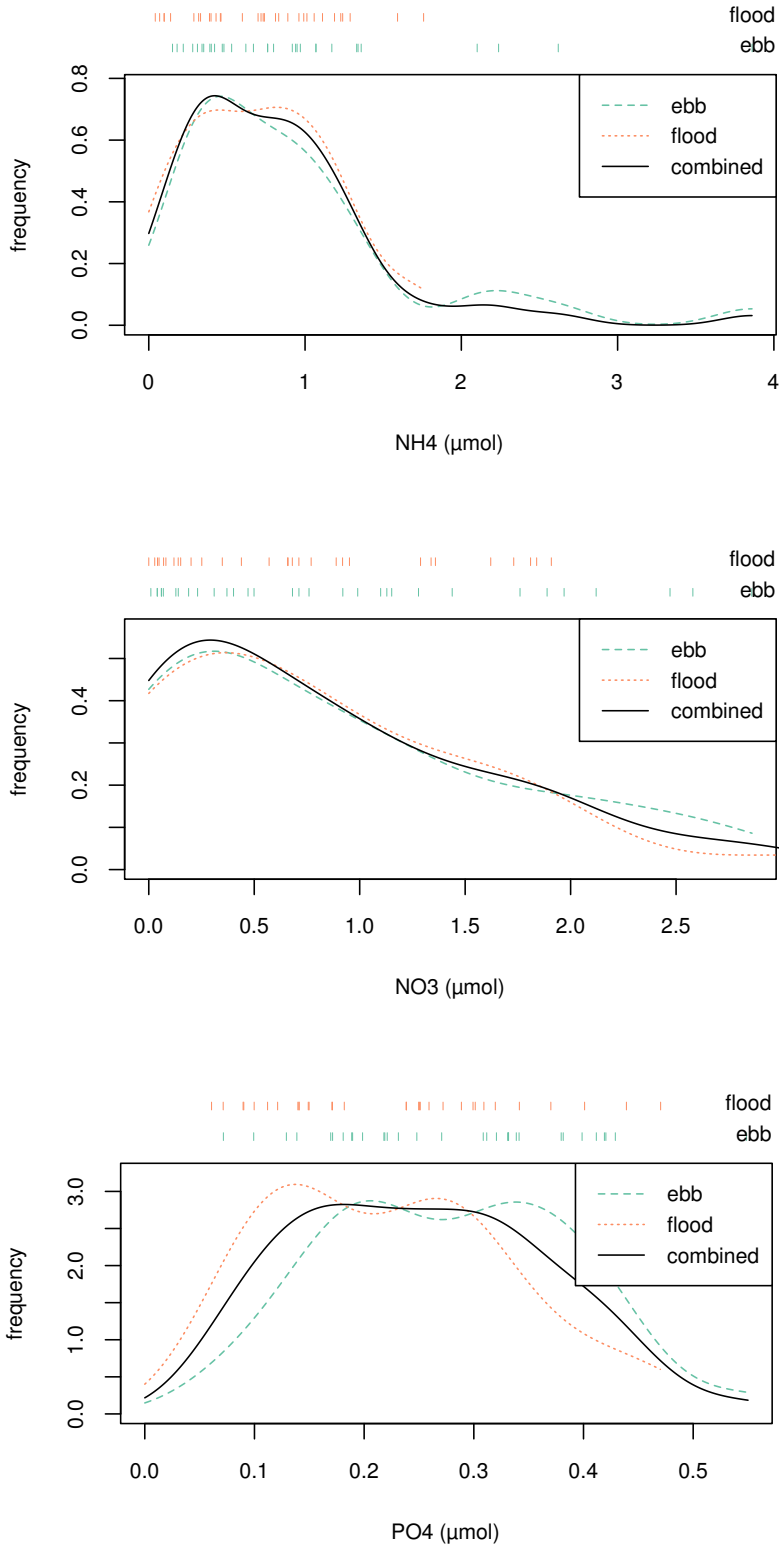

Figure 4.20: Probability density function (PDF) estimates for NH_4^+, NO_3^- and PO_4^{3-} based on fortnightly samples from site 6, ebb vs. flood tides. PDFs were estimated as in Figure 4.3.

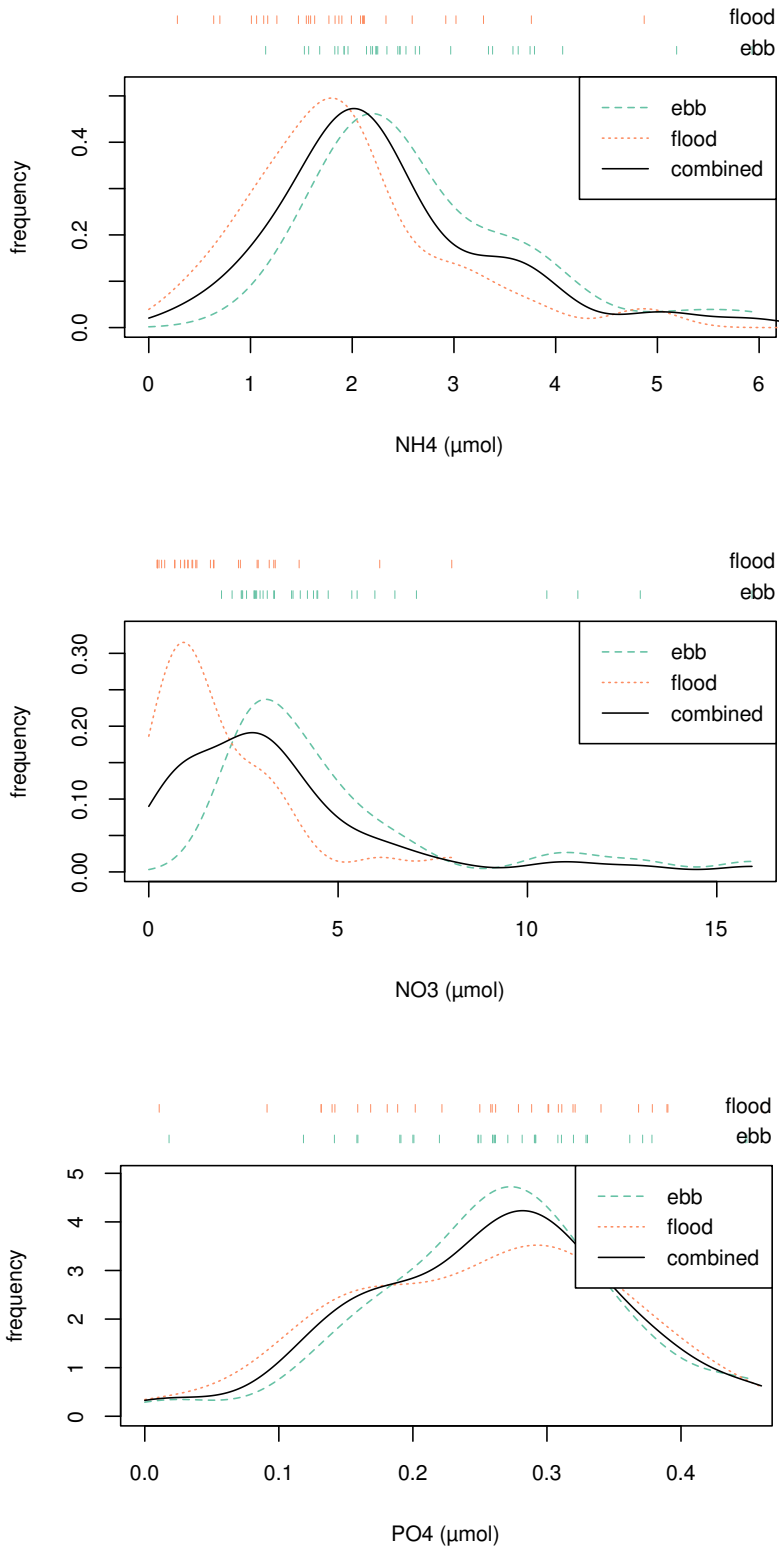

Figure 4.21: Probability density function (PDF) estimates for NH_4^+, NO_3^- and PO_4^{3-} based on fortnightly samples from site 7, ebb vs. flood tides. PDFs were estimated as in Figure 4.3.

4.B Appendix: ebb and flood bar plots for all sites

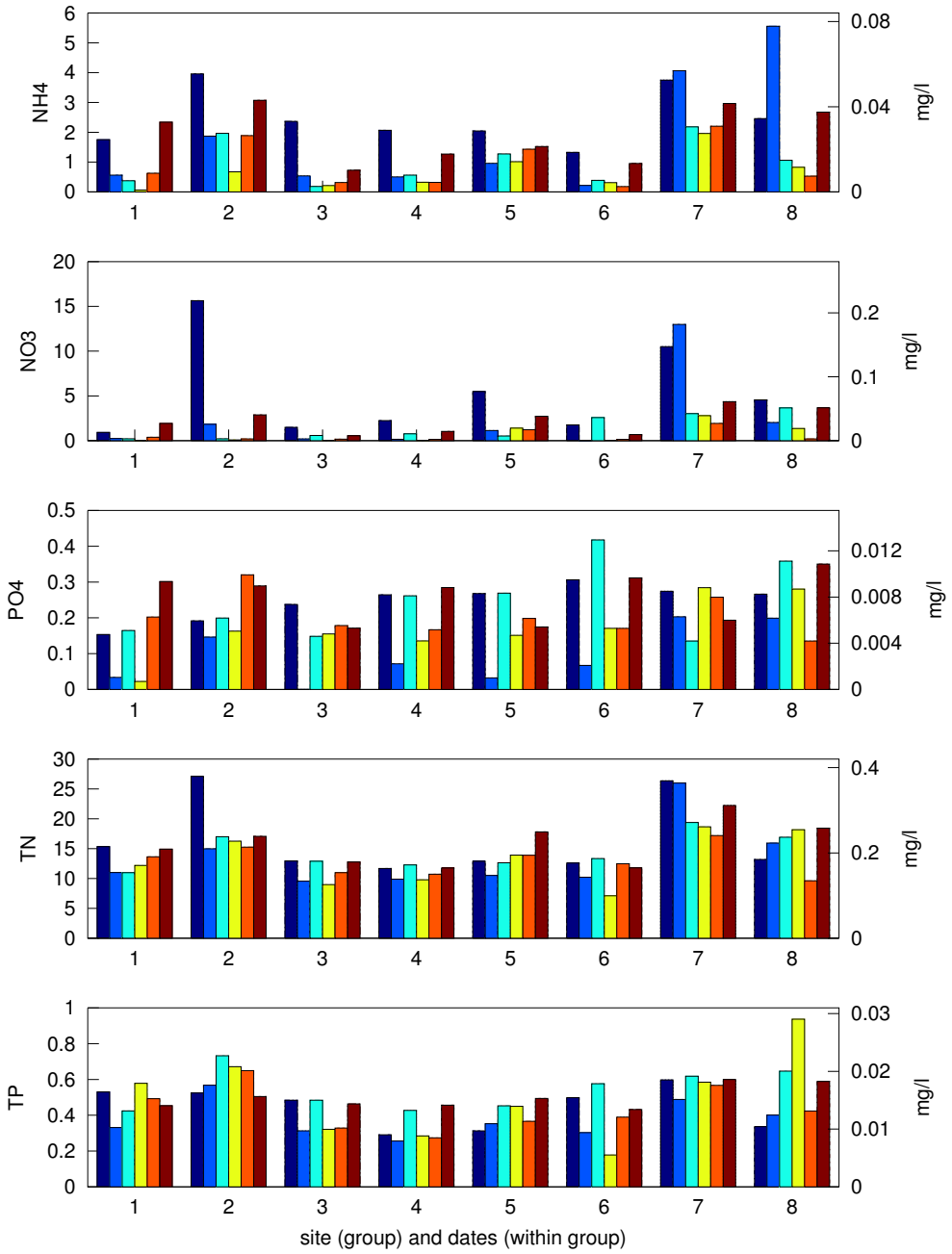

Figure 4.22: Outgoing / ebb tide water column nutrient concentrations at 8 sites over 6 approximately bimonthly sampling dates from southern hemisphere winter to winter. Each group (1-8) of bars shows data from one site, and each bar within a group data from a single date (from left to right: 2012/07/18, 2012/09/27, 2012/12/12, 2013/02/08, 2013/04/08, 2013/06/06).

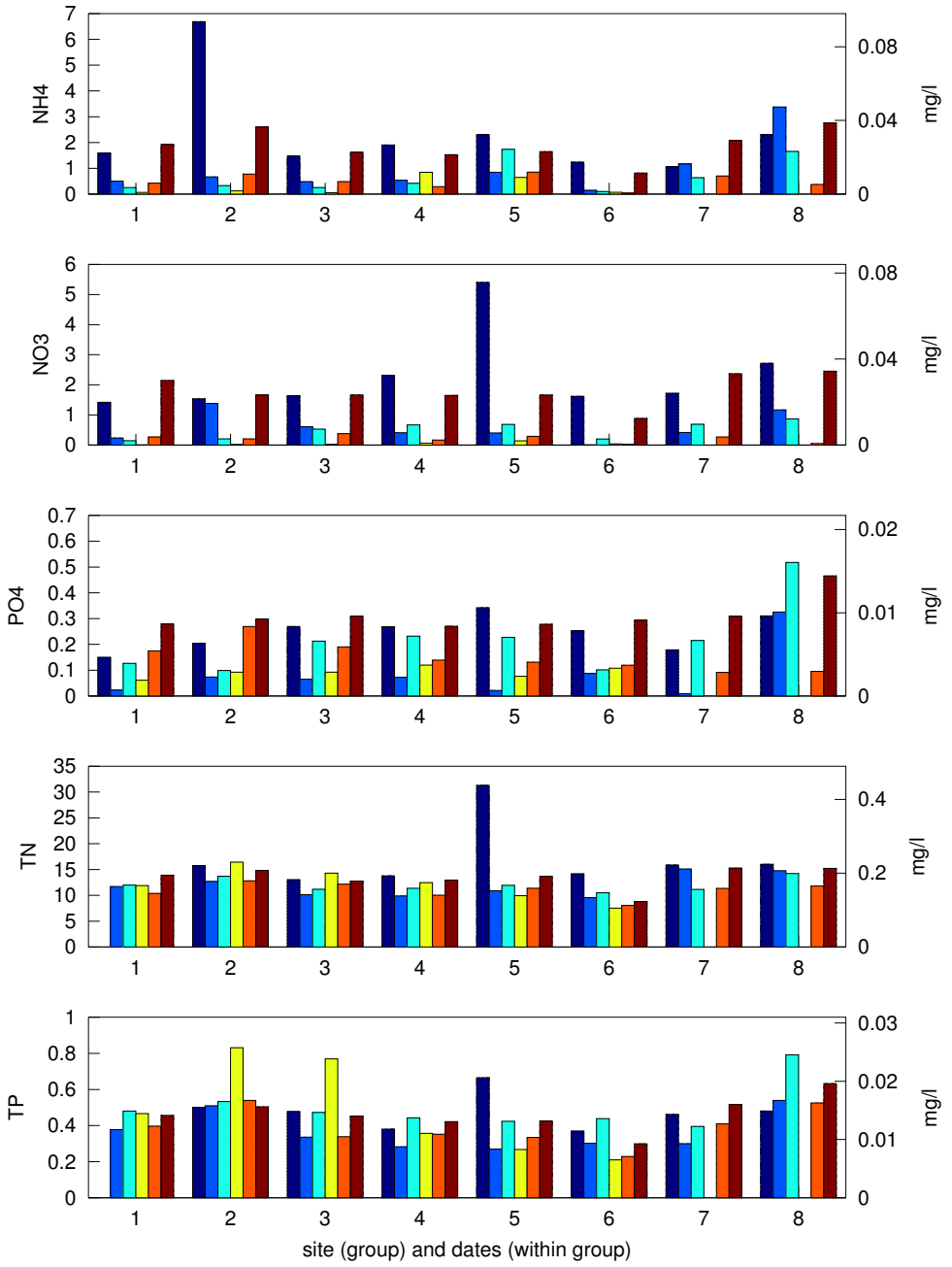

Figure 4.23: Incoming / flood tide water column nutrient concentrations at 8 sites over 6 approximately bimonthly sampling dates from southern hemisphere winter to winter. Each group (1-8) of bars shows data from one site, and each bar within a group data from a single date (from left to right: 2012/07/18, 2012/09/27, 2012/12/12, 2013/02/08, 2013/04/08, 2013/06/06).

Chapter 5

General discussion

5.1 Summary of findings

In Chapter 2, we presented an algebraic short-term equilibrium solution for *Ulva* tissue nitrogen quota dynamics, derived from the ordinary differential equation form of a classic *Ulva* growth model using a computer algebra system. The low computations cost of using the derived equilibrium solution in contrast to the numerical integration of the system of ordinary differential equations allowed us to apply sensitivity analysis and calibration algorithms requiring a large number of model evaluations. The global Sobol' sensitivity analysis showed that the tissue nitrogen quota is influenced to the same order of magnitude by the dominant environmental forcing variables (especially dissolved inorganic nitrogen fractions) as by the uncertainty in physiological model parameters. Accurate measurements of the environmental conditions, especially inorganic nutrient fractions, are therefore equally important as accurate estimates and ranges of the physiological parameters. While the former were subsequently provided by dedicated fieldwork and are described in Chapter 4, the latter would have to be addressed using detailed laboratory studies which are outside the scope of this thesis. Repeatedly running calibration algorithms with a random component on the same datasets resulted in broad and in some cases multimodal distributions for some model parameters. A single calibration deemed "successful" in terms of model performance should therefore not be relied upon to give a realistic estimate of the system's (in this case physiological) properties.

A zero-dimensional, dynamic simulation model of *Ulva* tissue nitrogen quota, tissue phosphorus quota and biomass was reimplemented in Chapter 3 to determine which of the environmental forcing variables are likely to control the development of seasonal blooms. Continuous simulations over a period of 14 years proved stable and were able to reproduce major patterns in both biomass and tissue nitrogen

quota at the same time, but underestimated the seasonal variability in tissue phosphorus quota. Different calibration approaches using data from either individual state variables or a combination of all three led to variations in model output for those state variables as well as for the uncertainty in calibrated parameter values. A calibration aimed at minimising the normalised sum of the cost functions of all three state variables was chosen as the best compromise. To derive realistic seasonal scenarios representing years of above and below average conditions in the environmental forcing variables, we fitted annual cosines to the 5th ("low") and 95th ("high") percentiles of historical observation data aggregated in monthly bins. Scenario simulations calculated for average, high and low conditions of each of the environmental forcing variables point to NH_4^+ and NO_3^- having the largest influence both on peak biomass of a seasonal bloom as well as the timing of its occurrence, while PO_4^{3-}, temperature, irradiance and turbidity had much smaller effects.

Both Chapters 2 and 3 showed, among other things, that accurate observation data of the inorganic water column nutrients are crucial for any application of an *Ulva* growth model. Although monitoring data of these nutrients is available for Tauranga Harbour, the existing data were collected only at sites close to shore and and with at highly variable times of the local tidal phase. To address these issues, a one-year survey programme was designed and the fieldwork carried out to collect nutrient data at a number of sites representative for distinct subregions within the harbour, and always at mid-tide of two consecutive ebb and flood tides. Approximately bimonthly samples taken at eight sites throughout the harbour indicated substantial differences in ambient concentrations between subregions, but the small sample size prevented a conclusive interpretation. Fortnightly samples taken at the harbour entrance showed significantly higher concentrations of PO_4^{3-} on the ebb compared to the flood tides. Fortnightly samples taken at a second site further upstream, in contrast, showed this behaviour for NH_4^+ and NO_3^-, but not for PO_4^{3-}. Probability density function estimates were derived from the fortnightly data and showed clear differences between nutrient fractions, sites and tides. For comparison and further use, these different estimates might best be described by two-parameter gamma distribution functions. To examine the influence of small changes in the timing of samples taken during an ebb or flood tide, we simulated the transport of passive tracers representing water column nutrients using a hydrodynamic model. Simulations showed that especially around mid-tide, the contribution of different upstream water bodies may change rapidly at a sampling site, emphasising the need to standardise the sampling time relative to the local dominant tidal phase. Subregions within the harbour also showed different degrees of connectivity, and

sometimes counter-intuitive mid-term upstream transport of waterbodies entering the main harbour at a point relatively far downstream. This behaviour is likely to be common in estuaries with a complex geometry such as Tauranga Harbour, and passive tracer hydrodynamic modelling could help both in the design of and interpretation of data collected in nutrient monitoring programmes.

5.2 Conclusions

Of the environmental factors for which historical observation data are available (inorganic nitrogen and phosphorous concentrations in the water column, temperature and irradiance), the inorganic nitrogen concentrations dominate the modelled development of seasonal *Ulva* tissue nutrients and biomass accumulations (blooms) in Tauranga Harbour. The relatively simple, zero-dimensional growth model implemented and applied in Chapter 3 paves the way for scenario analysis of future developments or management options. Although the description of tissue phosphorus quota dynamics still leaves room for improvement, research progress is currently unlikely to be limited by the lack of applicable models. Rather, this research highlights the importance of comprehensive and accurate, long-term observation data on *Ulva* abundance (or preferably biomass), environmental forcing variables (especially nutrients), and well-constrained estimates of the physiological parameters of *Ulva* growth.

5.3 Suggestions for future research

For routine monitoring of low intertidal and especially subtidal *Ulva* abundance, the "dropcam" employed in this study is a cheap and simple option, but requires substantial time to record images from only a few stations along each transect. This is in part due to the difficulty of settling the dropcam frame on the seafloor from a boat that is usually still moving slightly, even if actively driven against any current present. Alternatively, a digital camera mounted on an underwater towed or remotely controlled platform that never touches the seafloor could be used for faster, routine monitoring e.g., Morris et al., 2014. Knowledge of the exact distance from the seabed would not even be required to determine the percentage of cover, but if desired, an absolute length scale could be determined from parallel laser beams mounted on the glider and visible on the seafloor in the pictures obtained, as routinely used in AUV/ROV applications. Artificial lighting would be advantageous, and could especially simplify the development of image processing algorithms to

determine percentage of cover from a large number of images automatically.

An extensive spatial sampling of *Ulva* tissue for genetic analysis could help determine the number of genotypes actually present in Tauranga Harbour (building on the findings of Heesch et al., 2007). Preferably, sampling should occur at different seasons, since it is likely that the relative contribution of individual species to the total abundance (and therefore also the probability of sampling individual species) will vary between seasons (Guidone and Thornber, 2013). Subsequently, the variability between the observed genotypes in terms of the physiological parameters included in growth models should be examined by laboratory experiments to determine whether a single-species model approach is justified, or whether a multi-species approach should be taken instead.

Recent advances in hyperspectral remote sensing have made it possible to differentiate between groups of macrophytes (Abrams et al., 2002). Satellite or low-altitude aerial acquisition could provide spatial abundance data on both benthic macroalgae (e.g., *Ulva* spp.) as well as spermatophytes (e.g., *Zostera* spp. Limited coverage, resolution and in the case of some sensors also spectral resolution remain a problem (Alexander et al., 2008), and accurate determination of absolute biomass becomes difficult with increasing percentage of cover. Nevertheless, relatively successful classification of macroalgae cover has been reported (Karpouzli and Malthus, 2006), and should be explored further.

One of the marked differences in the process descriptions between the two models used in Chapters 2 (based on Solidoro et al. (1997)) and 3 (based on Guimaraens et al., 2005) is the influence of temperature on growth. Solidoro et al. (1997) use a sigmoid formulation, which saturates and therefore does not produce an inhibition at very high temperatures, while Guimaraens et al., 2005 use a Gauss formulation, which has clear optimum at intermediate temperatures and then inhibits growth as temperatures rise further. In Tauranga Harbour, water temperatures are relatively high in summer, especially so in the large shallow areas of most of the upstream subregions. A more detailed analysis could compare these two formulations and determine whether that chose by Guimaraens et al., 2005 is indeed a better choice.

In addition to absolute biomass, the *Ulva* growth model could be extended to account for the life stage and possibly general size structure within the population (e.g., Martins et al., 2008). The observation data necessary for calibration and validation of this additional variable are easily obtained from manual measurements, either on samples collected from the supra- and intertidal at low tide or from cage-mounted nets in the subtidal, or from digital camera images of the seafloor. Although the fragmentation of large tissue pieces is a complex process,

The growth model used in Chapter 3 could be improved by in addition to tissue nitrogen and phosphorus also incorporating tissue carbon as a state variable (e.g., Ren et al., 2014). The atomic ratios of carbon to nitrogen and phosphorus may be more reliable indicators of nutritional state than those of nitrogen and phosphorus to dry weight. The incorporation of carbon as a state variable would also facilitate the coupling to a biogeochemical or any other closed mass-balance model in which carbon is likely to be traced.

Several slightly different mathematical descriptions of tissue nitrogen and phosphorus quota dynamics have been published and implemented in *Ulva* growth models, but currently there seems to be a lack of consensus on a single, best description. A multi-model study could compare these descriptions by applying all of them to multiple datasets from laboratory and field observations. Comparisons should be restricted to the smallest sub-models in which differences in performance and transferability are likely to be observed, to minimise the potentially confounding influence of differences in other sub-models (e.g., mortality). To facilitate this, both observation data and "ready to run" implementations of the relevant model code such as those presented in this study should be made freely available.

The transport of *Ulva* could be further examined using a hydrodynamic model that includes resuspension, advection and settling of macrophyte tissue pieces (Salomonsen et al., 1999; Oldham et al., 2010; Pattiaratchi et al., 2011). Even without a coupling between growth and transport models, this could help to evaluate the current intertidal *Ulva* abundance monitoring sites, and potentially choose more diverse or representative sites.

Regular nutrient sampling at the harbour entrance at a constant local tidal phase seems the most valuable approach to further our understanding of the short-term to seasonal nutrient dynamics in Tauranga Harbour. The sampling frequency should be at least monthly, but if possible close to every five to ten days to increase the chance of observing the influence of episodic events.

Ideally, nutrient sampling within the estuary would be complemented by regular offshore sampling to quantify the influence of changes in offshore concentrations of nutrients caused by mesoscale circulation patterns such as seasonal upwelling. If resources are insufficient to carry out dedicated regular surveys, sampling from private (e.g., recreational) or commercial (e.g., ferries or fishing charter boats) "ships of opportunity" should be considered. Alternatively, if the degree of mixing of the tidal plume with the coastal ocean waterbody can be determined using a numerical hydrodynamical model, offshore nutrient concentrations could also be estimated from the ebb/flood balance of concentrations at entrance. To this end, full tidal cy-

cles at for example hourly intervals should be sampled first at the harbour entrance to ensure that individual mid-tide samples are sufficiently representative.

For the nutrient data presented in this thesis, reliable error estimates for individual data points were not available. Although replicate samples were taken, initial difficulties with the automatic wet-chemical analysis led to a loss of samples, significant delays in the processing and higher than initially estimated costs, so that limited available sample volume as well as funding prohibited the analysis of replicate samples. Replicate samples should ideally be analysed for at least a regular subset of samples, and this tradeoff between data volume and data quality must be kept in mind when planning an improved nutrient sampling design.

Regular comprehensive sampling of all distinct subregions within Tauranga Harbour is very labour- and cost-intensive, and unlikely to be feasible for any extended period of time. A coupled watershed-estuary nutrient model would help by providing nutrient input estimates for smaller tributaries which are not regularly sampled, and work supporting the development of such a model for Tauranga Harbour has already been carried out (Morcom, 2013; Monahan, 2014).

Appendix A

Macroscopic characteristics of drifting *Ulva* populations

Drifting *Ulva* biomass was determined both in terms of the absolute amount of unattached *Ulva* spp. present in the water column as well as the horizontal transport of this material. For this purpose, cage-mounted nets were deployed at site 7 of the nutrient sampling programme, in a constricted channel connecting the Waikareao sub-estuary to the main Tauranga harbour.

A first cage built to collect drifting macrophytes was constructed from welded steel bars, in three separate but stackable layers of 100 cm width by 100 cm length by 30 cm height (Figure A.1). It was designed to be deployed both as a vertical stack of three layers with just under 1 m height in total, as well as three separate individual cages, e.g., at three sites along a cross-channel transect simultaneously. Although deployed successfully twice, this design proved rather heavy, bulky and unstable. Additionally, the simultaneous deployment of individual sections along a cross-channel transect was deemed impractical after first field tests, given the very limited time available around slack water in which they could be deployed and retrieved safely. It was therefore replaced by a second cage constructed in one piece and from aluminium tubes.

The second rigid metal cage holding four vertically separated nets (mesh width 4 mm) was built to improve on the first design, especially in terms of ease of deployment. The cage's outer dimensions are approximately 120 cm height by 100 cm width by 100 cm depth, each net's dimensions are approximately 30 cm height by 100 cm width by 100 cm depth (Figure A.2). The cage with the nets was anchored so that the nets' open sides were oriented perpendicular to the channel. Each deployment lasted from either a low tide to the next high tide (outgoing / "ebb" samples) or from a high tide to the next low tide (incoming / "flood" samples). More frequent

Figure A.1: The first cage constructed to collect drifting macrophytes (three separate but stackable layers, steel bars, welded).

emptying of the nets was not practical due to the high current speeds at the site.

Figure A.2: The second cage constructed to collect drifting macrophytes (one rigid outer frame with space for one to four vertical layers of nets, aluminium tubes, modular screw-fixed fittings/joints).

As expected for tissue that on its own is usually slightly negatively buoyant, the amount of drifting *Ulva* biomass in most cases decreased with distance from the seafloor (Figure A.3).

To save time when determining *Ulva* biomass from bulk samples taken in the field, a "spin-drying" method was trialled. When weighing bulk samples in the field, especially those taken from submerged nets / cages, it is difficult to judge how much excess water should be removed before weighing the "wet" weight. Ideally, bulk wet weight could be determined in the field after spin-drying, and only a small subsample retained for dry weight determination in the laboratory. The amount of weight lost by spin-drying (i.e., the "dripping" wet weight to spin-dried wet weight ratio, not to be confused with the wet weight to dry weight ratio) on site (spinning samples at arm's length in a mesh bag) varied from close to 0% to up to 60% for small samples, but stayed within the range of 10% to 30% for samples with a total weight of over approximately 2 kg (Figure A.4). Larger samples were separated into sub-samples of a maximum wet weight of approximately 4 kg for spin-drying. For future uses of this dataset that require accurate dry weight values, subsamples were taken and the wet weight to oven-dried weight ratio determined in the laboratory (data now shown).

Drifting *Ulva* biomass caught on the ebb tide was less than on the flood tide on 5 out of 6 dates (Figure A.5). Visual observations from a bridge slightly upstream of the sampling site did not indicate large cross-channel variation in the overall density of drifting *Ulva*.

Subsamples were frozen for laboratory analysis of the macroscopic tissue properties of size, sporulation and degradation. In four out of five cases where ebb and flood samples were available from the same date, median tissue size was clearly larger on the flood than on the ebb tide (boxplots in Figure A.7; beanplots in Figure A.8). Tissue size showed a fairly strong seasonal signal in the 2012/2013 season, with larger tissue sizes during the summer months and steadily decreasing towards winter, although this seasonal trend was not apparent when comparing 2012/04 with 2012/07. High degrees of sporulation were rare, but were encountered slightly more often in the warmer months (Figure A.9). Degradation clearly increased from 2012/07 with almost 50% with no visible degradation to over 80% with visible degradation in 2013/02, and still over 70% in 2013/06 (Figure A.10). Although in some cases, the degradation pattern did differ substantially between consecutive ebb and flood tides, there was no clear overall pattern (Figure A.11). It should also be noted that the visual estimation of the degree of degradation is by far the most subjective macroscopic property examined here. Since samples were

processed in batches corresponding to individual tides and dates (in contrast to randomised processing), it is quite possible that part of the variability in the data stems from changes in the visual estimate of the degree of degradation, not the actual degree of degradation itself.

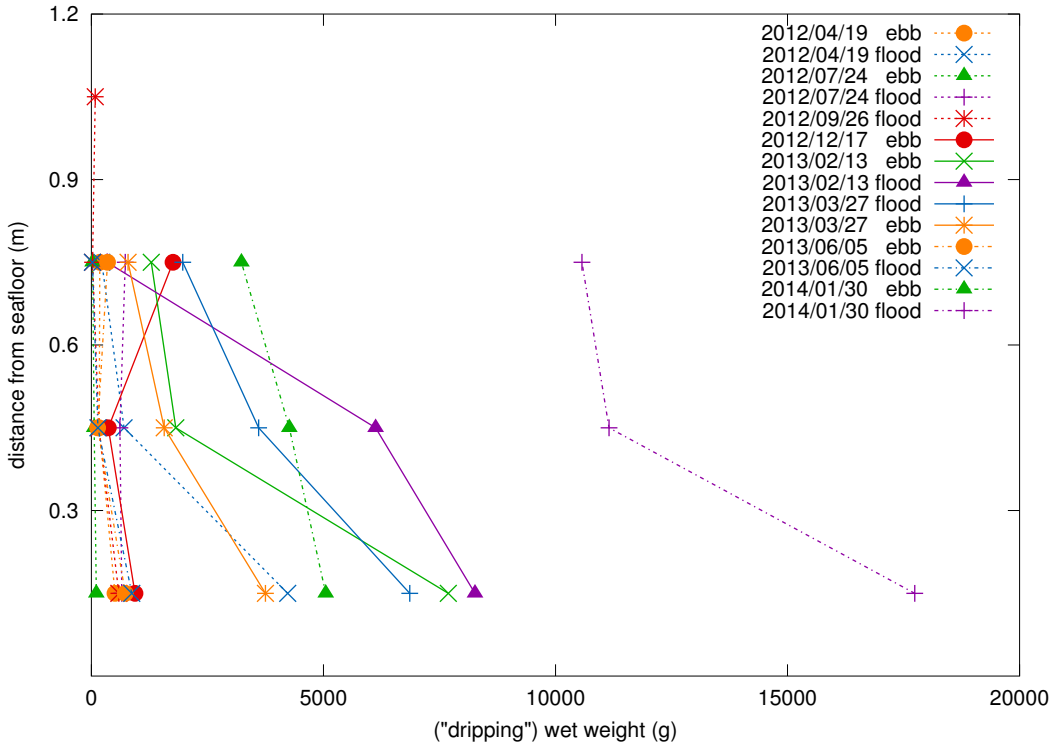

Figure A.3: Vertical distribution of drifting *Ulva* spp. biomass caught in 4 nets (height x width x depth: 30 cm x 100 cm x 100 cm) mounted in a rigid cage at the entrance of Waikareao estuary, with the open sides oriented perpendicular to the channel length.

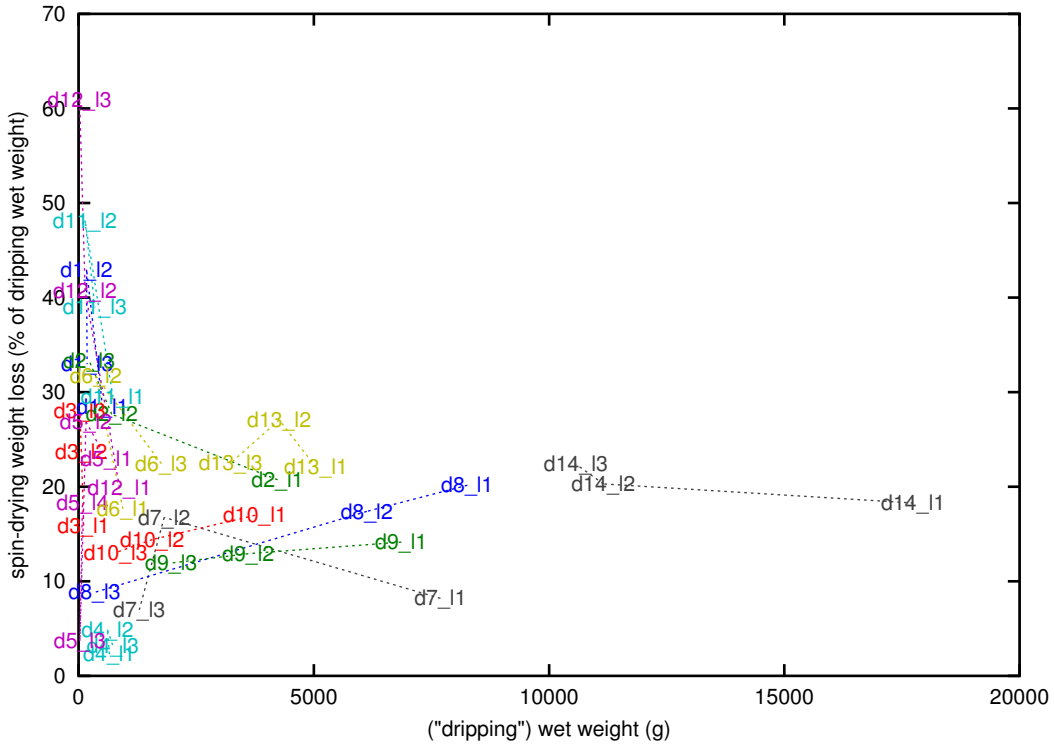

Figure A.4: Loss of weight by spin-drying of *Ulva* spp. samples caught in cage-mounted nets, in percent of ("dripping") wet weight. Data points are labelled with sample date index and (vertical) net layer, 1 being the bottom layer (e.g., "d1_l3" is the sample from the first date from the third layer).

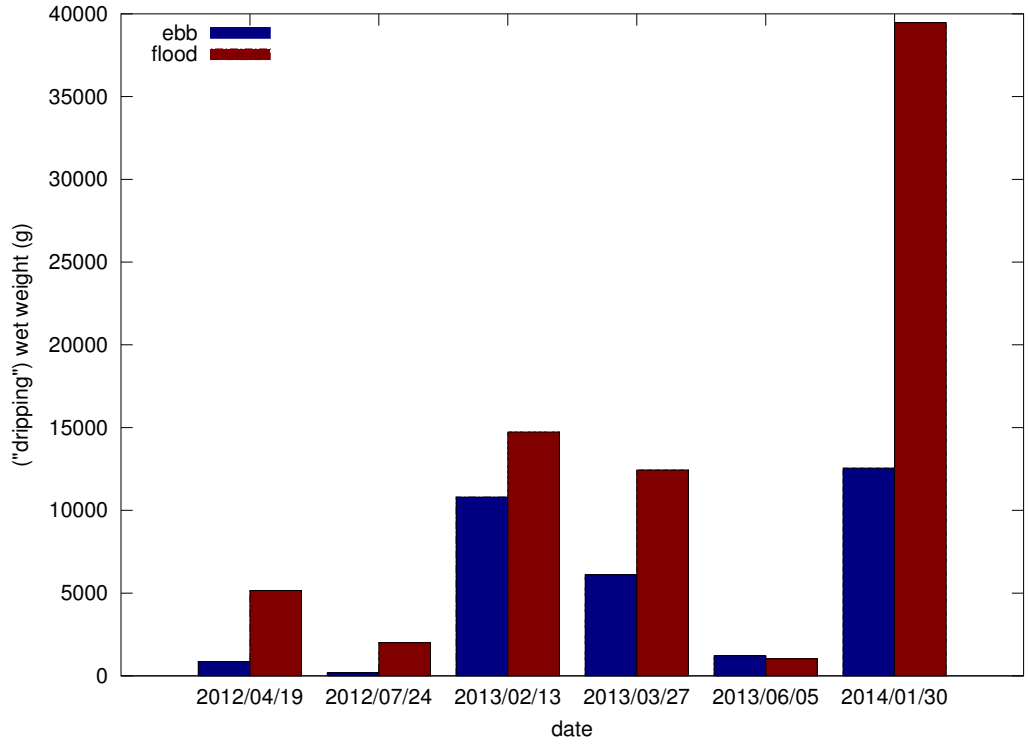

Figure A.5: Drifting *Ulva* biomass ("dripping" wet weight) caught on the ebb and flood tides (only shown for dates where both tides were sampled).

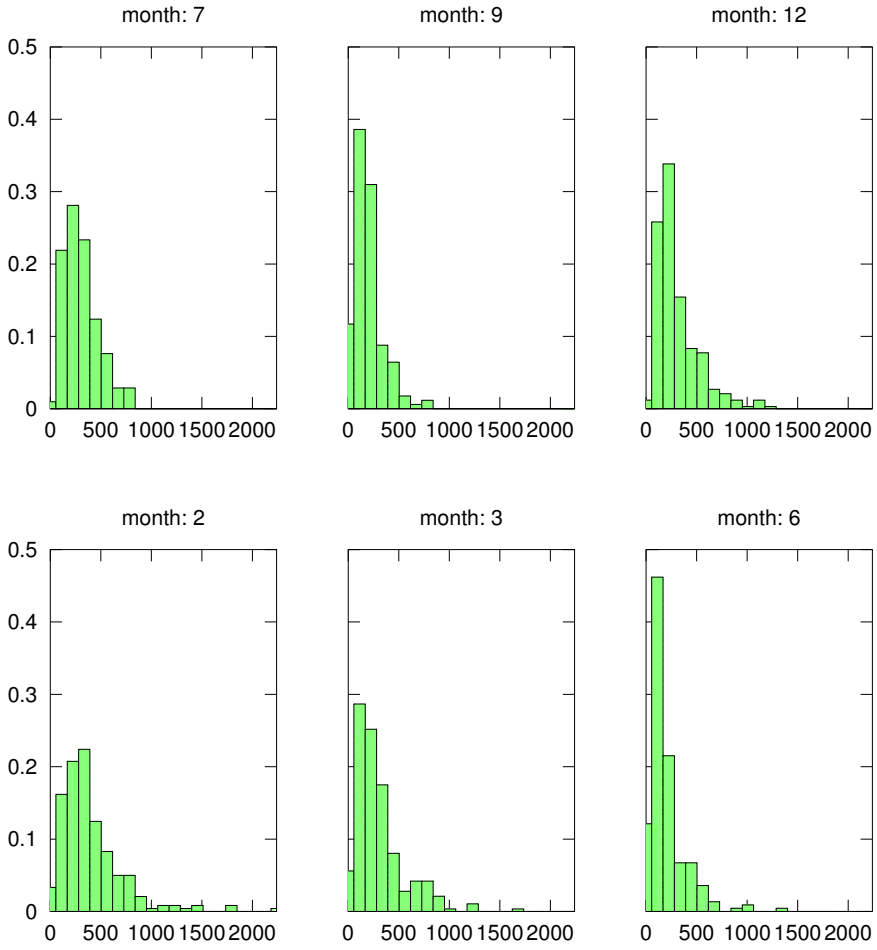

Figure A.6: Histograms of drifting *Ulva* thallus sizes (semi-major axis of enclosing ellipse) for the approximately bimonthly surveys between 2012/07 and 2013/06.

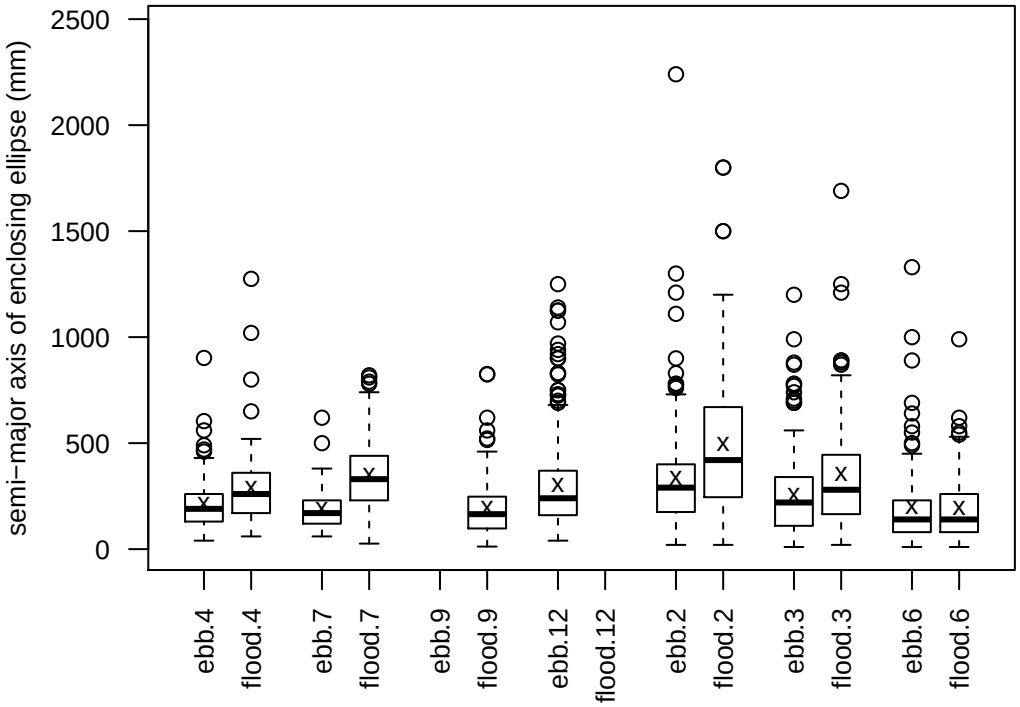

Figure A.7: Drifting *Ulva* thallus size in two ebb/flood tides at different calendar months between April 2012 and June 2013. Displayed are the distributions of the semi-major axis lengths of the visually estimated ellipse enclosing the flattened thallus (in most cases slightly greater than or equal to the longest linear dimension) as boxplots. Bold horizontal bars indicate the median, hinges the 25th and 75th percentile, whiskers extend to the lowest/highest data point within 1.5 times the interquartile range from the respective hinge, data outside this range are indicated by circles. Data for ebb.9 and flood.12 are not available.

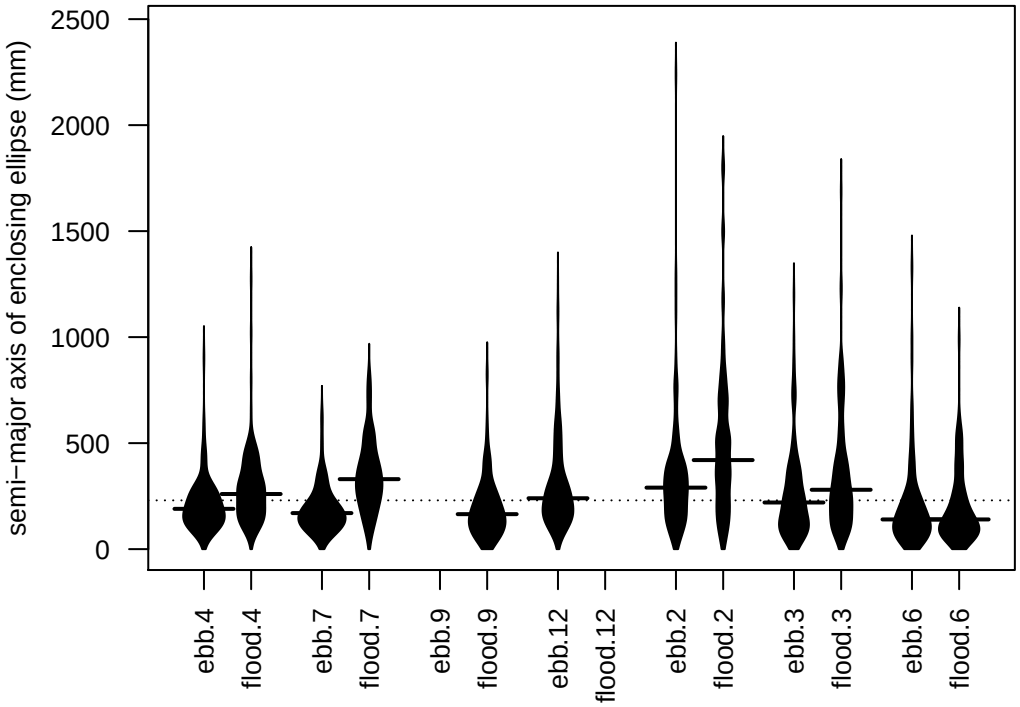

Figure A.8: Drifting *Ulva* thallus size in two ebb/flood tides at different calendar months between April 2012 and June 2013. Displayed are the distributions of the semi-major axis lengths of the visually estimated ellipse enclosing the flattened thallus (in most cases slightly greater than or equal to the longest linear dimension) as beanplots (estimated probability density function, Gaussian kernel, Sheather&Jones bandwidth, cutoff at zero). Bold horizontal bars indicate corresponding medians, dotted horizontal bar indicates overall median. Data for ebb.9 and flood.12 are not available.

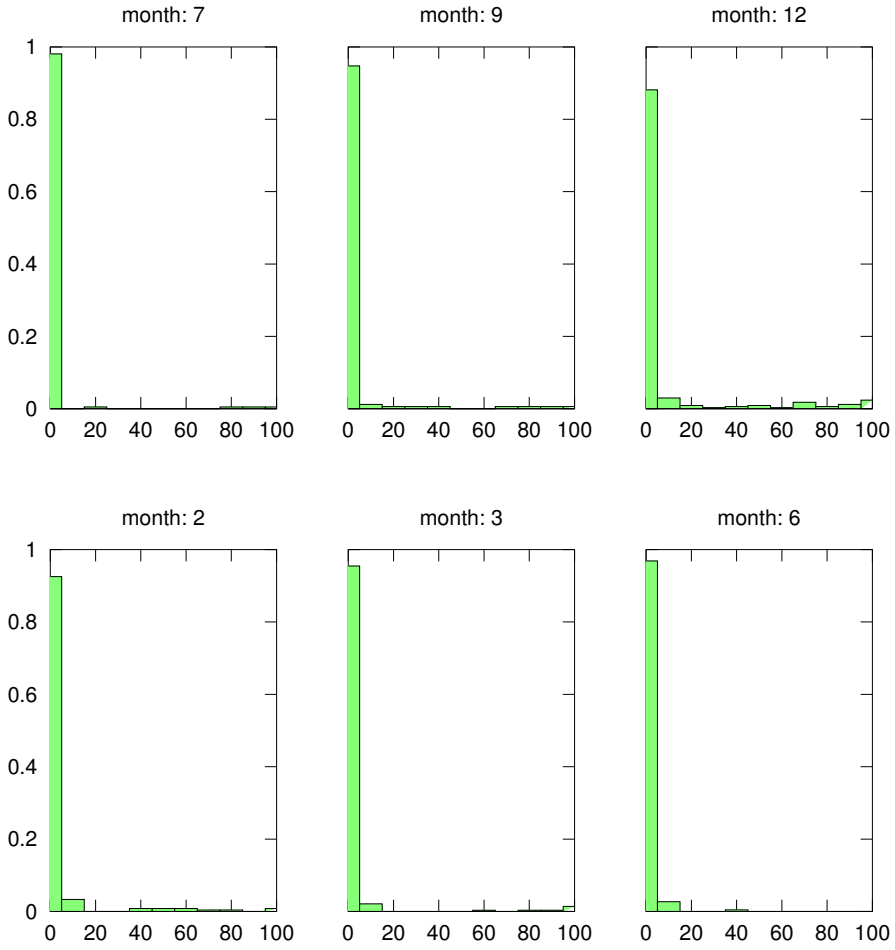

Figure A.9: Histograms of drifting *Ulva* sporulation (percentage of sporulated tissue area) for the approximately bimonthly surveys between 2012/07 and 2013/06.

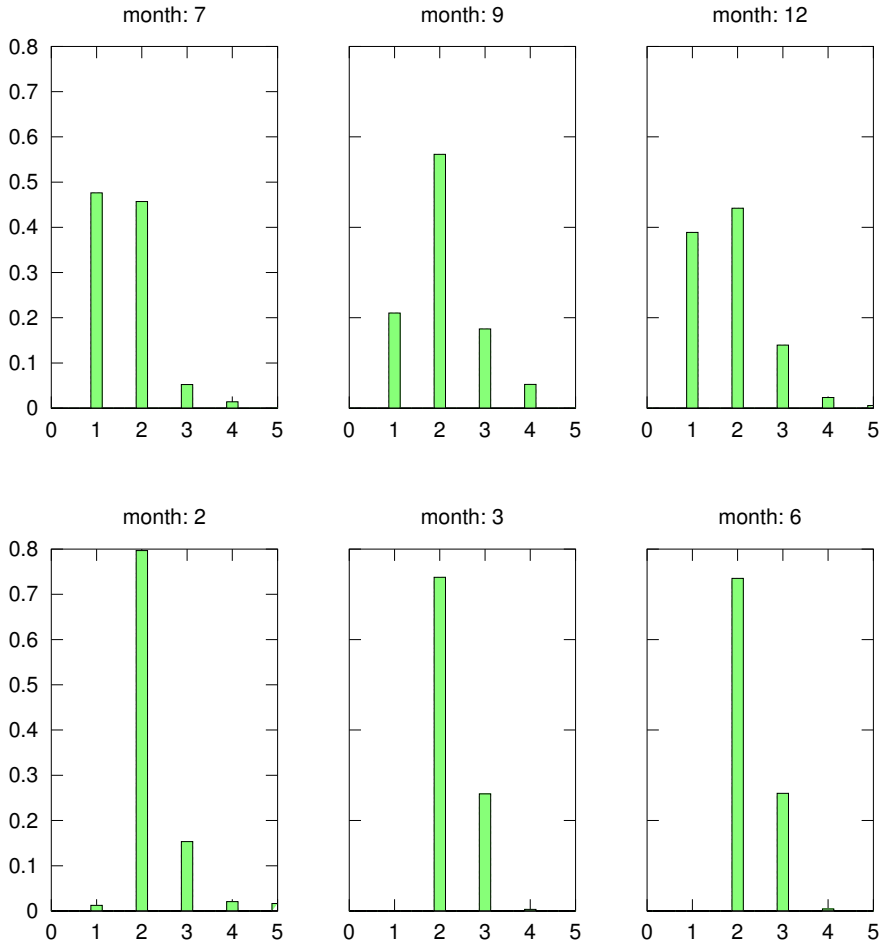

Figure A.10: Histograms of drifting *Ulva* degree of degradation (1 = no visible degradation to 5 = highly degraded) for the approximately bimonthly surveys between 2012/07 and 2013/06.

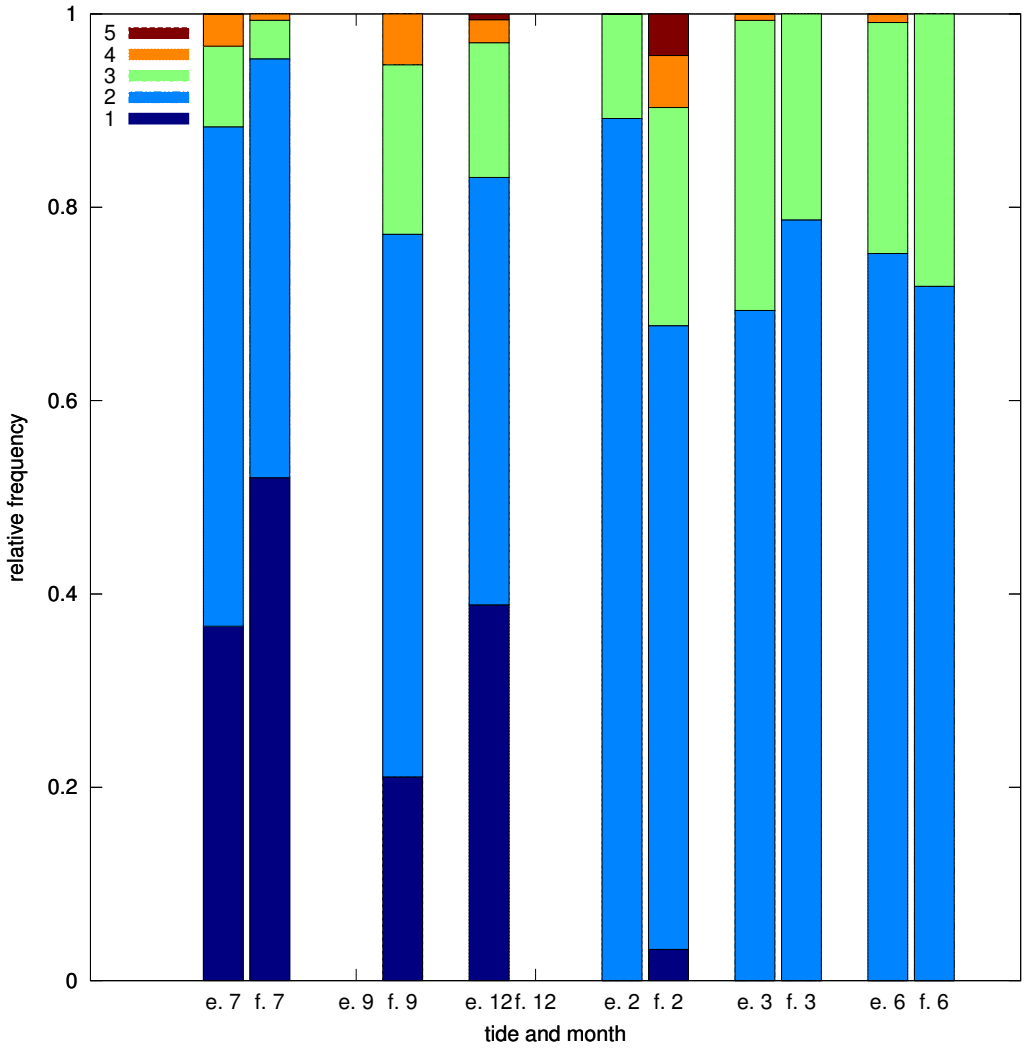

Figure A.11: Relative frequency of drifting *Ulva* degree of degradation (1 = no visible degradation to 5 = highly degraded) for the ebb ("e.") and flood ("f.") tides of the approximately bimonthly surveys between 2012/07 and 2013/06 (only month indicated in axis labels).

Appendix B

Inter- and subtidal *Ulva* abundance observed by dropcam

While intertidal abundance of *Ulva* is regularly surveyed by the Bay of Plenty Regional Council (Park, 2011), information on subtidal abundance is scarce. de Winton et al. (1996) carried out subtidal surveys using SCUBA divers in February/-March of the two consecutive years 1995 and 1996. Alongside the nutrient sampling programme described in chapter 4, we trialled the use of a submersible video camera ("dropcam") as a low-cost and easily deployed alternative to survey subtidal *Ulva* abundance. The dropcam was deployed from a boat around high tide at sites along four transects in the southern basin of Tauranga Harbour (Figure B.1). The video camera is mounted facing downward on a small rigid frame, and lowered by hand until it reaches the seafloor. Only a small time window around high tide is suitable for this kind of deployment, since at higher current speeds, it is difficult to deploy the frame in an upright position on the seafloor, and the image quality quickly degrades due to resuspended sediment. Additionally, for cross-channel transects required to survey sites at a range of depths in the same area, navigation also quickly becomes difficult at higher current speeds. Still images were later extracted from the video recordings to visually estimate abundance as percent coverage of the sediment by *Ulva*. Three of the four transect locations were chosen to overlap with sites surveyed by de Winton et al. (1996): Otumoetai corresponding to site F, Wairoa to site I and Te Puna Beach to site K. The fourth transect, Hunter's Creek, was chosen to be located in a sheltered sub-estuary not previously surveyed. Sites were spaced at a distance of approximately 200 m along each transect, leading to between 6 and 10 sites per transect and date. At each site, the dropcam was lowered to the seafloor, and three individual spots recorded within a few metres distance by repeatedly slightly raising and lowering the frame while the boat was drifting. The

visually estimated percentage of cover from the corresponding three still images was then averaged.

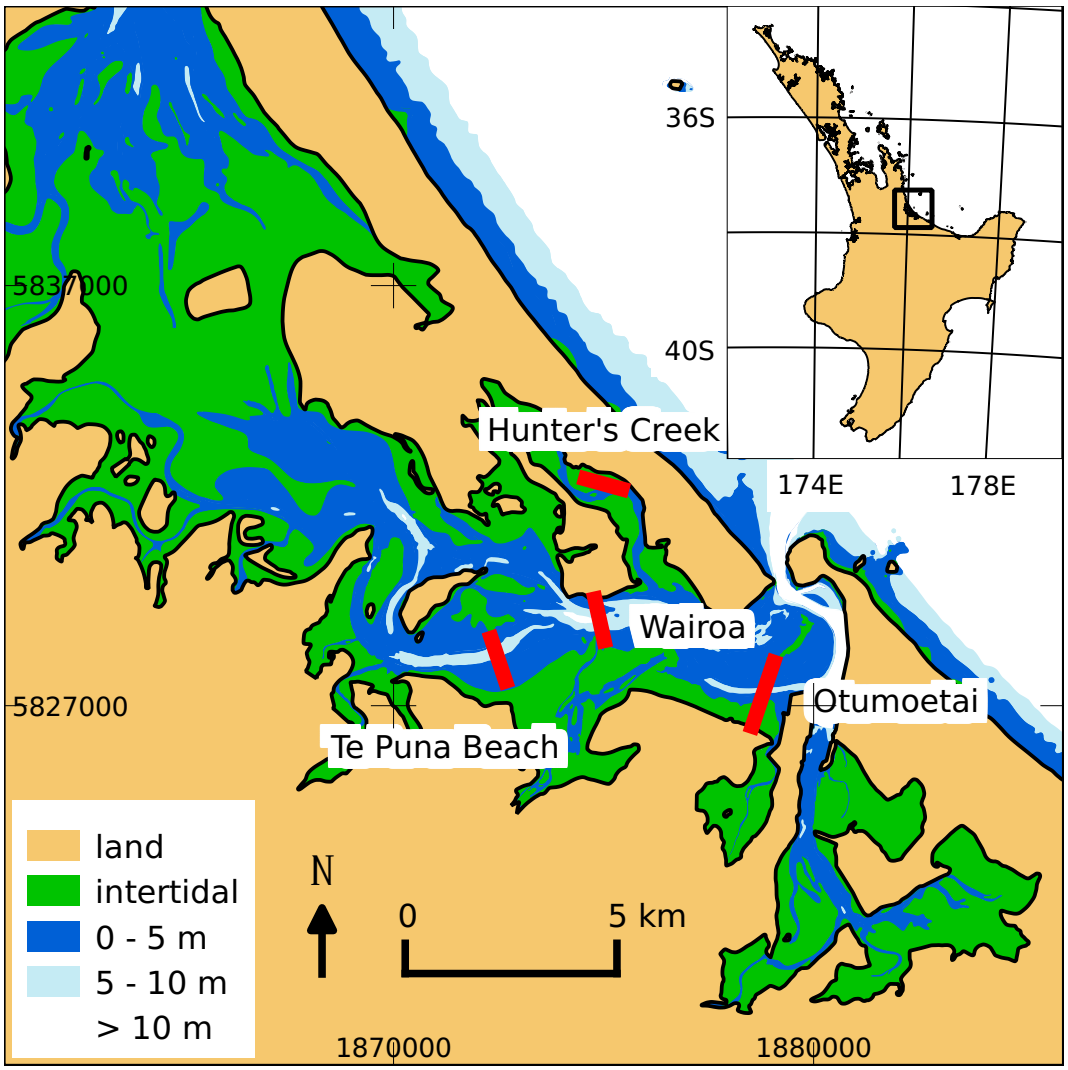

Figure B.1: Map of the southern basin of Tauranga Harbour (inset: location of Tauranga Harbour on the North Island of New Zealand) and location of dropcam survey transects. Map projections are NZTM2000, main map with coordinates in metres, inset map with coordinates in degrees.

Ulva abundance dependent on depth is shown in Figure B.2. The mean abundance over all stations was 5%, with no values above 5% at depths of 9 m or more. Sites in shallow areas are more numerous, but first calculating the mean over bins of 1 m depth to alleviate this bias still results in an overall mean of 5%.

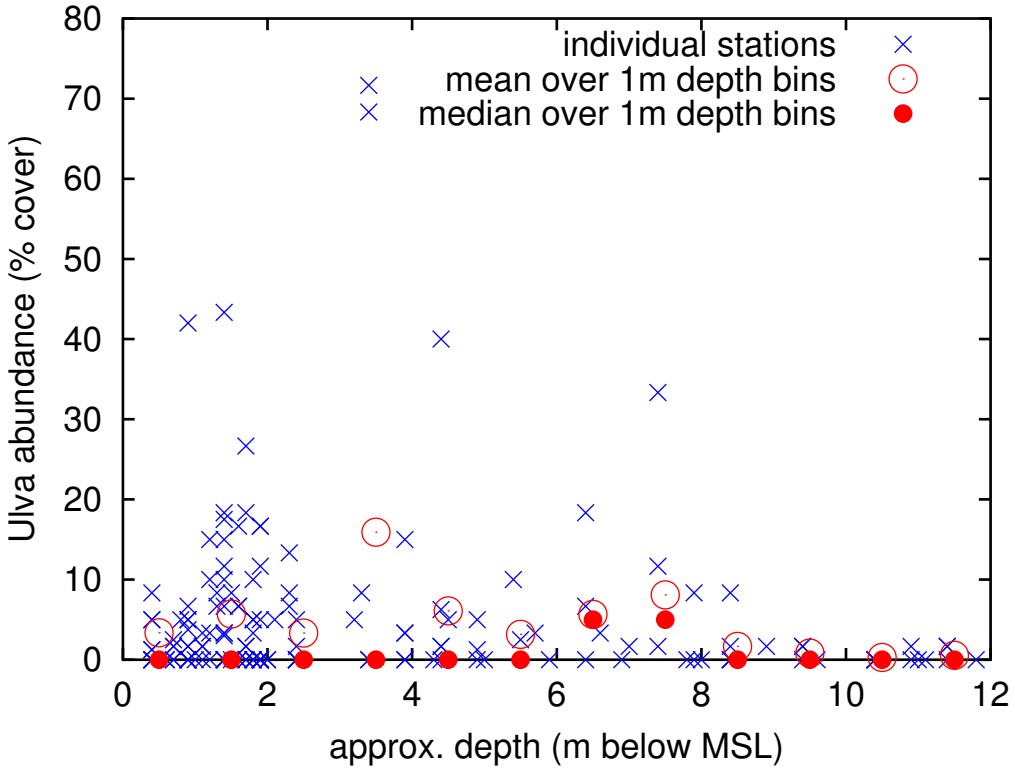

Figure B.2: *Ulva* abundance as observed by dropcam dependent on depth. Depths given relative to mean sea level (MSL) are approximate since no tidal correction has been applied. In addition to individual transect station values, mean values are given for bins of 1 m depth from 0 to 12 m.

The seasonal evolution of abundance is shown in Figure B.3, showing a clear summer peak in 2012/2013, with both mean values over 10% and maximum values over 70%, while the trial study in the summer of 2011/2012 (January 2012) shows abundance more similar to autumn or winter of the 2012/2013 season.

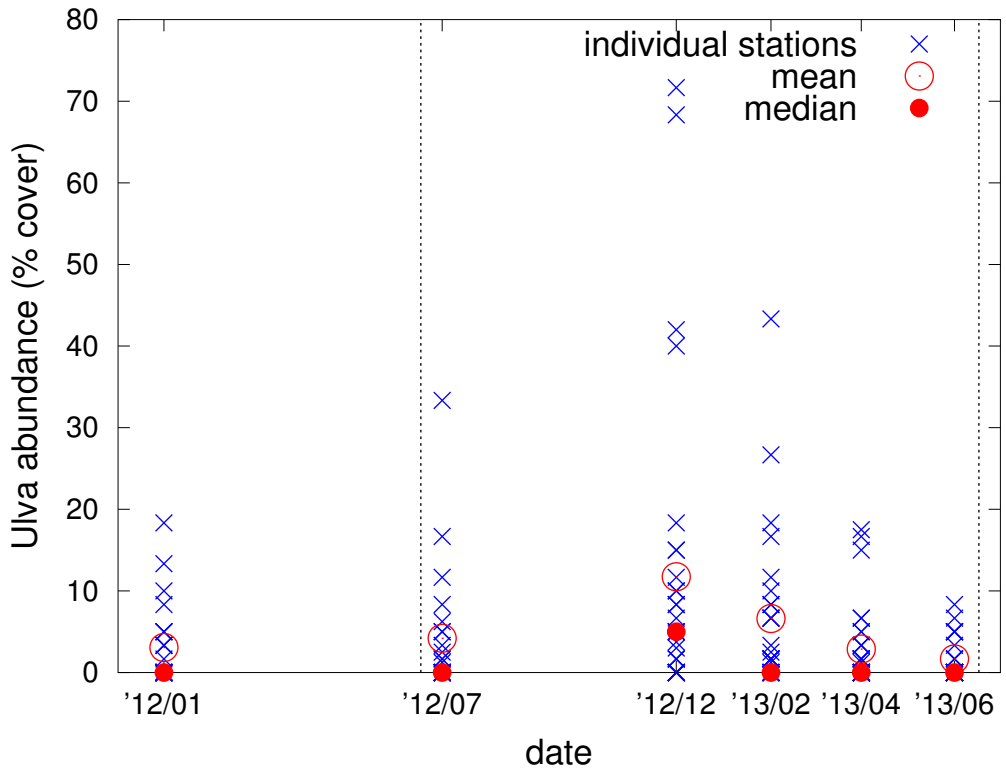

Figure B.3: *Ulva* abundance as observed by dropcam dependent on time from a pilot study (2012/01) and approximately bimonthly surveys between 2012/07 and 2013/06 (data from 2013/09 not available). In addition to individual transect station values, mean and median values are given for each survey date. Dashed vertical lines show the 1st of July of each calendar year to indicate average winter minima timing of temperature and irradiance.

Bibliography

Abrams, M., L. Alberotanza, S. Pignatti, R. Cavalli, and V. Tramutoli (2002). *EO-1 Validation in Venice, Italy: Urban Mapping, Lagoon Environment, and Bathymetry*.

Aldridge, J. N. and M. Trimmer (2009). "Modelling the distribution and growth of "problem" green seaweed in the Medway estuary, UK". *Hydrobiologia* 629.1, pp. 107–122. DOI: 10.1007/s10750-009-9760-6.

Alexander, D. J., D. E. Hart, and I. D. Marsden (2008). *Evaluation and Development of Techniques to Map Macroalgae in the Avon-Heathcote Estuary Ihutai*. Estuarine Research Report 35. Prepared for the Avon-Heathcote Estuary Ihutai Trust, Christchurch, New Zealand.

Alvera-Azcárate, A., J. Ferreira, and J. Nunes (2003). "Modelling eutrophication in mesotidal and macrotidal estuaries. The role of intertidal seaweeds". *Estuarine, Coastal and Shelf Science* 57.4, pp. 715–724. DOI: 10.1016/S0272-7714(02)00413-4.

Arhonditsis, G, G Tsirtsis, and M Karydis (2002). "The effects of episodic rainfall events to the dynamics of coastal marine ecosystems: applications to a semi-enclosed gulf in the Meditteranean Sea". *Journal of Marine Systems* 35.3-4, pp. 183–205. DOI: 10.1016/S0924-7963(02)00081-7.

Arhonditsis, G. B. and M. T. Brett (2004). "Evaluation of the current state of mechanistic aquatic biogeochemical modeling". *Marine Ecology Progress Series* 271, pp. 13–26. DOI: 10.3354/meps271013.

Aveytua-Alcázar, L., V. F. Camacho-Ibar, A. J. Souza, J. Allen, and R. Torres (2008). "Modelling Zostera marina and Ulva spp. in a coastal lagoon". *Ecological Modelling* 218, pp. 354–366. DOI: 10.1016/j.ecolmodel.2008.07.019.

Baretta, J., W. Ebenhöh, and P. Ruardij (1995). "The European regional seas ecosystem model, a complex marine ecosystem model". *Netherlands Journal of Sea Research* 33, pp. 233–246. DOI: 10.1016/0077-7579(95)90047-0.

Barr, N. G. (2007). "Aspects of nitrogen metabolism in the green alga *Ulva*: developing an indicator of seawater nitrogen loading". Ph.D. thesis. University of Auckland. URL: http://hdl.handle.net/2292/2522.

Bay of Plenty Polytechnic (2010). *New studies indicate sea lettuce blooms caused by human activity, not weather patterns*. Online at http://www.boppoly.ac.nz/index.cfm?objectid=3ACD43F8-D7E9-3C27-6023F3B9297C1567. Accessed 2011/08/24. Archived version at http://www.webcitation.org/61AQXwk7b.

Bendoricchio, G., G. Coffaro, and C. Demarchi (1994). "A trophic model for *Ulva rigida* in the Lagoon of Venice". *Ecological Modelling* 75, pp. 485–496. DOI: 10.1016/0304-3800(94)90042-6.

Bioresearches (1989). *Factors influencing the growth of the sea lettuce, Ulva in south-eastern Tauranga Harbour, December 1989*. Report by Bioresearches Ltd. for Tauranga District Council. Available from the Tauranga City Library, Tauranga, New Zealand.

— (1991). *The growth of the sea lettuce, Ulva in south-eastern Tauranga Harbour, December 1990*. Report by Bioresearches Ltd. for Tauranga District Council. Available from the Tauranga City Library, Tauranga, New Zealand.

Brodersen, R., F. Nielsen, J. C. Christiansen, and K. Andersen (1987). "Characterization of binding equilibrium data by a variety of fitted isotherms". *European Journal of Biochemistry* 169, pp. 487–495. ISSN: 1432-1033. DOI: 10.1111/j.1432-1033.1987.tb13636.x.

Bruhn, A., J. Dahl, H. B. Nielsen, L. Nikolaisen, M. B. Rasmussen, S. Markager, B. Olesen, C. Arias, and P. D. Jensen (2011). "Bioenergy potential of *Ulva lactuca*: Biomass yield, methane production and combustion". *Bioresource Technology* 102.3, pp. 2595–2604. DOI: 10.1016/j.biortech.2010.10.010.

Brush, M. J. and S. W. Nixon (2010). "Modeling the role of macroalgae in a shallow sub-estuary of Narragansett Bay, RI (USA)". *Ecological Modelling* 221.7, pp. 1065–1079. DOI: 10.1016/j.ecolmodel.2009.11.002.

Campbell, S. (2001). "Ammonium requirements of fast-growing ephemeral macroalgae in a nutrient-enriched marine embayment (Port Phillip Bay, Australia)". *Marine Ecology Progress Series* 209, pp. 99–107. DOI: 10.3354/meps209099.

Clark, M. P. and J. A. Vrugt (2006). "Unraveling uncertainties in hydrologic model calibration: Addressing the problem of compensatory parameters". *Geophysical Research Letters* 33.6, p. L06406. DOI: 10.1029/2005GL025604.

Coffaro, G. and M. Bocci (1997). "Resources competition between *Ulva rigida* and *Zostera marina*: a quantitative approach applied to the Lagoon of Venice". *Ecological Modelling* 102.1, pp. 81–95. DOI: 10.1016/S0304-3800(97)00096-3.

Corbett, D. R. (2010). "Resuspension and estuarine nutrient cycling: insights from the Neuse River Estuary". *Biogeosciences* 7, pp. 3289–3300. DOI: 10.5194/bg-7-3289-2010.

Cotton, A. D. (1910). "On the Growth of *Ulva* latissima, L. In Water Polluted by Sewage". *Bulletin of Miscellaneous Information (Royal Gardens, Kew)* 1910.1, pp. 15–19.

— (1911). "Appendix IV: On The Growth Of *Ulva latissima* In Excessive Quantity, With Special Reference To The *Ulva* Nuisance In Belfast Lough". *Seventh Report of the Royal Commission on Sewage Disposal*, pp. 121–142. House of Commons Parliamentary Papers Online / ProQuest, London.

Cousins, J. (2007). *Councils set to tackle beach sea lettuce problem*. Online at http://www.bayofplentytimes.co.nz/news/councils-set-to-tackle-beach-sea-lettuce-problem/975096/. Accessed 2012/06/11. Archived version at http://www.webcitation.org/68LGhpPIg.

— (2009). *BEACH MENACE: Tauranga mum wants fresh air for walks*. Online at http://www.bayofplentytimes.co.nz/news/beach-menace-tauranga-mum-wants-fresh-air-for-walk/1009786/. Accessed 2012/06/11. Archived version at http://www.webcitation.org/68LHTgrCQ.

— (2010). *950 TONNES - That's how much rotting sea lettuce has been removed from beaches*. Online at http://www.bayofplentytimes.co.nz/news/950-tonnes-thats-how-much-rotting-sea-lettuce-has-/1013806/. Accessed 2012/06/11. Archived version at http://www.webcitation.org/68LHW0A1V.

Cuddington, K., M.-J. Fortin, L. R. Gerber, A. Hastings, A. Liebhold, M. O'Connor, and C. Ray (2013). "Process-based models are required to manage ecological systems in a changing world". *Ecosphere* 4. DOI: 10.1890/ES12-00178.1.

Cukier, R. I., C. M. Fortuin, K. E. Shuler, A. G. Petschek, and J. H. Schaibly (1973). "Study of the sensitivity of coupled reaction systems to uncertainties in rate coefficients. I Theory". *The Journal of Chemical Physics* 59.8, pp. 3873–3878. DOI: 10.1063/1.1680571.

Davis, R. A. J. and T. R. Healy (1993). "Holocene coastal depositional sequences on a tectonically active setting: southeastern Tauranga Harbour, New Zealand". *Sedimentary Geology* 84, pp. 57–69. DOI: 10.1016/0037-0738(93)90045-7.

de Lange, W. P. and T. R. Healy (1990). "Renourishment of a Flood-Tidal Delta Adjacent Beach, Tauranga Harbour, New Zealand". *Journal of Coastal Research* 6.3, pp. 627–640.

de Winton, M., J. Clayton, and I. Hawes (1996). *Subtidal Ulva within Tauranga Harbour: 1995/96*. NIWA Consultancy Report BPR70205/1 prepared for Environment B.O.P. Available from the Bay of Plenty Regional Council, Whakatane, New Zealand.

de Winton, M., I. Hawes, J. Clayton, P. Champion, and R. K. Smith (1998). *Sea lettuce dynamics and ecophysiology in Tauranga Harbour, Bay of Plenty*. NIWA Client Report BPR802 prepared for Environment B.O.P. Available from the Bay of Plenty Regional Council, Whakatane, New Zealand.

Droop, M. R. (1968). "Vitamin B12 And Marine Ecology. IV. The Kinetics Of Uptake, Growth And Inhibition In *Monochrysis lutheri*". *Journal of the Marine Biological Association of the United Kingdom* 48, pp. 689–733. DOI: 10.1017/S0025315400019238.

Duarte, P. and J. Ferreira (1997). "A model for the simulation of macroalgal population dynamics and productivity". *Ecological Modelling* 98.2-3, pp. 199–214. DOI: 10.1016/S0304-3800(96)01915-1.

Dyer, K. R (1973). *Estuaries: a physical introduction*. John Wiley. ISBN: 0471229059.

Eaton, J. W., D. Bateman, S. Hauberg, and R. Wehbring (2014). *GNU Octave manual: a high-level interactive language for numerical computations*. CreateSpace Independent Publishing Platform.

FitzGerald, D. and M. Miner (2013). "10.7 Tidal Inlets and Lagoons along Siliciclastic Barrier Coasts". In: *Treatise on Geomorphology*. Ed. by J. F. Shroder. San Diego: Academic Press, pp. 149–165. DOI: 10.1016/B978-0-12-374739-6.00278-5.

Fletcher, R. L. (1996). "The Occurence of "Green Tides" - a Review". In: *Marine Benthic Vegetation: Recent Changes and the Effects of Eutrophication*. Ed. by W. Schramm and P. H. Nienhuis. Springer, pp. 7–43. ISBN: 3540581065.

Flindt, M. R., M. A. Pardal, A. I. Lillebø, I. Martins, and J. C. Marques (1999). "Nutrient cycling and plant dynamics in estuaries: A brief review". *Acta Oecologica* 20.4, pp. 237–248. DOI: 10.1016/S1146-609X(99)00142-3.

Fujita, R. M. (1985). "The Role Of Nitrogen Status In Regulating Transient Ammonium Uptake And Nitrogen Storage By Macroalgae". *Journal of Experimental Marine Biology and Ecology* 92, pp. 283–301. DOI: 10.1016/0022-0981(85)90100-5.

Golberg, A., E. Vitkin, G. Linshiz, S. A. Khan, N. J. Hillson, Z. Yakhini, and M. L. Yarmush (2014). "Proposed design of distributed macroalgal biorefineries: thermodynamics, bioconversion technology, and sustainability implications for developing economies". *Biofuels, Bioproducts & Biorefining* 8, pp. 67–82. DOI: 10.1002/bbb.1438.

Gregory, M. B., J. DeVivo, E. M. DiDonato, C. J. Wright, and E. Thompson (2013). *Protocol for Monitoring Estuarine Water and Sediment Quality in Selected Southeast Coast Network Parks*. Natural Resource Report NPS/SECN/NRR—2013/644. National Park Service, Fort Collins Colorado.

Guidone, M. and C. S. Thornber (2013). "Examination of *Ulva* bloom species richness and relative abundance reveals two cryptically co-occurring bloom species in Narragansett Bay, Rhode Island". *Harmful Algae* 24.0, pp. 1–9. DOI: 10.1016/j.hal.2012.12.007.

Guimaraens, M. A. de, A. d. M. Paiva, and R. Coutinho (2005). "Modeling *Ulva* spp. dynamics in a tropical upwelling region". *Ecological Modelling* 188, pp. 448–460. DOI: 10.1016/j.ecolmodel.2005.04.023.

Gutenkunst, R. N., J. J. Waterfall, F. P. Casey, K. S. Brown, C. R. Myers, and J. P. Sethna (2007). "Universally Sloppy Parameter Sensitivities in Systems Biology Models". *PLoS Computational Biology* 3.10, pp. 1871–1878. DOI: 10.1371/journal.pcbi.0030189.

Han, T., S.-H. Kang, J.-S. Park, H.-K. Lee, and M. T. Brown (2008). "Physiological responses of Ulva pertusa and U. armoricana to copper exposure". *Aquatic Toxicology* 86, pp. 176–184. DOI: 10.1016/j.aquatox.2007.10.016.

Haslett, S. (2009). *Coastal Systems*. 2nd ed. Routlege / Taylor & Francis. ISBN: 0203893204.

Hayden, H. S., J. Blomster, C. A. Maggs, P. C. Silva, M. J. Stanhope, and J. R. Waaland (2003). "Linnaeus was right all along: *Ulva* and *Enteromorpha* are not distinct genera". *European Journal of Phycology* 38, pp. 277–294. DOI: 10.1080/1364253031000136321.

Heesch, S., J. Broom, K. Neill, T. Farr, J. Dalen, and W. Nelson (2007). *Genetic diversity and possible origins of New Zealand populations of Ulva*. Biosecurity New Zealand Technical Paper No: 2007/01.

Henley, W. and J. Ramus (1989). "Optimization of pigment content and the limits of photoacclimation for *Ulva rotundata* (Chlorophyta)". *Marine Biology* 103, pp. 267–274. DOI: 10.1007/BF00543357.

Herbert, R. (1999). "Nitrogen cycling in coastal marine ecosystems". *FEMS Microbiology Reviews* 23.5, pp. 563–590. DOI: 10.1016/S0168-6445(99)00022-4.

Ho, Y.-B. (1975). "The Use Of *Ulva lactuca* L. As An Indicator Organism For Marine Pollution". Ph.D. thesis. University of Liverpool.

Hodges, B. and C. Dallimore (2006). *Estuary, Lake and Coastal Ocean Model: ELCOM v2.2 Science Manual*. Centre for Water Research, University of Western Australia.

Hume, T. M. and C. E. Herdendorf (1988). "A Geomorphic Classification of Estuaries and its Application to Coastal Resource Management - A New Zealand example". *Ocean and Shoreline Management* 11, pp. 249–274. DOI: 10.1016/0951-8312(88)90022-7.

Hume, T. M., T. Snelder, M. Weatherhead, and R. Liefting (2007). "A controlling factor approach to estuary classification". *Ocean & Coastal Management* 50, pp. 905–929. DOI: 10.1016/j.ocecoaman.2007.05.009.

Imberger, J., T. Berman, R. R. Christian, E. B. Sherr, D. E. Whitney, L. R. Pomeroy, R. G. Wiegert, and W. J. Wiebe (1983). "The Influence of Water Motion on the Distribution and Transport of Materials in a Salt Marsh Estuary". *Limnology and Oceanography* 28.2, pp. 201–214. DOI: 10.4319/lo.1983.28.2.0201.

Janssen, P. H. M. and P. S. C. Heuberger (1995). "Calibration of process-oriented models". *Ecological Modelling* 83, pp. 55–66. DOI: 10.1016/0304-3800(95)00084-9.

Johnson, S. G. (2013). *The NLopt nonlinear-optimization package, version 2.4.1*. URL: http://ab-initio.mit.edu/nlopt.

Jones, M. (1993). "Simple boundary correction for kernel density estimation". *Statistics and Computing* 3.3, pp. 135–146. DOI: 10.1007/BF00147776.

Kaelo, P. and M. Ali (2006). "Some Variants of the Controlled Random Search Algorithm for Global Optimization". *Journal of Optimization Theory and Applications* 130.2, pp. 253–264. DOI: 10.1007/s10957-006-9101-0.

Karpouzli, E. and T. Malthus (2006). *An assessment of QuickBird satellite data as a routine means of assessing green macroalgal weed cover within intertidal areas for the purpose of classifying transitional waters for the WFD, OSPAR and UWWTD*. Report produced for the Scottish Environment Protection Agency (SEPA) under Research Contract No R50021PUR.

Kjerfve, B. (1994). "Coastal Lagoons". In: *Coastal Lagoon Processes*. Elsevier.

Land Information New Zealand (2013). *Tidal Level Information for Surveyors*. Online at http://www.linz.govt.nz/geodetic/datums-projections-heights/vertical-datums/tidal-level-information-for-surveyors. Accessed 2013/07/29. Archived version at http://www.webcitation.org/6IScBrf8X.

Land Information New Zealand (2014). *Standard Port Tidal Levels*. Online at http://www.linz.govt.nz/hydro/tidal-info/tide-tables/tidal-levels. Accessed 2014/07/03. Archived version at http://www.webcitation.org/6QmVczckL.

Lapointe, B. E. and K. R. Tenore (1981). "Experimental Outdoor Studies With *Ulva* fasciata Delile. I. Interaction Of Light And Nitrogen On Nutrient Uptake, Growth, And Biochemical Composition". *Journal of Experimental Marine Biology and Ecology* 53, pp. 135–152. DOI: 10.1016/0022-0981(81)90015-0.

Li, P. and Q. D. Vu (2013). "Identification of parameter correlations for parameter estimation in dynamic biological models". *BMC Systems Biology* 7, p. 91. DOI: 10.1186/1752-0509-7-91.

Li, Y., C. Tang, J. Zhu, B. Pan, D. O. Anim, Y. Ji, Z. Yu, and K. Acharya (2015). "Parametric uncertainty and sensitivity analysis of hydrodynamic processes for a large shallow freshwater lake". *Hydrological Sciences Journal* 60, pp. 1078–1095. DOI: 10.1080/02626667.2014.948444.

Liu, D., J. K. Keesing, P. He, Z. Wang, Y. Shi, and Y. Wang (2013). "The world's largest macroalgal bloom in the Yellow Sea, China: Formation and implications". *Estuarine, Coastal and Shelf Science* 129, pp. 2–10. DOI: 10.1016/j.ecss.2013.05.021.

Loucks, D. P., E. v. Beek, J. R. Stedinger, J. P. Dijkman, and M. T. Villars (2005). "Model Sensitivity and Uncertainty Analysis". In: *Water resources systems planning and management: an introduction to methods, models and applications*. UNESCO. Chap. Model Sensitivity and Uncertainty Analysis, pp. 255–292. URL: http://hdl.handle.net/1813/2804.

MacKenzie, L. (2004). "River inputs, re-mineralisation and the spatial and temporal distribution of inorganic nutrients in Tasman Bay, New Zealand". *New Zealand Journal of Marine and Freshwater Research* 38.4, pp. 681–704. DOI: 10.1080/00288330.2004.9517270.

Marinov, D., J. M. Zaldivar, A. Norro, G. Giordani, and P. Viaroli (2008). "Integrated modelling in coastal lagoons: Sacca di Goro case study". *Hydrobiologia* 611, pp. 147–165. DOI: 10.1007/s10750-008-9451-8.

Martins, I. and J. C. Marques (2002). "A Model for the Growth of Opportunistic Macroalgae (*Enteromorpha* sp.) in Tidal Estuaries". *Estuarine, Coastal and Shelf Science* 55, pp. 247–257. DOI: 10.1006/ecss.2001.0900.

Martins, I., M. Pardal, A. Lillebø¸, M. Flindt, and J. Marques (2001). "Hydrodynamics as a Major Factor Controlling the Occurrence of Green Macroalgal Blooms in a Eutrophic Estuary: A Case Study on the Influence of Precipitation and River

Management". *Estuarine, Coastal and Shelf Science* 52.2, pp. 165–177. DOI: 10.1006/ecss.2000.0708.

Martins, I., A. Marcotegui, and J. C. Marques (2008). "Impacts of macroalgal spores on the dynamics of adult macroalgae in a eutrophic estuary: High versus low hydrodynamic seasons and long-term simulations for global warming scenarios". *Marine Pollution Bulletin* 56.5, pp. 984–998. DOI: 10.1016/j.marpolbul.2008.01.025.

McCallum, H. (2000). *Population Parameters: Estimation for Ecological Models*. Blackwell Science.

McGrath, J. K., J. P. O'Kane, K. J. Barry, and R. C. Kavanagh (2007). "Channel-adaptive Interpolation for Improved Bathymetric TIN". In: *Proceedings of the 9th International Conference on GeoComputation, Maynooth, Ireland*. URL: http://www.geocomputation.org/2007/6B-Algorithms_and_Architecture_2/6B2.pdf.

Molnar, J. L., R. L. Gamboa, C. Revenga, and M. D. Spalding (2008). "Assessing the global threat of invasive species to marine biodiversity". *Frontiers in Ecology and the Environment* 6.9, pp. 485–492. DOI: 10.1890/070064. URL: http://conserveonline.org/workspaces/global.invasive.assessment.

Monahan, B. (2014). "Estimation of inorganic nitrogen loading to the Southern Tauranga Harbour". B.Sc. (Hons) thesis. University of Waikato.

Moore, J., S. C. Doney, J. A. Kleypas, D. M. Glover, and I. Y. Fung (2001). "An intermediate complexity marine ecosystem model for the global domain". *Deep Sea Research Part 2* 49, pp. 403–462. DOI: 10.1016/S0967-0645(01)00108-4.

Morand, P. and X. Briand (1996). "Excessive growth of macroalgae: A symptom of environmental disturbance". *Botanica Marina* 39.6, pp. 491–516. DOI: 10.1515/botm.1996.39.1-6.491.

Morcom, C. P. (2013). "Nitrogen yields into the Tauranga Harbour based on sub-catchment land use". M.Sc. thesis. University of Waikato.

Morris, K. J., B. J. Bett, J. M. Durden, V. A. I. Huvenne, R. Milligan, D. O. B. Jones, S. McPhail, K. Robert, D. M. Bailey, and H. A. Ruhl (2014). "A new method for ecological surveying of the abyss using autonomous underwater vehicle photography". *Limnol. Oceanogr.* 12, pp. 795–809. DOI: 10.4319/lom.2014.12.795.

Ménesguen, A., P. Cugier, and I. Leblond (2006). "A New Numerical Technique for Tracking Chemical Species in a Multisource, Coastal Ecosystem Applied to Nitrogen Causing *Ulva* Blooms in the Bay of Brest (France)". *Limnology and*

Oceanography 51.1, pp. 591–601. DOI: 10.4319/lo.2006.51.1_part_2.0591.

Nezlin, N. P., K. Kamer, and E. D. Stein (2007). "Application of Color Infrared Aerial Photography to Assess Macroalgal Distribution in an Eutrophic Estuary, Upper Newport Bay, California". *Estuaries and Coasts* 30, pp. 855–868. DOI: 10.1007/BF02841339.

Novakowski, K. I., R. Torres, L. R. Gardner, and G. Voulgaris (2004). "Geomorphic analysis of tidal creek networks". *Water Resources Research* 40. DOI: 10.1029/2003WR002722.

Nyholm, N. (1978). "A Simulation Model For Phytoplankton Growth And Nutrient Cycling In Eutrophic, Shallow Lakes". *Ecological Modelling* 4, pp. 279–310. DOI: 10.1016/0304-3800(78)90011-X.

Öberg, J. (2005). "Model simulations of conditions suitable for the establishment of *Enteromorpha* sp. (Chlorophyta) macroalgal mats". *Marine Biology Research* 1, pp. 97–106. DOI: 10.1080/17451000510019042.

Oldham, C. E., P. S. Lavery, K. McMahon, C. Pattiaratchi, and T. W. Chiffings (2010). *Seagrass wrack dynamics in Geographe Bay, Western Australia - Synopsis*.

Oreskes, N. and K. Belitz (2001). "Philosophical Issues in Model Assessment". In: *Model Validation: Perspectives in Hydrological Science*. Ed. by M. G. Anderson and P. D. Bates. Wiley.

Park, S. (1996). *Sea Lettuce Monitoring In The Bay Of Plenty - Changes In Abundance, Nutrients And Environmental Influences For The Period July 1992 - June 1996*. Bay of Plenty Regional Council Environmental Report 96/23. Available from the Bay of Plenty Regional Council, Whakatane, New Zealand.

— (2007). *Sea Lettuce Monitoring in the Tauranga Harbour 1991-2007*. Bay of Plenty Regional Council Environmental Publication 2007/20. Available from the Bay of Plenty Regional Council, Whakatane, New Zealand.

— (2011). *Sea Lettuce and Nutrient Monitoring in Tauranga Harbour 1991-2010*. Bay of Plenty Regional Council Environmental Publication 2011/06. Available from the Bay of Plenty Regional Council, Whakatane, New Zealand.

Pastres, R., K. Chan, C. Solidoro, and C. Dejak (1999). "Global sensitivity analysis of a shallow-water 3D eutrophication model". *Computer Physics Communications* 117, pp. 62–74. DOI: 10.1016/S0010-4655(98)00164-7.

Pattiaratchi, C., S. Wijeratne, and C. Bosserelle (2011). "Sand and seagrass wrack modelling in Port Geographe, south-western Australia". In: *Coasts and Ports 2011, Perth, Western Australia, 28-30 September 2011*.

Pauly, D., V. Christensen, and C. Walters (2000). "Ecopath, Ecosim, and Ecospace as tools for evaluating ecosystem impact of fisheries". *ICES Journal of Marine Science: Journal du Conseil* 57, pp. 697–706. DOI: 10.1006/jmsc.2000.0726.

Pedersen, M. F. and J. Borum (1997). "Nutrient control of estuarine macroalgae: growth strategy and the balance between nitrogen requirements and uptake". *Marine Ecology Progress Series* 161, pp. 155–163. DOI: 10.3354/meps161155.

Perrot, T., N. Rossi, A. Ménesguen, and F. Dumas (2014). "Modelling green macroalgal blooms on the coasts of Brittany, France to enhance water quality management". *Journal of Marine Systems* 132.0, pp. 38–53. DOI: 10.1016/j.jmarsys.2013.12.010.

Radhakrishnan, K. and A. C. Hindmarsh (1993). *Description and Use of LSODE, the Livermore Solver for Ordinary Differential Equations*. URL: https://computation.llnl.gov/casc/nsde/pubs/u113855.pdf.

Raue, A., C. Kreutz, T. Maiwald, J. Bachmann, M. Schilling, U. Klingmüller, and J. Timmer (2009). "Structural and practical identifiability analysis of partially observed dynamical models by exploiting the profile likelihood". *Bioinformatics* 25, pp. 1923–1929. DOI: 10.1093/bioinformatics/btp358.

Rautenberger, R. and K. Bischof (2006). "Impact of temperature on UV-susceptibility of two Ulva (Chlorophyta) species from Antarctic and Subantarctic regions". *Polar Biology* 29, pp. 988–996. DOI: 10.1007/s00300-006-0141-6.

Raven, J. A. and R. Taylor (2003). "Macroalgal growth in nutrient-enriched estuaries: A biogeochemical and evolutionary perspective". *Water, Air, and Soil Pollution* 3.1, pp. 7–26. DOI: 10.1023/A:1022167722654.

Ren, J. S., N. G. Barr, K. Scheuer, D. R. Schiel, and J. Zeldis (2014). "A dynamic growth model of macroalgae: Application in an estuary recovering from treated wastewater and earthquake-driven eutrophication". *Estuarine, Coastal and Shelf Science* 148, pp. 59–69. DOI: 10.1016/j.ecss.2014.06.014.

Runca, E., A. Bernstein, L. Postma, and G. Di Silvio (1996). "Control of macroalgae blooms in the Lagoon of Venice". *Ocean & Coastal Management* 30.2-3, pp. 235–257. DOI: 10.1016/0964-5691(95)00065-8.

Salomonsen, J., M. Flindt, O. Geertz-Hansen, and C. Johansen (1999). "Modelling advective transport of *Ulva lactuca* (L) in the sheltered bay, Møllekrogen, Roskilde Fjord, Denmark". *Hydrobiologia* 397, pp. 241–252. DOI: 10.1023/A:1003790625535.

Saltelli, A. (2002). "Making best use of model evaluations to compute sensitivity indices". *Computer Physics Communications* 145, pp. 280–297. DOI: 10.1016/S0010-4655(02)00280-1.

Saltelli, A., K. Chan, and E. M. Scott, eds. (2000). *Sensitivity Analysis*. Wiley. ISBN: 0471998923.

Schramm, W. and P. H. Nienhuis, eds. (1996). *Marine Benthic Vegetation: Recent Changes and the Effects of Eutrophication*. Springer. ISBN: 3540581065.

Sfriso, A. (1995). "Temporal and Spatial Responses of Growth of *Ulva rigida* C. Ag. to Environmental and Tissue Concentrations of Nutrients in the Lagoon of Venice". *Botanica Marina* 38.1-6, pp. 557–573. DOI: 10.1515/botm.1995.38.1-6.557.

Smith, V. H. (2003). "Eutrophication of Freshwater and Coastal Marine Ecosystems A Global Problem". *Environmental Science and Pollution Research* 10, pp. 126–139. DOI: 10.1065/espr2002.12.142.

Sobol', I. M. (1990). "On sensitivity estimation for nonlinear mathematical models". *Matematicheskoe Modelirovanie* 2.1, 112–118. In Russian.

— (1993). "Sensitivity analysis for non-linear mathematical models". *Mathematical Modelling and Computational Experiment* 1, 407–414.

Solidoro, C., C. Dejak, D. Franco, R. Pastres, and G. Pecenik (1995). "A Model For Macroalgae And Phytoplankton Growth In The Venice Lagoon". *Environment International* 21, pp. 619–626. DOI: 10.1016/0160-4120(95)00080-5.

Solidoro, C., G. Pecenik, R. Pastres, D. Franco, and C. Dejak (1997). "Modelling macroalgae (*Ulva rigida*) in the Venice lagoon: Model structure identification and first parameters estimation". *Ecological Modelling* 94, pp. 191–206. DOI: 10.1016/S0304-3800(96)00025-7.

Stein, W. A. et al. (2013). *Sage Mathematics Software (Version 5.11)*. The Sage Development Team. URL: http://www.sagemath.org/.

SunLive (2010). *Sea lettuce summer looming*. Online at http://www.sunlive.co.nz/news/9741-sea-lettuce-summer-looming.html. Accessed 2011/08/24. Archived version at http://www.webcitation.org/61AQvyysJ.

Swaney, D., D. Scavia, R. Howarth, and R. Marino (2008). "Estuarine classification and response to nitrogen loading: Insights from simple ecological models". *Estuarine, Coastal and Shelf Science* 77, pp. 253–263. DOI: 10.1016/j.ecss.2007.09.013.

Swart, H. de and J. Zimmerman (2009). "Morphodynamics of Tidal Inlet Systems". *Annual Review of Fluid Mechanics*. DOI: 10.1146/annurev.fluid.010908.165159.

Tay, H. W., K. R. Bryan, C. A. Pilditch, S. Park, and D. P. Hamilton (2011). "Variations in nutrient concentrations at different time scales in two shallow tidally dominated estuaries". *Marine and Freshwater Research*. DOI: 10.1071/MF11102.

Tay, H., K. Bryan, W. de Lange, and C. Pilditch (2013). "The hydrodynamics of the southern basin of Tauranga Harbour". *New Zealand Journal of Marine and Freshwater Research*, pp. 1–26. DOI: 10.1080/00288330.2013.778300.

Teichberg, M., S. E. Fox, Y. S. Olsen, I. Valiela, P. Martinetto, O. Iribarne, E. Y. Muto, M. A. V. Petti, T. N. Corbisier, M. Soto-Jiménez, F. Páez-Osuna, P. Castro, H. Freitas, A. Zitelli, M. Cardinaletti, and D. Tagliapietra (2010). "Eutrophication and macroalgal blooms in temperate and tropical coastal waters: nutrient enrichment experiments with *Ulva* spp." *Global Change Biology* 16, pp. 2624–2637. DOI: 10.1111/j.1365-2486.2009.02108.x.

Timmermann, K., S. Markager, and K. E. Gustafsson (2010). "Streams or open sea? Tracing sources and effects of nutrient loadings in a shallow estuary with a 3D hydrodynamic-ecological model". *Journal of Marine Systems* 82.3, pp. 111–121. DOI: 10.1016/j.jmarsys.2010.04.008.

Valiela, I., J. McClelland, J. Hauxwell, P. J. Behr, D. Hersh, and K. Foreman (1997). "Macroalgal blooms in shallow estuaries: Controls and ecophysiological and ecosystem consequences". *Limnology and Oceanography* 42, pp. 1105–1118. DOI: 10.4319/lo.1997.42.5_part_2.1105.

van Maanen, B., G. Coco, and K. Bryan (2013). "Modelling the effects of tidal range and initial bathymetry on the morphological evolution of tidal embayments". *Geomorphology* 191, pp. 23–34. DOI: 10.1016/j.geomorph.2013.02.023.

Verity, P. G. (2002). "A decade of change in the Skidaway River estuary. I. Hydrography and nutrients". *Estuaries* 25.5, pp. 944–960. DOI: 10.1007/BF02691343.

Viaroli, P., M. Bartoli, R. Azzoni, G. Giordani, C. Mucchino, M. Naldi, D. Nizzoli, and L. Tajé (2005). "Nutrient and iron limitation to *Ulva* blooms in a eutrophic coastal lagoon (Sacca di Goro, Italy)". *Hydrobiologia* 550, pp. 57–71. DOI: 10.1007/s10750-005-4363-3.

Wainwright, H. M., S. Finsterle, Y. Jung, Q. Zhou, and J. T. Birkholzer (2013). "Making sense of global sensitivity analyses". *Computers & Geosciences* 65, pp. 84–94. DOI: 10.1016/j.cageo.2013.06.006.

Ward, B. A., M. A. Friedrichs, T. R. Anderson, and A. Oschlies (2010). "Parameter optimisation techniques and the problem of underdetermination in marine biogeochemical models". *Journal of Marine Systems* 81, pp. 34–43. DOI: 10.1016/j.jmarsys.2009.12.005.

Williams, S. L. and J. E. Smith (2007). "A Global Review of the Distribution, Taxonomy, and Impacts of Introduced Seaweeds". *Annual Review of Ecology, Evolution and Systematics* 38.1, pp. 327–359. DOI: 10.1146/annurev.ecolsys.38.091206.095543.

Willmott, C. J. (1982). "Some Comments on the Evaluation of Model Performance". *Bulletin of the American Meteorological Society* 63, pp. 1309–1313. DOI: 10.1175/1520-0477(1982)063<1309:SCOTEO>2.0.CO;2.

Willmott, C. J. and K. Matsuura (2005). "Advantages of the mean absolute error (MAE) over the root mean square error (RMSE) in assessing average model performance". *Climate Research* 30, pp. 79–82. DOI: 10.3354/cr030079.

Zaldívar, J., F. Bacelar, S. Dueri, D. Marinov, P. Viaroli, and E. Hernández-García (2009). "Modeling approach to regime shifts of primary production in shallow coastal ecosystems". *Ecological Modelling* 220, pp. 3100–3110. DOI: 10.1016/j.ecolmodel.2009.01.022.

Zeldis, J. R. (2004). "New and remineralised nutrient supply and ecosystem metabolism on the northeastern New Zealand continental shelf". *Continental Shelf Research* 24.4-5, pp. 563–581. DOI: 10.1016/j.csr.2003.11.008.

Zhang, S., R. J. Karunamuni, and M. C. Jones (1999). "An Improved Estimator of the Density Function at the Boundary". *Journal of The American Statistical Association* 94.448, pp. 1231–1240. DOI: 10.1080/01621459.1999.10473876.